Diagnostics for time-varying exhaust reconstruction applied to a low-power Pulsed Plasma Thruster:

Thruster design, development, and characterization

by

María Scherezade Barquero Balsera

A dissertation submitted by in partial fulfillment of the requirements for the degree of Doctor of Philosophy in

Aerospace Engineering

Universidad Carlos III de Madrid

Advisor(s):

Mario Merino Martinez
Jaume Navarro Cavallé

Tutor:

Mario Merino Martinez

July, 2025

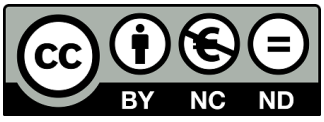

To my mother.
A mi madre, Toni Barquero. A mi madre como mujer. A mi madre como madre. A ti, mamá.

As always, *to my auntie*, mi tía Alti;
who was also the first person from whom I heard about research.

A mi Extremadura; mi hogar.

Los plasmas; los thrusters; el cátodo de Hayabusa2; nuestra cámara grande; el primer instante en que una tuerca se afloja al usar la llave; la caja grande de cables, las cajas llenas de reguladores de gas; conectar o desconectar un conector banana; el ruido de las bombas; la alerta ante el sonido de una descarga fuera de la cámara; las azoteas de Leganés desde el despacho, las azoteas de la Universidad; las paredes rojizas de ladrillo; la imagen de la luz de una farola reflejada en una de ellas, vista desde el ventanal de la primera planta cuando ya ha anochecido; el sol, el mármol rojo y el pasillo vacío del ala de laboratorios o las escaleras que llevan al garaje; los "aliens" en el mármol; bajar planta por planta las escaleras del fondo del departamento y observar las tres ventanas, atravesar la Universidad a oscuras con una pequeña linterna; aquel IEPC en el MIT; la inmensidad de aquellos laboratorios en ISAS, y sus barandillas, sus pasillos y aquellos ventanales al ataradecer y cuando la noche; la taza de té de la señora Miwako Funada; ...

ACKNOWLEDGEMENTS

Funding Acknowledgments

This research has been supported by the following projects:

- The MARTINLARA Regional Project (Millimeter wave Array at Room Temperature for INstruments in LEO Altitude Radio Astronomy) [1] funded by the Comunidad de Madrid under Grant reference S2018/NMT-4333 MARTINLARA-CM.
- The ESPEOS project, funded by the Agencia Estatal de Investigación (Spanish National Research Agency) under Grant number PID2019-108034RB-I00/AEI/10.13039/501100011033.
- The ADAPT project, co-funded by the Agencia Estatal de Investigación (Spanish National Research Agency) and the European Union under Grant number PID2023-150052OB-I00.

Additional funding come from the MadridFlightOnChip (MFOC) project, co-funded by the Comunidad de Madrid and European Regional Development Fund Operational Programme 2014-2020, under Grant reference Exp. 49.520608.9.18 / Op. code DGII/01/21/003-18.

Finally, the Japan Aerospace Exploration Agency (JAXA) assumed the full cost of the experiments conducted at its facilities, which are included in this thesis through Appendix D.

Personal Acknowledgments

(This section is admittedly long. :))

I write now with the peace that comes from knowing this thesis has, in some small way, contributed to the fascinating field of unsteady EP (Electric Propulsion) plasmas.

What I hope to carry most from this period is a deep appreciation for being part of academic spaces, where inspiration arises from a constant awareness of the vastness of knowledge, and where I have found clarity in my desire to continue doing research. I now know that I enjoy research grounded in scientific reasoning, especially when it involves experimental work that remains connected to equations.

This enriching period has been shaped by many contributors: above all, my supervisors, but also peers in the pulsed EP field (including publication reviewers) and PhD colleagues, and, undoubtedly, my mother. In line with my choice to focus on the positive, to treat challenges as opportunities to grow wiser and to avoid repeating past mistakes, I want to reflect below on the positive contributions each of them has had on me during this time.

I want to begin by recognizing myself. Though this thesis opens with the name assigned to me by bureaucracy, I choose to begin this acknowledgment with my true name: Scherezade Barquero. I value the learning, the resilience I have shown, the proactivity I have developed, the conviction and self-confidence I have consistently maintained, and the happiness I have always tried to seek. I'm proud of my willingness to always engage with what I perceive as difficult, overcoming fear with the determination that it will never hold me back. I am proud of being driven by curiosity and the desire to understand, by a refusal to feel ashamed of what I don't know, and by the decision to never let the opinions of others limit me.

Second, I would like to express my sincere gratitude to my thesis advisors, Mario Merino and Jaume Navarro-Cavallé, for their continuous guidance throughout this PhD process. I also thank Professor Eduardo Ahedo, who guided me at the beginning of this journey and mentors the former two, thus laying the foundation on which the standards of the Plasmas and Space Propulsion Team (EP2) are built. / I espe-

cially thank Mario, my tutor, for being a constant point of reference throughout this period. / They have fostered a highly demanding yet deeply empowering environment, one that instills the conviction to push forward, no matter the challenge. Their intellectual strength, critical rigor, relentless pursuit of knowledge and excellence, and the high standards they hold for themselves and others have profoundly shaped my understanding of what meaningful research truly demands, and have inspired me to continually aspire to it. This context has taught me not only about the subject matter, structure, or critical thinking, but also about ambition, pragmatism, assertiveness, and perseverance. Above all, it has made me acutely aware of the ever-present room for improvement, growth, and deeper understanding in everything we do.

Pulsed EP was new to the group's expertise, making this PhD particularly challenging in its own way. However, I feel my supervisors and I have grown together through this project, and I really hope our professional paths remain connected.

To conclude this dedication to my supervisors, I also want to thank their responsibility and hard work in fostering a strong funding environment, where I never had to worry about financial limitations affecting my research needs. Finally, I thank the institutional support during the health issues I have faced in this period, granting an extension of my PhD deadline and safeguarding my labor rights.

Third, I also want to express my gratitude to JAXA for accepting our proposal to conduct research at their ISAS facilities, a priceless opportunity to expand my knowledge not only in EP but also in high TRL (Technology Readiness Level) systems. I especially want to acknowledge Kazutaka Nishiyama Sensei, head of the EP Laboratory, for dedicating time to me; learning firsthand from someone who has played a key technical role in historic missions like those involving the Hayabusa mission series has been an experience of immense value.

Additionally, I would like to thank the reviewers of the two journal papers on Pulsed Plasma Thrusters we have published. Their thorough and insightful reviews, which align with the critical perspective my supervisors and I strive to maintain in our research, have resulted in more clear and meaningful publications. In the same way, we appreciate the constructive feedback of the international reviewers, aimed at improving the clarity and impact of the dissertation.

About my closest colleagues in STEM (Science, Technology, Engineering, and Mathematics), I want to say that their intelligence and dedication to their own work have been a constant source of inspiration throughout my research journey. From the beginning of my master's thesis through these years of doctoral work, I have been fortunate to connect with surprising minds from many different places and fields whose achievements and, often, multifaceted character have motivated me to grow and strive for excellence. Focusing on my PhD peers at EP2: although each of our theses has been largely independent (and thus, often, solitary), the supportive environment we have shared, free from competition and filled with mutual encouragement, laughter, and thoughtful exchanges when needed, has made this journey deeply human. I am grateful for the opportunity to learn from such diverse perspectives and for the friendships that have blossomed along the way. This gratitude extends to all of you, from those I met at the very beginning, some of whom have already gone on to contribute to industry or academia around the world, or to launch their own venture with IENAI, to those who joined in the later years of my PhD, with whom, curiously, I have had the pleasure of connecting on a more personal level. / I feel fortunate to have shared this journey with you. / While I generally prefer not to list names in writing, I feel compelled to acknowledge those with whom I shared the most throughout this journey, my office mates for the greater part of the PhD: my querido amigo Kique (Enrique) Bello, Alberto Marín, ever ready to help, and, also as close companions through the many beautiful but long days in our underground lab, Tatiana Perrotin, always a safe space, and Marco Inchingolo. (Respectively thanks to these two individuals, the group now also possesses its own Hall and ECR thrusters.)

Marco, I cannot separate you from the vivid imagery of my PhD journey; you are the generational peer whose technical reasoning I trust most, and on a personal level, you have become a part of me.

I would like to take a parenthesis to comment on the role of Tatiana and me as women in STEM

within EP2, as well as that of our predecessors. She and I started the PhD when Sara Correyero and Xin Chen, pioneers, were the only women researchers in the EP2 group. Indeed, Sara was also the first woman PhD student in the department. Although our team has grown significantly in number since then, no additional women have joined as PhD candidates nor postdocs. For long periods, Tatiana and I, along with Sadaf Shahsavani and Firozeeh Foroozan from other research groups within the department, remained the only female presence among PhD candidates, with almost no women in higher research positions across the department. However, it is also fair to note that other research teams in the department have made progress in gender diversifying. While, personally, I have not found this situation problematic within my own research group or institution, unfortunately I cannot say the same about all the professional spaces in which I have participated. Now that Tatiana will be the only woman researcher remaining at EP2, as I have recently joined the National Fusion Laboratory at the CIEMAT, I sincerely hope that my admired EP2 group takes meaningful steps to address this imbalance and foster a more inclusive and representative environment. I extend this desire to the EP field itself, where achieving gender diversification, to include women and non-binary researchers, remains a significant challenge as well. / Working for gender parity in our field is also an individual responsibility, for which we all have to engage in critical self-reflection. This starts by trying to understand why there is a dramatic gender gap when choosing engineering studies, and promoting and participating in effective policies to save it. Furthermore, contributing to create work environments that allow women to focus solely on our research, without having to reclaim space that is often consciously or unconsciously denied, remains a challenge in many scenarios. In those places, having to overprove ourselves and strive for our work to be recognized is a hard reality; in addition, an extreme level of assertiveness is often required to avoid facing this without "tarnishing" your image, which is not only exhausting but also unfair.

Others at the UC3M have also contributed to make this period more beautiful, including some of our administrative colleagues and members of the cleaning staff, especially Mariángeles, ensuring that my beloved lab remained not only clean but also an emotionally welcoming space every day.

To conclude my thanks to colleagues from professional settings, I want to acknowledge our Japanese student peers at the JAXA EP Laboratory. Marco and I were warmly hosted by them, and together with Ani (Anivid) Pedros, they made our research experience abroad truly memorable.

* * *

On a deeply personal note, and without a doubt the foundation for everything else to develop, I want to thank my mother, Toni Barquero, for being my only truly meaningful personal support key to getting this PhD.

I want to thank her for her unwavering support and encouragement, which have nurtured my self-confidence, conviction, and determination, and for always helping me imagine any path as possible, and trust in my ability to follow it. She has always nurtured me with love but also honesty, offering constructive critical perspectives that has helped me grow. From her, I learned to take emotional and professional responsibility, to act with assertiveness, and to recognize the strength in walking away from places where one does not deserve to be. She is the most intelligent, strong and empathetic person I have ever met; the person I admire and who inspires me the most; the one who has shaped my understanding of success and courage, and their relativity. I admire her endless curiosity and how she never stops learning, writing, reflecting, and using both her voice and presence to spark change everywhere, committed to helping others shine. / Mamá, you are the person with whom I have shared the most enriching conversations; while I hope to give you some inspiration in return, I know that so much of who I am becoming is rooted in what you have given me. Y, sobre todo, te debo tiempo, mamá.

I would also like to dedicate a few words to my family, to share with them some of the things I have learned from each of them. By "family", I refer strictly to those with whom I share a space grounded in love, support, and a daily sense of home; for me, it consists solely of the people on my mother's side.

I feel privileged to belong to this caring and supportive circle that celebrates each other's successes and stands together in difficult times. Within this family, I especially want to recognize my core circle: my grandmother, my two sisters Carolina and Almudena, and two of my cousins, Pedro Antonio and Inés.These four veinteañeras are smart, resilient, brave, and compassionate. Thank you to them for always helping each other move forward, motivating me to do my best to be at least a small support they can rely on when needed. I feel incredibly lucky to be part of this amazing party crew.

A ti, abuela, te quiero. Gracias por haber compartido tus raíces con nosotras para que tuviésemos una base sobre la que crecer y diverger; mi pasado termina en aquél que tú ya no sentías tuyo. Gracias por no haberles enseñado a tu hijo e hijas a criticar a otros seres, y porque, junto al abuelo Antonio, hicisteis que se les grabase que *para comida y libros, todo*. Sonrío cada vez que te recuerdo tratando de memorizar la palabra "aeroespacial", o contando por teléfono que no te preguntaran por bodas sobre mí, porque yo estaba muy ocupada haciendo cohetes. / Eres buena, abuela. / Desde siempre, mientras nos contabas, con tu ganchillo entre esas hipnotizantes manos, ha sido imposible no apreciar tu profunda memoria y tu amplio vocabulario... sin embargo, ha sido la madurez la que me ha hecho ser consciente de que lo que además posees es numerosas y muy valiosas cualidades para la narrativa. Ojalá hubieras vivido en otra época. Aunque sabes qué, gracias por nuestras llamadas diarias por whatsapp, (*"¿¡Quién lo iba a decir, compañera!?"*) porque las he vivido con la verdadera sensación de que este presente nos estaba perteneciendo a ambas.

To Almudena, my relentless and ambitious (gen-Z) soul. Thank you for the generosity with which you share about your life, always told in a way that is so deeply permeable to the emotions you could be experiencing, whether enthusiasm or anything else. It is a constant reminder not to pass through life superficially. Determination, conviction, and vehemence are powerful tools when balanced with empathy, and I am sure you have everything within you to achieve the perfect balance for success. Thank you for showing me what resistance means, and for your desire to become better. While I have many examples in mind of how you have overcome challenges, and many reasons to be proud of you, I would like to focus on one of the greatest lessons I have learned from having you as my sister: what becoming better means. It comes simply from increasing the love you give and allowing yourself to receive it. I am not sure you even realize how much you have taught me about this.

To Carolina. So smart and so close to me that you look into my eyes and really know what I am probably thinking. Thank you for teaching me about self-improvement, about doing your best, for showing how confidence can be always rebuilt step by step, and for inspiring us all with the humility but remarkable joy that surround your personal and professional great achievements. I admire your commitment to living as an example, even when it feels overwhelming, and for reminding us of the vital importance of presence in nurturing the affective connections. Thank you for your generosity and constant effort to understand what others need, always striving to be better and fully present in every way possible (conscious, attentive, empathetic, joyful, and helpful). I do owe you for your continuous, active and mature presence in everything I do; always making sure I feel supported, no matter the distance, no matter the time, no matter your tiredness. Thank you for your awareness of the power of love, as well as symbolism to express appreciation; thank you for finding boundless joy in the small things.

To Inés, thank you for always *asking these "how" and "why" questions* that resonate so deeply with my own; and also for the thoughtful silences that follow, filled with respectful curiosity and space for reflection. Conversations with you leave me less certain of my answers, and that is a priceless gift. I am so proud of everything you've achieved; not only in the physics nerd world we both share but in every other aspect of who you are. Thank you for showing us how to how to embrace difference with bravery and perseverance in so many areas of your life, making it not just something to admire, but something to aspire to. Thank you for unconsciously teaching us what it means to grow, to rebuild home; finding new places to belong in whatever the space that allow a smile and a breath to exist, like a song from a beloved band.

To Pedro Antonio, I deeply admire the humble way in which you approach your professional achievements, which are far from ordinary, and the responsibilities that come with them. I admire and deeply

respect the doctor you are, but, as Grandma once said, I admire even more, the part of your person that you bring into your profession. You have a remarkable ability to take action where change is possible, while also accepting what cannot be changed. You take on responsibility, whether fair or not, and continue moving forward, always striving to enjoy every moment of life to the fullest, always having fun. I deeply admire your strength, intelligence, and your ability to see beyond your own bubble. It takes true wisdom to use humor the way you do, genuinely, and without concern for appearances.

Moving on to friends, many, old and new, have contributed to my personal growth over these six years in Madrid. Nonetheless, I especially want to dedicate this to four successful women whose deep connections with me have been built over years and who are constants in my daily life. Mis amigas; we learn from each other about the need for, and joy of, sharing, presence, and love, beyond kilometers.

To close this section, I come back to me. I consider myself a very lucky girl. / I would like to believe that walking through illness in my own body has not brought anything truly new, nothing I had not already started learning by witnessing others I love go through it from places far more painful than mine. I would like to believe that it was twelve years ago, not in these more recent ones, that I began, all at once, to realize how much more there is to learn about empathy, about putting things into perspective, about wanting to love more, about the urgency of wanting to live while one is still alive and in a condition to do so. Still, I do carry a certain clarity now; one that reminds me of how short memory can be, how fragile our constructs are, and how limited the usefulness of fear really is. It has brought me peace, enough to release the weight of needing concrete answers, to live more lightly, to speak more firmly. I'm proud of the woman I am building, of the awareness and desire for growth, of my strength, my practicality, and the commitment to live each day with the conviction that it is worth living for its own sake.

If I look back at a younger Scherezade, speaking to her peers during graduation speeches or just to herself, I would tell her: thank you, you are truly on your way. You have evolved but remain someone who recognizes herself beyond changes, and you are becoming a scientist. A job does not define or dignify a person, but I consider it a gift to be on the path toward the dreams one has for herself.

As I have tried to convey, I have sought to find happiness in each day of work. However, I want to leave the following as a reminder for the future. I have learned that while I have found purpose in the research I have carried out; passion does not justify keeping a consistent routine of overwork and late nights no matter the circumstances, as it has been during my PhD. This was driven by my strong conviction and internal pressure to meet the high standards I believed were necessary to build a competitive profile. Probably like many, across different levels, I have internalized that regardless of personal or professional challenges, what matters most is producing (meaningful, publishable) results; either you meet expectations or step aside. Although I still prioritize professionally enriching environments despite their demands, I also no longer want to continue proving that kind of strength to myself. These reflections remind me of the need to set boundaries, not to sacrifice balance, but also to commit to finding the tools that allow one to keep pursuing excellence within these boundaries. Concerning this, I have also come to see the value of developing a solid research plan from the start, to use time both efficiently and meaningfully, that is, toward work that is publishable. This reminder is especially important for when, in the future, I take on the responsibility of supporting my own PhD candidates, striving not to compromise their competitiveness within the standards of the status quo while helping to foster a healthier (and, if possible, also with better economical conditions) PhD experience.

Indeed, what a journey.

Here's to continuing to nurture that sense of freedom and deepening the feeling that, for a privileged few, the world can feel less distant and less limiting.

PUBLISHED AND SUBMITTED CONTENT

As an outcome of this thesis, the following journal articles and proceedings in relevant conferences have been published. The contributions are specified below. As noted below, these works are fully or partially reproduced as chapters in this document, with additional clarification provided in a footnote at the beginning of the relevant chapter. Nonetheless, the material from the following sources included in this thesis is not singled out with typographic means and references.

Journal articles about Pulsed Plasma Thrusters

1. **Ref. [2]:** S. Barquero (SB), J. Navarro-Cavallé (JNC), and M. Merino (MM), "Pulsed plasma thruster exhaust reconstruction", Plasma Sources Science and Technology (Q1), vol. 33, no. 4, p. 045007, April 2024. 10.1088/1361-6595/ad35e5. [Online.] These data are also openly available at 10.5281/zenodo.10908404. Chapter 5 fully transcripts this entry.

2. **Ref. [3]:** S. Barquero, J. Navarro-Cavallé, and M. Merino, "Reconstruction of the transient plume cross-section of a Pulsed Plasma Thruster", Plasma Sources Science and Technology (Q1), vol. 34, no. 5, p. 055003, May 2025. 10.1088/1361-6595/add20a. [Online.] These data are also openly available at 10.5281/zenodo.13820945. This DOI also includes a video showing the plume cross-section current density distribution changing over time. Chapter 6 fully transcripts this entry.

   In both publications [2] and [3], the experiment design and development, test execution and data acquisition, and data post-processing have been carried out by SB. The developments of the expansion model and reconstruction algorithm, respectively for [2] and [3], were a collaborative effort among all three contributors SB, MM and JNC. SB drew conclusions and wrote the paper, incorporating feedback from her advisors MM and JNC.

Other journal articles

1. **Ref. [4]:** S. Barquero, K. Tabata (KT), R. Tsukizaki (RT), M. Merino, J. Navarro-Cavallé, and K. Nishiyama (KN), "Performance characterization of the μ10 electron-cyclotron-resonance ion thruster using alternative propellants: Krypton vs. Xenon", Acta Astronautica (Q1), vol. 211, p. 750-754, October 2023. 10.1016/j.actaastro.2023.06.036. [Online.]

   In addition to the main research on Pulsed Plasma Thrusters, this dissertation includes results from a research collaboration with the Japan Aerospace Exploration Agency (JAXA), conducted during SB's research stay at JAXA's Electric Propulsion Laboratory. As these activities fall outside the primary scope of this thesis, they are presented in the appendices. This work comprises the first experimental comparison between Krypton and Xenon propellants in the Hayabusa2 and DESTINY$^+$ μ10 gridded ion sources, based on Electron Cyclotron Resonance (ECR) plasma generation, and their associated ECR neutralizer. The corresponding journal publication is fully reproduced in Appendix D.

   Concerning the contributions to [4]: KN proposed the experiment, RT got the Krypton and was responsible for overseeing safety management bureaucracy for operating with this gas, SB planned the tests which were approved by KN and RT. The ion sources and the cathode as well as the baseline setup for their operation are JAXA developments; Special mention concerning this work to KN and KT. SB also contributed to set up the experiment and was solely,full responsible for setting up the feeding system. Furthermore, SB operated the ion sources and the cathode, executed the tests, carried out data acquisition and post-processed the data. She drew conclusions and wrote the paper, incorporating feedback from all the coauthors (KN, RT, KT, MM and JNC).

[Selected conference papers and peer-reviewed journal papers are also available online on the Plasmas and Space Propulsion Team (EP2) website [5].]

Conference proceedings about Pulsed Plasma Thrusters

1. **Ref. [6]:** S. Barquero, J. Navarro-Cavallé, and M. Merino, "Design of an experimental ablative pulsed plasma thruster for micropropulsion", Space Propulsion Conference (SPC), No. 254, Association Aéronautique et Astronautique de France, March 17-19, 2021. Available online on the EP2 publications' website. Chapter 2 includes this entry with adaptations and some additional content.

   The thruster design and development have have been carried out by SB, with the advice of MM. The paper has been written by SB with feedback from MM and JNC.

2. **Ref. [7]:** S. Barquero, J. Navarro-Cavallé, and M. Merino, "Experimental plume characterization of a low-power Ablative Pulsed Plasma Thruster (APPT) ", 38^{th} International Electric Propulsion Conference (IEPC), No. 556, Electric Rocket Propulsion Society, Boston (MA), June 19-23, 2022. Available online on the EP2 publications' website. Chapters 3 and 4 include part of the content of this entry with adaptations and some additional material.

3. **Ref. [8]:** S. Barquero, J. Navarro-Cavallé, and M. Merino, "Time-Resolved Reconstruction of the Plume of a Pulsed Plasma Thruster (PPT)", 10^{th} Aerospace Europe Conference (EUCASS) / 9^{th} CEAS, No. 643, Lausanne, Switzerland, July 9–13, 2023. DOI: 10.13009/EUCASS2023-673. Available online on the EP2 publications' website.

4. **Ref. [9]:** S. Barquero, J. Navarro-Cavallé, and M. Merino, "Cross-sectional characterization of the exhaust of a Pulsed Plasma Thruster", 39^{th} International Electric Propulsion Conference (IEPC), No. 387, Electric Rocket Propulsion Society, Toulouse, France, June 23-28, 2024. Available online on the EP2 publications' website.

   References [7] and [8, 9] present preliminary work that led, partially and fully respectively, to the consolidated results published in the journal articles [2] and [3]. For this reason, their content is not directly included in the present document.

   For references [7, 8, 9], identical author contribution statement than that of the journal papers [2] and [3] applies.

Other conference proceedings

1. **Ref. [10]:** S. Barquero, K. Tabata, R. Tsukizaki, M. Merino, J. Navarro-Cavallé and K. Nishiyama, "Alternative propellant study (Krypton vs. Xenon) of the μ10 ECR Gridded Ion Thruster at its Hayabusa2 and DESTINY^{+} Missions", 34^{th} International Symposium On Space Technology and Science (ISTS), Kurume, 2023. Available online on the EP2 publications' website.

   This reference is based on the journal publication [4], which is fully reproduced in Appendix D.

   The author contribution statement for this work is identical to that provided for [4].

OTHER RESEARCH MERITS

Open access datasets

1. **Ref. [11]**: S. Barquero, J. Navarro-Cavallé, and M. Merino, "DATA from: Pulsed plasma thruster exhaust reconstruction" [2], ZENODO repository, 2024. Available under DOI 10.5281/zenodo.10908404.

2. **Ref. [12]**: S. Barquero, J. Navarro-Cavallé, and M. Merino, "DATA from: Reconstruction of the transient plume cross-section of a Pulsed Plasma Thruster" [3], ZENODO repository, 2024. Available under DOI 10.5281/zenodo.13820945.

Open source tools

1. **Ref. [13]**: S. Barquero, J. Navarro-Cavallé, and M. Merino, "TIME-SERIES ToF (Time-of-Flight) tool for exhaust reconstruction in unsteady electric propulsion", GitHub/ZENODO repository, 2024. Code for the journal paper "Pulsed plasma thruster exhaust reconstruction" [2].

2. **Ref. [14]**: S. Barquero, J. Navarro-Cavallé, and M. Merino, "WAVES (Wire Array for Variable Exhaust Scanning) tool for time-varying reconstruction of the the plume cross section in unsteady electric propulsion", GitHub/ZENODO repository, 2024. Code for the journal paper "Reconstruction of the transient plume cross-section of a Pulsed Plasma Thruster" [3]. Registered under DOI 10.5281/zenodo.14653074.

Other contributions in Conferences

1. **Ref.** [15]**:** S. Barquero, J. Navarro-Cavallé, and M. Merino, "Preliminary test campaign of an ablative pulsed plasma thruster for micropropulsion", 5^{th} International Workshop on Micropropulsion and CubeSats (MPCS), Toulouse, 2021. Oral presentation.

2. **Ref.** [16]**:** J. Navarro-Cavallé, M.R. Inchingolo, T. Perrotin, S. Barquero, P. Fajardo, M. Merino and E. Ahedo, "Experimental activities at the Plasma and Space Propulsion Team (EP2-UC3M)", EPIC Workshop, Naples, May 9-12, 2023.

Technical reports (funded projects)

1. **Ref. [17]:** S. Barquero, "Pulsed Plasma Thruster Design", NANOSTAR Student Challenges - Report, NANOSTAR consortium - Interreg Sudoe Programme through the European Regional Development Fund (ERDF), 2021.

2. **Ref. [18]:** S. Barquero, "Informe de modelado, simulación, requisitos y diseño preliminar de sistema de micropropulsión PPT (M18)", Millimeter wave Array at Room Temperature for INstruments in LEO Altitude Radio Astronomy (MARTINLARA) Project Report - Objective 4.1, Co-funded by the Consejería de Ciencia, Universidades e Innovación of the Comunidad de Madrid and the European Union, 2023.

3. **Ref. [19]:** S. Barquero, "Informe de ensayo y experimentación con prototipos PTT (M42)", Millimeter wave Array at Room Temperature for INstruments in LEO Altitude Radio Astronomy (MARTINLARA) Project Report - Objective 4.3, Co-funded by the Consejería de Ciencia, Universidades e Innovación of the Comunidad de Madrid and the European Union, 2023.

4. **Ref. [20]:** S. Barquero, “Informe de desarrollo de modelo de ingeniería de sistema de micropropulsión PPT (M48)”, Millimeter wave Array at Room Temperature for INstruments in LEO Altitude Radio Astronomy (MARTINLARA) Project Report - Objective 4.4, Co-funded by the Consejería de Ciencia, Universidades e Innovación of the Comunidad de Madrid and the European Union, 2023.

Undergraduate Student Tutoring

1. **Ref.** [21]**:** A. Cabello López, “Design and Development of a micro-PPT Thrust Balance”, Bachelor’s thesis (Grade: 10/10; Award: Proposed to Honors), Universidad Carlos III de Madrid, 2020. Supervisors: M. Merino and S. Barquero. Available online on the MARTINLARA Project website, (direct download HERE).

   [The design of proposed impulsive torsional thrust balance for low-power PPTs asymmetrical is based on a swing-gate configuration able to measure single impulse bits in the range of 5 – 100 μNs and thrust forces in repetitive shot operation of 1 –100 μN, with a estimated resolution of 0.1 μN. The response of the balance has been modeled by a simple pendulum analysis and a flexible beam study. The contribution of both models allows for the coverage of the effects induced on the deflection by damping, the different punctual masses and the harmonic normal modes that arise due to the excitation of the thruster.]

   This work was presented as one of the NANOSTAR Student Challenges (NANOSTAR consortium - Interreg Sudoe Programme through the European Regional Development Fund (ERDF), 2021). As well, it is included in the technology report “Informe de preparación de micro balanza de empuje y puesta a punto de laboratorio (M24)”, Millimeter wave Array at Room Temperature for INstruments in LEO Altitude Radio Astronomy (MARTINLARA) Project Report - Objective 4.2, Co-funded by the Consejería de Ciencia, Universidades e Innovación of the Comunidad de Madrid and the European Union, 2023 [22].

ABSTRACT

This research makes contributions to the field of experimental plasma diagnostic methodologies for flowing transient plasmas. It proposes, develops and implements two fast-to-implement, cost-effective diagnostic tools for the time-resolved, 3D reconstruction of transient plumes in unsteady electric propulsion (EP) systems. Both tools rely on electrostatic probes operating in the ion saturation regime. The techniques, named TIME-SERIES Time-of-Flight (ToF) and WAVES (Wire Array for Variable Exhaust Scanning), enable a more accurate and efficient analysis compared to existing methods. TIME-SERIES ToF isolates the different ion contributions, providing deeper insights than traditional ToF methods using the same data; WAVES enables cross-characterization of the plume with a faster approach than existing alternatives. Although they are standalone tools, their results complement each other, providing a more comprehensive approach to the dynamics of the entire transient plume.

These two techniques have been applied on the exhaust of a custom-built low-power ablative Pulsed Plasma Thruster (PPT) experimental platform. It exhibits parallel-rail (also referred to as rectangular or planar) and breech-fed configuration with polytetrafluoroethylene (PTFE or TEFLON™, $(C_2F_4)_n$) as propellant, and operates nominally at 1000 V of initial discharge voltage and 6 μF of bank capacitance (thus, at 3 J of stored energy). The thruster is named PμLSA (PULSed Ablative plasma thruster for micropropulsion), and its design, development and experimental characterization are also presented in this work. It has been validated for reliable ignition and has been the subject of electrical characterization and plume plasma diagnostics across various configurations, with particular emphasis on operational parameterization. The latter includes varying the discharge voltage and the bank capacity up to 10 J of discharge energy. Key findings from baseline electrical characterization reveal that the discharge signal exhibits damped oscillations with natural frequency on the order of 10^2 kHz and with the signal amplitude decaying by a factor of 10 after about 5 μs. Good repeatability of the electrical discharge curve among shots is observed. At nominal conditions the current signal peaks at 10 kA and each firing consumes approximately 4 μg of propellant.

Concerning the plume analysis, the two novel experimental tools introduced above have been investigated through their application to the PPT exhaust time-series data, alongside the traditional ToF methodology that forms the foundational framework for the first technique. This first technique, TIMES ToF, extends the traditional ToF methodology by going beyond simple feature probe-correlation, typically used to estimate average ion velocities. It introduces a model for the plume expansion and leverages the entire time-series dataset, enabling the isolation and detailed characterization of the different ion populations contributing to the exhaust. The new approach significantly improves both accuracy and interpretive insight. This expansion model reconstructs the exhaust as a combination of Maxwellian-like ion groups, each characterized by its own velocity, thermal spread, density, generation time, and divergence. In this study, the model parameters are obtained via least-squares fitting to the time-resolved ion-saturation current measurements from three axially-distributed single Langmuir probes placed downstream. Overall, a good fit is achieved with three ion groups, across the entire operational parametric space. These ion groups have mean velocities ranging from 50–70, 30–45 and 10–25 km/s respectively, with the second population arriving at the probes being the one driving the most of the plume current. Additionally, the time-integrated current within the ion collection time window exhibits a linear relationship with the discharge energy. This statement, combined with the observation that ion velocities for each population remain relatively constant across all study cases, suggests that the impulse bit scales linearly with discharge energy. This conclusion is consistent with direct measurements reported in the literature.

The second technique investigated, WAVES, enables the reconstruction of the 2D ion current density distribution across the exhaust cross-section at each time step, using ion-saturation-current data collected by a grid of electrostatic wire probes aligned with the two cross axes, together with a variable-separation algorithm to solve the inverse problem at each time step. This method allows for significant testing time

savings with respect to comparable approaches (by at least a factor of 7.5) and has the added advantage of being applicable to plumes of steady-state operation thrusters. Shown results include the PPT operating nominally. The proposed technique has been been able to capture asymmetries present in the PPT plume. These results reveal that the ion beam is single-peaked in the direction perpendicular to the electrodes at all times, while in the direction parallel to them is more outspread, as a characteristic of rectangular PPTs, and shows two peaks, one at each channel side. Furthermore, a small deviation of the current towards the cathode and one of the channel sides (within the parallel-to-electrode plane) is also found.

Separately from the previous work, the foundational elements of a paraxial three-fluid model for the in-channel ionization and acceleration of planar-PPT discharges are introduced as a basis for future research.

LONG SUMMARY

Objectives:

The present research makes contributions to the field of experimental plasma diagnostics methodologies for flowing transient plasmas.

It proposes two novel, cost-effective and easy-to-implement experimental plasma diagnostic techniques for the time-resolved and 3D reconstruction of transient plumes of unsteady electric propulsion systems. These methods, based on ion saturation current measurements from electrostatic probes operating in the ion saturation regime, provide deeper insights and enable a more accurate and efficient approach to analyzing the dynamics of transient plasma exhausts than existing comparable techniques. The two diagnostic tools developed are named TIME SERIES Time-of-Flight (ToF) and WAVES (Wire Array for Variable Exhaust Scanning) respectively. TIME-SERIES ToF isolates the different ion contributions, providing deeper insights than traditional ToF methods using the same data; WAVES enables cross-characterization of the plume with a faster approach than existing alternatives. Although they are standalone tools, their results complement each other, providing a more comprehensive approach to the dynamics of the entire transient plume.

On the one hand, the advantage of the TIME-SERIES ToF technique with respect to the traditional ToF methodology which is reinterpreting, is moving beyond simple feature probe-correlation, typically used to estimate average velocities, to individually characterize the velocity distribution of each one of the different ion populations involved by considering the entire time-series data and proposing a plume expansion model. On the other hand, the WAVES diagnostic tool enables accurate cross-sectional plume analysis together with offering significant time savings compared to conventional divergence scanning methods. In addition to assessing plume divergence, it allows for the investigation of space asymmetries. Furthermore, this second technique is also valid to explore steady plumes.

These two techniques have been applied on the exhaust of a custom-built low-power ablative Pulsed Plasma Thruster (PPT) experimental platform. It exhibits parallel-rail (also referred to as rectangular or planar) and breech-fed configuration with polytetrafluoroethylene (PTFE or TEFLON in particular, and ablative PPT. This work constitutes the first research on PPT technology developed in the country, both in academia and industry. In addition, this work marks the beginning of the Plasmas and Space Propulsion Team's (Equipo de Propulsión Espacial y de Plasmas, EP2) involvement in pulsed electric propulsion. Ablative PPTs essentially consist of a pair of electrodes (cathode-anode) shaping a channel-like configuration (coaxial or rectangular, alternatively referred to as planar or parallel-rail) connected to an energy storage unit, typically a capacitor bank. A solid propellant, commonly a dielectric and, in particular, polytetrafluoroethylene (PTFE or Teflon™, $(C_2F_4)_n$) is placed between the electrodes at one end of the channel. Once the capacitor bank is charged up to a sufficiently high voltage for, once a discharge trigger acts, enabling the channel breakdown over the propellant surface, a fraction of the propellant is ablated and ionized. This process is known as a discharge flashover. The resulting discharge current generates a self-induced magnetic field that causes the Lorentz force, which accelerates the plasma downstream and away from the device, producing thrust.

Serving as a research platform, the developed PPT breadboard model is named PμLSA (PULSed Ablative plasma thruster for micropropulsion). The thruster is a low-power, parallel-rail ablative PPT, and it operates nominally at 1 kV of discharge voltage and 6 μF of capacitance (thus corresponding to 3 J of stored energy). The system utilizes PTFE as the solid propellant, with discharge initiated by a 1.5 kV custom-designed metal-insulator-metal spark plug. The prototype is specifically designed to support rapid iteration of both operational and geometric discharge parameters, as well as electronics, thereby streamlining experimental research.

In this work, the experimental results from the investigation of PμLSA operation serve two main purposes: first, to enrich the existing database on PPTs by addressing both the characterization of ion distributions and the scarcity of time-resolved divergence data for pulsed plasma-based thrusters; and second, to validate the two newly developed diagnostic methods through their application to the exhaust plume of the developed breadboard model. Accordingly, electrical characterization and, for the plume study, both innovative plasma plume diagnostics (TIME-SERIES ToF and WAVES) alongside the traditional ToF technique, serving as a reference frame, have been employed. The research has been carried out across various configurations, with special focus on operational parameterization.

Motivation:

The motivation for the defined objectives is now summarized. To start, the selection of the PPT technology in this work is primarily motivated by the increasing demand for down-scalable electric propulsion solutions, driven by the growing interest of the market in small satellites and advancements in technology. This need is further reinforced by the growing importance of low-cost, reliable propulsion systems for very-limited-size and -power budget missions, with miniaturization not currently achievable with the most established electric thrusters, such as Hall Thrusters and Gridded Ion Thrusters. The inherent characteristics of ablative PPTs make them particularly well-suited to this context: their pulsed operation allows the power budget to remain minimally dependent on the discharge energy, while their structurally simple design, which is based on solid propellants and free from moving parts, tanks, or injection systems, enhances their miniaturization potential and reduces in-orbit failure probability in this regard. Additionally, in contrast to the most-immediate solid-propellant pulsed-operation plasma thruster, the vacuum arc thruster, PPTs do not involve significant cathode erosion. This thruster technology has proven potential for both secondary propulsion in larger satellite missions and reliable use in power-limited, size-constrained systems as a standalone system. Its suitability for primary propulsion roles on nanosatellites, platforms that typically lack on-board propulsion, is particularly relevant. Nonetheless, although they offer structural simplicity, one of the biggest challenges of PPTs has been their historically low thrust efficiencies. These efficiencies tend to degrade further as the system is miniaturized, especially below 10 J, the energy range relevant for highly size-constrained satellites. This underscores the need for fundamental research to better understand the physical processes governing the PPT plasma discharge mechanisms and plume dynamics, thereby opening up broader opportunities for thruster optimization and facilitating integration into satellite systems. Potentially related to this, despite being the first electric propulsion system flown in space (1964) and the availability of flight-qualified units, PPT commercial adoption remains limited with no commercial missions beyond technology demonstrations being reported so far. Nevertheless, several dozen PPTs have been flown for research purposes, with a wide number of applications, as well as technology demonstration purposes, establishing it as one of the leaders in its market niche.

The plume physics investigation plays a crucial role, not only in understanding discharge behavior and improving thruster performance, but also in anticipating potential interactions with the spacecraft, , which could pose risks to sensitive satellite subsystems such as solar panels, which is indeed a key consideration for thruster integration into satellite platforms. Advancing the understanding of the PPT transient plume and improving the diagnostic techniques available to characterize it motivated the second pillar of this thesis. The existing literature highlights two key limitations that specifically motivated the development of the two novel techniques introduced above. First, several studies have revealed the presence of multiple ion species and ionization states in the exhaust of PPTs, which are expected to degrade the thruster performance. The traditional ToF methodology, though widely used in the field due to its simplicity, it falls short in accurately capturing the complexity of the multi-ion-population nature of these types of plumes. Second, studies on exhaust divergence in plasma-based thrusters, beyond just PPTs, remain limited. In addition, the few existing methods often involve complex and time-consuming experimental setups. As a consequence, time-resolved divergence data are scarce.

Consequently, the requirements for the new techniques proposed to address these limitations were that they should feature a simple setup, be cost-effective, and offer improvements over existing methods by

either enhancing the information extracted from the measured data and/or reducing the overall testing time.

Description of the novel plume experimental techniques proposed I: TIME-SERIES ToF

The traditional ToF analysis are typically employed to straightforwardly estimate average ion speed but is here extended to also provide a first approximation of the plume expansion rate, inferred by the correlated peak current decrease along the axial, ToF probes. Nonetheless, while these two results are useful for initial estimates, they offer limited accuracy and physical insight, as the peak features may arise from the combined contributions of multiple ion populations with distinct properties, an aspect that this methodology inherently overlooks. Additionally, selecting a time reference for the peak feature becomes more complex as an ion population spreads more broadly over time. Finally, accurate characterization of the plume expansion rate must account for downstream reductions in ion current density caused not only by plume divergence, which dominates the lateral expansion, but also by the thermal spread of the different ion populations, which primarily drives the axial expansion.

To address these drawbacks, a novel method has been proposed for reconstructing the time-varying ion populations contributing to the exhaust. This technique, named TIME-SERIES ToF, utilizes data from three single Langmuir probes axially distributed downstream of the plume, operating in the ion saturation regime. The method models the plume expansion as a superposition of multiple Maxwellian-like distributions, each characterized by parameters such as charge-to-mass ratio, main velocity, thermal spread, creation time and location, divergence, and magnitude. These distributions are fitted to the measured data by considering the full time series. This approach allows for a more comprehensive analysis of the ion current curves compared to traditional ToF by providing an estimate of the axial velocity distribution for each ion group involved.

Despite its advantages, the TIME-SERIES ToF methodology also has some limitations, particularly in scenarios where certain parameters, such as divergence, are poorly conditioned. The accuracy of the results is also sensitive to the assumption of a constant probe collection area along the ToF probe set, as the proposal lacks a sheath model to account for plasma density variations and probe wake effects. To improve the fidelity of the results, it is recommended to supplement the method with additional axial and off-axis probes.

Description of the novel plume experimental techniques proposed II: WAVES

A second novel diagnostic system, named WAVES, is proposed to streamline the acquisition of off-axis data compared to the current state-of-the-art scanning methods, significantly reducing both setup complexity and testing time by a factor of 7.5. Additionally, the WAVES results complement those of the TIME-SERIES ToF technique by providing a more accurate description of the time-varying divergence of the plume.

The proposed method consists of a grid of electrostatic wire probes, aligned along the two transverse axes, and operating in the ion saturation regime. These probes measure the time-evolution of the line integrals of the cross-section distribution of the ion current density of a plasma exhaust. A variable-separation algorithm is then employed to solve the inverse problem, reconstructing the current density distribution at each time step from the data collected by the probe array. This technique enables the study of spatial asymmetries in the exhaust.

Consistent to the description above, this technique is capable of resolving the cross-sectional expansion of both steady-state and transient plumes.

Results I: The thruster

On the one hand, the design, development, and experimental study of a low-power ablative PPT with a parallel-rail discharge channel is presented. Initially, the system requirements are defined within the framework of the MARTINLARA regional project. A complete thruster module, serving as a breadboard model for investigation purposes, is then designed and developed, ensuring ease of iteration throughout the research conducted, particularly regarding electronic topology, operational discharge parameters (initial

discharge voltage and bank capacitance) and discharge chamber geometry ratios.

Following that, the experimental plan is implemented, primarily focusing on conducting electrical characterization of the discharge and an analysis of the plume plasma using electrostatic probes. Additionally, propellant consumption mass measurements have been taken and, through visible photography, inspections of the discharge sequence as well as of the channel surfaces after endurance tests have been carried out. The experimental plan first ensures reliable ignition and then characterizes some thruster's operational envelope under 10 J of discharge energy.

The developed PμLSA PPT experimental platform has been validated for reliable ignition for discharge voltages of 750 V and higher and the resulting plasma has been studied by means of electrical and plasma diagnostics. The electrical discharge signal exhibits damped oscillations with natural frequency on the order of 102 kHz, and with the signal amplitude decaying by a factor of 10 after about 5 μs. Good repeatability among pulses is observed, particularly during the first discharge cycle. It is suggested that secondary reignitions may occur at discharge reversal maxima.

At nominal conditions the current signal peaks at 10 kA and each firing consumes approximately 4 μg of propellant, with minimal propellant surface charring observed. Increased discharge voltage boosts waveform amplitude, while higher capacitance essentially lowers the natural frequency. Enhancing the electric field, by increasing the discharge voltage or reducing channel height, increases propellant consumption uniformity and reduces the accumulation of discharge byproducs and charring along its surface. In-channel plasma imaging reveals non-uniform profile within the cathode-to-anode direction, with hot spots distributed along the electrodes. Additionally, measurements of propellant consumption at various increased discharge voltages also showed a corresponding increase in consumption. Reported findings in the literature align with the previous results.

Results II: Novel plume diagnostic methodologies

Regarding the plume results, the TIME-SERIES ToF method, applied to axial ion saturation current measurements, has demonstrated improved accuracy over traditional ToF by isolating/characterizing the multiple ion populations in the thruster exhaust. Across the explored operational parameter space, three distinct ion groups were typically identified, with velocities ranging from 50–70 km/s, 30–45 km/s, and 10–25 km/s, which aligns with findings in the literature. The first two ion groups arriving at the probes, which are faster and more confined than the third, drive most of the plume current collected. Then these two ion groups are suggested to be the dominant contributors to the impulse bit; in addition, they represent different charge-to-mass ratios and are generated during the primary breakdown phase. The relative increase in the second and third ion groups with increasing discharge energy is larger than that of the first group.

The time-integrated probe current exhibits a linear trend with the discharge energy. This finding, assuming it is proportional to the ionized mass flow rate, combined with the observation that ion velocities for each population remain relatively constant across different operational cases, supports the linearity of the impulse bit with discharge energy. This conclusion is consistent with data obtained from direct measurements reported in the literature.

Concerning the off-axis plume study, the application of the WAVES technique have provided insights into the time-resolved lateral expansion of the plume with (at least) 7.5 time-savings factor with respect to comparable methods. Key findings have revealed the presence of spatial asymmetries, with observations principally including a more confined spread in the cathode-to-anode direction than in the one parallel to the electrodes, which is characteristic in planar PPTs. This can be attributed to the asymmetric, self-induced magnetic field. Second, a deviation of the ion beam towards the cathode and one of the channel sides is also observed. These asymmetries involving deviations in both planes are systematically reported in the literature; while the former aligns with the direction of the electric field, the latter may possibly be caused by slight setup misalignments. Third, a two-peaked profile along the axis parallel to the magnetic field is observed, while a single-peaked profile exists in the perpendicular direction. This double-peak observation, although uncommon and warranting further research, may be related to the reported evolution of different

ion populations observed in some studies.

Furthermore, the cross-sectional analysis allows to identify that is the second ion group arriving at the probes which drives most of the collected plume current, confirming its more significant role in determining the overall performance of the thruster.

Conclusions:

In conclusion, the development and application of the two novel experimental plasma-diagnostic-techniques proposed, TIME-SERIES ToF and WAVES, have enabled a more detailed analysis of transient plasma plumes compared to conventional methods, as demonstrated on the exhaust of a low-power ablative PPT. The breadboard model designed, developed and characterized within this work, the PμLSA thruster, has served as a flexible platform for experimental validation and further investigation.

These techniques aimed to address specific limitations of existing comparable methodologies, particularly the challenges in resolving multiple ion populations and characterizing plume divergence, especially in a time-resolved manner. Their implementation has overcome the identified limitations, provided a time-varying, three-dimensional description of the transient PPT exhaust, involving a more informative interpretation of the collected data while significantly reducing testing time with respect to the state of the art.

The plume results are consistent with the literature while contributing to a deeper understanding of the PPT discharge behavior, including the isolation/characterization of different ion population groups and their roles in the discharge process, as well as the observation of spatial asymmetries. These aspects are crucial not only for deepening the understanding of PPT discharges and evaluating thruster performance expanding opportunities for performance optimization, but also for informing risk assessment during satellite integration.

The diagnostic approaches presented in this work may be applicable to a broader range of electric propulsion systems, particularly of the interest of those exhibiting unsteady plume dynamics. Overall, this thesis combines diagnostic development with experimental thruster research, contributing practical tools and findings to the ongoing efforts in pulsed electric propulsion, as well as to the increasing research and market interest in miniaturized electric propulsion systems.

Side contributions: PPT modeling

Separate from the experimental efforts, this thesis also lays the groundwork for a paraxial three-fluid model of in-channel plasma ionization and acceleration in planar PPTs, intended as a theoretical foundation for future research. The model decomposes the flow dynamics into two primary directions: along the channel axis and along the discharge current, which runs from cathode to anode. The model assumptions are described and the axial components of the governing equations for the different plasma species are formulated, together with appropriate boundary and initial conditions. Finally, a finite-volume numerical scheme is identified to solve the system.

RESUMEN NO TÉCNICO EN ESPAÑOL

Título: "Diagnósticos para la reconstrucción temporal de plumas transitorias aplicado a un propulsor de plasma pulsado de baja potencia: diseño, desarrollo y caracterización del propulsor."

Esta investigación contribuye al campo de la propulsión eléctrica espacial a través del desarrollo de métodos experimentales de diagnóstico para plasmas transitorios direccionados. Se proponen dos técnicas diagnósticas novedosas, llamadas TIME-SERIES Time-of-Flight (ToF) y WAVES (Wire Array for Variable Exhaust Scanning), de bajo coste y fácil implementación, para la reconstrucción tridimensional y temporal de plumas de plasma transitorias generadas por sistemas de propulsión eléctrica no estacionaria. Basadas en medidas de corriente de saturación de iones mediante sondas electrostáticas, estas metodologías permiten una caracterización más precisa y eficiente que las técnicas comparables existentes. a técnica TIME SERIES ToF mejora la metodología ToF tradicional, superando la simple correlación de eventos puntuales entre sondas, al caracterizar individualmente la distribución de velocidades de cada población de iones mediante la consideración de la serie temporal de datos completa y la formulación de un modelo de expansión. Por su parte, WAVES permite reconstruir secciones transversales de la pluma, permitiendo detectar asimetrías espaciales a la vez que reduciendo significativamente el tiempo de caracterización respecto a métodos convencionales de divergencia; esta técnica es también aplicable a plumas estacionarias. Aunque las dos técnicas son herramientas independientes, sus resultados pueden complementarse entre sí proporcionando un enfoque más completo de la dinámica del chorro de plasma eyectado.

Por otro lado, la tesis presenta el diseño, desarrollo y caracterización del primer sistema de micropropulsión de baja potencia basado en plasma desarrollado en España: un propulsor de plasma pulsado (Pulsed Plasma Thruster, PPT) de tipo ablativo con propulsante sólido. Este trabajo representa la primera investigación sobre tecnología PPT en el país, tanto a nivel académico como industrial, y marca el inicio de la línea de investigación en propulsión eléctrica pulsada en el grupo EP2 (Equipo de Propulsión Espacial y de Plasmas). El prototipo se ha llamado PμLSA (PULSed Ablative plasma thruster for micropropulsion), y es un PPT ablativo de baja potencia, de configuración de canal de placas paralelas, que opera nominalmente a 1 kV de voltaje de descarga y 6 μF de capacitancia (correspondiente a 3 J de energía almacenada).

Los resultados experimentales obtenidos con el propulsor PμLSA persiguen dos objetivos: enriquecer la base de datos existente sobre PPTs, abordando tanto la caracterización de poblaciones iónicas como la escasa información sobre divergencia con resolución temporal, y validar las dos nuevas técnicas diagnósticas anteriormente descritas aplicándolas a la pluma del prototipo desarrollado. Para ello, se han empleado caracterizaciones eléctricas y diagnósticos de pluma mediante la técnica ToF tradicional, constituyendo un marco de referencia, TIME SERIES ToF y WAVES. Los ensayos se realizaron bajo diversas configuraciones, con especial atención a la parametrización operacional del disparo.

Las técnicas propuestas han superado las limitaciones de diagnóstico previamente identificadas en la bibliografía existente, proporcionando un análisis más completo de los datos y/o reduciendo significativamente el tiempo experimental respecto a dicho estado del arte. Los resultados obtenidos, siendo coherentes con la literatura existente, proporcionan un análisis más amplio, tridimensional y dependiente del tiempo, del funcionamiento de estos propulsores, incluyendo la caracterización individual de poblaciones de iones y su papel en la descarga, además de la observación de asimetrías espaciales. Estos aspectos son fundamentales no solo para mejorar la comprensión de los procesos físicos en PPTs y habilitar nuevas estrategias de optimización, sino también para facilitar la evaluación de riesgos de interacción entre la pluma y la plataforma satelital en la que ha de integrar. Asímismo, las técnicas diagnósticas desarrolladas pueden aplicarse a otros sistemas de propulsión eléctrica, especialmente aquellos con pluma transitorias, así como a otros rangos de potencia.

Finalmente, se introducen los elementos fundamentales de un modelo fluido para PPTs de configuración plana. Este trabajo se ha desarrollado independiente a lo anterior, como base para investigaciones futuras.

CONTENTS

1. INTRODUCTION 1

1.1. Context, motivation and thruster working principle 1

1.1.1. Detailed background framing the research questions 4

1.2. Objectives and methodology 6

1.3. Document structure 8

2. THRUSTER DESIGN 11

2.1. Introduction 11

2.2. Conceptual design 12

2.3. Detailed System Architecture 18

2.3.1. Thruster head 18

2.3.2. Propellant 19

2.3.3. Power Processing Unit 19

2.3.3.1 Alternative configurations for the spark plug circuit 24

2.3.4. Thruster chassis 26

2.4. Performance estimate based on electromechanical model implementation 26

2.5. Design point 29

2.6. Study ranges for the parametric analysis 31

2.7. Summary 31

3. THRUSTER OPERATION 33

3.1. Introduction 33

3.2. Testing facility and experimental setup 33

3.2.1. Thruster prototype 33

3.2.2. Vacuum chamber 33

3.3. Results 34

3.3.1. Shot-to-shot variability 34

3.3.2. Visual inspection of the discharge phenomena 34

3.3.3. Propellant mass consumption per firing 36

3.3.4. Main discharge electrical characterization 36

3.3.5. Spark plug discharge electrical characterization 40

3.3.6. Visual inspection of channel surfaces after endurance tests 43

3.3.6.1 Channel maintenance practices 44

3.4. Summary 45

4. PPT EXHAUST CHARACTERIZATION BY MEANS OF TRADITIONAL TIME-OF-FLIGHT 47
4.1. Introduction . . . 47
4.2. Experimental setup and methodology . . . 47
4.2.1. Additional experimental test cases . . . 49
4.2.2. Time-of-Flight methodology . . . 49
4.3. Results . . . 50
4.3.1. Ion saturation current measurements by Langmuir probes . . . 50
4.3.2. Time-of-Flight ion velocity . . . 53
4.3.3. Time-of-Flight plume expansion rate . . . 53
4.3.4. Limitations of the traditional Time-of-Flight technique . . . 53
4.3.5. Further validation of conclusions: Repeating experiments with variations in setup . . . 57
4.3.5.1 With a different thruster battery . . . 58
4.3.5.2 With electrostatic wire probes . . . 59
4.4. Summary . . . 63
5. TIME-SERIES TOF DIAGNOSTIC TECHNIQUE AND APPLIED RESULTS ON A PPT TRANSIENT EXHAUST . . . 65
5.1. Introduction . . . 65
5.2. Experimental setup . . . 67
5.2.1. PμLSA prototype . . . 67
5.2.2. Electric and plasma diagnostics . . . 68
5.3. Plume expansion model . . . 68
5.4. Results . . . 70
5.4.1. Electric circuit response . . . 70
5.4.2. Plume characterization . . . 71
5.4.3. Validity discussion of the plume expansion model . . . 76
5.5. Conclusions . . . 77
5.6. Acknowledgments . . . 77
5.7. Data availability statement. . . . 77
6. WAVES DIAGNOSTIC TECHNIQUE AND APPLIED RESULTS ON A PPT TRANSIENT EXHAUST . . . 78
6.1. Introduction . . . 78
6.2. Experimental setup . . . 80
6.2.1. PμLSA prototype . . . 80
6.2.2. Plume cross section scanner . . . 81
6.3. Cross-section reconstruction algorithm . . . 82

6.4. Results . . . 84
6.4.1. Electrical response of the discharge and propellant consumption . . . 84
6.4.2. Time-varying plume cross section characterization . . . 84
6.5. Conclusion . . . 90
7. CONCLUSIONS . . . 94
7.1. Future areas of research . . . 97
A. OVERVIEW OF ABLATIVE PPT PROTOTYPES . . . 100
A.1. Context . . . 100
A.2. Prototype examples . . . 102
B. GOOD PRACTICES FOR OPERATING ELECTROSTATIC PROBES IN THE ION SATURATION REGIME TO EXPLORE PPT EXHAUSTS . . . 106
B.1. Introduction . . . 106
B.2. Criteria for setting probe system parameters . . . 106
C. UNSTEADY PARAXIAL THREE-FLUID MODEL FOR PLANAR PPTS . . . 110
C.1. Model assumptions . . . 110
C.2. Governing equations . . . 111
C.2.1. Neutral bulk equations . . . 111
C.2.2. Ion bulk equations . . . 112
C.2.3. Electron bulk equations . . . 112
C.2.4. Induction equation . . . 112
C.3. Global equation system . . . 113
C.4. Boundary and initial conditions . . . 114
C.5. Proposed procedure for numerical solving . . . 114
C.5.1. Characteristic lines . . . 114
C.5.1.1 Derivation of the plasma Mach lines . . . 115
C.5.2. Algorithm . . . 116
C.6. Summary . . . 119
D. PERFORMANCE CHARACTERIZATION OF THE μ10 ELECTRON-CYCLOTRON-RESONANCE ION THRUSTER USING ALTERNATIVE PROPELLANTS: KRYPTON VS. XENON . . . 121
D.1. Introduction . . . 121
D.2. Experimental setup . . . 121
D.3. Results . . . 124
D.4. Conclusions . . . 127
BIBLIOGRAPHY . . . 128

LIST OF FIGURES

1.1 Pulsed plasma thruster operation scheme and the developed prototype operating. 2

2.1 Different iterations of the developed PPT breadboard model. 13
2.2 Discharge channel features. 20
2.3 PμLSA power segment schematic. 20
2.4 Concept timing scheme of the different processes involved in a thruster firing. 23
2.5 Alternative spark plug circuit schematics. 25
2.6 Numerical solution of the Snowplow electromechanical model. 29

3.1 Reconstructed ablative PPT discharge sequence by means of visible photography 35
3.2 Main firing electrical discharge curves: nominal conditions 37
3.3 Main firing voltage curve along individual shots: high frequency noise affectation. 38
3.4 Main firing electrical discharge curves: operational parameterization. 39
3.5 Spark plug discharge electrical curve. 40
3.6 Influence of the electric field on the pre-breakdown lag time. 42
3.7 PTFE surface degradation after endurance tests. 44
3.8 Electrode surface degradation after endurance tests. 45

4.1 Time-of-Flight plasma probe setup. 48
4.2 Ion saturation current measured by a single Langmuir probe positioned downstream along the thruster axis. 50
4.3 Abnormal firings. 51
4.4 Ion saturation current measurements by the Time-of-Flight Langmuir probe arrangement across the study operational case-matrix. 52
4.5 Dependence of the Langmuir-probe ion saturation current measurements with the discharge operational parameters. 54
4.6 Dependence of the Langmuir-probe ion saturation current peak measurements with the discharge operational parameters. 55
4.7 Dependence of the Langmuir-probe Time-of-Flight velocity results with the discharge operational parameters. 56
4.8 Dependence of the Langmuir-probe Time-of-Flight plume expansion rate results with the discharge operational parameters. 57
4.9 Ion saturation current measurements by the Time-of-Flight Langmuir probe arrangement across the study operational case-matrix using Battery 2A. 58
4.10 Dependence of the Langmuir-probe ion saturation current measurements with the discharge operational parameters using Battery 2A. 59

4.11 Dependence of the Langmuir-probe ion saturation current peak measurements with the discharge operational parameters using Battery 2A. 60

4.12 Dependence of the Langmuir-probe Time-of-Flight velocity results with the discharge operational parameters using Battery 2A. 61

4.13 Ion saturation current measured by a wire electrostatic probe positioned downstream along the thruster axis. 62

4.14 Dependence of the Time-of-Flight velocity results with the discharge voltage using electrostatic wire probes. 62

4.15 Dependence of the ion saturation current peak measurements with the discharge voltage using electrostatic wire probes. 63

5.1 PμLSA PPT prototype discharge channel and power schematic. 67

5.2 Initial stages of the PPT discharge sequence by means of photography. 68

5.3 ToF experimental setup and plume-expansion-model divergence paramenter. 69

5.4 Evolution of the fit error as a function of the number of ion groups considered. 70

5.5 Anode voltage discharge waveform for the nominal case. 71

5.6 Ion saturation current measurement by the Langmuir probe nearest to the channel for the nominal case and fitted ion contributions. 71

5.7 Ion saturation current measurements by the ToF Langmuir probe arrangement and fitted reconstructed signals across the study operational case-matrix. 74

5.8 Peak current of the different ion contributions across the study operational case-matrix. . . 75

5.9 Dependence between the time-integrated current and the discharge energy. 75

6.1 Plume cross-section scanner used for the *WAVES* diagnostic system. 80

6.2 Cartesian grid used for the *WAVES* diagnostic system. 82

6.3 Anode voltage discharge waveform. 85

6.4 Ion saturation current measurements for the plume cross-section central “cross-hair” measured by the *WAVES* plume cross-section scanner at nominal conditions. 86

6.5 Ion saturation current measurements within the RT quadrant of the plume cross-section at nominal conditions. 87

6.6 Reconstructed current density and surface charge density distributions within the plume cross-section through the implementation of the *WAVES* algorithm at nominal conditions. . 89

6.7 Reconstructed total current collected by the Cartesian grid at nominal conditions. 90

6.8 Plume divergence estimates at nominal conditions. 91

6.9 Voltage bias sensitivity analysis example. 93

A.1 PPT efficiency graph. 102

B.1 Ion saturation current measurements close to the channel. 107

B.2 Ion saturation current measurements obtained through same-class shunt resistors of different resistance. 108

C.1 High-level scheme of the proposed algorithm. 117
C.2 Low-level scheme of the point-propagation function. 118
C.3 Some standard schemes about the numerical implementation of the Method of the characteristics. 119

D.1 Ion-source experiment setup. 122
D.2 Cathode experiment setup. 123
D.3 Krypton vs. xenon comparison of the screen and acceleration current for the two study ion sources. 124
D.4 Krypton vs. xenon comparison of the estimated discharge loss for the two study ion sources. 125
D.5 Krypton vs. xenon measured current-voltage curves of the study cathode. 126

LIST OF TABLES

2.1 PμLSA breadboard model design point and intended study ranges. 12

2.2 Different thruster batteries tested. 22

2.3 Electromechanical-model based performance estimate as a function of discharge parameters. 29

5.1 Plume expansion model fitted parameters. 73

A.1 Selected sample of low-power class ablative, planar, breech-fed, PTFE-propelled pulsed plasma thrusers. 101

D.1 Characteristics of the ion-source experiment. 123

D.2 Characteristics of the cathode experiment. 124

D.3 Krypton vs. xenon ion source performances. 126

1. INTRODUCTION

1.1. Context, motivation and thruster working principle

Electric propulsion (EP) [23, 24, 25, 26, 27] involves the use of electrical heating and/or electric and magnetic fields to accelerate a propellant, thereby generating thrust. High exhaust velocities between 10–100 km/s are typically achieved. EP offers a significantly higher specific impulse in comparison to chemical propulsion (CP), but generates lower thrust [28], which limits its suitability for in-orbit operation. Additionally, EP systems require an external electrical power source. The primary advantage of EP lies in its greater specific impulse, enabling more efficient use of propellant mass, an especially valuable trait for long-duration space missions.

The wide range of uses of EP depends on the thruster type and the nature of the mission, from secondary propulsion maneuvers such as attitude control, station keeping or drag compensation, to primary ones as orbit raising. EP devices can be categorized into various types based on their operational principles. The traditional classification distinguishes between electrothermal propulsion systems, electrostatic and electromagnetic devices. Concerning the former, the propellant is electrically heated and then expanded through a nozzle, such as in arcjets and resistojects. About the latter, while propellant can be ionized through various methods it is accelerated down the discharge chamber by the application of electric, magnetic or electromagnetic body forces respectively. Ion thrusters and the different types of electrosprays, involving ionic liquids, make use of electric fields for acceleration. In electromagnetic thrusters, the ionized propellant is accelerated by the interaction of the electric current driven through the plasma stream with magnetic fields (external and/or self-induced). E.g., steady-operation based EP such as Hall thrusters and magnetoplasmadynamic thrusters. Pulsed-operation electromagnetic EP encompasses all variants of Pulsed Plasma Thrusters (PPT) [29, 30, 31, 32, 33] and vacuum arc thrusters [34, 35, 36, 37]. [A PPT variant [38, 39, 40] designed to operate on electrothermal principles is exempt from this category.] The issue of limited lifetime due to electrode erosion can be mitigated using an electrodeless [41, 42, 43] discharge to generate the plasma and magnetic nozzles to accelerate it. Electrodeless plasma sources always involve AC power; the specific frequency leads to different electromagnetic coupling to the ionized gas. Examples of electrodeless thrusters are the electron cyclotron-resonance thruster and the helicon plasma thruster. Ion thrusters and Hall-effect thrusters represent the most mature and well-established EP technologies currently in use. In contrast, some of the other concepts discussed remain at the prototype stage, lacking a robust heritage in real applications, largely due to an incomplete understanding of the underlying physics governing their operation.

For the purposes of this work, a brief aside is provided to outline the fundamentals of electromagnetic Pulsed Plasma Thrusters (PPTs) [29, 31, 44, 45], with a particular emphasis on ablative variants as it is the object of study of this research. PPTs can be categorized based on different aspects. Regarding propellant types, PPTs can operate by injecting a gas [46, 47, 48] or a liquid [49, 50, 51, 52, 53, 54, 55, 56, 57, 58], which typically is non-volatile, or by means of providing a solid propellant [59, 60, 61, 62, 63, 32, 64, 65]. The latter, referred to as ablative PPTs, represent the standard. They essentially consist of a pair of electrodes (cathode-anode) shaping a channel-like configuration, coaxial or rectangular[1]. These electrodes are connected to an energy storage unit, typically a capacitor bank. A solid propellant [66, 49, 67] is placed between the electrodes at one end of the channel,a single bar in breech-fed configurations or multiple ones in the side-fed one. The propellant is commonly a dielectric and, in particular, polytetrafluoroethylene (PTFE or TEFLON™, $(C_2F_4)_n$). Once the capacitor bank is charged up to a sufficiently high voltage V_0 for, a discharge trigger acts enabling the channel breakdown[2] over the propellant surface, and thus fraction

[1] Rectangular PPTs are also referred to as parallel-rail or planar, without excluding the possibility of exhibiting non-null channel divergence or electrode tapering angles.

[2] Electrical breakdown occurs when an insulating material is exposed to an electric field exceeding its breakdown voltage, impart-

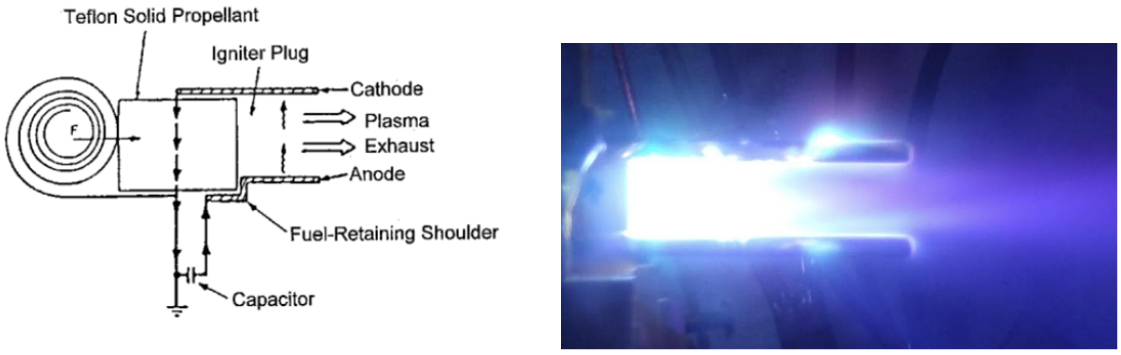

(a) (b)

Figure 1.1: **(a): Discharge channel of a breech-fed ablative Pulsed Plasma Thruster (PPT) basic operation scheme [29]. (b): The operation of an ad-hoc PPT breadboard model developed for the present investigation, named PμLSA (PULSed Ablative Plasma Thruster for micropropulsion), is captured by means of photography.**

of the propellant is ablated and ionized. This process is known as a surface flashover [69, 70, 71, 72]. The resulting discharge current generates a self-induced magnetic field that causes a Lorentz force, which accelerates the plasma downstream and away from the device, producing thrust. Figure 1.1 illustrates, in panel (a), the previously described planar, breech-fed configuration, and in panel (b), the breadboard model developed in this work in operation. Alternatively, the method used to supply discharge energy can be inductive rather than a direct connection to the discharge electrodes, as in some gas-fed PPTs [73], but inductive PPTs can be understood as a separate thruster category.

The discussion on the context of EP is now resumed [74, 75]. Pioneer research lines on EP date on the late 1950s [76]. In 1964, in the midst of the Cold War, the Soviet Union puts the very first EP system in-orbit: an ablative PPT for three-axis attitude control on board of the Zond-2 probe [29]. This success was followed in 1965 by the USA, when the first ion engine was deployed on the Low Earth Orbit (LEO) aboard the GGSE-2 mission, after several years of multiple sub-orbital attempts. After these two milestones, various USA resistojets also made it to LEO. In 1966, the URSS successfully placed another ion thruster into orbit with the Yantar-1 mission. Since then, numerous spacecraft equipped with onboard EP systems have been operated in space. Notable demonstration missions of EP for interplanetary travel beyond the Geostationary Orbit (GEO) include Deep Space 1 (NASA), SMART-1 (ESA), and HAYABUSA (JAXA). Today, it has become a well-established and widely used technology for non-(high-thrust) impulsive in-orbit propulsion. Further elaborating on it, ambitious examples of other interplanetary science missions using EP are the Hayabusa2 and Dawn missions, with a primary propulsive role, and the Bepi-Colombo missions for trajectory correction [77, 78]. They have advanced scientific exploration while also fostering collaboration with private partners. These missions mostly involve ion thrusters and Hall thrusters, which are currently leading technologies in the field of EP. Modern commercial satellite platforms commonly integrate EP with CP [79, 80], exemplified by Thales Alenia's Spacebus NEO, which also offers a full-EP version; similarly, Airbus' ADS and the full-electric E3000 platforms demonstrate the growing adoption of EP in the industry. Hybrid CP and EP concepts that share propellant resources, such as those based on water [81], are also currently under investigation. Examples of European Space Agency (ESA) initiatives using EP involving research and telecommunications applications, in collaboration with commercial partners, include the Artemis, Alphasat, Small GEO missions, and, full-EP, the NeoSat Programme and the Electra

ing sufficient energy to electrons to transition into the conduction band. This leads to a sudden surge in current and typically results in irreversible physical or chemical degradation of the material. Breakdown may manifest through bulk, surface, or gas conduction mechanisms. Ideal insulators, which would not accumulate charge under carrier injection, do not exist in practice. All real insulating materials exhibit a finite breakdown threshold and are susceptible to conductive transitions under sufficiently high fields [68]. Dielectrics, a subset of insulators, exhibit polarization in response to electric fields.

satellite. Indeed, the Artemis mission marked Europe's first experimental use of EP for satellite transfer, achieving up to 90% fuel savings compared to conventional CP [77, 78]. Industry initiatives like the satellite large constellations of SpaceX, Starlink, propelled by ion thrusters, and OneWeb, employing Hall thrusters, illustrate the increasing engagement of commercial enterprises in EP [82, 83]. These two private initiatives have revolutionized the in-orbit scenario, drastically increasing the number of spacecraft in orbit. Focusing on EP, the count has risen from a few hundred [75] to thousands.

Many challenges affect EP expansion prospects [84, 75, 78]. For example, the focus on cost reduction and downsizing spacecraft necessities together with the rapid evolution of technology has increased the interest in miniaturized payloads [31, 37, 85, 75, 86]. Indeed, near to 3000 CubeSats are forecasted to be launched over the 2020s; among them, around 400 are expected to be addressable (able to communicate) [78]. However, CubeSats usually do not have on-board propulsion [87, 64]. For reference, a study highlights that a 180 kg spacecraft at 400 km altitude typically has a lifespan of about 70 days without propulsion. Using an ablative PPT, its lifetime has been shown to extend by approximately eight times, compared to around five times with chemical propulsion (CP) [88]. Nonetheless, achieving low-power operation is particularly challenging for steady-state plasma thrusters, which are notoriously difficult to scale-down/miniaturize [85]. By contrast, in pulsed EP, since they inherently operate in pulsed mode, the discharge energy per pulse can be controlled independently and irrespectively of the available input power by modifying the pulse rate. This characteristic makes pulsed EP a viable alternative for low-power satellite applications. Then, pulsed EP systems offer significant flexibility in their application. They are a viable alternative for on-board propulsion in low-power satellite systems, serving as the primary propulsion for small satellites [62, 89, 65] (for example, for drag compensation in nanosatellites), but also to be employed as a secondary propulsion system in larger satellites.

This thesis addresses the micropropulsion field through the development and characterization of the first low-power, plasma-based propulsion system designed in Spain. Among the existing pulsed-plasma EP concepts, the ablative PPT [32, 64] stands as one of the simplest structural solutions, combining the benefits of minimal dependence on power input with high functional simplicity, enhancing its potential for compactness, lightweight and cost-effective design [32, 33]. This technology has been chosen not only for its research potential but also for its market value, comparable to that of competing EP technologies, such as vacuum arc thrusters, as well as non-plasma-based systems like resistojets and electrosprays [75, 90]. Ablative PPTs have the advantage over vacuum arc thrusters of not consuming the cathode as propellant.

The reviewed literature on PPTs highlights the need for further fundamental research, particularly due to the low efficiencies reported [91, 92], which decrease with down-scalability (see Appendix A). A deeper understanding of the physics underlying the discharge process is crucial for enhancing thrust efficiency. Focusing on the PPT exhaust, plume studies are important not only for assessing discharge physics and thruster performance but also for evaluating potential plume/spacecraft interactions [93, 94, 95], a drawback to careful consider for satellite integration because of the impingement of energetic particles onto delicate surfaces, as instruments or solar panels. Two aspects identified in the reviewed plume literature motivate our work. First, in combination with a probe system, the traditional time-of-flight (ToF) technique is commonly used to characterize the exhaust velocities of pulsed EP systems like PPTs [96, 97, 98, 99, 95, 61, 100, 94]. Among diagnostic techniques for the exhaust of unsteady EP, ToF stands out for its simplicity, as it relies solely on feature correlation from measurements obtained with spaced probes. However, previous investigations of PTFE PPT plumes have revealed the existence of several ionization waves and, consequently, multiple ion populations with various species and ionization states in the generated plasma, employing diverse diagnostic techniques [2, 65, 96, 97, 98, 99, 95, 61, 100, 94]. Hence, the traditional ToF methodology provides limited insight, offering only average velocity values as inherently fails to account for the multiple ion populations contributing to the selected feature to correlate. This limitation restricts opportunities for in-depth discussions of the underlying physics, necessitating the use of other diagnostics to gain further information. Second, studies on PPT plume divergence have been relatively scarce [95, 94, 101, 93, 98, 102], available time-resolved data on this regard are limited and the experimental processes involved are time-

consuming and require complex setups. It is worth noting that, alongside our own research efforts on plume expansion [7, 2, 3], renewed interest has emerged in recent years from several research groups [103, 65, 104, 105]; nevertheless, the previously identified aspects remain relevant.

A more comprehensive discussion of the relevant literature on the former two aspects, the identified limitations and their consequences is provided in Section 1.1.1.

1.1.1. Detailed background framing the research questions

[3]

Multiple research teams have experimentally investigated PPTs [102, 61, 107], highlighting the complexity of its discharge physics [23, 108]. The simultaneity and spatial coincidence of different mechanisms hinder their separated analysis. Furthermore, for the usual propellants, the resulting time-varying plasma may be composed of multiple chemical species (also including electrode material), with different molecular mass and charge states, each with a different divergence angle [97, 95, 61, 100, 2].

Prior investigations on PTFE PPT plumes using diverse diagnostic methodologies have probed the existence in the generated plasma of several ionization waves and, in turn, multiple ion populations, involving various species and at different ionization states. E.g., Langmuir probes [98, 102, 7, 109] have been used, as well as direct methods to identify the species, such as residual gas analyzers [110, 98] or optical diagnostics, mainly optical emission spectroscopy [97, 95, 99, 100, 61, 111, 107]. These discovered characteristics have a negative impact on propulsive performances is negative, as generating any other than singly-charged ions incurs in extra ionization energy losses. Moreover, as multiply-charged ions are accelerated to different velocities, the resulting distribution of kinetic energy in the exhaust penalize thrust generation. Measurements carried out with the direct methods above have studied the diverse plasma constituents of different rectangular PPT fed with PFTE and operating across a broad discharge energy range. Overall findings reveal a wide range of ionized species of fluorine (F) and carbon (C) up to the third charge state. These investigations notably identified neutral C_xF_y compounds and, even, electrode materials [97, 112]. Predominantly observed ion states include C^+, F^+ and C^{2+}. Mostly, time-of-flight (ToF) in combination to other diagnostics is used to characterize the velocity of the different ion constituents and results widely vary from 10—60 km/s [96, 97, 98, 99, 95, 61, 100, 94], often commonly reporting the existence of one of the plasma groups around 40 km/s. Although marginal exceptions at higher speeds have also been published [113, 114]. In [97], the following speed ranges were reported for distinct species: as $C \sim 5-20$ km/s, $C^+ \sim 20-30$ km/s, $C^{2+} \sim 30-40$ km/s, $F \sim 5-15$ km/s, $F^+ \sim 15-20$ km/s and $F^{2+} \sim 20-30$ km/s. Multiple ion groups are also observed in other types of pulsed plasma devices with similar diagnostics above, as in gas-fed PPTs [47, 48] and vacuum arc thrusters (VATs) [34, 35]. In the former, the findings include the presence of highly ionized electrode material too.

Among all experimental diagnostics for the plume exhaust, the ToF technique based on probe measurements stands out for its simplicity. Traditionally, it has been used to determine the ion mean velocity, by computing the time interval between the occurrence of the same feature in the time signal at two locations (e.g., peaks). In this manner, applied to single Langmuir probe measurements, Gatsonis et al. [98] and Barquero et al. [7] have provided evidence of the existence of two ion populations with velocities around 60 km/s and 30 km/s, respectively, on two different PPT devices. Furthermore, it is possible to obtain a first estimate of the exhaust plume divergence rate from the decrease in peak current value from one ToF probe to the next [7].

However, simply correlating peaks or other features among probe signals neglecting the fact that the exhaust likely consists of more than one ion group (each one of them potentially originating at a different

[3] This chapter presents partial reproductions of the introduction sections from the following journal articles, together with additional content: S. Barquero, J. Navarro-Cavallé, and M. Merino, "**Pulsed Plasma Thruster Exhaust Reconstruction**", Plasma Sources Science and Technology, 2024 [2], and S. Barquero, J. Navarro-Cavallé, and M. Merino, "**Reconstruction of the Transient Plume Cross-Section of a Pulsed Plasma Thruster**", Plasma Sources Science and Technology, 2025 [106].

time, and with different charge/mass ratios, velocities, densities, thermal spreads and divergence rates) yield a lack of accuracy. The overlapping contributions of individual ion groups may result in none of the observed peaks coinciding with the actual maximum of any of them. Thus, that basic approach can only provide an "average" velocity of the exhaust. As well, ion current density of each ion group decreases downstream not only due to the divergence, but due to the axial thermal spread. Hence, a naive calculation of the divergence based on the peak value of the ion current density at each probe overestimates the plume divergence rate in case the thermal spread is non-negligible.

Although traditional ToF offers speed and simplicity as a first approach, relying solely on feature–probe correlation while disregarding the full time-series data represents a loss both for fundamental research but also for performance assessment aiming at explaining variations in thruster efficiency. Ignoring the complete dataset sacrifices our knowledge of species composition and formation processes. Furthermore, the main practical limitation of providing only average velocities lies in the ambiguity regarding which ion species the velocity corresponds to and in what quantity. Moreover, this average velocity may not accurately represent the true mean velocity of any individual species, especially in cases where multiple populations overlap, producing broad, flat features in the time domain that introduce high uncertainty in feature selection. Consequently, thrust estimates based on these averages incur significant errors, the acceptability of which depends on the application context; in many cases, direct measurements may become necessary rather than merely complementary. In low-power, budget-constrained contexts, where minimizing expenditure is paramount, the requirement for additional direct measurements may prove impractical. Then, offering simple, cost-effective experimental alternatives that estimate thrust with greater accuracy than electrical characterization is potentially beneficial.

In addition, assessing the exhaust plume divergence angle is crucial both for performance evaluation and for thruster integration into the spacecraft platform, since energetic particle impingement can damage delicate surfaces such as instruments and solar panels. In this context, determining the instantaneous plume divergence and identifying the associated ion species are essential to accurately assess their cumulative impact.

Previous studies on PPT plume divergence are relatively scarce [95, 94, 101, 93, 98, 102], while a renewed interest in them has been shown in recent years by different research groups [103, 7, 2, 65, 104, 105]. All the identified studies on this matter refer to rectangular channel configurations running on PTFE, and typically fed by their channel breech [95, 94, 101, 93, 65, 98, 102, 103, 105], except for a non-volatile liquid-propellant PPT [104]. Plume divergence data from these works principally rely on current measurements, mostly carried out by electrostatic probes, Faraday probe (FP) [93, 65, 104] and Langmuir probes (LPs) [95, 94, 101, 98, 102, 103], with the exception of one case using a Rogowski coil instead [105]. Overall, these investigated plumes exhibit single-peaked cross-sections, with some degree of deviation from the thruster axis, and significantly wider divergence along the plane parallel to the electrodes compared to the plane perpendicular to them.

Crucially, many of those works ignore or have a limited treatment of the time-dependent aspects of the exhaust divergence. Time-resolved data [95, 65, 104, 2] are necessary to address the behavior of the distinct ion populations generated during the discharge, which may differ from time-averaged results. It is worthy to highlight the time-dependent off-axis characterizations carried out by Jakubczak et al. [65] and Antropov et al. [95]. By means of a FP Jakubczak et al. studied a 1 J/1 kV ablative PPT [65]. Their results principally revealed that the ion current density distribution dropped up to 10% of its maximum at about ±30° from the thruster axis for the cathode-anode direction, and ±45° for the direction parallel to the electrodes. The ion current distribution's divergence, defined at the point where the ion current falls below 10% of its maximum, shows two temporal peaks, with ion collection detectable at all times up to ±85°. Particularly remarkable is the work of Antropov et al. [95], who used cylindrical LPs to investigate the exhaust of a (side-fed) PPT operating between 80–100 J 2.5–2.8 kV. The study aimed to reconstruct the current-voltage curve at various times, which is challenging in pulsed plasmas due to the impossibility of performing a voltage sweep during a single firing. Although the procedure was briefly described and

the curves themselves were not provided, the reported density results were proven to be valid using other diagnostic methods. Results, which exclusively referred to the plane parallel to the electrodes at one of the channel sides, exhibited a single peak in space that moved in time towards the thruster axis, on average located around 44° from the thruster axis. The magnitude dropped up to the 10% of its maximum at about 80°.

In addition, all the previous studies also rely on local probe measurements and on a single probe, which requires multiple firings to scan the full cross-section. Note that performing a full scan without assuming any symmetries exacerbates this issue. However, omitting those simplifications is justified by the inherent asymmetries of the planar configuration, the need to assess manufacturing defects that may cause plume deviations, and the fact that multiple ion species are generated at different instants and by distinct mechanisms [2, 103]. These factors give rise to non-negligible differences in ion dynamics and spatial distributions, which can significantly influence both surface impingement effects and performance estimates compared to a more simplified scenario.

The latest, combined with the need to achieve statistical significance at a single location through repetitive firing, makes the entire plume cross-section scanning process time-consuming. Increasing the number of firings will lead to higher propellant consumption and potentially greater electrode erosion, both affecting the response of the thruster throughout the entire characterization.

The former highlights the need to reduce the testing time required for performing a time-resolved full plume cross-section scan, which becomes especially valuable when paired with an approach that does not require extensive setup.

With this, two main limitations are identified as the research questions to address. First, the constraints of traditional ToF methods as the standard approach to transient plume studies, along with their untapped potential to provide deeper insights into plume physics even when relying solely on axial measurements. Second, the need for a faster but accurate description of the entire plume cross-sectional domain. To address these issues, the development of new experimental methodologies is considered necessary. It is useful to follow a progressive strategy by designing these methodologies to independently address each limitation, even though they may share aspects. This approach allows each method to stand alone while their combined results can provide a more comprehensive understanding of the entire plume dynamics. Limiting the scope of each technique simplifies the problem, facilitates diagnostic debugging, and enables evaluation of the added value of adopting more complex setups in future iterations, or the benefits of using both methods together versus individually, depending on specific needs.

1.2. Objectives and methodology

The focus of this research is on experimental diagnostic methods for exhaust reconstruction of unsteady EP, with applications to ablative PPT plumes.

The present thruster prototype constitutes the first Spanish PPT, which has been designed and developed under the frame of the MARTINLARA project[4]. It is the first Spanish plasma-based propulsion system with potential for on-board micropropulsion and the first Spanish pulsed plasma-based EP, marking the start of the Plasmas and Space Propulsion Team's (EP2) [5] research into pulsed plasmas.

Aiming to contribute to a better understanding of the PPT discharge physics through the operation of prototypes, several challenges associated with this technology have been identified in Section 1.1 motivating the thesis objectives. As a consequence, this dissertation is structured around two high-level objectives,

[4]The MARTINLARA regional project (Millimeter wave Array at Room Temperature for INstruments in LEO Altitude Radio Astronomy) [1] is funded by the Comunidad de Madrid under Grant reference MARTINLARA-CM S2018/NMT-4333. The project aimed to promote the access to space to small, ground-breaking technologies by the development of a nanosatellite mission for in-orbit demonstration. It integrates various technologies for space applications, including radio astronomy, Earth observation, space photonics, and electric space propulsion.

which are divided into a series of sub-objectives listed below. While the second of these two objectives represents this thesis's contribution to the field, namely the description and implementation of two novel experimental plasma diagnostic techniques, the first objective focuses on the development of the thruster prototype, which is necessary for the application of those techniques.

1. **Objective 1:** The design, development, and experimental study of a low-power rectangular ablative PPT

   (a) Definition of the system requirements within the context of the MARTINLARA project.

   (b) Design and development of a low-power class ablative PPT complete research breadboard model, easy-to-iterate in terms of electronic topology and discharge chamber geometry ratios.

   (c) Definition of the experimental plan ensuring accuracy and reliability of experimental data, based on:

      i. identification of technological problems;

      ii. validation of reliable ignition:

      iii. assessment of the parametric space for the thruster geometrical and operational conditions, with a focus on the operational* ones (based on capacitance C and discharge voltage V_0 variation);

      iv. and, within the operational range, carrying out electrical characterization of the discharge and

      v. plasma plume characterization by means of electrostatic probes.

   (d) Preparation of the EP2 laboratory facilities for the operation and monitoring of the PPT technology, and development of the different experimental setups for the planned test campaigns.

   (e) Conduction of firing[5] tests and data acquisition up to obtain a comprehensive set of electrical and plume plasma measurements at different thruster configurations, to characterize thruster operation and explore the influence of design parameters in the discharge process, and analysis and reporting of the experimental results.

   While lessons learned may inform potential thruster upgrades and discharge parameters, this research does not focus on thruster optimization.

   (*) Beyond its research significance, prioritizing operational over geometric parameterization is crucial for in-orbit PPT operation, which justifies why this research emphasizes it. As an alternative for thrust variability to that achieved by adjusting the firing frequency within the limits of available input power, V_0 adjustments offer a simpler and more reliable way to modify the impulse bit than altering the channel geometry ratio.

2. **Objective 2:** The design and application of easy-to-implement, fast, and cost-effective diagnostic tools for the time-resolved, 3D reconstruction of transient plumes in unsteady EP systems, relying solely on current measurements from electrostatic probes placed downstream in the plume and operating in the ion saturation regime. This second pillar involves:

   (a) Plume characterization using traditional ToF methodology (based on feature probe correlation) to Langmuir probe and wire electrostatic probe measurements. Ion velocities and an initial estimate of the plume expansion rate are calculated. This study serves as a reference for comparison with the proposed novel techniques (below) aimed at addressing the identified limitations of this method.

   (b) TIME-SERIES ToF Technique: Design of a novel diagnostic technique to reconstruct the time-expansion of the different ion constituents of the exhaust, characterizing them through axial

[5] Synonyms for "firing" in this work can include "bit," "shot," and "discharge."

Langmuir probe measurements fitted to a proposed expansion model for unsteady plumes based on Maxwellian distributions. This approach aims to provide greater accuracy and insight than traditional ToF analysis by enabling the isolation of distinct ion contributions. The velocity distributions of the various ion populations involved are calculated, including their mean velocity, thermal spread, creation time and location, magnitude, and divergence.

(c) WAVES Technique (Wire Array for Variable Exhaust Scanning): Design of a novel diagnostic technique for the reconstruction of the time-varying exhaust cross-section using a grid of wire probes distributed across the cross-section plane and aligned with the cross-axes, which measure line integrals of the ion saturation currents. An algorithm based on variable separation and least-squares is proposed to solve the cross-section current density distribution of the plume at each time step, which makes the tool suitable for both transient and steady-state thruster plumes. This technique aims to provide an accurate off-axis characterization of the plume while significantly reducing testing time with respect to comparable approaches reported in the literature.

(d) Development of the former two proposed techniques, TIME-SERIES ToF and WAVES, and their implementation in the specific case of the ad-hoc PPT breadboard model operation; and data acquisition and analysis, and reporting of the results. This aims, on one hand, to validate the previous diagnostic techniques, and on the other, to expand the 3D, time-resolved PPT plume experimental database and the physical discussions regarding it.

While constituting standalone works, the results of the two novel techniques proposed can complement each others.

1.3. Document structure

An overview of the structure and organization of the this dissertation beyond the Introduction is presented. The different chapters are outlined by a brief description of their content and relevance to the research objectives.

- **Chapter 2** presents the PPT breadboard model, beginning with a summary of the developed System Design Requirements (SDR) document [18] for the MARTINLARA project. The chapter then outlines the applied design methodology, provides an overview of the thruster architecture, and concludes with the final definition of the design point. Both power and mechanical hardware are described, alternative electronics topologies for the discharge triggering are discussed and a performance estimate is provided.

  This chapter includes with adaptations the content of the proceedings for the 2021 Space Propulsion Conference (SPC), "Design of an experimental ablative pulsed plasma thruster for micropropulsion" [6], and some additional material.

- **Chapter 3** addresses thruster operation by assessing reliable ignition and discharge characterization within the study operational and geometrical parametric space. This characterization is fundamentally electrical. The chapter starts with an introduction to the dedicated testing environment, followed by a qualitative overview of the discharge sequence through visible photography. It then presents mass propellant consumption data, as well as the electrical characterization of both the main and triggering discharges. Finally, findings from visual inspection of the discharge chamber surfaces after repeated firings are presented

  This chapter includes with adaptations part of the content of the proceedings for the 2022 International Electric Propulsion Conference (IEPC), "Experimental plume characterization of a low-power Ablative Pulsed Plasma Thruster (APPT)" [7], and some additional material.

- **Chapter 4** employs the traditional time-of-flight (ToF) technique to estimate average velocities of the various ion populations present in the exhaust and to provide a preliminary assessment of the plume

expansion rate. The technique is applied to single electrostatic probes working in the ion saturation regime. Both single Langmuir probes and wire electrostatic probes are used.

This chapter includes with adaptations part of the content of the proceedings for the 2022 International Electric Propulsion Conference (IEPC), "Experimental plume characterization of a low-power Ablative Pulsed Plasma Thruster (APPT)" [7], and some additional material.

- **Chapter 5** presents the time-resolved PPT exhaust reconstruction by a new analysis technique, named TIME-SERIES ToF, which re-interprets ToF by considering the entire time-series of the current probe data. This allows for a higher level of accuracy and insight than traditional ToF methodology. The proposed approach is based on a plume expansion model to fit to the time-series data of single Langmuir probes working in the ion saturation regime distributed downstream the thruster axis. The plume expansion model is defined by the superposition of different Maxwellian-like ion groups, each one being characterized by its own mean velocity, thermal spread, initial density, generation time and divergence rate. The experimental setup and the plume expansion model are presented before describing the results. The results begin with a brief electrical characterization, followed by the plume measurements; the study covers a range of operational parameters for the thruster discharge. Finally, a discussion about the validation limits of the present diagnostic proposal is included.

  This chapter directly transcripts the journal article "Pulsed Plasma Thruster exhaust reconstruction", published in Plasma Sources Science and Technology in April 2024 under DOI 10.1088/1361-6595/ad35e5 [2]. Preliminary work has been disseminated in [8].

- **Chapter 6** addresses the limitations of the previous technique in accurately describing plume divergence based solely on axial measurements. It introduces a novel experimental method, named WAVES (Wire Array for Variable Exhaust Scanning), to reconstruct the time-varying 2D ion current density distribution of the exhaust cross-section. This is achieved using a grid of wire electrostatic probes operating in the ion saturation regime to measure the line-integrated current along two transverse directions downstream of the plume, combined with a variable separation algorithm and a least-squares method to solve the inverse problem. The discharge is electrically characterized before describing the plume results.

  This chapter directly transcripts the journal article "Time-varying reconstruction of the plume cross-section of a Pulsed Plasma Thruster", currently under review in Plasma Sources Science and Technology [3]. Preliminary work, not included here, has been disseminated in [7, 9].

- **Chapter 7** summarizes the conclusions of this research and outlines potential directions for future work.

- **Appendix A** provides an overview timeline of scientific research and R&D on PPTs, with a focus on ablative variants.

- **Appendix B** Outlines the procedures followed for setting up electrostatic probes operating in the ion saturation regime to investigate the PPT exhaust, while accounting for potential spurious discharges.

- **Appendix C**: Establishing a foundation for future research, the basis of a three-species plasma-physics based fluid numerical model for in-channel plasma ionization and acceleration in planar pulsed plasma thrusters (PPTs) have been developed alongside the experimental work of this thesis. The model decomposes the flow dynamics into two primary directions: along the channel axis and along the discharge current, which runs from cathode to anode. Throughout the chapter, the assumptions and the derivation proof leading to the axial governing equation system are discussed as well as the necessary boundary conditions are listed. Using a finite-volume scheme, the Method of Characteristics is identified as suitable for solving the problem, and the key elements of an algorithm for its implementation are introduced.

  This work constitutes a first outlook into the efforts required for PPT plasma-based modeling, and has been carried out under the supervision of Professors Eduardo Ahedo and Mario Merino.

- **Appendix D:** Additional experimental research was conducted in collaboration with the EP Laboratory at the Institute of Space and Astronautical Science (ISAS) of the Japan Aerospace Exploration Agency (JAXA). The study object of this work was their Electron-Cyclotron-Resonance Gridded Ion Thruster μ10, at its versions for the Hayabusa2 and DESTINY$^+$ missions [115]. Research efforts mainly focused on investigating the use of alternative propellants on three different high TRL (Technology Readiness Level) devices, the two ion sources and their neutralizer-cathode; these results have been journal published under DOI 10.1016/j.acta astro.2023.06.036 [4], whose content is directly transcripted in the present appendix.

Chapters 5 and 6, and Appendix D include content taken verbatim from the published articles [2], [106], and [4], respectively. For the former two chapters, repetitions with other sections have been intentionally retained to preserve consistency with the original work. In addition, discrepancies in nomenclature across chapters may exist to preserve the original content of the journals. The author apologizes for any distraction this may cause to the reader.

2. THRUSTER DESIGN[6]

2.1. Introduction

Across the present chapter the design of a small pulsed plasma thruster (PPT) breadboard model, named PμLSA (PULSed Ablative plasma thruster for micropropulsion), is presented.

The high-level design requirements guiding the selection of the PPT type include the need for a prototype suitable for exploring the micropropulsion operational range, as well as considerations of design simplicity and ease of manufacturing. Helping in this, the design of the device has been informed by existing proposals; which also facilitates a more straightforward comparison of the results with the existing literature. Consistently, the selected configuration has entailed a simple structure, rectangular, and minimizes failure risks by avoiding moving parts or injection systems. In addition, the PPT has been designed to prioritize experimental research, aimed at better understanding the discharge physics, taking precedence over engineering decisions. Thus, the design has to enable throttleable firing by modifying the operational point. In addition, it shall offer flexibility for rapid iteration and acceptance of modifications in both channel geometry and electronics.

As a consequence, design choices have led to PμLSA featuring an ablative, breech-fed, rectangular configuration, and being operated with PTFE. Its sizing has been based on approximate scaling laws derived by the inspection of existing low-power class comparable PPTs [97, 102, 30, 61, 116] and simple electromechanical models [23]. Table A.1 in Appendix A provides useful specifications on a selected sample of comparable prototypes used as references, compiling their nominal geometrical and operational configurations, operational ranges, and measured performance. In the present chapter, Table 2.1 refers to PμLSA, summarizing the nominal configuration along with the study ranges of interest addressed in this document. Figure 2.1 shows a real view of PμLSA together with some previous design iterations[7]. The design of PμLSA and preliminary versions was presented in previous works [6, 2], along with experimental results reported in [15, 7, 8, 2, 9, 106].

The overview of the PPT design comprises three main subsystems: (1) the thruster head, which includes the discharge channel and embedded spark plug used to trigger ignition; (2) the propellant system; (3) the electronics and (4) the structural platform (also referred as mounting structure or thruster chassis). Regarding (3), the thruster requires its own Power Processing Unit (PPU) to store and release the discharge energy by providing controllable firing via a robust triggering subsystem. The variation of the thrust, by modifying the discharge parameters, is also enabled to meet research needs. Subsystem (1), the thruster head, and the energy storage unit, part of subsystem (3), are mounted in close proximity to enhance efficiency by minimizing the initial inductance of the discharge path [23]. As a result, the capacitor bank is tested within the chamber, attached to the thruster platform. The assembly is secured to an aluminum platform (4), which is, in turn, mounted on an auxiliary setup that allows the prototype to be placed inside the vacuum chamber and enables adjustable alignment with the diagnostic probes used in subsequent chapters.

[6] Part of this chapter incorporates content from the 2021 Space Propulsion Conference (SPC) paper "**Design of an experimental ablative Pulsed Plasma Thruster for micropropulsion**" [6], coauthored by S. Barquero, J. Navarro-Cavallé, and M. Merino.

[7] The thruster upgrades have primarily focused on, on the one hand, chassis simplification and reduction of initial circuit inductance, and on the other hand optimization of channel geometry ratios, aiming to increase the discharge energy consumed per shot per shot by adjusting channel length (see Section 2.4) and reducing the deposition of discharge by-products on the propellant surface through variation of the energy-to-area ratio (see Section 3.3.6 of Chapter 3).

Parameter	Nomenclature	Unit	Nominal point	Study range
h	Channel height	cm	1	0.5–1.5
w	Channel width	cm	1	-
ℓ	Channel length	cm	4.5	1.5, 4.5
E_0	Available discharge energy	J	3	0.1 – 15.6
V_0	Channel electrode voltage bias	kV	1	0.5–2.5
C	Capacitance	μF	6	1–9

Table 2.1: **PμLSA breadboard model design point and intended study ranges within the scope of this document.**

The remainder of the chapter is organized as follows: Section 2.2 discusses the design specifications in detail and their immediate design choices. Section 2.3 summarizes the architecture of the PPT breadboard model. In Section 2.4, performance is estimated using electromechanical models to inform the selection of the design point. The design point itself, also known as nominal or reference configuration, is described in Section 2.5. Finally, Section 2.6 outlines the parametric case framework for the investigations conducted in this work. To conclude, Section 2.7 provides a brief summary of the chapter.

2.2. Conceptual design

The design requirements outlined above establish a set of high-level specifications that guide the design choices. The present section[8] elaborates on these specifications and the rationale behind the associated design decisions:

1. **Ease of design and manufacturing, informed by existing knowledge and heritage:**

   (a) **PPT configuration:**

   i. **Ablative PPT:** The ablative PPT, utilizing a solid propellant, simplifies design and operation compared to liquid- or gas-fed PPTs by eliminating the need for storage tanks and an injection system.

   ii. **Rectangular channel:** In turn, the selected rectangular configuration, compared to coaxial ones, benefits from a significantly larger body of research, facilitating design informed by existing devices. It is also more straightforward in terms of manufacturing and offers more uniform operation, as coaxial configurations typically face challenges concerning preferential discharge paths [117].

   iii. **Parallel rail channel and rectangular electrodes:** In turn, the most fundamental configuration is chosen, which involves no flaring or tapering angles, with non-zero angles associated with improvements in the gas-dynamic and electromagnetic components respectively.

   iv. **PTFE, breech-fed:** PTFE[9] is chosen as the propellant for its established role as the standard in the ablative PPT field (see Apendix A). The material exhibits several advantageous properties that make it suitable for this use: electrical properties include good dielectric performance, with a dielectric constant close to 2, ensuring reliable insulation under high-voltage conditions; thermal characteristics are equally favorable, with a decomposition point typically appreciable above 400°C and high thermal stability, which, along with low outgassing and volatility, makes it suitable for vacuum environments. From a mechanical

[8]The present list constitutes a revisited version of the high level specifications for the design of the requested PPT applying to this research stage, of low Technology Readiness Level (TRL). Although the information is not presented in the official engineering form of a System Design Document (SDD), a preliminary SDD document [18] was developed at the beginning of the present PhD investigation for the low-power class PPT commissioned under the frame of the MARTINLARA Project to set the basis for a future CubeSat payload for tech demo.

[9]Carbon's ionization threshold is approximately 11.26 eV and Fluorine's, 17.42 eV.

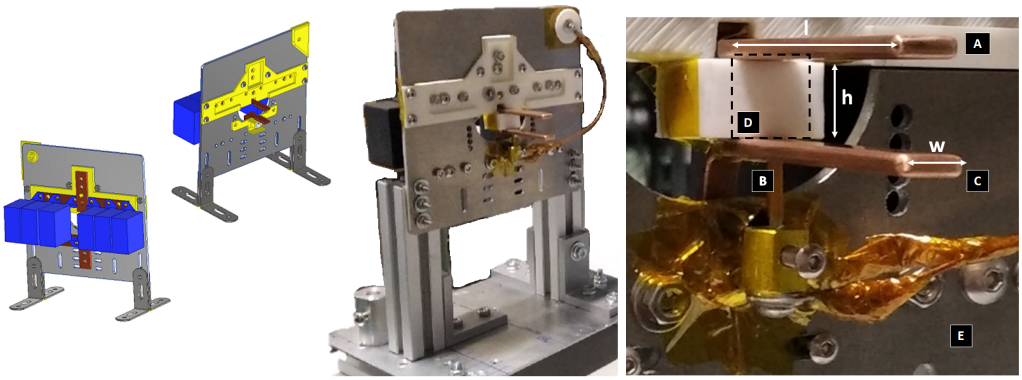

(a) (b)

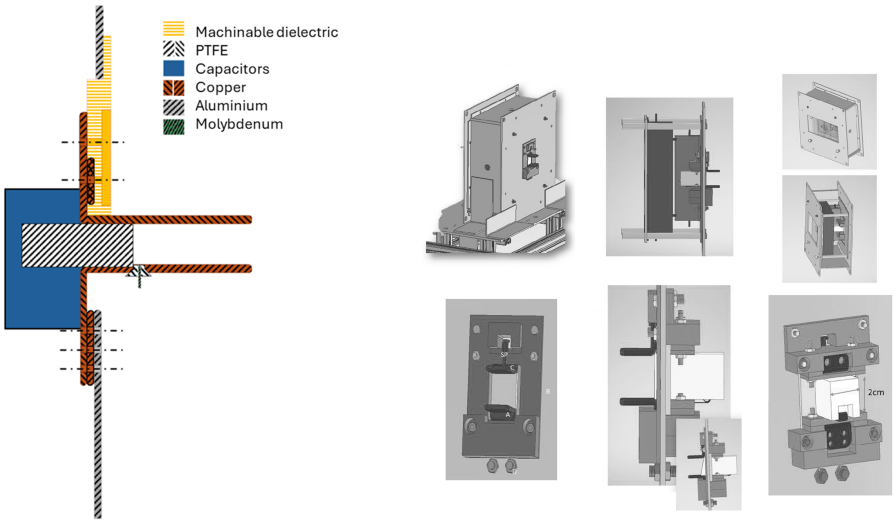

(c) (d)

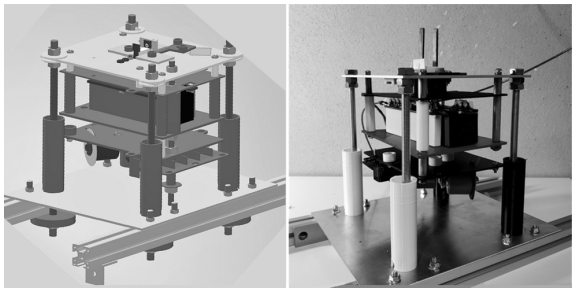

(e)

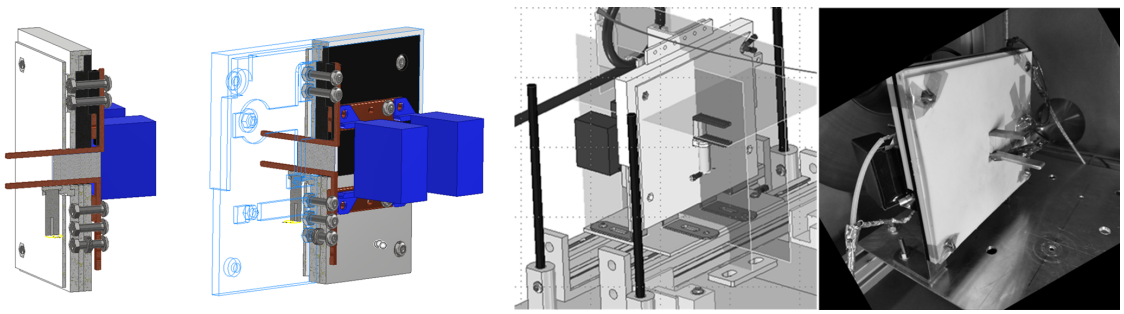

(f)

Figure 2.1: **Different iterations of the developed PPT breadboard model.** (a): CAD (left) and real (right) views of PμLSA (PPT version number 5 (v5)).(b): Close-up of the PμLSA discharge channel. "C" is the cathode electrode,"A", the anode electrode, "B", the spark plug, "D", the effective propellant surface (PTFE), and "E", the mounting structure. Dimensions l, h and w stand for channel length, height and width respectively. (c): Conceptual sketch of the cross-section view of PμLSA. (d): CAD views of the v1 PPT iteration. (e,f): and CAD (left) and real (right) views of the v2 and v4 PPT iterations.

perspective, the material maintains its shape and integrity under the standard mechanical stress conditions typical of these devices, many of which have successfully flown, and features a low density of 2.2 g/cm^3, contributing to lightweight designs. Additionally, it offers a low friction coefficient, beneficial for feeding systems designed with a spring mechanism to enable sliding. Finally, its chemical properties, including non-toxicity and low reactivity, enhance safety and compatibility with other system components and testing.
Feeding from the thruster discharge channel breech and involving a single PTFE bar, is selected for its simplicity, as opposed to side-fed configurations, despite reports of efficiency improvements in certain devices [29].

(b) **PPU:** The prototype requires its own PPU, which shall store and release the discharge energy (power segment), providing controlled (control segment) firing under varying operational conditions.

i. **Main discharge circuit:**

- The power segment is responsible for storing the discharge energy and preparing it for use by boosting the bus voltage to the high levels required for the discharge. The standard approach involves a capacitive circuit, with a DC-DC converter charging capacitors to store the discharge, which are connected to the discharge electrodes.
  In addition, although quantitative efficiency requirements do not apply, it is advisable to improve electrical efficiency (proportion of discharge energy converted into kinetic energy relative to resistive losses). To help improve it, on the one hand, the capacitor bank should be placed as close as possible to the discharge channel to reduce the initial inductance of the discharge path L_0, thereby reducing wire losses during the plasma discharge; on the other hand, the initial circuit resistance, R_0, should be minimized to reduce resistive losses. Also, the initial resistance of the circuit R_0 shall be reduced to minimize resistive loses. Consistently, selected capacitors should exhibit low equivalent series inductance (ESL) and equivalent series resistance (ESR).
- Discharges shall be monitored/counted.
  Comment about the design choice: This is done in this work by means of the oscilloscope.
- The system shall allow for variability in thruster discharge conditions.
  Comment about the design choice: This has been done in this work by either varying the PPU input voltage on the low voltage side to change the high voltage bias between the thruster electrodes and/or by replacing the capacitor bank.

ii. **Triggering circuit:**

- Thruster firing is led by a triggering system that provokes the breakdown of the discharge channel. The triggering system must necessarily lead to the main discharge breakdown on the first attempt when nominal conditions apply. Control signals at the selected thruster firing frequency are applied to the triggering system.
  Triggering the main discharge by an external means is required because the ignition voltage of a 1 cm discharge channel gap far exceeds typical ones of comparable devices[10]. Then, a triggering system supplies the initial free charge carriers required to

[10]The Paschen law describes the breakdown voltage as a function of pressure and electrode gap for a given gas. It reveals that there is a minimum value of the pressure-electrode gap product, beyond which the required electric field for breakdown increases asymptotically [118]. Beyond the Paschen minimum, the pressure becomes low enough that the mean free path of charged particles increases significantly, reducing chances for collisions. In metal–vacuum–metal (MVM) gaps [119], vacuum arcs necessarily form from electrode material by different mechanisms.

In the case of N_2, a limit case as this gas exhibits a higher breakdown voltage compared to other gases, the former transition occurs at approximately 0.5 mbar for a 1 cm gap.

Exceptions to Paschen's Law have been widely reported [120] at nano- and micro-scale electrode gaps, indicating the influence of additional mechanisms.

initiate the discharge. The energy associated with the triggering system shall be negligible compared to that of the main discharge.
Consistent to this, the power segment of the PPU shall include both the main discharge and triggering system power circuits. Control shall be applied to produce firings at a specified frequency, which can be achieved by applying control exclusively to the activation of the triggering system.

- The standard triggering system is spark-plug type [121, 122, 123], either based on a metal-insulator-metal (MIM) or a metal-vacuum-metal (MVM) gap. Essentially, the operation of the former is based on a surface flashover discharge along the dielectric surface filling the gap, and the second, on a (cathodic) vacuum arc [124]. Their power circuit can be either capacitive or inductive. It shall be possible to modify the initial voltage of the triggering system.
  Comment about the design choice: For the present work, MIM spark plugs are selected for their lower ignition voltage, and a capacitive approach, analogous to the main discharge, is adopted to simplify the PPU design. The spark plug is designed in-house to enable greater control over its tuning. A control element, externally controlled, opens and closes the spark-plug power line on its low-voltage (LV) side. This control allows to set the main firing frequency. Along the different experiments, the control over the switches has been carried out by means of a function generator (BK Precision 4055), and microcontroller-based platforms (such as Arduino) with specific drivers.
  The triggering voltage can be modified by varying the input voltage on the low voltage side of its PPU power segment.

(c) **Criteria for determining the design point:** The thruster design point, including channel length l, width w, height h, and operational conditions such as breakdown voltage V_0 and bank capacitance C (and consequently discharge energy $E_0 = CV_0^2/2$), shall be determined based on approximate scaling laws and simple electromechanical models. These laws are derived from the inspection of existing ablative PPTs of the same class used in microsatellites. A summary of the reference PPTs collected in Table A.1 of Appendix A are summarized below. Electromechanical models are implemented in Section 2.4 to further inform the design point.

i. **Channel size:** The channel size standard range places on the cm scale. Common values are 1 cm for h and w, and 1–a few cm for l.

ii. **Discharge operational point:** For V_0, a typical setting is about 1 kV, with 500–2500 V serving as a representative range for exploratory studies. The selection of C is constrained by the architectural limitations imposed by nanosatellite size and weight standards, and is placed on the μF scale. E_0 is a consequence of V_0 and C, locating under 10 J.
Previous studies found that a low energy-to-area ratio E_0/A causes PTFE surface charring, likely due to carbon atom and/or ion backflow [125, 126, 127]. The parameter h plays a key role in this process, as it influences the electric field intensity. This leads to carbon film growth, which is more difficult to evaporate than PTFE, negatively impacting efficiency. However, a wide range of ratios has been observed in the reference PPTs, so no further requirements on this matter are set.

iii. **Triggering parameters:** Generalities about the spark plug emitter/dielectric materials, shape, size, relative position with respect to the thruster propellant, polarity and operational point (triggering voltage $V_{sp,0}$, triggering energy) can be inferred from existing prototypes, but specifications are determined by the own practical experience. The triggering voltage is typically set to 1 kV in devices with spark plugs with sharp electrodes, Research tests range across several kV [63] to anticipate ignition difficulties associated with degradation, aiming to gain insight into lifetime reliability.

2. **Expected performance, power demand and firing frequency:**

(a) **Energy range and expected performance:** Comparable PPTs [97, 102, 30, 61, 116] with a stored discharge energy not exceeding 10 J, mostly under 5 J, typically provide a specific impulse in the range of hundreds of seconds and an impulse bit on the order of tens of μNs. [Note that, alternatively, the thrust, defined as the time-integrated impulse bit, can be increased simply by increasing the firing frequency.]

Comment about the design choice: Electromechanical models are implemented in Section 2.4 to further inform the design point, providing a performance estimate aimed at matching the cited ranges.

(b) **Power demand:** Power demand to a potential satellite bus must be compatible with nanosatellite platforms, thus below 20 W, with bus voltage and current set in alignment with CubeSat standards. [It is assumed that in orbit, when the thruster module is active, the power generated by the satellite will be primarily allocated to its operation. Note that due to its pulsed nature, the power consumption can be reduced virtually to zero by decreasing the firing repetition frequency.]

This requirement primarily affects the power segment of the PPU, by constraining the power rate of the DC-DC converters. Alternatively, input current and slew rate constraints imposed by the satellite bus can be potentially bypassed by incorporating a storage unit at the input of the thruster PPU; however, this approach is not considered in the present work.

(c) **Main firing frequency:** The upper and lower limits of the firing frequency are determined by the power-limit of the PPU (in turn, determined by the requirement 2(a)), and the experimental needs related to chamber background pressure and oscilloscope data-saving time. The former is fundamentally constrained by the power segment, while the latter requires the firing frequency to be low enough to allow the chamber pressure to return to its ultimate dry level between pulses.

Comment about the design choice: A firing frequency[11] of 0.1 Hz is therefore established. Pumping system and oscilloscope information is included in Section 3.2 (Chapter 3).

3. **Experimental suitability:** The experiment shall meet the requirements imposed by its operational nature and those derived from the research experimental plan.

(a) **Capacitor characteristics driven by the nature of PPT discharges:**

i. Discharge capacitors must be non-polar because of the current-reversal nature of the thruster underdamped discharge.

ii. Additionally, the use of non-piezoelectric capacitors simplifies architecture demands and reduces failure risk;

iii. and avoidance of ferroelectric materials, may favor repeatability.

iv. These have to be non-electrolytic, to be vacuum suitable explained below in the requirement 3.c.i.

v. Finally, low ESR and ESL are convenient to favor discharge efficiency.

(b) **Endurance:**

i. **Spark plug reliability** is reported to be a sensitive issue in the literature due to erosion and contamination [128]. A requirement of $2.5 \cdot 10^4$ firings is set for the spark plug system to ensure it does not interrupt the longest test conducted, the one presented in Chapter 6.
Comment about the design choice: Following the methodology presented in that chapter, and to be conservative, this figure includes a safety factor of 3 to discard spurious discharges and a factor of 10 for spark plug activation per main firing performed.

ii. Consistently, the **main capacitor bank** should ensure at least 1000 discharges.

[11] From now on, the term "firing frequency" will exclusively refer to the main firing frequency.

(c) **Vacuum operation and facilities:** The ablative PPT discharge can develop if the background pressure remains under $1 \cdot 10^{-4}$ mbar. Hence, the prototype and its setup shall be suitable for vacuum operation, and, in particular, in the dedicated EP2 facilities.

i. **Vacuum operation:** Electronics components, interfaces and structural materials must be vacuum suitable. Vacuum certificate is not required.

A. **Structural materials:** Applying, low outgassing and mechanical strength; low affinity to water, low absorbent capability or high resistance to radiation are not necessary at this research stage.
Special care for thermal dissipation associated to the channel electrodes has not been reported as a typical requirement in the referenced PPTs.
(The remaining enumeration of material requirements, unrelated to vacuum requirements, includes the following: thermal stability and chemical resistance are essential for the discharge channel components. Electrodes should exhibit good electrical conductivity and strength, and are recommended to be manufacture-friendly. Additionally, a balance between strength and good emissivity is important for the spark plug electrode. For insulating materials, a high dielectric constant, thermal resistance, and manufacturability are key considerations. Structural material elements should be metallic wherever possible and demonstrate robustness.)

B. **Electronics:** In the context of electronics, materials with a low vapor pressure under vacuum conditions are allowed. Hence, components including liquids or any material which could evaporate or sublimate in a vacuum, are forbidden, as electrolytic capacitors. Components with low heat dissipation needs are also preferable. Special attention has to be put on sealed components, and the properties of the sealing materials in vacuum, as well as the component rating for pressure gradients in case it applies.
[At least, the main discharge capacitor bank has to be operated under vacuum consistently to requirement 1(b,i).]

C. **Good design practices to avoid electrical hazard inside the chamber:** On the high voltage side, the risk of electrical hazards increases during the experiment as pressure lowers. Breakdowns between biased points are more likely to occur as the background pressure decreases up to reaching the Paschen minimum, beyond which the likelihood of this type of breakdown substantially lowers. However, surface flashovers become more favorable instead.
Hence, general good practices to address this challenge include, among others, avoiding sharp sharp geometries for metallic elements; maintaining sufficiently large clearance gaps between metallic elements differently biased; in gaps dielectrically filled, retracting the edges of the metallic elements with respect to the insulators; and covering biased elements with insulating coatings.
[Regarding the discharge channel, clearance around it is beneficial to avoid perturbing the plasma; additionally, blunt channel edges to promote a uniform discharge are also recommended.]

ii. **Size:** The breadboard prototype will be tested inside the HEDRON vacuum chamber, a cube of 50x50x50cm at the EP2 Laboratory facilities. The access to its inside is limited by a 25 cm-diameter window.
Note that, even though satellite integration requirements are not applicable, and thus the prototype is not subject to any size or weight requirements relative to satellite standards, the reference PPTs for design (Table A.1 in Chapter A) are compatible with size and weight CubeSat standards. This fact highlights the potential for adapting the selected design in future R&D stages to meet similar conditions, while it remains out of the scope of the present dissertation.
It is convenient for the prototype to exhibit mass distribution symmetry.

iii. **Electrical interface:** Two medium high-voltage (MHV) feedthroughs at HEDRON are available to power the prototype.

(d) **Electromagnetic compatibility:** The electromagnetic noise generated during thruster operation must not impede the proper functioning of the thruster control and the diagnostic systems.

(e) **Design for rapid iteration:** The prototype shall exhibit flexibility to enable rapid iteration and accommodate modifications of both geometric and operational modifications, as well as of the electronics.

(f) **Discharge monitoring:** Visual access to the discharge during its in-channel phase has to be enabled.

In addition, the main discharge and triggering circuits should allow for electrical monitoring.

4. **Priority for cost-effectiveness:**

(a) **PPU components:** A space-suitability certificate is not required, and where possible, components should be sourced as commercial-off-the-shelf (COTS) to minimize costs and development time for the thrusters. While non-COTS, optimized electronics may offer superior accuracy and endurance, this research prioritizes cost-effectiveness, flexibility for iteration, and ease of acquiring spare parts.

When evaluating the voltage or current ratings of components to determine their appropriateness, it is essential to consider the characteristic of the event as well as the fatigue response of the component (/material). Frequencies of interest are on the order of hundreds of kHz for the main discharge phenomena and tens of MHz for ignition and reignition phenomena. The latter generates high-amplitude noise and is particularly problematic for control components.

(b) **High voltage (HV):** Due to the increased difficulty in managing risk for electrical hazard, the number of components working at HV should be reduced as much as possible. Indeed, available COTS electronics reduce for HV operation.

2.3. Detailed System Architecture

Plasma generation and dynamics within a PPT discharge are influenced by factors such as energy availability, channel bias, geometry, electrode circuitry, and material properties. A PPT prototype with flexible adjustment capabilities has been developed for experimental analysis to study the impact of these factors.

The complete architecture of the developed PPT prototype, based on the design choices derived from the specifications outlined in Section 2.2, is now presented.

In order to facilitate iteration, a modular solution has been considered. The following subsystems are involved: 1) the thruster head, 2) the propellant system, 3) the PPU and 4) the chassis. These are described along next subsections. [Any sensing system is beyond the scope of the present chapter and will be addressed in the following ones.]

2.3.1. Thruster head

In the developed PPT, the thruster head consists of a discharge channel formed by two rectangular electrodes made of copper: the cathode (lower) and the anode (top), known as the main electrodes, which extend axially to define a parallel-rail channel. The electrode edges are blunt to reduce arcing risk. At the channel rear, a PTFE bar is clamped between the two electrodes to serve as the thruster propellant. The main cathode is electrically connected to the chassis, which is grounded to the vacuum chamber.

Besides, the cathode accounts with the incorporation of a in-house MIM spark plug. A 1 mm-diameter cylindrical electrode made of molybdenum (Mo), bevel-sharp at its tip and fitted into a 2 mm outer-diameter

PTFE cylinder, is embedded in the main cathode as the spark plug emitter. The emitter tip is flush with the edge, sharp, of the main cathode hole; the PTFE filler is slightly recessed compared to the metal components. The spark plug is centered along the electrode width, and next to the propellant surface. The anode role of the spark plug is played by the main cathode (grounded), and thus the emitter is negatively polarized. A cross-section view of the prototype illustrating the former components is included in Figure 2.1(c).

To fulfill experimental needs, a geometrical variation of the discharge channel is allowed by modifying h through electrode relocation, and w, l and shape by easily replacing the electrode. Figure 2.2 illustrates these features. The geometrical ranges of interest for this research work are shown in Table 2.1.

Electrode thickness is a crucial parameter for withstanding manufacturing loads and structural integrity during operation, i.e., managing the thermal loads, especially in vacuum conditions where heat dissipation is limited. A main electrode thickness of 3 mm has been selected, demonstrating suitability for up to $5 \cdot 10^4$ thruster firings. No special measures for thermal dissipation associated with electrode heating have been deemed necessary to apply.

Some considerations about the former thruster head geometrical parameters:

1. With fixed V_0, increasing h reduces the electric field., and vice versa.
2. The energy-to-propellant-area ratio E_0/A is an important factor in PPT design concerning ablation as described in the requirement 1.(c,ii). However, comparing thrusters solely by this metric may be unreliable if both h and w vary, affecting results differently.
3. In an ideal parallel plate configuration[12], the electric field between the plates is nearly uniform, except at the edges. The larger the electrode width w relative to height h, the less significant the border effects.
4. Finally, while the spark plug discharge intensity should not further affect the main discharge beyond triggering it, its location and discharge intensity may influence the uniformity of propellant ablation. Relevant MIM spark plug factors are electrode separation and geometry, emitter and spacer material, and the relative location with respect to the main propellant bar.

2.3.2. Propellant

A single PTFE bar is used to fed the thruster, clamped between the electrodes at its breech, as no mechanisms to automatically reposition the propellant surface have been required.

The effective propellant surface area A is limited by the channel l and w. However, the propellant bar is not restricted from exhibiting a wider section than w aiming to observe potential deposition of discharge byproducts. The propellant surface and the electrodes initially form a perpendicular angle.

2.3.3. Power Processing Unit (PPU)

The channel electrodes are connected to an energy storage unit, specifically a capacitor bank as is standard in PPTs. These elements form the discharge path: Once the capacitor bank is charged to V_0, high voltage and large enough to sustain the plasma discharge (helped in triggering), the spark plug is ignited to provoke the breakdown of the channel over the propellant surface, thus, releasing the stored energy for the main discharge E_0 to the main electrodes. Hence, coordination between the spark plug operation and the

[12]Outside the scope of this work: Insulated nozzles and flared electrodes enhance gas dynamics. While the former may also preserve ion momentum, flared electrodes reduce the axial electric field by increasing h. Tapered electrodes converging at the channel exit concentrate the electric field, and when combined with flared electrodes, may help mitigate electric field reductions due to channel divergence.

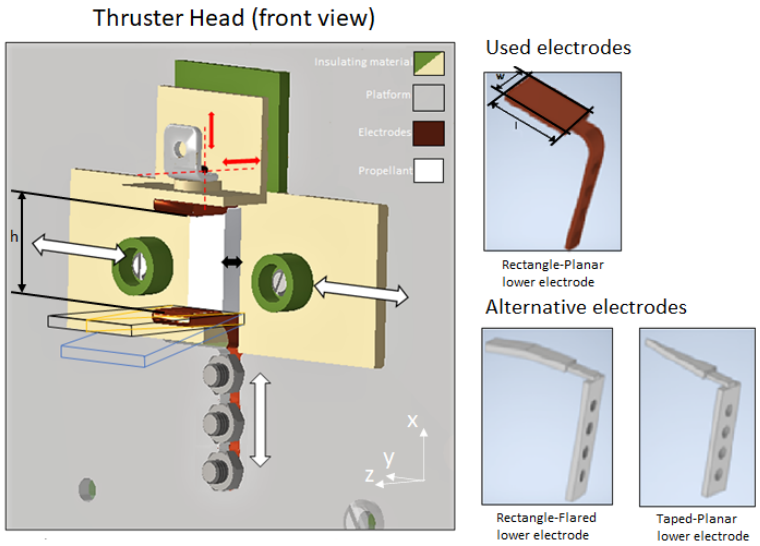

Figure 2.2: **Discharge channel features: acceptance of geometry modifications in electrode length l, width w, height h and shape (flaring and tappering angles) through electrode translation and replacement.** The image represents a CAD view of the PPT iteration version v2, whose features are analogous in PμLSA (iteration version v5).

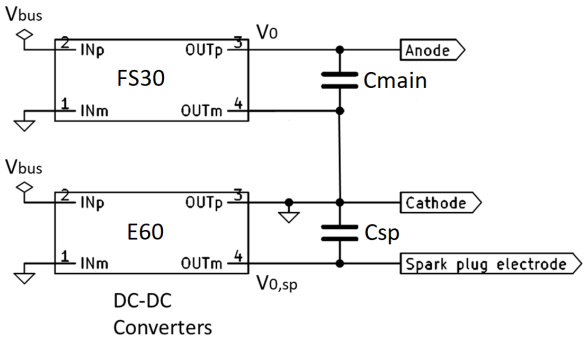

Figure 2.3: **PμLSA power segment schematic**.

main battery charge level is required to fire the thruster at desired operational conditions. Also, to provide consistent thrust, controlled pulses are required for the thruster to fire at a specific frequency.

The Power Processing Unit (PPU) manages the charge and discharge cycles. The PPU consists of two segments: (1) the power segment, which raises the voltage to operational levels and stores the discharge energy for both the main discharge and spark plug circuits, and (2) the control segment, which, by acting on the triggering system, provides repetitive firing at an adjustable frequency.

The main circuit is capacitive, but the similarities and degree of independence between it and the spark plug circuit can vary, and different circuit alternatives have been explored: V1–V4. The primary configuration, V1, which has been used for the experimental results presented in this dissertation, is presented within the present section, while alternative configurations are introduced in Section 2.3.3.1.

In V1, the PPU power segment involves two analogous capacitive circuits: one dedicated to the main discharge and the other to the spark plug discharge. These two subcircuits remain independent, with control applying solely to the spark plug's charging process. The power schematic basis of V1 is shown in Figure 2.3 and explained below:

1. A voltage elevation pre-conditioning stage is required to raise the voltage from the bus voltage to discharge conditions. [In this work, power supplies are used (MCP 350W-200V) to represent the low-voltage satellite bus in each of the two circuits respectively.] XP Power EMCO flyback DC-DC converters have been employed for this purpose; the FS30 model for the main circuit and the E60 for the spark plug. Respectively, with nominal maximum input voltage/output voltage/consumed power of 12 V/3 kV/ 10 W and 15 V/6 kV/ 3 W. This product line exhibits isolation between the input and the output sides, and can allow for floating output. Isolation between the satellite bus (low voltage) and the high voltage circuit stages is a recommended practice in real scenarios, to protect the satellite bus from potential failure propagation.

   Ground loops are avoided by connecting all grounds in the PPU power segment to a single point, which is then directly secured to the vacuum chamber.

2. After the voltage preconditioner, there is the capacitor bank charge stage. Ceramic capacitors and metallized-polypropylene (MKP) film capacitors meet the required specifications listed in Section 2.2 and are available at the kV high-voltage range. However, the availability of MKP capacitors becomes more limited at voltages above several kilovolts. Both types of capacitors also exhibit low ESR and ESL [129], making them preferable for high-frequency applications by promoting a more efficient power delivery. MKP capacitors can outperform ceramic capacitors at high frequencies, presenting lower dissipation factors and also a more stable capacitance.

   When comparing surface-mount capacitors to screw-terminal ones, both offer robust connections. On one hand, screw-terminal capacitors simplify experimental iteration. On the other hand, while surface-mount capacitors do not offer this advantage, they facilitate compact assemblies and automated manufacturing, making them ideal for high-density circuit board designs, though this is not a requirement for this work. Additionally, they are less commonly available in MKP variants.

   Based on the reasons above, screw-terminal ceramic capacitors have been employed in the triggering circuit, where efficiency is less critical and a wider voltage range is required to test the in-house developed spark plug. In particular, a VISHAY 715C50KTT56 Disc Capacitor: 560 pF, 50 kV DC/34 kVrms, N4700-dielectric. Meanwhile, screw-terminal MKP capacitors have been selected for the main circuit.

   Throughout this dissertation, various thruster batteries (i.e., for the main discharge) were used along the different experimental campaigns. These involve different VISHAY MKP capacitor models and slight modifications to the bus arrangement to accommodate them and to be adapted to C-parametric studies. They all are listed in Table 2.2, and have been electrically characterized in Chapter 3. The specific battery used for each plume study shown in this dissertation is indicated in the table above, and referenced accordingly where applicable along the document.

   The need of changing the battery arose because the original battery, Battery 1, suffered an electrical breakdown during an endurance test not included in this work. Note that all these batteries were used for the preliminary work required for each consolidated study, not presented in this document, which contributed to their usage time. However, none of the batteries used experienced significant degradation affecting their capacitance or electrical curves during the experiments presented here.

Table 2.2: **Different thruster batteries were used throughout this work, primarily differing in capacitor models and their accommodation within the bus bar.** The capacitor model for Battery 1 is MKP386M510125JT4, and for Battery 2, it is Vishay MKP386M510200YT4. The numbers in parentheses distinguish between experimental campaigns, sorted by date. The configuration of Battery 2B is more compact than that of Battery 2A, with all the capacitors being directly screwed to the bus bar as in Battery 1, reducing the circuit's initial resistance and inductance, and yielding a discharge voltage waveform closer to the ideal RLC circuit.
[Battery 2B (2) has been used in two campaigns, the preliminary version of Chapter 6's work [9] (not included here) and the additional testing for the consolidated work presented here [106]; however, it is denoted simply as (2) for the sake of simplicity. /Missing numbers correspond to data not shown in this document nor published.]

Plume campaigns	Battery	Dissemination
Electrical characterization included in Chapter 3	1 (1)	[8, 2]
ToF single Langmuir probe data, used for the main analysis in Chapter 4 and exclusively in Chapter 5	1 (3)	[8, 2]
ToF wire electrostatic probe data, used for the secondary analysis in Chapter 4	1 (2)	[7]
ToF single Langmuir probe data used for the secondary analysis in Chapter 4	2A (1)	-
Wire electrostatic probe data used in Chapter 6	2B (2)	[9, 106]

High-impedance paths (slim resistor RSHVS2.5, 2.5 W, 10 kV, 10 MΩ) between the batteries and ground have been added to discharge them when the circuits are off, thereby reducing risks during periods of inactivity.

3. The plasma discharge circuits connect, respectively, each battery with the corresponding electrodes.

   To improve electrical efficiency of the main circuit, measured as the proportion of discharge energy converted into kinetic energy vs. resistive losses, a low initial inductance L_0 improves it [23] (see requirement 1(b,i) in Section 2.2). To this end, the MKP capacitors are mounted on a bus made of copper bars attached to the platform at the thruster head back, symmetrically distributed at both sides of the channel. The rest of the main circuit, which includes the voltage elevation stage, is kept outside the chamber. [Although not required with the current configuration, the DC-DC converters used have been verified as suitable for operation inside the chamber.]

   Since considerations regarding spark plug efficiency do not pertain to system requirements, the entire spark plug circuit, excluding the spark plug itself, was placed outside the vacuum chamber.

Capacitance C, electrode voltage V_0 (and, hence, pulse energy E_0) modifications are allowed in the main circuit, respectively by change of capacitors and selectable DC-DC converter input voltage. In the case of the spark plug, replacing of the capacitor bank and selectable input voltage are also allowed. However, $V_{sp,0}$ is primarily determined by the physical properties of the spark plug and a minor dependence on V_0. Since its charging process is significantly slower than its discharge phenomenon whatever the selected input voltage, it ignition occurs once $V_{sp,0}$ reaches the minimum emitter voltage required for its breakdown. This fact also establishes the spark plug firing frequency.

Regarding PPT control applied to the spark plug power circuit in V1, a description is provided below, and a schematic illustrating the timing of the various processes involved is shown in Figure 2.4.

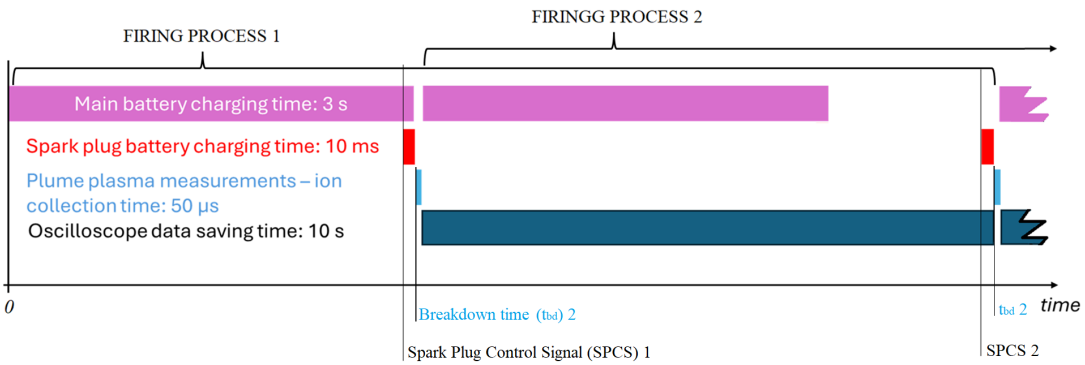

Figure 2.4: **Concept timing scheme of the different processes involved in a thruster firing illustrated for an initial firing (1) and its consecutive one (2), being representative of any other further one.** Focusing on Firing Process 2, there is no control signal to initiate the charging of the main battery; instead, it begins charging automatically once the electrical discharge process has occurred. The electrical process accounts for the in-channel plasma, and so it takes less time than the plume probes' data collection period. After the main battery is fully charged, the system waits for the oscilloscope to finish saving data from the previous discharge. Once this process is complete, a control signal is sent to the spark plug circuit, closing its power circuit and initiating its charging. When the spark plug reaches a sufficiently high voltage, it discharges autonomously, without the need for further control signals, and triggers the breakdown of the main discharge.
To capture the relevant data, the oscilloscope internal trigger is set to detect the voltage drop in the signal monitoring the main battery anode. It records data starting a few microseconds before this voltage drop and continues through the end of the ion collection period measured by the farthest plume plasma probe.

1. PPT control is applied to the spark plug power circuit, by placing a control element on its low-voltage side, externally controlled by a microcontroller or function generator. This configuration allows the circuit to open or close its power segment as required. The spark plug battery charges until its voltage is high enough to provoke a flashover between the emitter and the main cathode across the dielectric surface filled gap. This breakdown voltage $V_{sp,0}$ depends on the spark plug's material, geometry, size, and temperature, and also on the main channel bias. The spark plug is designed to generate a discharge strong enough to initiate a flashover along the thruster's propellant surface at a specific channel voltage, V_0. Its energy is notably lower than that of the main discharge, not to impact the main discharge process after the triggering it.

   High-voltage transistors and Pickering 68-1-A-12/2D dry reed relays have been used as control elements. Transistors have been especially sensitive to the high voltage ignition noise

   Note that the spark plug circuit operates on a timed basis, remaining open for a finite time interval. In case this time exceeds the charging time of the spark plug circuit, on the order of 10 ms, resulting in multiple spark plug discharges. However, these do not affect the main firing because of the different time-scales. On the one hand, the main discharge, lasting tens of microseconds, is completed well before the next spark plug discharge occurs. On the other hand, the spark plug's charging period is short enough relative to the main circuit's that these extra discharges occur when the main circuit is essentially discharged. Additionally, these additional spark plug discharges are advantageous in cases where the main firing fails to trigger, offering another opportunity for ignition. This feature is particularly valuable when operating at V_0 significantly below the design point or during the late stages of the spark plug's operational life.

2. The main firing frequency is adjustable but top constrained by the power capability of the main DC-DC converter, which determines the minimum main capacitor bank charging time to reach the se-

lected operational V_0. Alternatively, accommodating the oscilloscope data-saving time requirement during experiments can be a stricter constraint to set the maximum firing frequency. As a consequence, a reference firing frequency of 0.1 Hz has been established.

No special measures for thermal dissipation associated with PPU heating have been deemed necessary to implement.

The thruster is powered using coaxial cables that pass through MHV feedthroughs and connect to screw terminals on the thruster side.

Finally, an oscilloscope is used to monitor and count both the main and spark plug firings.

2.3.3.1 Alternative configurations for the spark plug circuit

Alternative ignition configurations have been preliminarily tested to reduce circuit voltages at locations other than the spark plug gap. To this aim, the voltage peak across the gap is generated inductively. Lowering voltages from kilovolts to hundreds of volts offers several advantages, including reduced demands on the output of the voltage elevation stage, greater availability of COTS components, as well as easier PCB design and facilitation of its down-scalability. In addition, an inductive scheme for spark plug triggering allows for greater decision-making over its ignition voltage compared to a capacitive circuit, provided a sufficiently high voltage slew rate. Inductive-based spark plugs are common in the literature [123].

Details of these alternatives are provided below:

- **V2: "Pure" Inductive Circuit**

  A purely inductive circuit can be used for spark plug ignition, consisting of a power supply, an inductor, and a switching element. The load, i.e., the spark plug, is placed in parallel to the inductor, as shown in Figure 2.5(a). During a first phase, the switch keeps the load line open, allowing current to flow through the inductor and store magnetic energy. When the switch closes the load branch, the collapsing magnetic field induces a voltage peak across the inductor, which, if the circuit is properly sized, causes the spark gap to ignite.

- **V3a,V3b: Capacitor-ignition coil Circuit** To store energy in a capacitor while still benefiting from the voltage peaks induced by a voltage transient across an inductor, an alternative to adding a capacitor in parallel with the inductor in V2 must be considered, as this would convert the circuit into a resonant one. Instead, considering a capacitive stage, an additional inductive branch involving a step-up transformer, also known as an ignition coil, can be coupled in parallel to the capacitor. The primary winding is placed in parallel with the capacitor, with the circuit branch controlled by a switch, and the secondary winding is connected in parallel with the load, i.e., the spark plug gap. In this configuration, during the capacitor's charging phase, the ignition coil is disconnected. Once the capacitor is charged, the switch closes the branch, allowing the capacitor to release its energy to the primary coil, which induces a voltage peak in the secondary winding. If the circuit is properly sized, this voltage peak shall be large enough to ignite the spark gap.

  Two subversions are presented: V3a and V3b. In V3a, shown in Figure 2.5(b), the basic concept is presented; for simplicity, without including a voltage elevation stage prior to the capacitor, as done in V2 and V4 (below) too. [Also for the sake of simplicity, the high-resistance paths for discharging the capacitors when the circuit is off have been omitted in V3–V4.] For reference, using a Cetronic TC-31 ignition coil, if applying 200 V to the primary winding, an output of 3 kV is obtained at the secondary. V3b incorporates an in-house boost-topology DC-DC converter to elevate the voltage from the bus level to V3a. Figures 2.5(c) and (d) respectively illustrate an example for V3b and its simulated voltage outputs in LTspice (with a Cetronic TC-31 ignition coil and ESR of both capacitors set to zero), useful to estimate the peak voltage at the spark plug emitter. The DC-DC converter developed

for the V3b approach is equivalent to using any other COTS DC-DC converter, such as the flyback-topology one used in V1, but in-house alternatives facilitate debugging and offer greater flexibility for customization.

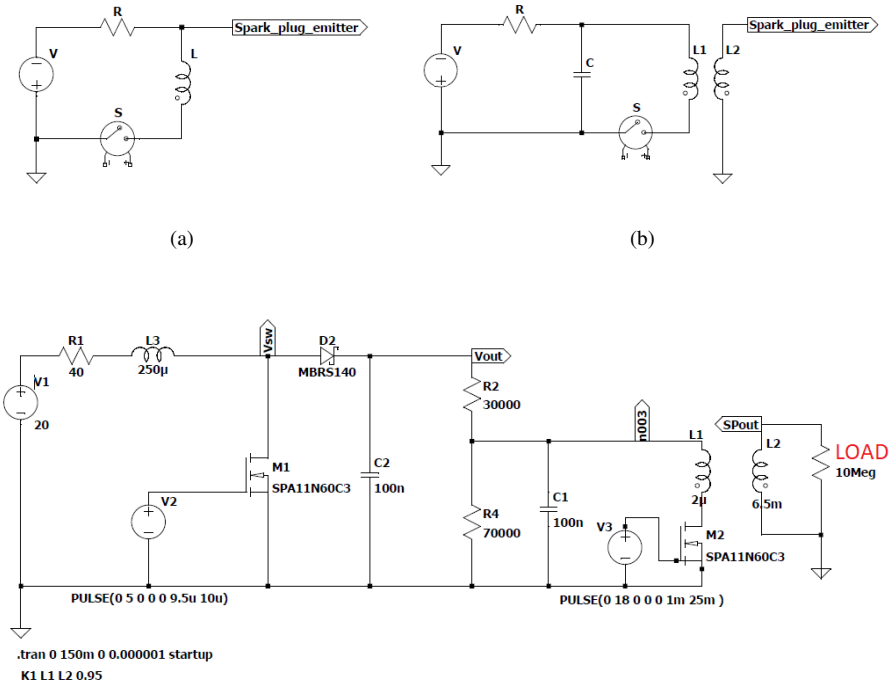

Figure 2.5: **Alternative power and control schematics for the spark plug circuit.** (a): version V2, inductive; (b): V3a, capacitor-transformer; (c): V3b, in-house boost DC-DC converter; (d): Simulation results of V3b; (e): V4, thyristor control.

Several observations apply to the V3b example presented vs. its actual implementation. First, the polarity of the spark plug must be inverted to negative, as described in Section 2.3.1. Second, the power sources used in the simulation example to control the MOSFETs should be replaced with drivers, such as the UCC53x0, if control is to be achieved using microcontroller-based platforms. Third, the diode used in the simulation must be replaced with one properly rated, such as the Vishay BYV26C-TAP diode. Fourth, the MOSFET used in the primary-winding branch limits the specifications of

the ignition coil; an alternative MOSFET is the SPA11N60C3. Fifth, Transient Voltage Suppressors (TVS) may be beneficial on the primary-winding branch to protect the control circuitry when the spark plug ignites.

Finally, **configuration V4** proposes an **alternative control schematic incorporating "self-automation"** to the inductive versions described above, through the use of a thyristor whose activation is linked to the main battery's charge level. Self-automation refers to the system's ability to be directly activated by the PPU power segment, without the need for external control. Figure 2.5(e) illustrates this configuration, exemplified over the V3a design.

2.3.4. Thruster chassis

The thruster mounting structure, structural platform or thruster chassis provides a robust envelope for the thruster head and electronic boards. It is illustrated in Figure 2.1(a).

The chassis is essentially a 160 mm $\times$ 170 mm aluminum plate with a central cutout that accommodates the channel electrodes and the propellant bar, which extend axially toward one of the plate's faces. Capacitor banks are attached to the rear face of the chassis using screws, symmetrically distributed on both sides of the channel. While the channel cathode is mechanically connected to the chassis, the channel anode it is electrically insulated. This insulation is achieved using a dielectric piece that also serves a structural role by supporting the capacitors on their anode side. A series of holes define discrete positions that allow the channel height to be adjusted by vertical displacement of the cathode over the platform. The propellant surface is positioned close to 1 cm from the platform, and the cutout includes a 5 cm diameter clearance area around the channel. Both features are designed to limit plasma perturbations caused by potential differences between it and the platform. The metallic part of the platform is electrically connected to the vacuum chamber ground.

On the underside of the platform, two 30 mm $\times$ 30 mm standard aluminum profiles are attached on either side of the channel. These profiles are vertically oriented relative to the floor and serve as the structural interface for securing the thruster system to the support structure that accommodates it inside the vacuum chamber.

The latest is an auxiliary setup structure that also allows for adjustable alignment with the diagnostic systems described in subsequent chapters. Mounted on it, the thruster channel is oriented opposite to the pumps.

2.4. Performance estimate based on electromechanical model implementation

Electromechanical models applied to the in-channel plasma stage are commonly used to guide the selection of the design point. These models estimate how the thruster configuration influences performance, aiming to identify a design point that satisfies the system requirements. These models are derived from simplified versions of the plasma momentum conservation equation and the series RLC circuit equation, as described in [23]. These models provide a general overview of PPT discharge behavior, despite their limitations in fully capturing its complex physics.

Before presenting the model, the Cartesian coordinate system used in the experimental study on PPTs in this dissertation is described. The z-axis points away from the thruster, downstream the plume. The x-axis is parallel to the electric field and is negative relative to it (cathode-to-anode direction). The y-axis completes the right-handed trihedron and is parallel to the self-induced magnetic field. The (0,0,0) point locates on the center of the propellant surface. Note that, in this work the x axis is vertical and the y axis, horizontal, contrary to typical x, y plot arrangements. The coordinate system has been shown in Figure 2.1(c).

In the electromechanical models used for rectangular PPT configurations, it is typically assumed that the plasma follows an axial (z) approximation, concentrated within a sheath of infinitesimal thickness δ with constant properties. This sheath is movable along the discharge channel over the discharge period and is characterized by specific resistance and inductance time laws. The resulting system of equations is:

$$\frac{\mathrm{d}}{\mathrm{d}t}(mv) \approx hw \int_{\delta} jB \;\mathrm{d}z = \int_{\delta} IB \;\mathrm{d}z = IB\delta = I(\frac{\mu_0}{2w} I)\delta \approx \frac{1}{2}\mu_0 \frac{h}{w} I^2 \tag{2.1}$$

$$0 = \frac{1}{C} I + \frac{\mathrm{d}}{\mathrm{d}t}\left(L\frac{\mathrm{d}I}{\mathrm{d}t} + I\frac{\mathrm{d}L}{\mathrm{d}t}\right) + \frac{\mathrm{d}}{\mathrm{d}t}(R\, I) \tag{2.2}$$

where t refers to time, m is the ionized mass, $v = \frac{\mathrm{d}z}{\mathrm{d}t}$ to the axial velocity, j is the current density, $I = I_x$ to the ion current (anode-to-cathode, $-x$ axis), $B = B_y$ to the magnetic field ($-y$), μ_0 is the vacuum permeability, and L and R are the discharge circuit inductance and resistance respectively, modeled as a initial component (L_0, R_0) plus the plasma contribution ($L_p(t)$, $R_p(t)$). The t-dependence of v, I, L and R is omitted for clarity. The relationship between B and I follows Ampere's law. The final step in Eq. 2.1 is valid if $h/d \ll 1$.

The assumptions of the equation system above are now presented in greater detail. On the one hand, the momentum equation assumes (1) locally-concentrated nature of the plasma density distribution as a sheet of negligible thickness with constant properties within its entire volume, being axially current free. (2) This formulation takes the 1D approximation in z, deprecating edge effects and derivatives along the cross directions (x, y) and thus taking properties at the channel center line. (3) The sheet is assumed to be fully ionized and no distinction between charge nor mass is done between the ions contributing to the current. (4) Taking $h/w \ll 1$, as width is much larger than height, magnetic field lines can be assumed perpendicular to the current, and so, the Lorentz force always point towards the channel exit. In this case, the following plasma inductance approximation $L_p(t) = (\mu_0 h/w)\, z(t)$ can be used, where μ_0 is the vacuum permeability. (5) In general, as the model lays aside specific terms for particle interaction or pressure terms (cold ions), it does not allow for any recovery of thermal energy. (6) The plasma resistance R_p is assumed constant. (7) Finally, additional assumptions can apply to the mass term defining different model versions. In the Slug model the time-dependence is removed while the Snowplow model retains it to represent the entrainment of additional ambient mass as the plasma sheath propagates down the channel. On the other hand, for the RLC circuit equation, the plasma sheet is considered as a resistance, commonly constant as total ionization is assumed since the beginning, and a time-dependent inductance term. The plasma sheet travels along the channel by the dynamics described in the momentum equation.

To investigate how the operational initial conditions (which include initial discharge voltage V_0, initial ionized mass m_0, initial circuit inductance L_0 and resistance R_0) along with the constant bank capacitance C, influence the plasma solution computed using the Snowplow model, a parametric study on C, L_0 and total resistance R is conducted around a reference point defined for this section.

The time-series solution for the sheet current, velocity and axial location are presented in Figure 2.6 for a parametric space around a reference point marking magnitude limits for the variables involved. The reference conditions are: $V_0 = 1000$, and $C = 6\ \mu$F, hence, $E_0 = 2$ J; $m_0 = 1\ \mu$g; $L_0 = 10$ nH and $R = 10$ mΩ, which accounts for R_0 and the plasma contribution. According to the system specifications listed in Section 2.2, these values are derived from data on existing low-power PPTs [96, 29, 130, 131, 132, 89, 133, 134, 64, 65, 104] and take into account size and weight constraints, as well as considerations regarding electrical efficiency η_e. Regarding η_e, defined as the fraction of discharge energy converted into kinetic energy rather than resistive losses, in [23], R.G. Jahn estimates it in a specific way to provide a means to constrain the range of interest for L_0 and R_0. In addition, the same work by this author discusses the role of structural constraints in parameter selection. These two discussions have been considered and are summarized as follows:

- On the one hand, the proposed formulation for η_e is presented.

First note that the power delivered by the capacitance to the circuit can be divided into a rate of resistive heat generation (I^2R), rate of energy stored in magnetic fields ($\frac{1}{2}\,\mathrm{d}(LI^2)/\mathrm{d}t$) and rate of work done on the moving plasma sheet ($^1/_2\, I^2\dot{L}$), the energy delivered to the circuit along the discharge time constitutes the integral of the first (resistive) and last (dynamic) power terms. Hence, η_e can be defined as the ratio of the kinetic energy term to E_0. [This definition assumes the dynamic energy term as completely convertible into kinetic energy neglecting dynamical losses, as well as considers the resistive term a total loss despite partially contributing the thermal energy of the fluid.] Finally, an estimate of the magnitude of η_e fully based on inductance terms can be obtained if E_0 is approximated as $^1/_2\, L_0 I^2_{ideal,max}$ in an ideal scenario where R is null, thus yielding $\eta_e < \Delta L/L_0$, where ΔL is the increment of the inductance along the discharge time. With non-zero R, $\Delta L = \int I\dot{L}\mathrm{d}t$. If the former efficiency criterion is not met, it implies either that excessive resistive losses occur or that the plasma element leaves the circuit before the current pulse is completed, resulting in residual energy remaining in the capacitance or the electromagnetic field.

As a consequence of this formulation, efficient discharges will exhibit ΔL comparable to L_0. Thus, $R < \dot{L}$. For reference, using the formulation of assumption (5) above in the dynamical equation to estimate $\dot{L}$, a range [1 10] mΩ is obtained for an assumed ion velocity between [10 100] km/s [2, 114]. This corresponds to [1 10] nH for the same velocity range and an electrode length of [1 10] cm.

- On the other hand, the selection of the μF-scale for the main capacitance is compared to the most efficient solution.

  This range aligns with the size and weight constraints of nanosatellites. However, it does not meet the condition of maximized efficient energy transfer for the typical L, R values in PPTs. That is, applying a constant RLC circuit approach, the critical damping condition, which represents the most efficient energy transfer, is given by $C = 4L/R^2$. This yields a capacitance on the order of hundreds of Farads for $L = 10$ nH and $R = 10$ mΩ, significantly larger than the study case, thus making low-power class PPTs to operate underdamped. Additionally, the subsequent lower peak currents reduce structural demands on PPTs, making this solution more suitable for miniaturization.

  Hence, considering a damping ratio defined as $\beta = R\sqrt{C/L_0}$, as in simple RLC circuits: when $\beta \gg 1$, the V,I curves are predisposed to an overdamped waveform; when $\beta \ll 1$, the solution tends to be oscillatory. However, also considering the dynamical equation in Eq. 2.2, it becomes evident that excessive $\dot{L}$ also contributes to distorted damped waveforms, analogous to the effect of C. This is reflected in the damping parameter $\alpha = C^2V_0^2\mathrm{d}L/\mathrm{d}z/L_0$, which plays a role in the normalized dynamical equation equivalent to β for the normalized circuit one.

Consistently, the solution presented in Figure 2.6(a) is underdamped for I, with a period under 2 μs ($T \approx 2\pi\sqrt{L_0C}$) and involving current reversal. The discharge extinguishes after about 6—10 μs. The current peaks at 15 kA at around 0.5 μs and drops to approximately 10 kA after one cycle. Resulting v peaks at about 10 km/s. The sheet travels a distance of half a centimeter before the first zero that reverses the current. The existence of a current reversal does not necessarily constrain the channel length to this dimension, as both the current and the self-induced magnetic field reverse in phase, hence, the Lorentz force continues pointing towards the channel exit, albeit in a pulsating manner. Nonetheless, the literature typically associates large enough maxima/minima of the voltage curve with secondary reignitions [23, 2], potentially resulting in the generation of a separate plasma bulk.

Figure 2.6(b) shows the parametric analysis carried out as a function of on C, L_0 and R. The negative effect on performance caused by an increase in L_0 and R is evident, whereas increasing C improves it. This translates to maintaining the same current rise time while increasing the I and v peaks by a factor of approximately 1.5.

The provided solution enables a rough estimate of the impulse bit, i.e., the time integrated thrust, as $I_{bit} \approx {}^1/_2{}^{\mathrm{d}L}/_{\mathrm{d}z} I^2_{peak}\Delta t_{peak}$, which only accounts for the electromagnetic component. The specific impulse

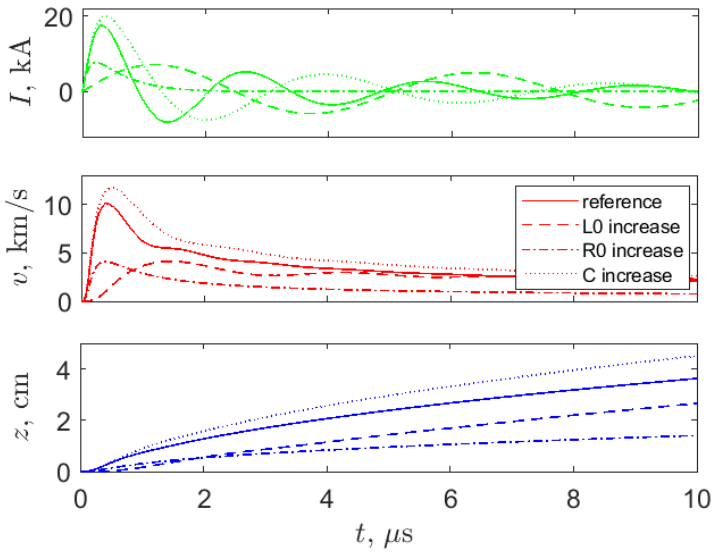

Figure 2.6: **Numerical solution of the Snowplow electromechanical model [23] for the ion current I, the ion velocity v and traveled distance z.** Reference operational point (a): 1 kV of discharge voltage and 6 μF of capacitance (assumed 1 μg of initial ionized mass, $R = 10$ mΩ, and $L_0 = 10$ nH). The parametric study (b) modifies L_0 to 100 nH, R to 100 mΩ (a reasonable maxima) and C to 10 μF in the respective three parametric study cases. Channel density considered to compute the ionized mass entrained by the sheet as it advances is set to 0.0165 kg/m^3 as a rough approximation for PTFE; reducing this by one order of magnitude results in a doubling of the velocity.

$I_{sp} = v_{exhaust}/g_0$[13] can also be approximated with v_{peak} from the simplified model. For the reference case, they are about 40 μNs and 1000 s respectively, aligning with the measured values for comparable PPTs [31]. Table 2.3 collects these performance metrics for the parametric cases studied in Figure 2.6(b), confirming previous conclusions.

Parameter	Unit	Reference point	Increment of initial inductance L_0	Increment of total resistance R	Increment of capacitance C
Peak current	kA	17.5	7	7.5	20
Impulse bit	Nμs	50	10	10	60
Specific impulse	s	1000	500	500	1200

Table 2.3: **Performance estimate based on the solution of the Snowplow electromechanical model [23].** Reference operational point: 1 kV of discharge voltage and 6 μF of capacitance (assumed 1 μg of initial ionized mass, $R = 10$ mΩ, and $L_0 = 10$ nH). The parametric study modifies L_0 to 100 nH, R to 100 mΩ, and C to 10 μF in respective cases.

2.5. Design point

The design point of the rectangular- and parallel-electrode PTFE PμLSA prototype is defined by the following aspects:

1. Channel size

[13] Although using the same symbol I for both current and impulse metrics is not ideal, it has been retained for consistency with related publications [7, 4, 2, 9, 106] and standard nomenclature for propulsion performance metrics. Readers unfamiliar with the field should exercise caution to avoid confusion.

2. Structural keys

3. PPU keys

4. Operational point

Before detailing it, the framework for channel size and operational point, derived from the discussions throughout the chapter, is summarized. On the one hand, based on the preliminary analysis presented in Section 2.4, the operational range of interest sets around 1000 V for V_0 and between 1-–10 μF for C. For channel sizing, the former V_0 is associated to h around 1 cm, and the range of interest for l spans 0.5–5 cm. About w, although the calculations use an expression for dL/z that minimizes if border effects are negligible, assuming $h/w \approx 0.1$, this ratio does not typically apply in real devices to avoid an excessively large electrode width w. Consequently, w is set at the centimeter scale, but the present design will not consider the former ratio either. On the other hand, the representative E_0 of low-power comparable PPTs (see Table A.1) typically lies between 1 J and 10 J, with the focus of this work primarily on values about 5 J.

Building on this, the design point is presented in Table 2.1. It geometrically features $h = 1$ cm, $l = 4.5$ cm, and $w = 1$ cm.

Structural keys also include 3mm-thickness copper electrodes with intentionally blunt edges, a grounded cathode, and the centered embedding of an in-house MIM spark plug within the cathode. The spark plug features a negatively polarized Mo electrode, 1 mm-diameter, with a sharp tip, and housed in a PTFE cylinder with a 2 mm outer diameter. Initially, the spark plug's outer diameter is tangent to the propellant surface. The assembly is mounted on a metallic chassis designed to provide clear spacing around the discharge channel, reducing discharge perturbation. Channel geometry modifications of interest involve h variation achieved by repositioning of the electrodes.

The PPU power segment consists of two analogous but separate capacitive circuits: one for the main discharge and another for the triggering system. Firing control is managed by externally opening or closing the spark plug's power circuit. Both circuits incorporate a voltage preconditioning stage, which elevates the input voltages from low-power power supplies to high voltage using COTS Flyback DC-DC converters. The capacitor banks are connected to the thruster discharge channel and the spark plug, respectively. To minimize initial inductance, the main capacitor bank is screwed to a 3 mm-thickness copper bus bar located at the back of the discharge channel; it consists of MKP-film capacitors with low ESR and ESL (see Table 2.2). Capacitor voltages for both circuits can be adjusted by varying the input voltage to their respective DC-DC converters, with nominal maximums of 3 kV in the case of the one for the main circuit and 6 kV for the spark plug. Adjusting the bank capacitance requires replacing the existing unit. [Power is brought to the prototype inside the chamber by means of coaxial cables connected to the MHV chamber feedthroughs.]

The main discharge operation conditions of $V_0 = 1$ kV, $C = 6$ μF and thus $E_0 = 3J$ and $E_0/A = 3$ J/cm^2. The main firing frequency is set to 0.1 Hz. [The initial resistance R_0 is verified to be less than 0.1 Ω and the initial inductance L_0 about 10 nH (computed from measurements taken with a Keysight E5063A Vector Network Analyzer).]

The spark plug nominally ignites at around $V_{sp,0} = 1.5$ kV for nominal V_0 and exhibits a nonimal capacitance of 560 pF. Operation reliability throughout its lifetime ($2.5–5 \cdot 10^4$ firings) has been verified.

From this point onward, the previously defined geometrical and operational configuration will be referred to as the nominal or reference point, as parametric studies are explored in this thesis. The study ranges for these will be defined in Section 2.6.

2.6. Study ranges for the parametric analysis

The parametric study in this PhD dissertation examines both geometric and operational discharge parameters for the main discharge, with a primary focus on the latter. The study ranges, defined in Table 2.1, are detailed below:

1. First, in Chapter 3 and in an introductory context, discharge reconstruction results using photography are presented for nominal channel geometry and also with shorter electrodes, to enable backflow observation.

2. Mass measurements have been carried out at V_0 = 1000 and 1500 V.

3. The general electrical characterization carried out in Chapter 3 studies the influence of V_0 between 500–2500 V and C up to 9 μF. Additionally, the different batteries used within this work, featuring different capacitor model and accommodation on the bus bar, are also characterized. Furthermore, the effect of the channel electric field on the breakdown initiation is studied within this velocity range and for h between 0.5 and 1.5 cm. Visual observations of the electrode surface after endurance tests are in agreement with this geometrical range.

4. Plume studies involve solely operational parameterization. Single Langmuir probe ToF data in Chapters 4 and 5 follow the ABC case matrix. It is defined as follows:

   - C set at (3, 6, 9) μF and
   - V_0 at (750, 1000, 1500) V.

   Then, E_0 ranges between 0.84 and 10.13 J.

   Each of these nine study cases are labeled. The naming system employs an alphanumeric code, where the letter (A–C) corresponds to increasing capacitance, and the number (1—3) corresponds to increasing voltage. The nominal configuration is defined as the central case, B2, which corresponds to C = 6 μF and V_0 = 1000 V, resulting in E_0 = 3 J.

5. Electrostatic wire plume probe data are presented in Chapter 4 for a ToF study and in Chapter 6 for plume cross-section reconstruction. On the one hand, in Chapter 4, V_0 parameterization is conducted between 500 and 2500 V. On the other hand, Chapter 6 focuses exclusively on the nominal point.

2.7. Summary

A rectangular ablative PPT prototype named PμLSA (PULSed Ablative plasma thruster for micro/μ-propulsion) has been designed to be a versatile and compact experimental platform, intended to study the low-power operation of this technology, i.e., at the micropropulsion operational range. This prototype represents the first PPT designed and tested in Spain.

The PμLSA breadboard model is the result of several previous iterations [6, 15]. It holds a rectangular, parallel-rail, breech-fed configuration, and has been operated with PTFE. The electrodes are made of copper and the cathode is grounded. The discharge channel nominally exhibits a 4.5 cm length, 1 cm height and 1 cm width discharge channel and operates at 1000 V, 6 μF and 3 J. Once the main capacitor bank is charged up, thruster ignition is triggered by an in-house MIM spark plug (Mo emitter/PTFE filler) embedded on the main cathode electrode, and nominally works at about 1.5 kV, negatively polarized. The firing frequency is set to 0.1 Hz to enable the acquired data to be saved between shots.

The power segment of the PPU consists of two analogous but independent capacitive circuits for the main and triggering systems. The main capacitor bank is mounted at the rear part of the thruster discharge channel, while the rest of the PPU is kept outside the chamber.

The system allows for the variation of the operational point by modifying the PPU input voltage and replacing the capacitor bank. Furthermore, it also enables the modification of the thruster head geometry (height, length, width, channel flaring angle and electrode shape) by repositioning or replacing the electrodes.

3. THRUSTER OPERATION [14]

3.1. Introduction

The present chapter collects the results of the first campaign carried out on the developed PPT prototype. The goals of this work involve ignition validation and the characterization of the operational envelope. To achieve this, the dependence of the spark plug and main discharges on a series of geometrical and operational parameters of interest, as defined in Section 2.6 of Chapter 2, is analyzed through electrical characterization. Furthermore, various additional tests provide data on average propellant consumption per firing and offer insights into the discharge sequence and channel surfaces after endurance tests, based on visual inspections captured by photography in the visible spectrum. The two visual analyses serve distinct purposes: the first familiarizes the reader with discharge behavior before a quantitative analysis, while the second provides insight into the long-term effects on channel components. The former results have been disseminated in [15, 7].

The remainder of the chapter is organized as follows. To begin, Section 3.2 introduces the testing facilities and the experimental setup, including the probes used for the measurements in this chapter. Afterwards, the study results are presented in Section 3.3 across multiple subsections. Section 3.3.1 provides context on shot-to-shot firing variability. Section 3.3.2 follows with a photographic reconstruction of the discharge sequence. The propellant consumption mass measurements are presented in Section 3.3.3. Section 3.3.4 presents the main discharge electrical characterization, first at the nominal point and later analyzing the effects of varying operational parameters. The electrical study of the triggering discharge is covered in Section 3.3.5, describing its behavior under different thruster operational conditions. Finally, qualitative statements from the visual inspection of channel surfaces after repetitive firing are outlined in Section 3.3.6. To close the chapter, a summary of the key findings is presented in Section 3.4.

3.2. Testing facility and experimental setup

3.2.1. Thruster prototype

The PPT breadboard model object of experimental study is described in Chapter 2. The thruster nominal geometrical and operational point is set respectively to $h = 1$, $w = 1$ and $l = 4.5$ cm, and $V_0 = 1000$ V and $C = 6\ \mu$F, resulting in $E_0 = 3$ J.

A geometrical and operational parameterization analysis is carried out as defined in Section 2.6 of Chapter 2.

Within this chapter, the different batteries listed in Table 2.2 in Chapter 2 are electrically characterized. Identifying the similarities and differences between cases allows for assessing how variations in battery response translate into plume differences, and thus helps define the applicability limits of the general conclusions drawn from the plume tests described in Chapters 4, 5, and 6, which involve different batteries.

3.2.2. Vacuum chamber

The ablative PPT discharge can develop if the background pressure remains under $1 \cdot 10^{-4}$ mbar. Hence, the thruster prototype is operated inside Hedron, a 50 cm-edge cubic vacuum chamber available at the

[14] Part of this chapter incorporates content from the 2022 International Electric Propulsion Conference (IEPC) paper "**Experimental plume characterization of a low-power Ablative Pulsed Plasma Thruster (APPT)**", [7], coauthored by S. Barquero, J. Navarro-Cavallé, and M. Merino.

EP2 laboratory. High voltage feedthroughs are used for the charging lines of the main and sparkplug capacitor banks, and BNC ones for the rest of diagnostic probes. The vacuum system of Hedron consists of a mechanical vacuum pump (Edwards nXDS Scroll pump, 10 m^3/h) and a turbomolecular pump (Edwards next400, 400 L/s(N_2)). The ultimate pressure reached is in the 10^{-6} mbar range. At each firing, the pressure experiences a perturbation below $2 \cdot 10^{-5}$ mbar, and is able to drop down to the ultimate pressure within a few seconds.

PPE4KV Teledyne LeCroy (400 MHz) 100:1 voltage passive probes are used to monitor the main and spark plug discharges respectively. [Yokogawa 701937 (500 MHz) 10:1 passive probes are used to any other voltage monitoring.]

Probe signals are simultaneously read by an eight-analog-channel Yokogawa DLM5000 oscilloscope. The oscilloscope sampling frequency is set at 100 MHz. [One order of magnitude higher sampling frequencies were employed to confirm that the previous value was sufficient to study fast phenomena, such as the spark plug discharge and primary and secondary breakdown initiation.] The main discharge signal triggers the data-saving process for all simultaneous diagnostics. [The oscilloscope trigger setting must account for the high-frequency, high-amplitude noise associated with the breakdown process affecting the main discharge signal.]

Mass measurements have been carried out with a SHIMADZU AUW220D analytical balance with resolution up to 10 μg. The propellant consumption per firing within the parametric range of interest exceeds the balance's capabilities; therefore, an average value is calculated from measurements taken over an accumulated number of firings. [This data have been acquired during the campaign described in Chapter 6, which was conducted using Battery 2B, as specified in Table 2.2 in Chapter 2.]

Photographs are taken using a PHOTRON FASTCAM MINI UX50 (not used in fast recording mode) and the camera of an Oppo Reno 10x with additional attenuation filters. Both cameras operate in the visible light spectrum. Further camera specifications and exposure settings are not provided, as they are not critical for the qualitative discussions in this chapter.

3.3. Results

3.3.1. Shot-to-shot variability

Shot-to-shot variability in PPTs refers to the differences in the discharge behavior observed between individual thruster firings. This variability can manifest with a different impact in image, electrical and plasma diagnostics' data. Potential factors contributing to shot-to-shot variability by affecting the plasma dynamics potentially include inconsistencies in propellant ablation and electrode erosion and contamination. Quantifying this variability is crucial for providing a reliable, predictable thruster performance.

As a result, the electrical and plasma diagnostics presented in this work are based on multiple firings (also referred to as repetitive firing) to ensure statistical significance. Data is typically presented as the mean and standard deviation, usually based on 50 firings.

[No impact on the reported measurements was observed due to thruster or probe degradation.]

3.3.2. Visual inspection of the discharge phenomena

A representative reconstructed discharge sequence through photography is presented in Figure 5.2 for two channel lengths including nominal (a) and shorter (b). The sequence provides qualitative insight into the discharge dynamics, helping to contextualize subsequent quantitative analyses. One can observe the discharge evolving from the spark plug plasma, located at the base of the thruster propellant on the cathode, towards the anode along the propellant surface. This process ignites the main channel, forming a plasma

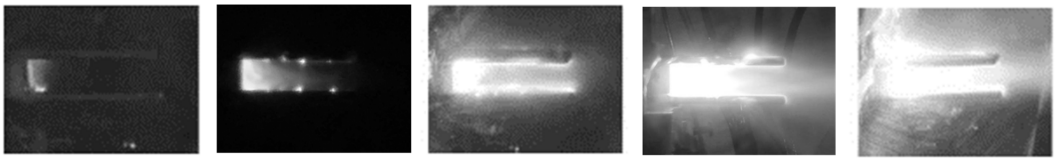

(a)

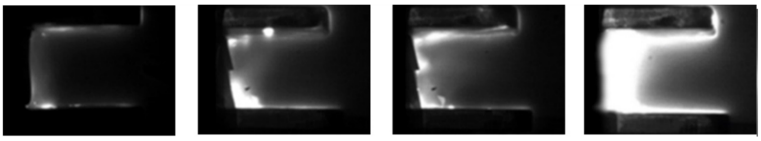

(b)

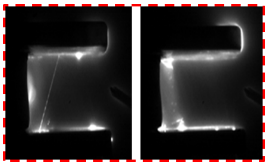

(c)

Figure 3.1: **Different stages along an ablative PPT discharge sequence by means of visible photography.** (a): 1 cm electrode height h, 4.5 cm electrode length l. (b,c): h= 1 cm, l = 1.5 cm.

that propagates downstream until ejection.

The cathode-to-anode plasma profile is non-uniform. Canting of the plasma sheet and some hot spots on the electrodes are visible. These findings are consistent with the literature [100, 135]. In addition, concentration at the electrode edges is observed. Accumulation of discharge byproducts after multiple firings on the electrode surface yield on deposition patterns that agree with this finding, as it will be shown in Section 3.3.6.

With the shorter electrodes configuration, light on the anode top surface at the channel exit is non-negligible, suggesting blackflow, while not for nominal l = 4.5 cm. This is illustrated in Figure 5.2(c), and it is further supported by the presence of charred material staining that electrode region, as presented below in Section 3.3.6. Figure 5.2(c) also shows some straight paths, which are commonly observed; while they could result from ejected particulate emission [136, 137], they may also be artifacts.

The preceding images support the hypothesis that channel ignition occurs via propellant surface flashover[15], further corroborated in the next section by confirming consistent propellant consumption. Even though

[15] A surface flashover [69, 138, 70, 71, 72] is a less demanding phenomena than a vacuum arc in terms of electrode bias. It begins with a localized charge accumulation, which triggers surface charge propagation along the insulator surface. This process is accompanied by desorption from the insulator surface and partial ionization of the desorbed gas, creating a conductive path. As this chain reaction intensifies, the density of the desorbed gas layer increases, further enhancing desorption and favoring gas-phase ionization. If this process is intense enough, a full electrical breakdown occurs translating into the discharge of the stored energy. Transitions from cathode-initiated to anode-initiated flashovers have been reported.

The prebreakdown phase is highly scenario-dependent. One of the principal mechanisms associated to it, by secondary electron emission avalanche, may originate externally along the propellant surface or within the subsurface. However, internal avalanches are typically associated with slower pre-breakdown charging processes and higher defect densities due to trapped charges than external ones.

Then, the vacuum-insulator interface plays a critical role in surface flashover. It constitutes a region of discontinuity due to pronounced differences in physical properties between the surface, where the presence of defects is also higher, and bulk of the insulating material. Surface atoms must readjust to minimize surface energy, forming a dynamic transition region where the dielectric and vacuum environment merge. Different "layers" can be distinguished within this interface (from the surface towards the bulk), with different strength of intermolecular forces inversely correlated with vacuum strength. Increased vapor pressure favors gas desorption.

channel breakdown can occur in the absence of a propellant bar by means of a vacuum arc [62], it requires a higher electric field than cases with propellant.

3.3.3. Propellant mass consumption per firing

To estimate the main-discharge ablated mass per firing m_{bit}, the PTFE consumption has been averaged along repetitive firing by measuring the propellant bar at the beginning and at the end of a firing set.

To this purpose, to improve statistical significance, various firing sets at nominal operation conditions have been carried out with 875, 1161 and 1992 shots each. This leads to respective averaged mass consumption figures of 3.66, 4.03 and 3.89 μg. After averaging over the total of firings, it is found that the ablated mass per firing falls within 3.9 ± 0.2 μg, for both the unweighted and weighted means across the different firing sets.

The same procedure has been carried out after increasing V_0 from nominal (1000 V) up to 1500 V. A series of firing sets consisting of 538, 1840, and 1598 shots, respectively, yield propellant consumptions per firing of approximately 6.2, 6.4 and 6.6 μg. Both unweighted and weighted means give a result 6.4 ± 0.2 μg. Hence, the prototype exhibits higher consumption compared to the nominal V_0, with the ratio between the consumptions being similar to that between the two voltages.

Both, the order of magnitude and trends with the operational parameter are consistent with data reported in the literature for comparable PPTs [29, 31].

Note that, as it was described in Chapter 2, the propellant bar was extended beyond the effective consumption area, defined by the parameters h and w, to enable observation of backflow effects. Throughout these firing sets, deposition on the extended surface areas was visually observable; however, its contribution was not quantitatively evaluated. As a result, the mass consumption values presented above carry some uncertainty. Specifically, they may lead to an overestimation of the ablated material available for acceleration down the channel, since a portion of it remains redeposited locally on the propellant surface.

3.3.4. Main discharge electrical characterization

The anode voltage response $V(t)$ at the nominal point ($V_0 = 1000$ V and $C = 6$ μF) is shown in Figure 3.2 for the different batteries used. It is averaged over multiple shots (see Section 3.3.1); the shaded area represents the standard deviation σ estimate. From $V(t)$, the discharge current signal $I(t) = -C\mathrm{d}V(t)/\mathrm{d}t$ has been computed.

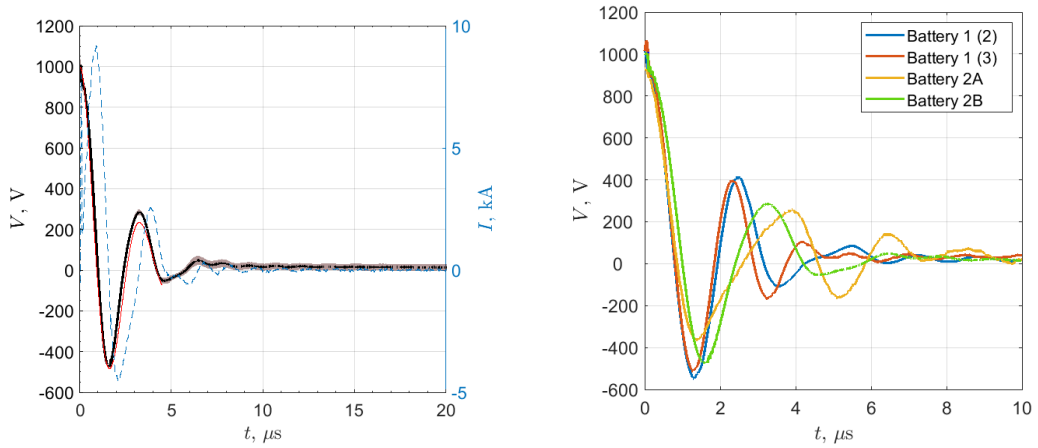

(a) (b)

Figure 3.2: **Time signal of the anode voltage $V(t)$ at nominal discharge conditions**. (a): V(t) averaged over 300 firings (thick,black), its standard deviation (shaded area), the constant-parameter RLC circuit fit (thin,red) and computed current signal $I(t)$ (discontinuous line) for Battery 2B (2), used for the work presented in Chapter 6 (see Table 2.2 in Chapter 2). The standard deviation σ is plotted as $\pm\sigma/2$ with respect to the mean. (b): Comparison between the $V(t)$ of the different batteries listed in such table. The electrical characterizations of Battery 2A and 2B remain consistent across all its respective campaigns, then the campaign identification number between brackets has been omitted for these batteries.

The signals exhibit underdamped behaviour with natural frequency ω on the order of magnitude of 100 kHz, and with the signal amplitude decaying by a factor of 10 after about 5 μs. Good repeatability among pulses is observed, especially along the first cycle of the discharge. The estimated resistance (R) and inductance (L) values from fitting an RLC circuit with constant parameters to the first cycles of the discharge are around 40 mΩ and 40 nH respectively.

Computed $I(t)$ peaks at about 10 kA at approximately 1 μs after the breakdown, as it is 90° shifted with respect to $V(t)$. This value aligns with the prediction from the Snowplow electromechanical model presented in Section 2.4 in Chapter 2. The magnetic field can be estimated using Ampère's law, $B = \mu_0 J/2w$, reaching a peak of about 0.6 T. These results are consistent with reported values for comparable PPTs [100, 65].

While all the batteries show analogous behaviour, batteries 2 exhibit slightly lower frequency than 1.

High-frequency oscillations superimposed to $V(t)$ are seen at the first instants of the discharge on the order of magnitude of 10 MHz, and typically at the signal minima. The former relates to the spark plug operation and the subsequent process leading to channel breakdown. The later could be related to channel reignitions that may occur upon voltage inversion [23, 100, 139, 135, 48]. This is better illustrated in Figure 3.3 through $V(t)$ for individual firings.

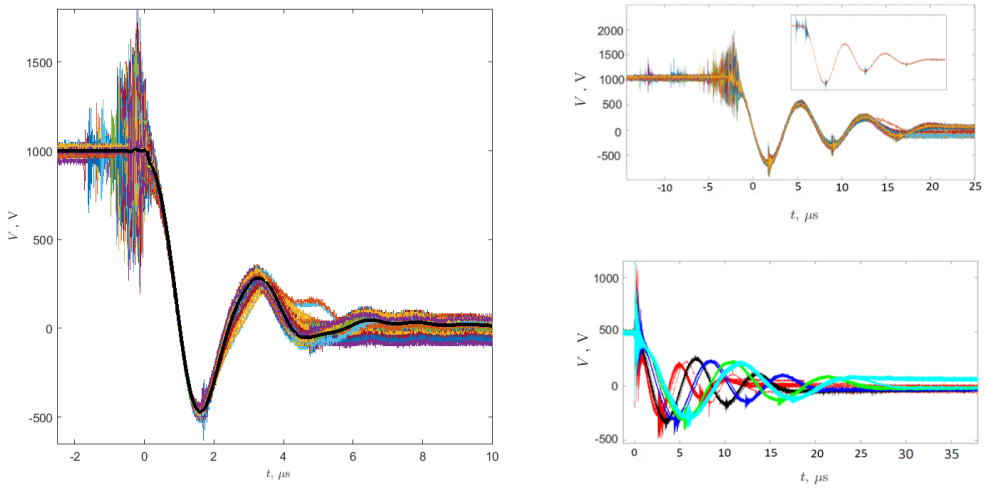

(a) (b)

Figure 3.3: **Time signal of the anode voltage $V(t)$ to allow for the observation of superimposed high-frequency oscillations.** (a): Battery 2B (2) at nominal configuration (1cm-channel height h, 1000 V of discharge voltage V_0 and 6 μF of main capacitance) across individual firings (color) and their mean (black); (b): Battery 1 (1) at two different configurations across individual firings: (top) h=1 cm, V_0=1000 V, C=5 μF, (bottom) h=0.5 cm, V_0=500 V and different C=1–5 μF impacting $V(t)$ essentially on increasing the discharge frequency and discharge time.

Even though the accuracy of the HV voltage probes is lower at low voltages, the later oscillations in $V(t)$ could still be a consequence of the plasma discharge circuit instead of an artifact due to measuring circuit coupling. Figure 3.3(b, top) supports this hypothesis showing how these oscillations are also subject to the noise potentially associated to channel reignitions; in addition, these late oscillations are also negligible under certain discharge configurations.

The variation of $V(t)$ with V_0 and C is illustrated in Figure 3.4(a) for the mean measurements of the central "cross-hair" cases of the ABC study matrix (see Section 2.6 in Chapter 2). As it can be noted, the response is qualitatively the same as in the nominal case. V_0 variation impacts the signal amplitude; increasing capacitance C is expected to decrease the oscillation frequency ω and to enlarge the discharge time. The oscillation natural frequency can be formulated as $\omega = \sqrt{1/LC - R^2/4L^2}$ using the constant-parameter RLC circuit approach. Increasing capacitance C is expected to decrease the oscillation frequency ω, which can be formulated as $\omega = \sqrt{1/LC - R^2/4L^2}$ using the constant-parameter RLC circuit approach.

The estimated R and L values from fitting an RLC circuit with constant parameters to the first cycles of the discharge of the $V(t)$ signal of Battery 1 (3) are between 20–40 mΩ and 20–40 nH respectively. Increasing V_0 causes the amplitude of the oscillations to grow, while R and L slightly decrease and ω marginally increases. Larger values of C mean that R slightly decreases, while L and ω slightly increase, and result in a voltage response that deviates more from an ideal RLC circuit.

In practice, varying C necessitates adding/replacing capacitors to the main bank, which inherently modifies L_0 and R_0 (see Section 2.3.3 in Chapter 2). Consequently, the resulting voltage curves exhibit slight amplitude variations alongside frequency effects. While impact of using batteries under nominal discharge conditions has already been illustrated in Figure 6.3, below, Figure 3.4(b) presents the effect of operational parameterization on a different battery. The findings remain consistent with the previous conclusions for the other battery (Figure 3.4(a)).

However, the repeatability of later cycles in $V(t)$ decreases as V_0 deviates from its nominal value. E.g., for Battery 2A (1), a significant number of firings did not fully discharge it at E_0 under nominal.

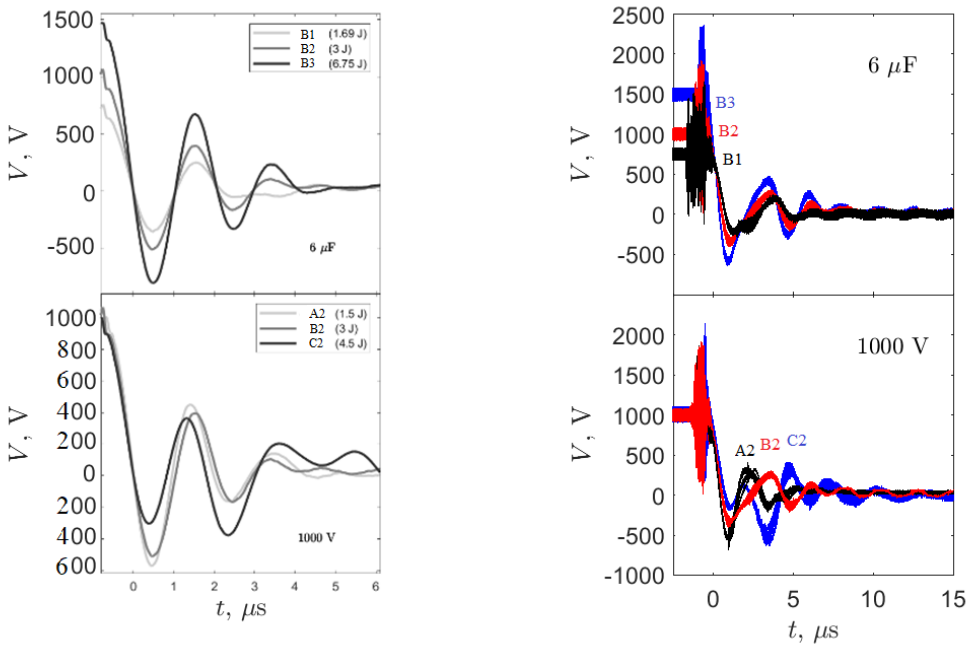

(a) (b)

Figure 3.4: **Influence on the discharge initial voltage V_0 (top) and capacitance C (bottom) on the main anode voltage curve $V(t)$ for the central "cross-hair" cases of the ABC study matrix (see Section 2.6 in Chapter 2).** Presented data belong to the original (a) and repeated (b) Langmuir probe Time-of-Flight experiment discussed in Chapter 4, differing only in the battery used.
(a): Battery 1 (3) and showing the measurement means; (b): battery 2A (1) and showing the individual firings. [For (b), in cases A2 and B1, abnormal voltage curves showing incomplete battery discharge have been excluded.]

Finally, electromagnetic interference from the main discharge has been observed. It provokes low-amplitude perturbation at the main discharge frequency on the spark plug coaxial charging signal in up to a few hundreds volts. It also slightly perturbs the in-plume current measurements, which are also brought out of the chamber via coaxial cables, as it will be shown in Chapter 4–6). In addition, the main channel discharge still perturbs an oscilloscope voltage probe located at approximately 20 cm from the channel along its exit plane, and at the atmospheric side of a chamber view-port, with voltages under 10 V. However, as this interference does not negatively affect the respective purposes of the affected probes, no additional shielding requirements are considered necessary.

3.3.5. Spark plug discharge electrical characterization

Before selecting the MIM configuration presented in Section 2.3 of Chapter 2, different spark plugs, based on MVM and MIM configurations were tested. Explored configurations included variations in electrode separation (which is on the order of millimeters), tip shape, emitter materials (copper, molybdenum, tungsten, steel), filler materials (Kapton, PTFE), polarity, and designs with or without the main cathode serving as the spark plug's second electrode. A MIM spark plug was preferred over MVM designs due to its lower ignition voltage requirements. Among other MIM designs, the selected configuration facilitates manufacturing.

The discharge voltage response over time of the in-house spark plug $V_{sp}(t)$ is represented in Figure 3.5(a). It is also underdamped, with an oscillation frequency of approximately 10 MHz. The discharge extinguishes after 0.2 μs. Its breakdown initiation voltage V_{sp0} sets at approximately 1–2 kV at nominal discharge conditions, exhibiting non-negligible statistical dispersion within this range. This is attributed to electrode erosion and uncertainties in the discharge location for each shot. A change in V_{sp0} varies the signal amplitude of the voltage discharge response over time of the spark plug capacitor $V_{sp}(t)$, as in Figure 3.5(b). Apart from this variation the $V_{sp}(t)$ response demonstrates good repeatability in the initial oscillation periods.

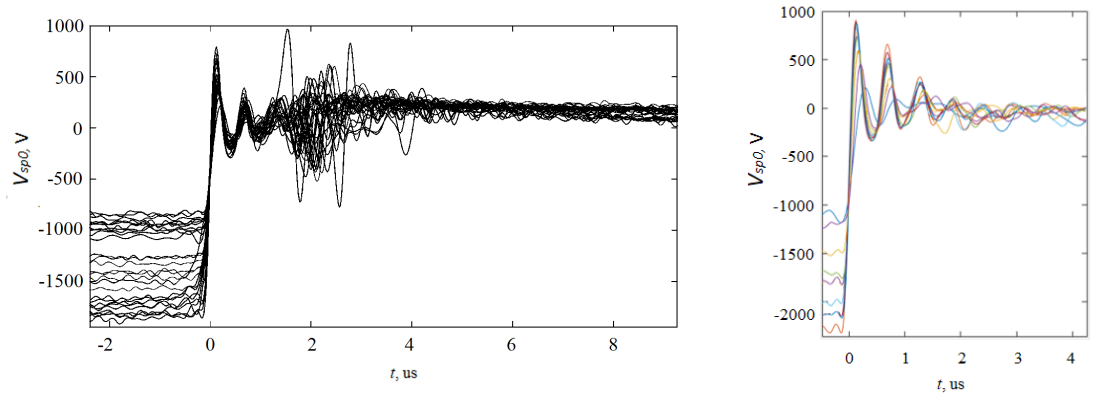

(a) (b)

Figure 3.5: **Time signal of the spark plug cathode voltage $V_{sp}(t)$ amont multiple firings when operated under nominal thruster firing conditions (a) and as a function of the initial discharge voltage $V_{sp0}(t)$(b).**

With the spark plug ignition, a flashover along the main propellant surface is intended to be triggered. Thruster ignition reliability is defined as the probability that the spark plug will successfully ignite the propellant and cause the main channel breakdown, allowing the thruster to fire. The small delay between the operation of the spark plug and the main channel breakdown, which occurs when the channel actually breaks down after spark plug operation, is referred to as the pre-breakdown lag time, τ_{bd}.

The influence of the electric field on τ_{bd}, referred to how the applied electric field affects the delay between the initiation of voltage application and the actual electrical breakdown of the gap, has been represented in Figure 3.6. A higher electric field generally reduces this lag time by accelerating ionization processes, while lower fields result in longer delays due to slower charge carrier buildup as well as higher associated shot-to-shot dispersion. At nominal h, τ_{bd} varies between [0.4 2.2] μs for a V_0 range between [2500 500] V. The variation in τ_{bd} for values of h lower than the nominal can be considered negligible within the V_0 range of interest.

Modifying the V_0 or, equivalently, varying h consistently, not only affects τ_{bd} but also thruster ignition reliability. The aforementioned trend may cause τ_{bd} to progressively increase until it ultimately no longer results in channel breakdown. At $h = 1$ cm, it substantially decreases for V_0 under 750 V. At these low V_0 it is sometimes required multiple spark plug discharges. The dependence of V_{sp} on channel parameters can be mitigated by using inductive ignition circuits, such as those presented in Section 2.3.3.1 in Chapter 2, provided they are properly sized to ensure a sufficiently high $\mathrm{d}V_{sp}/\mathrm{d}t$. However, as discussed in Section 2.3 also in Chapter 2, the implemented PPU control scheme provides multiple spark plug discharges per operation to ensure successful thruster ignition. Once main ignition occurs, any remaining spark plug pulses do not interfere with the discharge due to the differing time scales. [The spark plug firing frequency is on the order of 100 Hz, determined by the power rate of the DC-DC converter (≤ 3 W) and the capacitance of its battery.]

The channel electric field additionally influences spark plug discharge characteristics, including V_{sp0} and its shot-to-shot statistical dispersion. Just as the spark plug's location, geometry, and operating conditions determine its effectiveness in triggering the main channel under specific thruster conditions, certain aspects of its discharge behavior are also shaped by the channel conditions. Overall, the effect of increasing/decreasing V_0, or equivalently decreasing/increasing h, generally leads to a drop/rise in V_{sp0} and its dispersion among firings. For V_0 ranging below 500 V to 2.5 kV and h between 0.5 and 1.5 cm, V_{sp0} varies from approximately 3 kV to just under 1 kV. V_{sp0} remains within 1–2 kV for nominal h and V_0, while for higher electric fields it reduces up to 1–1.5 kV, as well as tend to increase as the electric field decreases. Nonetheless, the identification of trends in V_{sp0} with the discharge parameters is complex due to the high sensitivity of the spark plug discharge to the degradation of its elements, leading to shot-to-shot variability enhanced by lifetime degradation.

Additional remarks about V_{sp0} apply. On the one hand, initial spark plug ignition sometimes requires higher voltages, between 5–10 kV, to thermally condition the emitter. On the other hand, spark plug lifetime potentially increases V_{sp0} and reduces the intensity of the plasma it generates, due to erosion and deposition of byproducts. These byproducts typically consist of charred material, which is carbon-rich and thus conductive. This situation can ultimately lead in several ways to plasma discharge preclusion, which constitutes the end of life of the spark plug. These include situations where the required V_{sp0} exceeds PPU capabilities, the generated plasma is too tenuous, or the charred deposits are excessive, causing a short circuit in the spark plug. The spark plug short-circuit scenario can sometimes be reversed by significantly increasing V_{sp0} compared to the nominal. In the event that the spark plug reaches the end of its life, readjustment is required, such as cleaning, replacing the emitter, or renewing the dielectric filler. Nonetheless, up to $2.5\text{–}5 \cdot 10^4$ spark plug firings, readjustments are typically not required.

The former changes in the operation of the spark plug are not observed to negligibly affect the main discharge once triggered. In fact, the spark plug plasma has been proved to be negligible in comparison to the main discharge one, both visually, as illustrated in Figure 5.2, which reconstructs the discharge sequence through photography, and through plume-downstream ion-saturation-current measurements analogous to

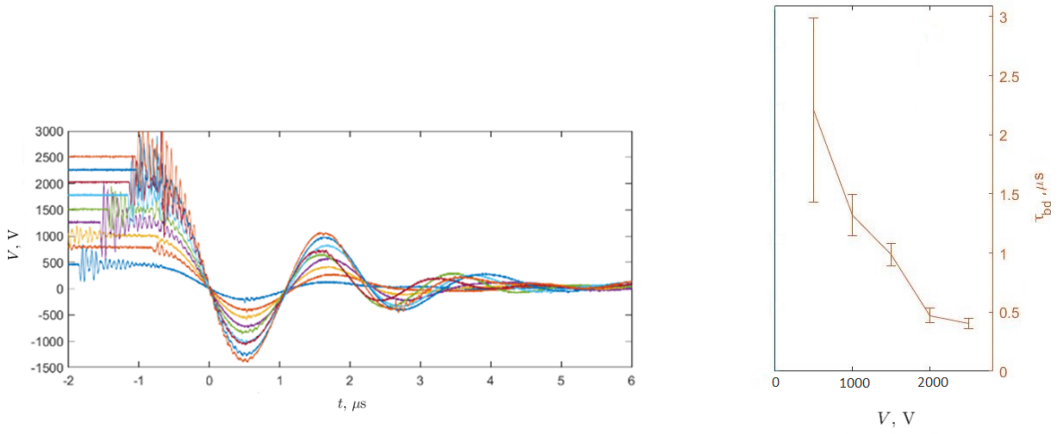

(a) (b)

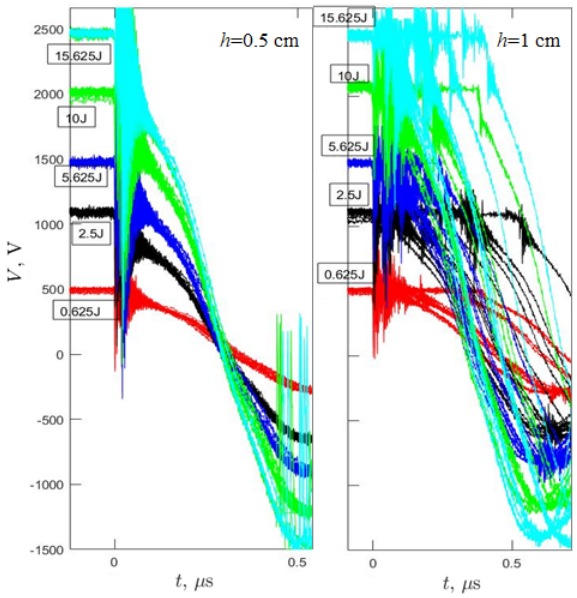

(c)

Figure 3.6: **Influence of discharge parameters on pre-breakdown lag time τ_{bd}.** (a): Anode voltage waveform $V(t)$ for varying initial discharge voltages V_0 using Battery 1 (2) at nominal conditions, capacitance $C = 6$ μF, channel height $h = 1$ cm across individual firings. [10 Hz low-pass filtered discharge noise superimposed on the $V(t)$ means.] (b): τ_{bd} as a function of V_0 computed from the (a)-dataset. (c): Close view to the breakdown initial instants of $V(t)$ among repetitive firing as a function of V_0 and at various h for Battery 1 (1) at $C = 5$ μF.

the plasma measurements described in Chapter 4. [In the second case, for the spark plug plasma to be expelled from the discharge channel, the channel electrodes must be biased; this is a typical scenario when main ignition fails.] Nonetheless, the spark plug location and operating conditions may influence the early stages of the main discharge. However, this study is beyond the scope of the present work.

Notably, spark plug ignition generates high-amplitude noise at its natural frequency, affecting not only the main capacitor bank but also nearby electronic equipment through electromagnetic interference, including plasma probes. This electromagnetic noise was still perceptible at distances of up to 5 meters from the thruster setup, with no information available for distances beyond that. Hence, shielding with special care for sensitive control elements must be considered, particularly for those used to control the spark plug operation itself.

Finally, as a side note, spurious discharges have occasionally occurred inside the DC-DC converters during operation, regardless of whether they were inside or outside the vacuum chamber. Different units of the same model exhibited the same behavior. This typically occurred in the unit for the spark plug, as a result of spark plug operation. However, this has not been seen to compromise individual tests or the DC-DC converter's performance throughout the entire experimental campaign. [These circumstances motivated the development of the alternative circuit V3b, presented in Section 2.3.3.1 of Chapter 2, which features an in-house DC-DC converter as a potential solution.]

3.3.6. Visual inspection of channel surfaces after endurance tests

Observations on channel and propellant surface degradation after repetitive firing under different conditions are briefly discussed. These qualitative findings contribute to a better understanding of the long-term effects of operation on the thruster components.

Discharge byproducts can partially deposit on the channel surfaces, including both the electrodes and the PTFE surface. For $h = 1$ cm, at $V_0 \geq 1$ kV and nominal C, no deposition has been observed on the propellant area verified over approximately 10^4 firings. A clean propellant surface suggests ablation occurring across its entirety, although consumption is more pronounced in the central region and closer to the spark plug. However, material deposition has been detected on areas surrounding the discharge channel, with traces extending as far as the mounting platform. This deposition on the platform included charred material and white stains ranging from 0.1 mm to a few millimeters, which may result from the impact of expelled macroparticles from the propellant. These were observed on the thruster platform extending several centimeters from the channel location, as well as on the plume plasma probes' holder when placed within 20 cm of the PTFE surface.

At lower V_0 (or, equivalently, at larger h) and/or C, the propellant erosion area decreases, with byproducts and charred material depositing more rapidly on the remaining part of the surface. The latter, being carbon-rich and thus conductive, raises concerns about thruster malfunction when excessive [140], as it both increases the discharge energy required for ablation and may eventually cause a channel short circuit. Figure 3.7 illustrates the former assessments.

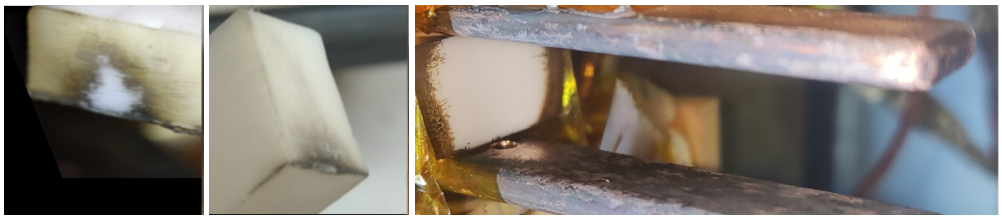

(a) (b) (c)

(d)

Figure 3.7: **Deposition and erosion on the discharge channel surfaces after repetitive firing.** (a): Electrode geometry: height h=0.5 cm, width w=1 cm, length l = 1.5 cm. Propellant surface: height=h, width=1.5 cm centered with respect to the thruster axis. Operational parameters: V_0= 1000 V, C= 5 μF, with the with Battery 1 (1). Picture after 200 thruster firings. (b): Same than (a) but with h = 1.5 cm and different propellant surface dimensions. Propellant height=h, width=0.5 cm centered with respect to the thruster axis. (c): Nominal configuration (h=1 cm, l = 4.5 cm, V_0= 1000 V, C= 6 μF) with Battery 1 (4) after several thousand firings. (d): h=1 cm, l = 4.5 cm, V_0= 750 V, C= 3 μF) with battery 2 after several thousand firings.

By contrast, electrode contamination is notable across all tested firing configurations, accumulating along the electrodes after repetitive firings, except in the area surrounding the spark plug (see Figure 3.7(d)). This region is visibly eroded, resulting in a clean copper ring. The observed electrode contamination consists of discharge byproducts and charred material, and no white stains have been observed on the electrodes. Deposition patterns have been identified in relation to the electric field, as shown in Figure 3.8. Overall, the cathode exhibits more uniform contamination along the entire electrode, while it tends to accumulate from the center to the edges as h increases.

Finally, at significantly lower l than nominal, backflow at the anode is suggested by the presence of charred material on the reverse surface of the anode near the thruster exit plane. This is consistent with the bottom discharge sequence reconstructed in Figure 5.2.

3.3.6.1 Channel maintenance practices

Electrode cleaning by surface polishing is typically performed every few thousand firings. Between these, the electrode state has not been observed to significantly influence the acquired data, neither electrical nor plasma measurements.

No mechanisms to automatically reposition the propellant surface have been implemented. Prior to each experimental campaign, the propellant surface is renewed and the propellant bar is reallocated. No relocation or manipulation of the propellant occurs during the mass measurement firing sequences.

(a) (b)

Figure 3.8: **Deposition and erosion on the discharge channel surfaces after repetitive firing.** Example featuring h=0.5 cm (a) and 1.5 cm (b), l = 1.5 cm, V_0= 1000 V, C= 5 μF with Battery 1 (1) after 200 firings.

3.4. Summary

The analysis in this chapter covers ignition validation and electrical characterization within the parameter space of interest for the PPT prototype described in Chapter 2. With this foundation, the characterization of the prototype plume can proceed, with results presented in the following chapters using various innovative plasma diagnostic techniques.

This experimental campaign characterizes the prototype operation as the final result of the design process. The present summary outlines the main findings of the experiments conducted, with a focus on electrical characterization. Additional tests included discharge photography, propellant mass measurements before and after endurance tests, and visual inspection of channel surfaces after endurance tests. Key findings are summarized below.

Qualitative introductory statements provide a general overview of the discharge behavior through visual inspection of photographs reconstructing a discharge sequence in the visible spectrum. It begins with the spark plug activation, followed by channel breakdown along the propellant surface, plasma bulk generation, and acceleration down the channel towards its ejection. The findings reveal a non-uniform cross-channel plasma profile along the channel gap, with observations of canting (plasma tilts in the direction perpendicular to the electrodes), concentration at the electrode edges, and hot spots [132].

The voltage response at the main and spark plug capacitor banks have been analyzed and statistical significance has been provided by calculating the mean and information about the data dispersion after repetitive firing. At nominal operational conditions (V_0 = 1000 V, C = 6 μF), the thruster firing voltage shows damped oscillations with a natural frequency of hundreds of kilohertzs and good repeatability, especially in the first oscillation periods. Estimated main discharge current peaks at about 10 kA, while the signal extinguishes at about 5 μs after the breakdown.

The operational parameterization analysis carried out for the thruster firing reveals several findings. First, the electric field intensity is a key factor in ensuring reliable ignition. A delay occurs between the spark plug and main channel breakdowns, which increases as the electric field decreases. Consequently,at a nominal discharge channel height, of 1 cm, main channel breakdown reliability has been observed to notably decrease below initial channel bias of 750 V.

Second, increasing the initial discharge voltage results in a corresponding increase in waveform amplitude. Overall, increasing capacitance, by modifying the capacitor bank, lowers the natural frequency and has been shown to cause the measured data to deviate from the ideal constant-RLC circuit response.

About the triggering discharge, its voltage responses is also underdamped with a natural frequency about 10 MHz. It also shows good repeatability within the first oscillation periods. However, the spark plug exhibits sensitivity to its own discharge location uncertainty, due to its coaxial configuration and the degradation experience by the surfaces involved with firing, leading to shot-to-shot dispersion in its triggering voltage. A minor dependence on the channel electric field has also been observed, with lower voltages

and reduced shot-to-shot dispersion as the field increases. The proven spark plug lifetime meets the system requirements, outlined in Section 2.2 in Chapter 2.

Visual inspection of surface deposition after endurance studies shows discharge byproducts, including charred,conductive material, accumulating on the electrode surfaces. These deposits are more pronounced towards the electrode edges as the channel height increases. Additionally, appreciable electrode erosion is observed only in the vicinity of the spark plug on the main electrodes at nominal operational conditions or larger.

By contrast, accumulation of discharge byproducts on the propellant surface has been found to be negligible at the nominal operational point. Reducing the energy-to-area ratio, either by increasing the channel size, decreasing the initial discharge, or reducing the bank capacitance, causes a smaller propellant consumption area and deposition of charred materials around it.

Finally, mass measurements reveal that, under nominal discharge conditions, the average propellant consumption per firing is around 4 μg. Propellant consumption has been observed to increase with the discharge voltage in agreement with reported data [31].

4. PPT EXHAUST CHARACTERIZATION BY MEANS OF TRADITIONAL TIME-OF-FLIGHT[16]

4.1. Introduction

The exhaust of the PPT prototype described in Chapter 2 is experimentally analyzed using traditional Time-of-Flight (ToF), which relies on feature probe correlation. This method is applied to three axially distributed Langmuir probes operating in the ion saturation regime. The results evaluate the average ion speed and plume expansion rate under various operational firing conditions. The present analysis is affected by several limitations inherent in the traditional ToF methodology (discussed later), which motivate Chapter 5. There, these limitations are addressed and overcome, leading to improved estimates of ion speed and divergence compared to those presented in this chapter.

In the literature, the traditional ToF methodology is typically applied to measurements from various probe systems [96, 94] to assess ion speed, by computing the time interval between the occurrence of the same feature in the time signal at two locations (e.g., amplitude/intensity peaks in time). However, its capability to additionally provide a preliminary estimate of the plume expansion rate is first explored in this work. A preliminary version of part of the present content was presented in [7].

To assess the extrapolation limits of the conclusions drawn from the conducted ToF experiments, the tests are repeated using different capacitors (Battery 2A (1) in Table 2.2 in Chapter 2) and, separately, wire electrostatic probes instead of local measurements. The latter also validates these probes and the second battery for the setup requirements in Chapter 6, while Chapter 5 employs the original battery (Battery 1 (3) of the referred table).

The remainder of the chapter is structured as follows. Section 4.2 details the experimental setup and methodology. Afterwards, the study results are presented in Section 4.3 across multiple subsections. Section 4.3.1 discusses the plasma probe measurements under nominal firing conditions and discusses the influence of operational discharge parameters. At the end of the section, plasma measurements under sole spark plug operation are also included. Section 4.3.2 presents the Time-of-Flight (ToF) velocity characterization, while Section 4.3.3 examines the plume expansion rate, both including trends with operational parameters following the presentation of nominal results. Section 4.3.5 summarizes additional studies conducted using different capacitors and wire electrostatic probes. Section 4.3.4 addresses the inherent limitations of the traditional ToF methodology. Finally, Section 4.4 summarizes the key findings and outlines the next steps.

4.2. Experimental setup and methodology

The PPT breadboard model object of experimental study is described in Chapter 2. The thruster nominal geometrical and operational point is set respectively to $h = 1$, $w = 1$ and $l = 4.5$ cm, and $V_0 = 1000$ V and $C = 6\ \mu$F, resulting in $E_0 = 3$ J. The thruster channel and Cartesian coordinate system used are respectively shown in Figure 2.1(b) of Chapter 2 and 4.2.

The thruster uses Battery 1 (data corresponding to battery 1 (3), see Table 2.2 in Chapter 2). It is electrically characterized in Chapter 3, along with all other batteries used throughout this dissertation. To assess the extrapolation limits of the conclusions drawn from the conducted ToF experiments, the tests are repeated under identical setup conditions, except for the use of a different capacitor bank, specifically, Battery 2A (1) from Table 2.2 in Chapter 2, which incorporates a different capacitor model of the same

[16] Part of this chapter incorporates content from the 2022 International Electric Propulsion Conference (IEPC) paper "**Experimental plume characterization of a low-power Ablative Pulsed Plasma Thruster (APPT)**", [7], coauthored by S. Barquero, J. Navarro-Cavallé, and M. Merino.

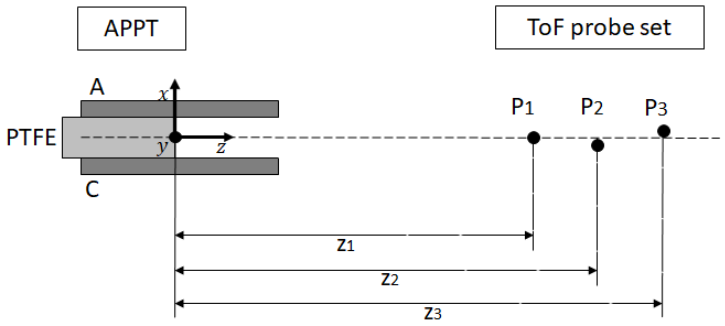

Figure 4.1: **Time-of-Flight probe (P) setup with respect to the PPT Coordinate reference system**. 'C' means cathode, and 'A', anode.

class as that in Battery 1.

An operational parameterization analysis is carried out as defined in the ABC case-matrix in Section 2.6 of Chapter 2.

The testing facilities, background pressure, voltage probes for discharge electrical monitoring and the generalities of the data acquisition system and process are described in Section 3.2 in Chapter 3.

Three electrostatic probes, single Langmuir proges, (LP_k with $k = 1, 2, 3$) have been developed for the present work, with tungsten tips of 0.5 mm diameter and 3 mm length. In this work, the longitudinal axis of each plasma probe is always oriented orthogonally to the incoming plasma flow, and slightly displaced laterally along x so as to avoid direct shadowing among them. These'probes are distributed along the thruster channel axis (centerline) in the downstream direction, placed at axial distances $z_1 = 26.2$ cm, $z_2 = 30.7$ cm and $z_3 = 35.0$ cm from the PTFE surface. Respecting the Cartesian coordinate system defined for the thruster, the ToF setup is illustrated in 4.2. The choice regarding z_1, z_2, z_3 is guided by the constrains imposed by both the vacuum chamber geometry, which limits the farthest distance to the thruster, and the risk of interfering with the discharge, which limits the nearest distance. It has also been considered that as plasma density increases, the likelihood of occasional spurious discharges at the electrostatic probes rises (see Appendix B). In such a case the data of that firing is discarded. In the present experiment, they affected the nominal case in less than 10% of the total firings, increasing to about 25% when V_0 was raised to 1500 V and C to 9 μF.

These LPs are biased negatively enough to operate in the ion saturation regime. The bias voltage V_b was set to -50 V, after verifying that at nominal operation conditions the measured ion current at the z locations of interest exhibited variations below shot-to-shot uncertainty upon changes in the probe bias in the range $[-50\ -100]$ V. A MCP350W-200V power supply is used to bias the three probes simultaneously. It is verified for all plume experiments that at the frequency of interest the power supply's current peak and slew rate rating are sufficient to accurately measure different signals simultaneously. Additionally, no differences are observed between signals measured separately or simultaneously, ruling out any circuit coupling effects.

The probe signals are routed out of the chamber through coaxial cables and BNC feedthroughs. Following the standard Langmuir Probe measuring circuit [141], current-to-probe for each probe is measured through the corresponding shunt resistor, which is biased with respect to ground at the selected V_b. The resistor used is a metalized carbon-film of 10 Ω of resistance. Measuring at both sides of the resistor is necessary to accurately register the perturbation on the bias during the plasma measurement, mostly due to the limited slew rate of the power supply.

Consistently, one power supply simultaneously negatively biases all the probes, with each probe drawing its respective current through its circuit branch. Both the effective provided bias signal $V_{b,eff}(t)$, which is perturbed with respect to the nominal bias V_b during the plasma interception by the probe, and the probe voltage $V_p(t)$, which is caused by plume current drainage, have to be monitored during the tests. Thus, the

ion current is calculated from the voltage difference between the probe voltage, and the bias signal, divided by the shunt resistance R_{shunt}.

The three probes are monitored simultaneously, and together with the bias signal and the electrical discharge curves of the main anode and the spark, which requires six analog channels of the eight-channel oscilloscope. Standard high-impedance voltage passive probes are used to bring the signals to the oscilloscope, in particular, Yokogawa 701937 (500 MHz) 10:1 passive probes. As in Chapter 3, the first zero of the anode voltage signal is used as data-saving trigger off all the diagnostic data. An effective breakdown instant $t = 0$ is defined relative to the former point and is consistently shifted across all shots in a dataset.

Over the experiment, no drift or secular changes have been noted in the measurements, concluding that the thruster/diagnostic[17] do not experience significant degradation. Nevertheless, minor surface changes on the probe electrodes and channel electrodes have been noted, likely due to contamination associated to the accumulation of discharge subproducts.

Recalling the statement in Section 3.3.1 of Chapter 2, 50 firings are considered to assess the repeatability, uncertainty/dispersion of the measurements.

4.2.1. Additional experimental test cases

Additionally, to further validate results and explore the convenience of a different probe configuration, the experiment is repeated using electrostatic wire probes instead of the single Langmuir probes above. This probe configuration is motivated by the needs of the experimental setup of Chapter 6, where these type of probes working in the ion saturation regime will be used to accurately study the cross-expansion of the PPT exhaust[18]. Hence, to validate those measurements as a foundation for Chapter 6 and further corroborate earlier results, the traditional ToF methodology has been applied to them enabling comparisons.These probes are biased under the same conditions described previously. They measure line integrals of the current density distribution j along the y-direction and are tungsten, elongated cylindrical rods with a diameter of 0.5 mm and a length of 190 mm, positioned at z locations of 28.7, 33.2 and 37.7 cm respectively.

[All probes referenced in this dissertation were built specifically for the purposes of this work.]

4.2.2. Time-of-Flight methodology

The time between a pair of correlated ion-saturation-current peaks between two probes can be used to estimate the average ion speed for the associated ion group. This provides a first estimate of the exhaust velocity, under the strong assumption that the exhaust features are frozen and therefore the two probes register the same features in the line series, only with a time delay.

The calculation of an average ion speed by this technique is straightforward. Being the spacing between two probes $k = 1, 2$, Δz_{12}, and the measured time delay between the corresponding correlated features (in this case, the current peaks), Δt_{12}, then the estimated ion velocity is $v_{12} \simeq \Delta z_{12}/\Delta t_{12}$.

In addition, an estimate of the exhaust plume expansion rate can be also provided, inferred from the decrease in peak current value across axially distributed ToF probes. That is, assuming a quasi-one dimensional expansion for the ion current density $j(x, y, z, t) \approx j(z, t)$, the plume current traversing the xy plane defined as the product of $j(z, t)$ and the plume cross-sectional area $A_{\text{plume}}(z, t)$ along correlated features is constant, $j_{\text{k,peak}} A_{\text{plume, k,peak}} = \text{Const.}$ for k=1,2,3 probes. Thus, simplifying notation the expansion rate can be expressed as $\mathrm{d}\ \ln A_{\text{plume}}/\mathrm{d}z = -\mathrm{d}\ \ln j/\mathrm{d}z$. This area rate can be estimated with finite differences using two or three probes.

[17] Probe cleaning was performed via electron bombardment by subjecting the probes to a thruster firing while applying a sufficient positive bias, with no observable impact on the measurements.

[18] Chapter 6 uses Battery 2B, analogous to battery 2A (Table 2.2)

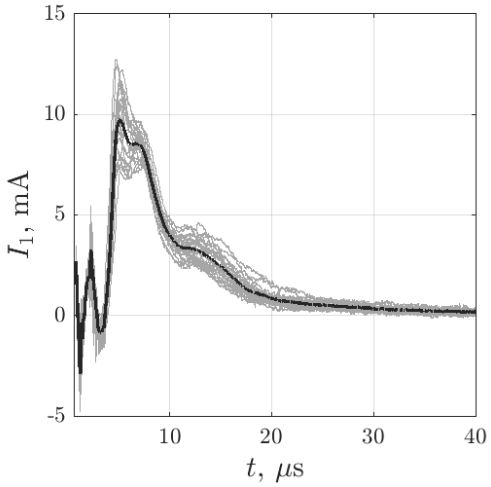

Figure 4.2: **Ion saturation current measured at Langmuir probe** 1**,** $I_1(t)$**, for the reference case B**2. Thin lines are individual firings, whilst the thick one represents the average over them.

4.3. Results

4.3.1. Ion saturation current measurements by Langmuir probes

Figure 5.6 displays the time-response of the measured ion saturation current at LP_1 at the nominal point (case B2), for individual shots and their average over them I_1. The probe begins collecting ion current at around 3.5 μs after the breakdown and the signal vanishes 30–40 μs afterward. The time interval between 0—3.5 μs primarily shows noise associated to the first instants after ignition (See Appendix B). For this reason, hereafter, the study focuses solely on the [3.5 30] μs time-window, the effective ion collection window. Despite the good repeatability of the voltage signal discussed in Section 3.3.4 of Chapter 3, probe current variability can be up to about ±25% with respect to the mean at some instants of time. In this experiment, datasets with unclear peaks or outlying probe values were discarded from the analysis.

The average time-response over the shots I_1, reveals three bumps, at $t_1 = 5.1$, $t_2 = 6.8$, and $t_3 = 12.4$ μs from the discharge breakdown. They are hypothesized to correspond to distinct ion groups (IGs), either because they are generated at different times or because they have a different charge/mass ratio and, then, are accelerated differently. The presence of multiple ion populations in PPT plumes has been extensively confirmed. Various diagnostic techniques, including Langmuir probes [98, 102, 7, 2, 109], residual gas analyzers [110, 98], and optical emission spectroscopy [97, 95, 99, 100, 61, 111, 107], have identified multiple ionization waves and different species at various ionization states.

Out of the three IGs, the first (IG1) and the second one (IG2) drive most of the current, are more focused and reach the probe at earlier times. They together mostly contribute to the peak value of the curve. The third ion group (IG3) reaches the probe later, and has a smaller but broader contribution.

The current measured by the three axially distributed LPs for the B2 case is found on the central subplot of Figure 4.4, which showcases the probe measurements as a function of V_0 and C. Measurements are represented by the mean across different firings and the standard deviation σ. Shots exhibiting evident abnormal current responses have not being included nor considered for the present analysis; they accounted for less than 40% of the total firings at each operational condition, primarily affecting datasets below approximately 3 J (see Figure 4.3).

As expected, the farther is the probe from the thruster, the later it starts collecting current. As well, the different peaks, hypothesized to be associated to different IGs, can be correlated along the different probes. The intensity of each one of these three bumps decreases with distance as plume expands, revealed by a

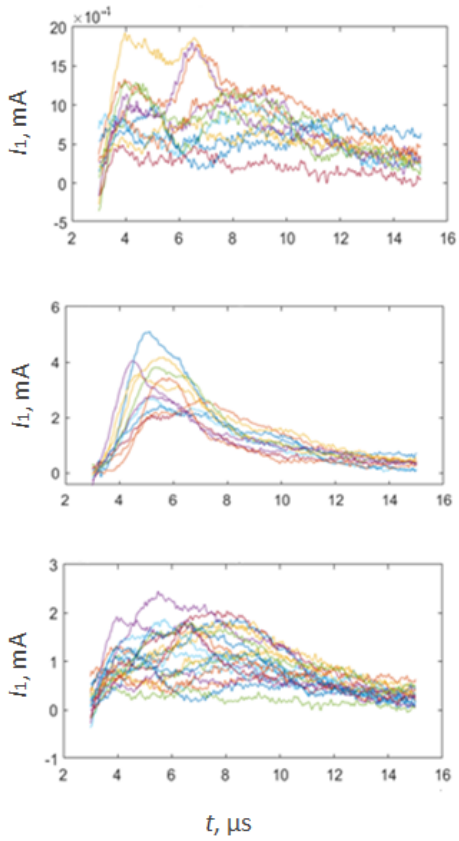

Figure 4.3: **Firing examples for the different types of operation identified in dataset A1** (750 V, 3 μF, see section 2.6 in Chapter 2). Except for the first one (top left), the remaining cases have been considered abnormal operation and thus discarded for the analysis. [The time axis is shifted by -0.8 μs relative to the other figures in this chapter.]

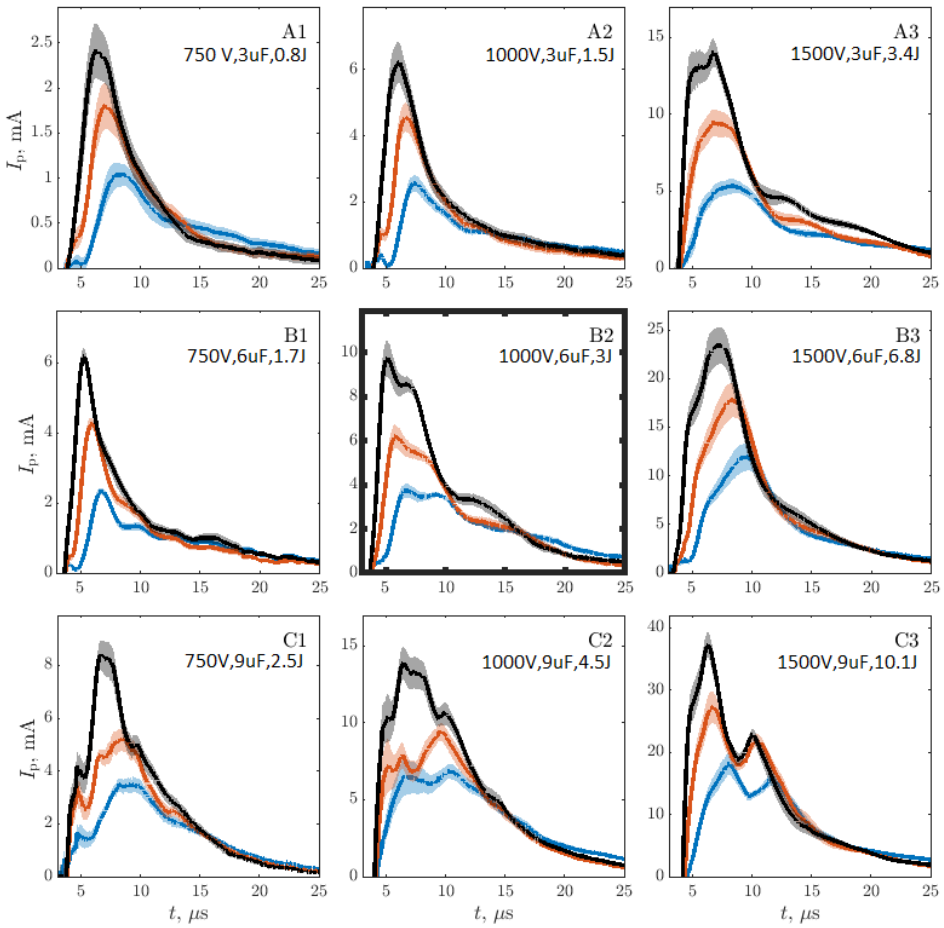

Figure 4.4: **Average ion saturation current $I_k(t)$ (solid lines) and standard deviation (shaded area) over multiple measurements for the three k Langmuir probes (LPs).** The standard deviation σ is plotted as $\pm\sigma/2$ with respect to the mean. LP_1 in black, LP_2 in red, and LP_3 in blue. Case labels are described in section 2.6 in Chapter 2. B2 is the central, nominal case. Mind the different y-axis scale in each panel.

decrease in peak current from one probe to the next between correlated bumps.

Regarding the influence of V_0 and C, Figures 4.5 and 4.6 aid in visualizing trends by focusing on LP_1 measurements of constant-V_0 and constant-C cases (from Figure 4.4), and the evolution of current peaks with these operational parameters, respectively. Overall, the discharge retains similar characteristics and trends to the reference case B2 throughout the whole study matrix. However, while in the nominal case the peak current decreases from one IG to the next, indicating a diminishing contribution of each subsequent IG to the signal, this trend shifts with E_0; the relative importance of the second and third peaks with respect to the first increases with C and especially with V_0 (see Figure 4.6(b),(c)). Note that as C increases, the shape of the current curves becomes more complex, but at least three main peaks remain easily identifiable in all cases, except for A1 and A2. In these exceptions, one and two bumps are observed, respectively.

In addition, the probe peak current linearly scales with E_0, as shown in Figure 4.6(c), suggesting a similar trend for the plume current. This is further confirmed by the time-integrated current along the ion collection window, also increasing linearly with E_0, as depicted in Figure 5.9 in Chapter 5 (not repeated

here). This trend is primarily driven by the increase in the first two current peaks, as previously discussed.

4.3.2. Time-of-Flight ion velocity

As outlined in the methodology, the time between a pair of correlated peaks between two probes can be used to estimate the average ion speed. Then, for the mean measurements at nominal operation average speeds for the three IGs of 50, 35, and 20 km/s, are respectively computed across the whole study matrix, as it is shown in Figure 4.7. The variation with V_0, C and E_0 does not reveal any clear trend.

The C2 and, and especially C3, cases are exceptions to the previous statement, exhibiting significantly larger velocities. However, note that the difficulty in identifying peaks in some cases, due to their association with wide/flat bumps or proximity to one another, may contribute to the generation of outliers when comparing current magnitudes of a given ion group across the study cases. Furthermore, the ambiguity in identifying correlation pairs along probes in some operational cases may additionally lead to ToF velocity outliers.

The absence of a clear increase in the computed ion velocity with rising E_0 suggests that the additional energy from higher V_0 and C may be spent in increased plasma production or dissipated as heat and other losses. This was confirmed in the previous section through the analysis of current magnitude behavior with operational parameters (see Figure 4.6) , indicating that at least part of the extra energy contributes to plasma generation in the different peaks and in the increase of the total plume current. This pattern further suggests that the impulse bit, i.e. the momentum in the exhaust, is linear on E_0, in agreement with existing direct measurements [96, 142, 143].

4.3.3. Time-of-Flight plume expansion rate

We have seen that a first estimate of the PPT plume expansion rate can be obtained from the decrease in peak current from one probe to the other. A quasi-one dimensional expansion assumption leads to $\mathrm{d}\ln A_{plume}/\ \mathrm{d}z = -\ \mathrm{d}\ln j_{peak}/\ \mathrm{d}z$. This ratio has been evaluated for the three IGs across the operational case matrix, as shown in Figure 4.8. The calculation yields an expansion rate of approximately $\mathrm{d}\ln A_{plume}/\ \mathrm{d}z = 10\ \mathrm{m}^{-1}$ for all IGs and cases, preventing the identification of clear trends. However, note that IG1 exhibits greater dispersion due to larger variations between probe pairs. Assuming aconstant value of $\mathrm{d}\ln A_{plume}/\ \mathrm{d}z = 10\ \mathrm{m}^{-1}$ for the expansion of the plume cross-sectional area, the area between the ToF probes is estimated to increase by above 50% from one probe to the next. Assuming $A_{0,plume}$ is the channel exit area of 1 cm^2, the area between LP1 and LP3 is estimated to range from 20 to 30 cm^2, corresponding to diameters of approximately 5 cm to 6.5 cm if the plume is assumed conically expanding. Although these assumptions likely lead to an underestimation of the plume expansion, and neglect the fact that plasma in the periphery likely behaves differently from that in the core of the beam (e.g., due to the presence of slow charge-exchange ions), they provide a simplified framework for analysis that is nonetheless supported by initial experimental observations. Ion saturation currents measured using single Langmuir probes off-axis, within the plane parallel to the electrodes and approximately at 25 cm from the thruster axis at the same axial positions as the ToF probes, were essentially null.

4.3.4. Limitations of the traditional Time-of-Flight technique

While the presented velocity values align with ion speeds reported by other authors [96, 98, 94], the traditional ToF methodology proves insufficient for establishing consistent ion speed dependencies on the studied parameters. A significant limitation in identifying clear ion velocity trends for v and the plume expansion rate based on peak-current trends may stem from the inherent constraints of this methodology in accurately define this magnitude under certain operational conditions. Consistently, the shot-to-shot dispersion in the results may arise from several factors.

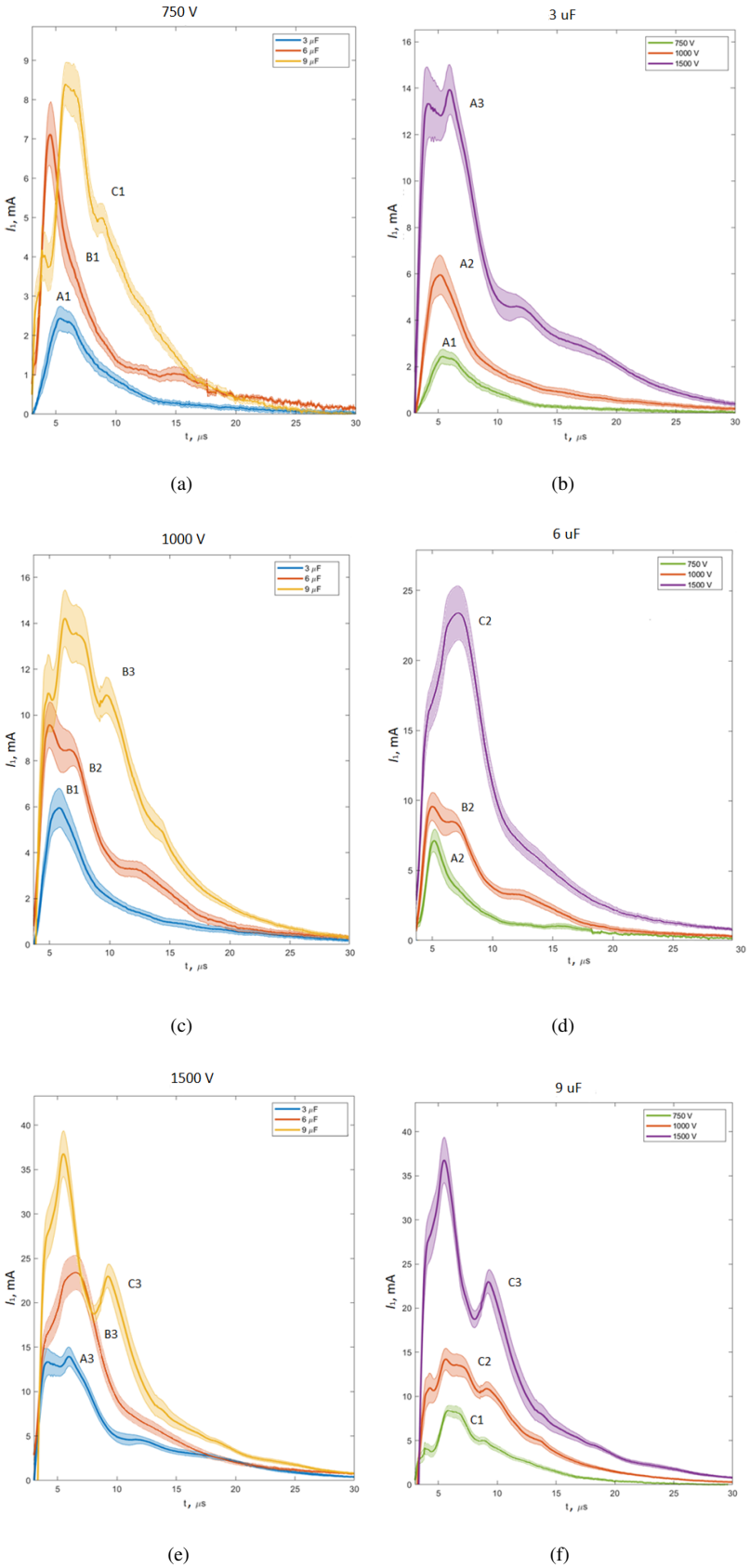

Figure 4.5: **Capacitance C (left) and discharge voltage V_0 (right) influence on the average ion saturation current $I_k(t)$ (solid lines) and standard deviation (shaded area) over multiple measurements for the Langmuir probe k=1**. The standard deviation σ is plotted as $\pm\sigma/2$ with respect to the mean. The ABC case-matrix described in section 2.6 in Chapter 2 and represented in Figure 4.4. Mind the different y-axis scale in each panel.

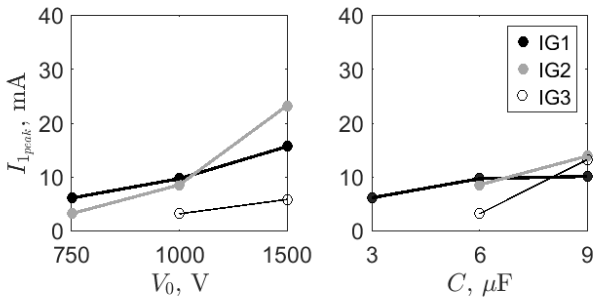

(a)

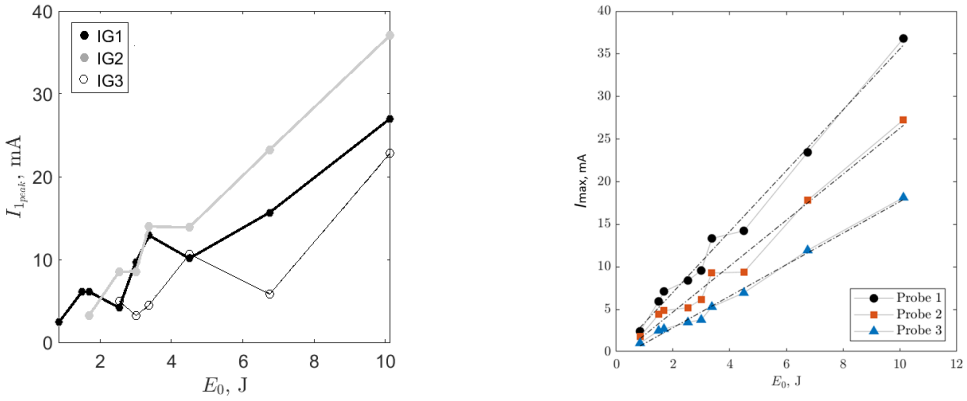

(b) (c)

Figure 4.6: **Peak probe current dependence with the operational discharge parameters.** (a): Dependence of the peak probe current at each ion group (IG) of Time-of-Flight Langmuir probe (LP) 1, $I_{1_{peak}}$, with the discharge voltage V_0 (left) and the bank capacitance C (right) for the central "cross-hair" of the case-matrix represented in Figure 4.4. (b): Trend of $I_{1_{peak}}$ for each IG with E_0. (c): Trend of the maximum peak for each the three probes, I_{max}, with E_0. [Unclear bumps are not included.]

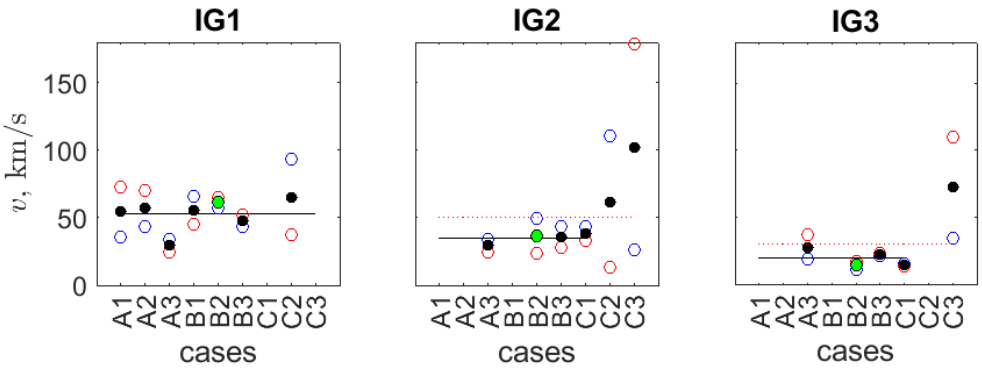

(a)

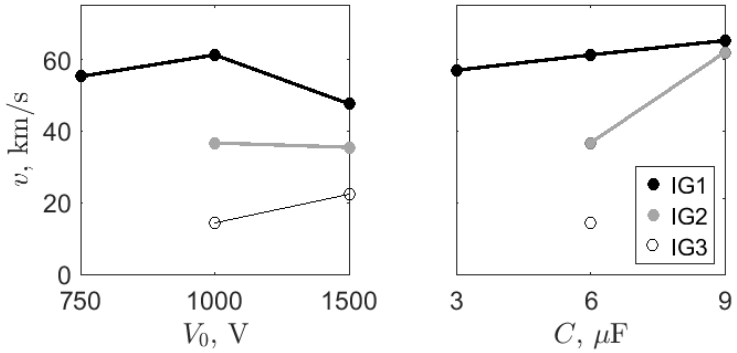

(b)

Figure 4.7: **[Dependence of the Time-of-Flight velocity v results with the operational discharge parameters.** (a): Ion speed for each ion group (IG) across the study matrix in Figure 4.4. In blue, results from probe 1-2 correlation, in red, from 2-3, and in black and filled, the average. Green filled dots represent the nominal case. The continuous black line represents the mean of the dataset, and the dot-red one the mean without outliers. (b): Dependence of the ion speed with the discharge voltage V_0 (left) and the bank capacitance C (right) for the central "cross-hair" of the study case-matrix. [Unclear bumps are not included.]

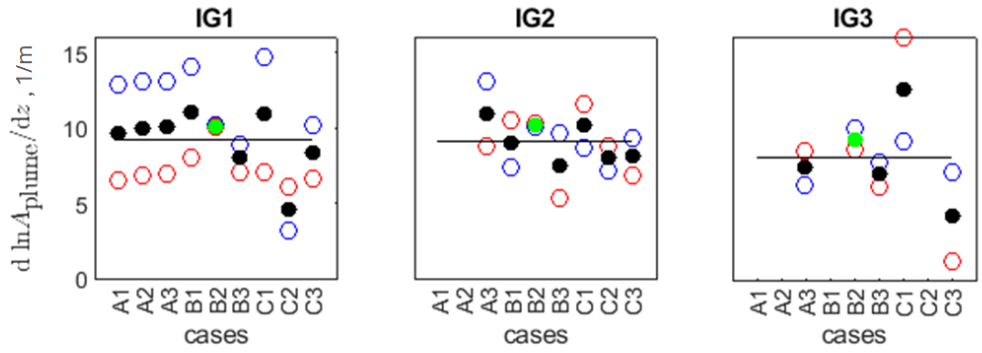

Figure 4.8: **Time-of-Flight expansion rate results for each ion group (IG) across the operational case matrix.** It is given by $\mathrm{d}\ln A_{plume}/\mathrm{d}z = -\mathrm{d}\ln j_{peak}/\mathrm{d}z$, where A_{plume} is the plume cross sectional area and z the thruster axis. In blue, results from probe 1-2 correlation, in red, from 2-3, and in black and filled, the average. Green filled dots represent the nominal case. The continuous black line represents the mean of the dataset. [Unclear bumps are not included.]

First, this approach overlooks the possible mixed contribution of ion populations with different characteristics within a given curve bump. Based simply in correlating peaks (or other features) among probe signals neglecting the fact that the exhaust likely consists of more than one evolving ion group (each one of them potentially originating at a different time, and with different charge/mass ratios, velocities, densities, thermal spreads and divergence rates) yield a lack of accuracy. The overlapping contributions of individual ion groups may result in none of the observed peaks coinciding with the actual maximum of any of them. Thus, that basic approach can only provide an "average" velocity of the exhaust.

Second, even ignoring those contributions, there is a growing difficulty to precisely identify the peak-feature reference time the wider and flatter a bump is.

In addition, when computing the plume expansion rate, the combined effect on the density decrease between probes, due to the thermal spread of the various ion groups along with the divergence, is also ignored with this methodology. Hence, a calculation of the divergence based on the peak value of the ion current density at each probe overestimates the plume divergence rate in case the thermal spread is non-negligible.

The limitations inherent to the traditional ToF methodology, as described, motivate the development presented in Chapter 5, where these issues are addressed and resolved, yielding improved and more insightful outcomes over those presented in this chapter.

4.3.5. Further validation of conclusions: Repeating experiments with variations in setup

According to the explanations provided in Section 4.2, the experiments were repeated twice, each with variations in the thruster setup and the probe setup, respectively.

On the one hand, a non-negligible variation in the ion current measurements was observed when using a different battery, Battery 2A (1) (see Table 2.2 Chapter 2), which features a different capacitor model and a slightly modified bus bar arrangement to accommodate the new components. Consequently, the electrical and traditional ToF characterization of Battery 2A (1) was conducted and compared to previous results to validate the outlined conclusions. The new battery discharge was electrically characterized in Section 3.3.4 in Chapter 3, while the associated ToF analysis is presented below in Section 4.3.5.1.

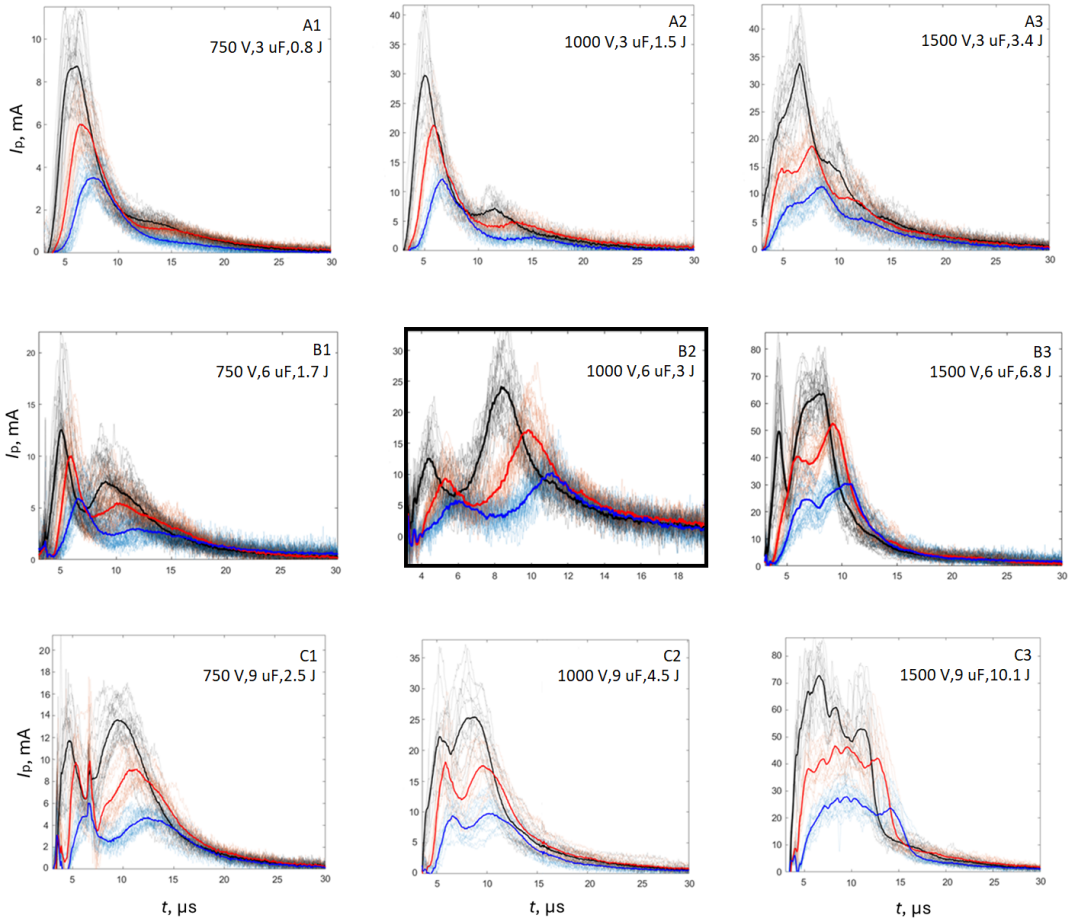

Figure 4.9: **Average ion saturation current $I_k(t)$ (thick lines) and individual-firing measurements (transparent lines) for the three k Langmuir probes (LPs) using a different thruster battery (Battery 2A in Table 2.2 in Chapter 2)**. LP_1 in black, LP_2 in red, and LP_3 in blue. Case labels are described in section 2.6 in Chapter 2. B2 is the central, nominal case. Mind the different y-axis scale in each panel.

On the other hand, in Chapter 6, electrostatic wire probes working in the ion saturation regime will be used to accurately study the cross-expansion of the PPT exhaust. [Chapter 6 uses Battery 2B, similar to battery 2A, whose results were described within this section.] To validate those measurements as a foundation for Chapter 6 and further corroborate earlier results, the traditional ToF methodology has been applied to them enabling comparison with the current findings. Note that the z locations of the new probes in this section (see Section 4.2.1) are similar to those of the original LP setup, facilitating a more direct comparison. These results are described in Section 4.3.5.2.

4.3.5.1 With a different thruster battery

Figure 4.9 presents the ion saturation current measurements for the whole operational case matrix for Battery 2A (1), including the measurments from the three ToF LPs. While the overall signal characteristics remain similar to those of Battery 1 (3), an increase in current magnitude is observed, particularly for the second IG, which makes the visual detection of a third ion population more challenging in some cases.

Figures 4.10 and 4.11(a),(b) show the behavior of the measurements with respect to the operational parameters V_0 and C, displaying the full time-series data and the current peaks, respectively. Additionally,

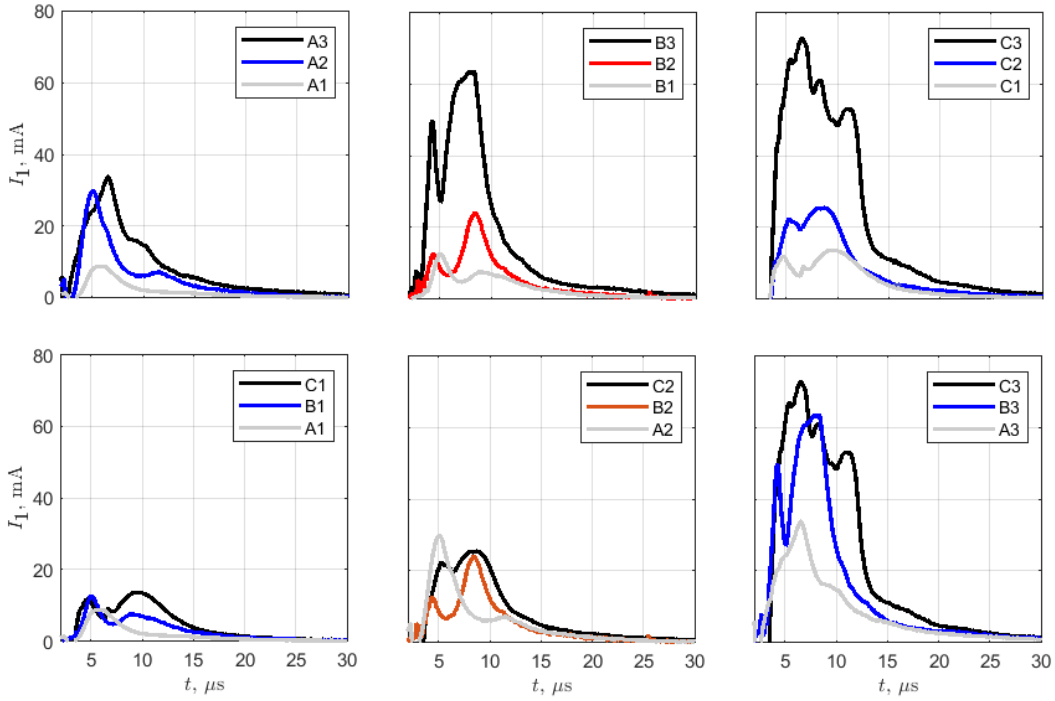

Figure 4.10: **Discharge voltage V_0 (top) and capacitance C (bottom) influence on the average ion saturation current $I_k(t)$ (solid lines) and standard deviation (shaded area) over multiple measurements for the Langmuir probe 1 using a different thruster battery (Battery 2A in Table 2.2 in Chapter 2)**. Case labels are described in Figure 4.9 and section 2.6 Chapter 2. B2 is the central, nominal case. In red, the nominal case, B2.

Figure 4.11(c) includes the time-integrated current within the ion collection window as a function of E_0. The previous conclusions are confirmed: any increase in energy typically results in a rise in peak current, particularly for the second ion population, and the integrated current scales linearly with E_0.

ToF ion velocities, presented in Figure 4.12, show consistent results with previous findings. On average, velocities are approximately 50, 35, and 20 km/s for each IG across all study cases, with C2 and C3 again as exceptions. No clear trends with C or V_0 are observed.

4.3.5.2 With electrostatic wire probes

Figure 4.13 presents wire probe data exemplified by an individual firing at $V_0 = 750$ V with nominal C. In agreement with the LP data, ion collection in the wire-probe measurements begins around 3.5 μs, with the 0–3.5 μs interval consisting mainly of noise and thus excluded from the analysis. Two or more current peaks can be easily distinguished in the three probes within the operational range of interest, separated to each other by about 5 μs. The observed peaks are hypothesized to correspond to different ion populations.

In spite of the good repeatability of the voltage signal as discussed in Section 3.3.4 in Chapter 3, the ion saturation current measured at the wire plasma probes shows a moderate variability.

The first peak is generally larger and has a higher associated velocity than the second one. The relative importance of the second bump increases at larger V_0.

As overview resolution of the first peak improves at lower V_0, while that of the second peak improves at

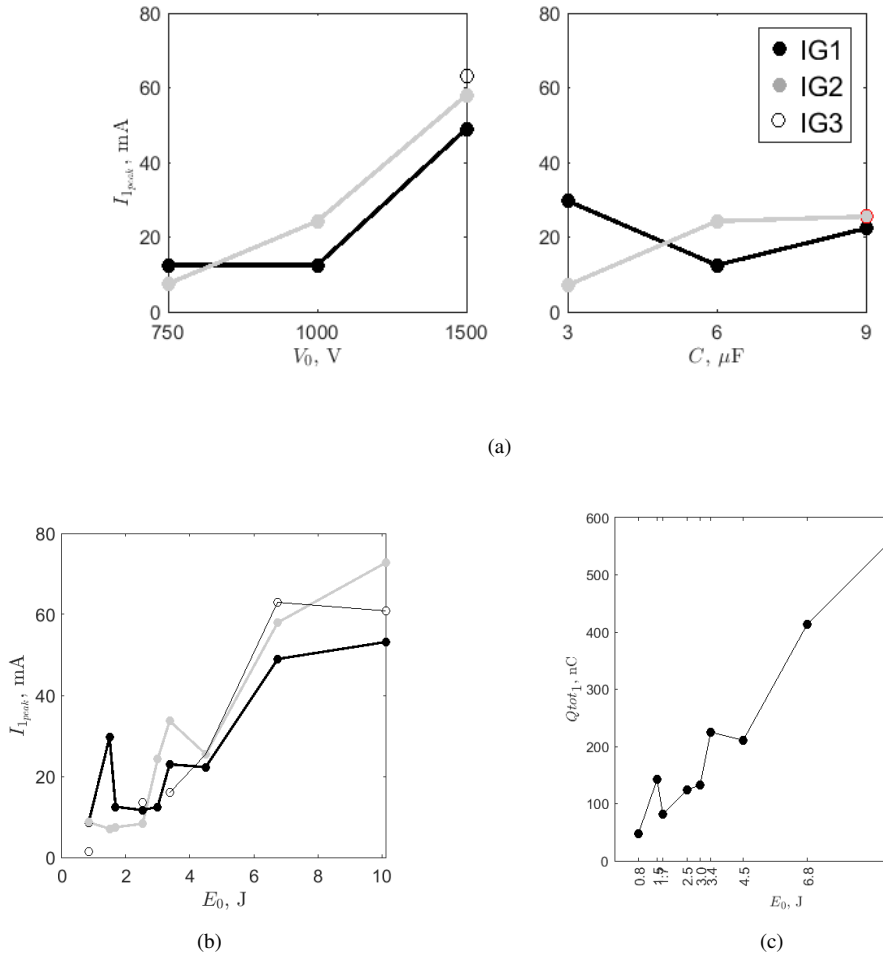

Figure 4.11: **Peak probe current dependence with the operational discharge parameters using a different thruster battery (Battery 2A in Table 2.2 in Chapter 2).** (a): Dependence of the peak probe current at each ion group (IG) of Time-of-Flight Langmuir probe (LP) k=1, $I_{1_{peak}}$, with the discharge voltage V_0 (left) and the bank capacitance C (right) for the central "cross-hair" of the case-matrix represented in Figure 4.4. (b): Trend of $I_{1_{peak}}$ for each IG with E_0. (c): Time-integrated current for LP_1, Q_{tot_1} within the ion collection window [3.3 30] μs. [Unclear bumps are not included.]

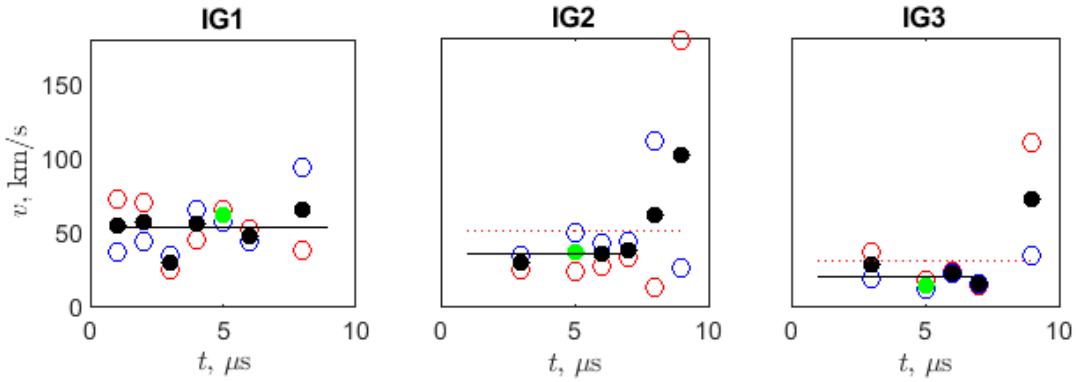

(a)

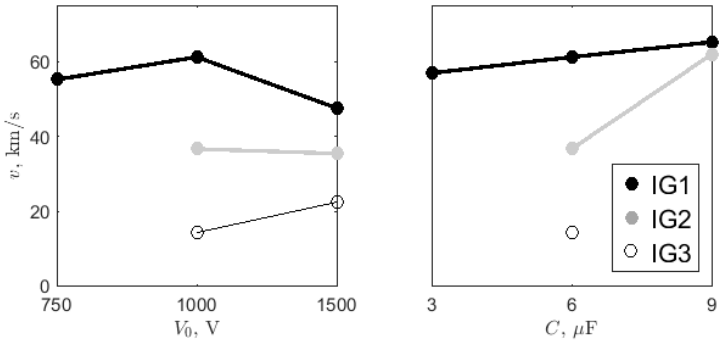

(b)

Figure 4.12: **[Dependence of the Time-of-Flight velocity v results with the operational discharge parameters using a different thruster battery (Battery 2A in Table 2.2 in Chapter 2).** (a): Ion speed for each ion group (IG) across the study matrix in Figure 4.4. In blue, results from probe 1-2 correlation, in red, from 2-3, and in black and filled, the average. Green filled dots represent the nominal case. The continuous black line represents the mean of the dataset, and the dot-red one the mean without outliers. (b): Dependence of the ion speed with the discharge voltage V_0 (left) and the bank capacitance C (right) for the central "cross-hair" of the study case-matrix. [Unclear bumps are not included.]

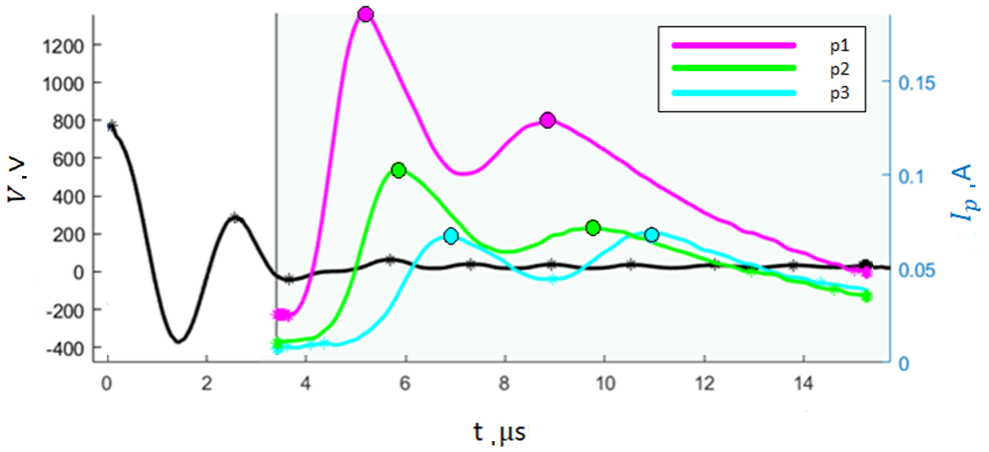

Figure 4.13: **Ion saturation current waveforms I_p measured by each probe in the three-probe ToF electrostatic wire probe setup (p=1,2,3).** The main anode discharge voltage V(t) is also represented. [Frequencies above 1 MHz are filtered.]

larger one, IG1 ion velocity has been characterized with data at $V_0 < 1250$ V, and the IG2 with $V_0 \geq 1250$ V. [As with the LP data, datasets with unclear peaks, or with outlying probe values, have been discarded for the velocity analysis.] Figure 4.14 displays the computed velocity of each population at different V_0 between 500 and 2500 V. These velocities are about 51 km/s for the first ion population and 33 km/s for the second one for all V_0. The v variations observed between cases are generally small and remain within the shot-to-shot dispersion. Therefore, it was not possible to identify any trends with V_0 under acceptable error in this experimental study. These conclusions are in agreement with the LP ones and reported ion speeds by other authors for comparable PPTs [96, 98, 94].

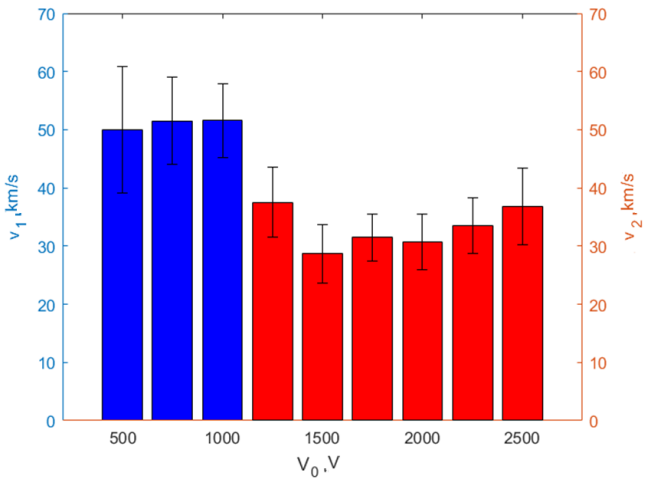

Figure 4.14: **Time-of-Flight results: velocity of ion groups 1 and 2 at different discharge voltages V_0.**

The fact that increasing V_0 does not lead to a clear increase in the computed ion velocity suggests that the energy increment associated with larger V_0 may go either to a larger production of plasma or lost as heat or other losses in the device. Fig. 4.15 displays the peak current measured at probe 1 as a function of V_0 for each of the two ion groups. Since the first ion current peak increases with V_0, it is confirmed that at least part of the extra energy is indeed increasing the production of the plasma associated with this peak. The value of the second peak, on the other hand, shows little dependency on V_0.

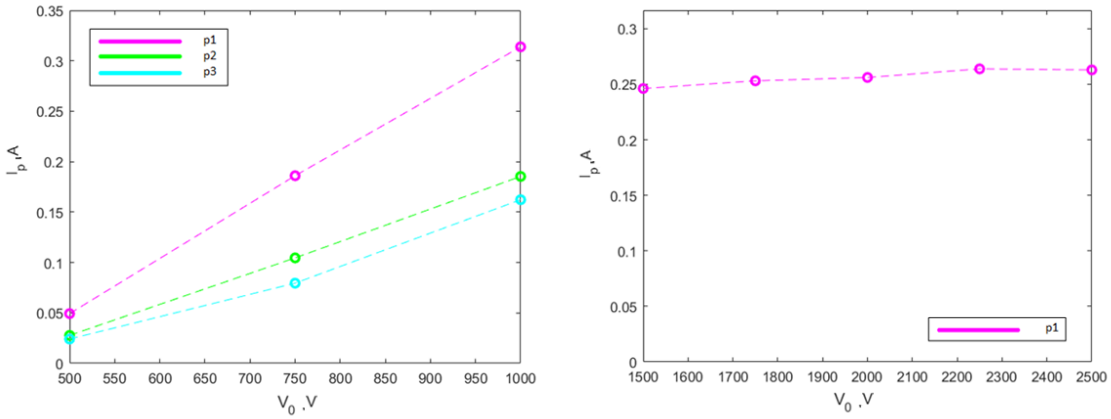

(a) (b)

Figure 4.15: **Dependence with the operational discharge parameters of the peaks of the ion saturation probe current I_p, measured by means of the three Time-of-flight (ToF) electrostatic wire probes setup (p=1,2,3).** Ion group 1 data is on the left, and ion group 2 data is on the right. The variation of I_p for ion population 2 at ToF probes p=2 and p=3 falls into the error margin of the measurements, and hence, these data have been ignored. [Mind (1) the variation of I_p for ion population 2 at probes 2 and 3 has been ignored as it falls into the error margin of the measurements; (2) the different scale for the y-axes.]

[Note that in Chapter 6, where wire probe ion saturation current data at closer z probe locations are presented for the thruster operating with Battery 2B, similar to Battery 2A addressed above, the second ion population consistently carries the highest current, and the third peak becomes recognizable.]

4.4. Summary

The transient plume of the PPT prototype described in Chapter 2 is experimentally analyzed using the traditional Time-of-Flight (ToF) technique, applied to ion saturation current measurements from three (ad-hoc) single Langmuir probes axially distributed downstream. This approach relies solely on feature correlation among probes. Additionally, this work also explores the ability of this technique to provide a preliminary estimate of the plume expansion rate, inferred from the decrease in peak current along probes. Experiments have been conducted under various operational conditions by varying V_0 and C. Conclusions were additionally validated across different thruster batteries as well as with the use of wire electrostatic probes instead of local probes. The main findings are summarized below. Part of this work has been presented in [7].

The results reveal three distinct ion populations, each traveling at a constant velocity of approximately 50, 35, and 20 km/s across the plume. Although ion velocities remain largely unaffected by increasing discharge energy, higher energy generally leads to increased current, primarily driven by the second ion population.

The time-integrated plume current scales linearly with the discharge energy. Combined with previous conclusions regarding ion speed and assuming proportionality between ion current and ionized mass [31], this suggests a linear relationship between impulse bit and discharge energy, consistent with findings reported in the literature [96, 142, 143].

A first assessment of the plume expansion rate by means of ToF estimates the axial derivative of the natural logarithm of the cross-sectional plume area. Findings reveal an approximate 50% increase in cross-sectional area between two consecutive ToF probe locations across all study cases.

Note that the traditional ToF technique, while useful for initial estimates, describing trends for the

different ion groups based on correlating peak values along probes alone presents inherent limitations. The main one, that each peak may result from a combined contribution of multiple ion populations. These ions groups potentially originate at different times, with distinct charge/mass ratios, velocities, densities, thermal spreads and divergence rates. In addition, accurate descriptions for the plume expansion rate must consider that the ion current density of each group decreases downstream not only due to plume divergence but also the thermal spread.

To address the former limitations, Chapter 5 proposes a method for reconstructing the parameters of the different ion populations from the complete time series data by establishing a model of their expansion.

5. TIME-VARYING RECONSTRUCTION OF THE TRANSIENT PLUME OF A PPT BY MEANS OF TIME-SERIES-BASED TOF [19]

This chapter presents the time-resolved exhaust reconstruction of the developed PPT using a novel analysis technique that reinterprets ToF by considering the entire time series of current probe data. This approach, named TIME-SERIES ToF, provides greater accuracy and deeper insight compared to traditional ToF methods. The content of this chapter is fully taken verbatim from a published article [2]. Some repetition with other chapters, particularly in the introduction and setup description, is intentionally retained to maintain consistency with the original work. The author apologizes for any distraction this may cause the reader. A preliminary version of this research was presented in [8], which also includes a variant of the present algorithm.

5.1. Introduction

Ablative Pulsed Plasma Thrusters (PPT) [29, 96, 30] are electromagnetic space propulsion systems that consist of a pair of electrodes (cathode-anode) shaping a channel-like configuration, connected to an energy storage unit, typically a capacitor bank. On one end of the channel, solid propellant, normally PTFE, is placed between the electrodes. Once the capacitor bank is charged up to a sufficiently large voltage V_0, a discharge is triggered by means of a spark plug over the surface of the propellant, whereby a fraction of it is ablated and ionized by the resulting electric current [69, 70, 72]. This discharge current also generates a self-induced magnetic field that causes a Lorentz force, which accelerates the generated plasma downstream and away from the device, generating thrust. Since PPTs operate in pulsed mode, the discharge energy per pulse can be controlled independently and irrespectively of the available input power, by modifying the pulse rate. This, combined with their simplicity and potential to be compact, makes PPTs ideal for microsatellites (with < 30 W being typical) [31, 30]. This contrasts with continuous-operation plasma thrusters, such as Hall thrusters, which are notoriously difficult to scale down to low powers [85].

The discharge process of ablative PPTs is complex and involves multiple phenomena, including breakdown, propellant ablation and dissociation, formation of the ionization layer and plasma generation, acceleration, and, finally, exhaust ejection and expansion [23]. The simultaneity and spatial coincidence of these mechanisms hinder their separated analysis [108]. Additional phenomena such as late-time ablation, [144, 95, 96, 97, 72, 145] secondary breakdowns, [23, 100, 139, 135, 48] and particulate emission [136, 137] can take place in the discharge. Furthermore, for the usual solid propellants used, the resulting plasma may be composed of multiple chemical species at different charge states [97, 61, 100].

As a consequence, a widely applicable and comprehensive theoretical description of the plasma physics at local level, taking into account all the major phenomena self-consistently at all the discharge stages, has proved elusive in PPTs [146, 147]. Ablation and flashover phenomena have been modeled in certain cases [148, 108, 149, 150, 145]. Regarding the discharge dynamics along the channel, most of the models broadly available are electromechanical approximations to it, where the plasma is assumed as a mobile sheet with an associated resistance and inductance [23, 29, 151, 152, 153, 92, 147, 150, 154]. These are useful to investigate trends and performance scaling parameters but lack physical insight [155]. More complex approaches to the plasma physics have been also proposed, including MHD and hybrid MHD-PIC models [156, 157, 158, 159, 160].

Beyond serving to characterize the performances of specific prototypes, laboratory measurements of the plasma exhaust are essential to supplement the models and to help in the understanding of PPTs. Since

[19] This chapter reproduces the journal paper: S. Barquero, J. Navarro-Cavallé and M. Merino, "**Pulsed Plasma Thruster exhaust reconstruction**", Plasma Sources Science and Technology, vol. 33, no. 4, p. 045007, April 2024 [2]. Paper DOI: 10.1088/1361-6595/AD35E5. Data DOI: 10.5281/ZENODO.10908404.

the 60s, manifold research teams have characterized Ablative PPTs at various energy levels [97, 94, 99, 95, 136, 110, 98, 139, 113, 161, 102, 126, 30, 143, 100, 61, 92, 107, 116, 109, 145, 72, 7]. Prior investigations on PTFE PPT plumes using diverse diagnostic methodologies have probed the existence in the generated plasma of several ionization waves and, in turn, multiple ion populations, involving various species and at different ionization states. E.g., Langmuir probes [98, 102, 7, 109] have been used, as well as direct methods to identify the species, such as residual gas analyzers [110, 98] or optical diagnostics, mainly optical emission spectroscopy [97, 95, 99, 100, 61, 111, 107]. The impact of this discovery on propulsive performances is negative, as generating any other than singly-charged ions incurs in extra ionization energy losses. Moreover, as multiply-charged ions are accelerated to different velocities by the fields, the resulting distribution of kinetic energy in the exhaust is suboptimal for thrust generation. Measurements carried out with the direct methods above have scrutinized the diverse plasma constituents across a broad discharge energy spectrum of parallel-plate PPT configurations, encompassing a wide range of species, extending up to the third charge state of fluorine (F) and carbon (C). These investigations notably identified neutral C_xF_y compounds and, even, electrode materials [97, 112]. Predominantly observed ion states include C^+, F^+ and C^{2+}. Mostly, time-of-flight (ToF) in combination to other diagnostics is used to characterize the velocity of the different ion constituents and results widely vary from 10—60 km/s [96, 97, 98, 99, 95, 61, 100, 94], often commonly reporting the existence of one of the plasma groups around 40 km/s. Although marginal exceptions at higher speeds have also been published [113, 114]. In [97], the following speed ranges were reported for distinct species: as $C \sim 5-20$ km/s, $C^+ \sim 20-30$ km/s, $C^{2+} \sim 30-40$ km/s, $F \sim 5-15$ km/s, $F^+ \sim 15-20$ km/s and $F^{2+} \sim 20-30$ km/s. Multiple ion groups are also observed in other types of pulsed plasma devices with similar diagnostics above, as in gas-fed PPTs [47, 48] and vacuum arc thrusters (VATs) [34, 35]. In the former, the findings include the presence of highly ionized electrode material too.

Among all experimental diagnostics for the plume exhaust, the ToF technique based on probe measurements stands out for its simplicity. Traditionally, it has been used to determine the ion mean velocity, by computing the time interval between the occurrence of the same feature in the time signal at two locations (e.g., peaks). In this manner, applied to single Langmuir probe measurements, Gatsonis et al. [98] and Barquero et al. [7] have provided evidence of the existence of two ion populations with velocities around 60 km/s and 30 km/s, respectively, on two different PPT devices. Furthermore, it is possible to obtain a first estimate of the exhaust plume divergence rate from the decrease in peak current value from one ToF probe to the next [7].

However, simply correlating peaks or other features among probe signals neglecting the fact that the exhaust likely consists of more than one ion group (each one of them potentially originating at a different time, and with different charge/mass ratios, velocities, densities, thermal spreads and divergence rates) yield a lack of accuracy. The overlapping contributions of individual ion groups may result in none of the observed peaks coinciding with the actual maximum of any of them. Thus, that basic approach can only provide an "average" velocity of the exhaust. As well, ion current density of each ion group decreases downstream not only due to the divergence, but due to the axial thermal spread. Hence, a naive calculation of the divergence based on the peak value of the ion current density at each probe overestimates the plume divergence rate in case the thermal spread is non-negligible.

To overcome these limitations, in this work it has been developed a method to reconstruct the parameters of the ion populations from the entire time series data, by establishing a model of their expansion. The main objective is to characterize the exhaust of an PPT breadboard model, named PμLSA (PULSed Ablative PPT for micro/μ-propulsion). Measurements of the PPT discharge voltage waveform and from three fast-sampled Langmuir probes, operating in ion-saturation mode and located along the discharge channel centerline, are used. Nine operating points are studied, varying the main electrode capacitor bank initial voltage (V_0) and capacitance (C). The model offers an accurate description of the exhaust in the first 30 μs with the superposition of only three ion groups. Results are used to discuss trends in the ion group parameters (relative magnitude, mean velocity, thermal spread, generation time and divergence rate) with V_0 and C.

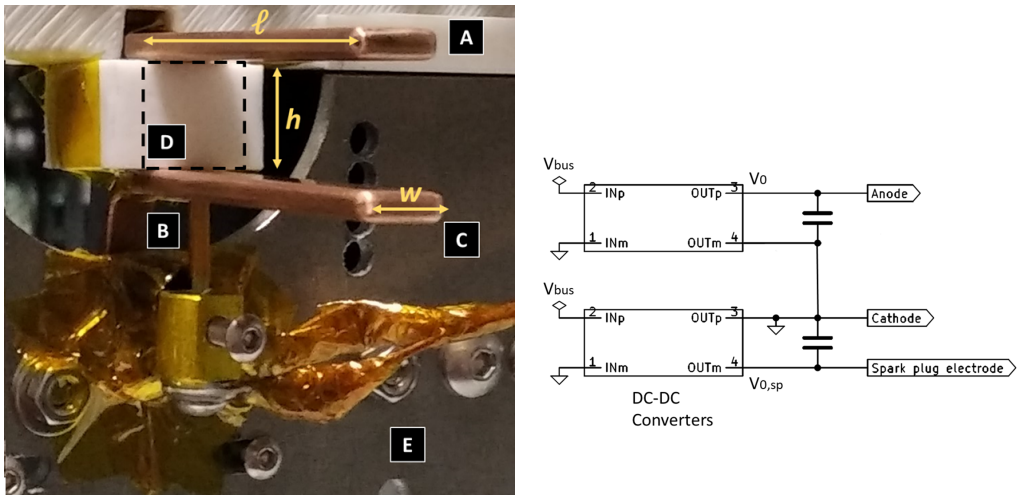

(a) (b)

Figure 5.1: **Discharge channel (a) and schematic basics (b) of the PμLSA PPT prototype.** "C" is the cathode electrode,"A", the anode electrode, "B", the spark plug, "D", the exposed propellant surface (PTFE), and "E", the mounting structure. Dimensions *l*, *h* and *w* stand for channel length, height and width, respectively.

The remaining part of the chapter is structured as follows. Section 5.2 presents the PPT prototype and the experimental setup. Section 5.3 describes the exhaust model and the fitting approach. Section 5.4 collects and analyzes the results and the validity of the expansion model. Finally, the conclusions are summarized in Section 5.5.

5.2. Experimental setup

20

5.2.1. PμLSA prototype

A low-power, breech-fed, parallel-rail, rectangular-electrodes PPT breadboard model, named PμLSA (Figure 5.1(a)), is the object of experimental study in this work. The design and sizing of this device is based on approximate scaling laws derived by the inspection of existing parallel-rail PPTs, as [97, 98, 30, 61, 116], and simple models [23]. The first ignition of the thruster was presented in [7]. Figure 5.2 shows three snapshots of the discharge sequence.

The device features a discharge space of length $\ell = 4.5$ cm length, height $h = 1$ cm, and width $w = 1$ cm. Electrodes are made of copper, with the cathode electrically grounded. A block of PTFE clamped between the rear part of the electrodes is used as propellant. Behind and in contact with the mounting structure, a capacitor bank of nominal capacitance (C), is connected to the main electrodes (cathode and anode). As in Figure 5.1(b), this capacitor bank is charged by a low-power DC-DC converter from typical microsatellite bus (low) voltages to a high voltage (V_0), and will provide the electric energy $E_0 = CV_0^2/2$ to the discharge. Once the former capacitor bank is charged up, reaching V_0, ignition is triggered by a 1.5 kV spark plug embedded in the channel through a hole in the cathode electrode. This is placed close to the propellant exposed surface. This igniter has been developed in-house, based on the flashover of a Metal-Insulator-Metal (MIM) gap. Molybdenum is used for the emitter electrode, PTFE for the dielectric filler

[20]The setup is identical to that described in Section 4.2.1 of Chapter 4. Thruster Battery 1 (4) is used (see Section 2.3.3 of Chapter 2).

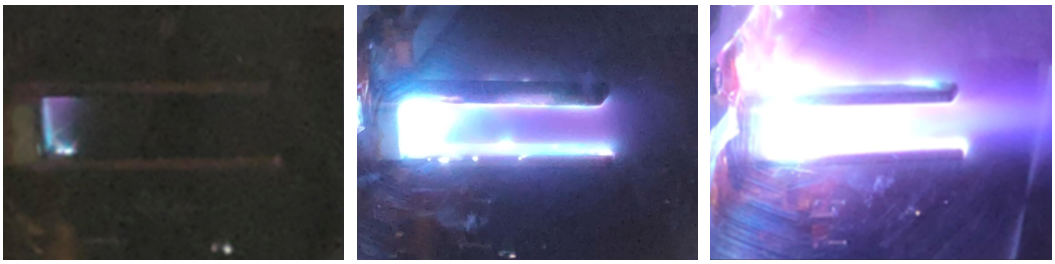

(a) (b) (c)

Figure 5.2: **Initial stages of the PμLSA PPT prototype discharge sequence by means of photography.**

and the main cathode of the thruster constitutes its reference electrode. The molybdenum rod is negatively biased with respect to the cathode. The spark plug is powered by an independent capacitive circuit with its own low-power DC-DC converter, whose discharge energy is negligible with respect to E_0. The firing frequency is set to 0.1 Hz.

A parametric study is performed on the main capacitor bank capacitance C, for 3, 6 and 9 μF, and on the discharge initial voltage V_0, for 750, 1000 and 1500 V. This involves a total of nine configurations, corresponding to E_0 ranging from 0.84 J to 10.13 J. Each study case is labelled according to the alphanumeric code presented in Table 5.1. The central configuration, B2 (6 μF and 1000 V), is the reference one for the operation of the device, with $E_0 = 3$ J.

The thruster is operated inside Hedron, a $50 \times 50 \times 50$ cm cubic vacuum chamber available at the EP2 laboratory at the Universidad Carlos III de Madrid (UC3M). High voltage feedthroughs are used for the charging lines of the main and sparkplug capacitor banks, and BNC ones for the diagnostic probes described in section 5.2.2. Hedron is equipped with a mechanical vacuum pump (Edwards nXDS Scroll pump, 10 m^3/h) and a turbomolecular pump (Edwards next400, 400 L/s (N_2)). The ultimate pressure reached is in the 10^{-6} mbar range. At each firing, the pressure experiences a perturbation below $2 \cdot 10^{-5}$ mbar, and is able to drop down to the ultimate pressure within a few seconds.

5.2.2. Electric and plasma diagnostics

Teledyne LeCroy high voltage passive probes were used for voltage monitoring of the main discharge capacitor bank.

Three cylindrical Langmuir probes (LP_k with $k = 1, 2, 3$) with tungsten tips of 0.508 mm diameter and 3 mm length are placed along the centerline of the discharge channel as shown in Figure 6.2, at axial distances $z_1 = 26.2$ cm, $z_2 = 30.7$ cm and $z_3 = 35.0$ cm. The tips of the LPs are oriented perpendicularly to the plasma exhaust, and slightly displaced laterally along x so as to avoid direct shadowing among them. The LPs are biased to work into the ion saturation regime. It was set at -50, after verifying that he measured ion current exhibited variations below shot-to-shot uncertainty upon changes in the probe bias in the range -50–-100 V.

An eight-channel Yokogawa DLM5000 oscilloscope is used for data acquisition from all the probes (voltage probes and LPs) synchronously. The oscilloscope sampling frequency is set at 100 MHz.

5.3. Plume expansion model

The ion saturation current measured by the k-th LP as a function of time, $I_k(t)$, is modeled as the sum of the contributions of multiple, overlapping ion groups (IGs). Each IG is assumed to consist of ions of the same charge/mass state. For the s-th IG, t_s denotes the initial instant of time (with respect to the beginning of the

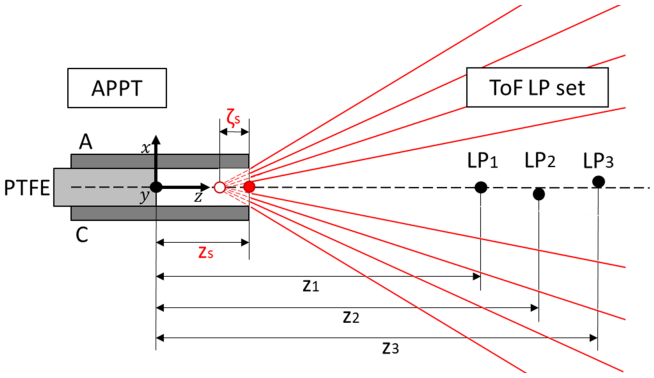

Figure 5.3: **Sketch of the experimental setup.** "A" refers to anode, and "C" to cathode. The three Langmuir Probes (LP_k with $k = 1, 2, 3.$) are placed at $(x, z) = (0, 26.2)$ cm, $(-1.5, 30.7)$ cm and $(1.5, 35.0)$ cm, respectively. The exhaust model parameters z_s, creation location, and ζ_s, position of the conical expansion vertex, are also illustrated in the Figure.

discharge) at which the IG is assumed to be a localized sheet of small thickness at position z_s. For the axial motion of the ions, a truncated Maxwellian *charge* distribution f_s is assumed. As an ansatz, and motivated by the assumptions above, it has been established the following shape for the distribution function of ions of the s-th IG at time t_s:

$$\begin{aligned} f_s(z, v > 0, t_s) &= \frac{Q_s}{\sqrt{\pi c_s^2/2}} \frac{\exp\left[-\dfrac{(v - \bar{v}_s)^2}{2c_s^2}\right]}{\operatorname{erf}\left(\bar{v}_s/\sqrt{2c_s^2}\right) + 1} \delta(z - z_s) \\ &\equiv F_s(v)\delta(z - z_s), \end{aligned} \tag{5.1}$$

where v is the axial velocity, and $\bar{v}_s$, c_s, and Q_s are respectively the axial mean velocity, the axial thermal velocity, and the electric charge per unit area of the IG. The denominator with the error function erf originates from truncating the Maxwellian to particles with $v > 0$.

As the IG travels downstream for $t > t_s$, the sheet expands axially due to its thermal spread c_s, and laterally as a cone with vertex located at a position ζ_s upstream from z_s (see Figure 6.2), which implies that f_s decreases quadratically with the distance to the vertex. This conical expansion introduces a multiplicative factor into the distribution function f_s at positions $z > z_s$:

$$Z_s(z) = \left[\frac{\zeta_s}{(z - z_s) + \zeta_s}\right]^2.$$

Any axial ion acceleration after time t_s is disregarded.

We are interested in computing the current density j_s due to the s-th IG as a function of (z, t). The amount of charge that crosses a unit area between time t and $t + \Delta t$ at position z is given by ions with velocities ranging from $v_1 = (z - z_s)/(t - t_s)$ to $v_2(\Delta t) = (z - z_s)/(t + \Delta t - t_s)$. Integrating, dividing by Δt, and taking the limit $\Delta t \to 0$ gives:

$$j_s(z, t) = -\lim_{\Delta t \to 0} \frac{1}{\Delta t} \int_{v_1}^{v_2(\Delta t)} Z_s(z) F_s(v) \, \mathrm{d}v = Z_s(z) F_s\left(\frac{z - z_s}{t - t_s}\right) \frac{z - z_s}{(t - t_s)^2}, \tag{5.2}$$

If the sum of the contributions of all IGs to ion current density is denoted as $j(z, t)$, then the (modeled) ion current collected at the k-th LP is

$$\tilde{I}_k(t) = j(z_k, t) A_k, \tag{5.3}$$

where A_k is the effective collection area of the probe.

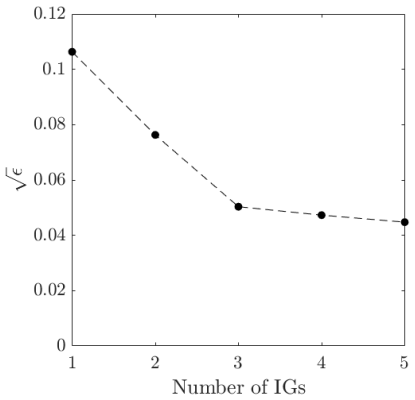

Figure 5.4: **Evolution of the fit error $\sqrt{\epsilon}$ with the number of IGs for the reference case B**2.

Assuming the effective collection area is the same for all the LPs ($A_k = A$), the normalized least squared error ε between the model and the experimental data is

$$\varepsilon = \frac{1}{3}\sum_k \varepsilon_k = \frac{1}{3}\sum_k \frac{\int \left[I_k(t) - \tilde{I}_k(t)\right]^2 \, dt}{\int I_k^2(t) \, dt}, \tag{5.4}$$

where the integrals span a specified time window in which the LPs collect ion current. Note that the average of the individual squared errors for each one of the three LPs (ε_k) is used to define ε. The numerical fit of the model to the data is carried out by minimizing ε with respect to the parameters of the IGs.

In this work, the integration time window is set to [3–30] μs, where most of the ion current is measured by the probes. A preliminary analysis led us to set the maximum number of IGs to 3, as a trade-off between model complexity and quality of the results, to avoid over-fitting. This is illustrated in Figure 5.4 for the reference case B2, where the evolution of the fit error with the number of IGs is seen to have an inflection point at 3 IGs. Similar trends are observed for the rest of experimental cases. Finally, the initial IG location is set to $z_s = 4.5$ cm for all the IGs, i.e., the initial sheet distribution is assumed to be at the exit of the channel.

5.4. Results

5.4.1. Electric circuit response

The anode voltage response $V(t)$ for the reference case B2 ($V_0 = 1000$ V and $C = 6$ μF) is shown in Figure 5.5 for multiple shots. The signal exhibits damped oscillations with natural frequency (ω) in the order of magnitude of 100 kHz, and with the signal amplitude decaying by a factor of 10 after about 5 μs. Good overall repeatability among pulses is observed, although small differences develop after the second period of the discharge.

The estimated resistance (R) and inductance (L) values from fitting an RLC circuit with constant parameters to the first cycles of the discharge are between 20–40 mΩ and 20–40 nH respectively across all parametric cases explored. Increasing V_0 causes the amplitude of the oscillations to grow, while R and L slightly decrease and $\omega = \sqrt{1/LC - R^2/4L^2}$ marginally increases. Larger values of C mean that R slightly decreases, while L and ω slightly increase, and result in a voltage response that deviates more from an ideal RLC circuit.

High-frequency noise in the order of magnitude of 10 MHz on $V(t)$ is noticeable around the breakdown instant, and sometimes at the signal minima/maxima. The later could be related to late reignitions that may occur upon voltage inversion [23, 100, 139, 135, 48].

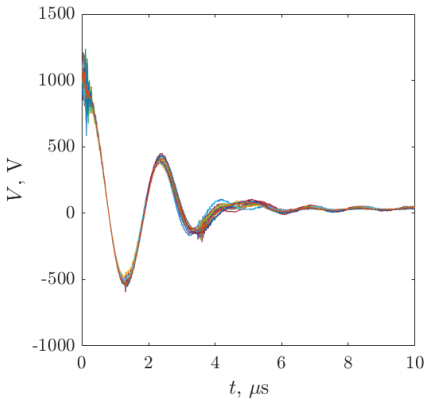

Figure 5.5: **Anode voltage discharge waveform $V(t)$ measured for the reference case B2.**

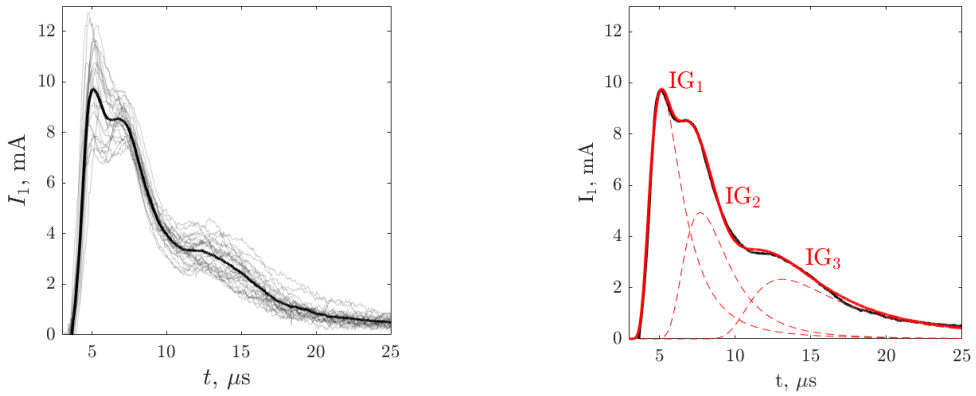

(a) (b)

Figure 5.6: **Ion saturation current measured at Langmuir probe** 1**, for the reference case B**2. In panel (a), thin lines are individual firings, whilst the thick one represents the average over them, $I_1(t)$. Panel (b) displays the reconstruction of the average current $I_1(t)$ (thick, black) with the model current $\tilde{I}_1(t)$ (thick, red), and the contributions of three IGs (dashed, red).

5.4.2. Plume characterization

Figure 5.6(a) displays the response of the measured ion saturation current at LP_1 in the reference case B2, for individual shots. The probe begins collecting current at around 4 μs after the breakdown, and the signal vanishes 30–40 μs afterward. Shots with evidently abnormal current responses (< 40% of the total) have been excluded. Despite the good repeatability of the voltage signal discussed in Subsection 5.4.1, probe current variability can be up to about ±25% with respect to the mean at some instants of time.

The average response over the shots, $I_1(t)$, reveals that three bumps are clearly visible, which are hypothesized to correspond to distinct IGs. Figure 5.6(b) presents the ion current model with three IGs fitted to the the mean probe current for the reference case B2, providing an example of the overall validity of the decomposition model proposed. Out of the three IGs, IG_1 and IG_2 drive most of the current, are more focused and reach the probe at earlier times. They together contribute to the peak value of I_1. IG_3 reaches the probe later, and has a smaller but broader contribution.

The fitted model parameters of the three IGs for the reference case B2 can be found in Table 5.1, together with the rest of the parametric cases explored in this work. For the reference case, the computed peak current value at probe LP_k attributed to IG_s, $\tilde{I}_{ks}^{max}$, and the fitting errors, are also shown. The average current $I_k(t)$

(including the standard deviation over the different firings) together with the fitted model $\tilde{I}_k(t)$, and the peak current $\tilde{I}_{ks}^{max}$, are shown for the three probes in the central panels of Figures 5.7 and 5.8, respectively.

Taking s as the IG index, mean velocity $\bar{v}_s$ decreases with s, and takes values that are consistent with those reported by other authors for other devices [97, 98, 61, 96, 99, 95, 100, 94]. The first two IGs originate roughly at the same time, about 0.8–1.1 μs (respectively) after the first zero of the discharge voltage waveform $V(t)$ (at $t = 0.8\,\mu$s), which coincides with the first maximum of discharge current between the electrodes. This is the delay that it would take ions traveling at a velocity $v = 56$–41 km/s (respectively) to move from the PTFE surface to the channel exit, which is the location considered for the generation of the IGs ($z_s = 4.5$ cm). These velocities are higher but comparable to the mean velocities $\bar{v}_s$ reported for the two first IGs, in Table 5.1. Analogously, the creation time for the third IG t_3 happens at about 2.8 μs after the second maximum (inverted) of the discharge current ($t = 1.9\,\mu$s). In this case, the delay is comparable to the time it would take ions at a velocity $v = 16$ km/s to reach the end of the channel, again similar to the reported $\bar{v}_s$ for IG_3.

The fact that IG_1 and IG_2 have a ratio $\bar{v}_1^2/\bar{v}_2^2 \simeq 2$ is compatible with IG_1 being composed of ions with 1.5–2.5 times the charge/mass ratio of IG_2, e.g. triply- and doubly-charged, or doubly and singly-charged ions, of the same element or compound, generated at roughly the same instant of time and accelerated by the same electromagnetic fields. However, considering that the masses of C and F are only a factor 1.6 apart, it is also possible that, alternatively or in addition, the two IGs correspond to ions of two different species.

The axial thermal velocity c_s of the IGs suggests ion temperatures around 10–15 eV, far larger than the temperature of the PTFE or the electrodes, indicating that, either ion heating is an efficient mechanism within the discharge and near plume, or more likely, that charge-exchange and other collisional processes with colder neutrals are giving rise to a thermal velocity spread comparable to the mean velocity of the group.

The ion current due to each IG measured at the probes depends on three parameters. First, Q_s, which describes the initial surface density of the s-th IG. Table 5.1 presents the product Q_sA, where A is the effective collection area of the probes. It is clear that the magnitude of each subsequent IGs decreases. Second, parameter ζ_s, which characterizes the lateral divergence of the exhaust. Its value increases with s, indicating that subsequent IGs would have a lower divergence rate than their predecessors. Lastly, the axial thermal velocity c_s discussed above, as axial thermal expansion, also causes each IG to flatten out downstream. Fitting the model allows separating these three contributions to the value of IG peak current $\tilde{I}_{ks}^{max}$, shown in Figure 5.8, which decreases from one probe to next probe. Peak current $\tilde{I}_{ks}^{max}$ also decreases from IG to next IG, meaning that the contribution to the signal of each subsequent IG is smaller.

The disagreement $\sqrt{\varepsilon}$ between the model and the actual measurements is below 10%. Nevertheless, the integral error of the fit does not distribute homogeneously among the three LPs. Indeed, the fit incurs in a larger error the farther is the probe, with $\sqrt{\varepsilon_1}$ below 3% and $\sqrt{\varepsilon_3}$ above 9%.

Figure 5.7 displays the average electric current signal at each of the three LPs, $I_k(t)$, the standard deviation over the different firings, and the model electric current $\tilde{I}_k(t)$, for all nine tested cases. The corresponding fit parameters are reported in Table 5.1. A good fit is found with just three IGs for all cases, with the exception of A1 and A2, which require only one or two IGs, respectively. Overall, the discharge retains the same characteristics and trends as the reference case B2. Nonetheless, there are several noteworthy aspects to be discussed.

First, the relative importance of IG_2 and IG_3 with respect to IG_1 increases with C and V_0. This effect is evidenced in the values of Q_sA and $\tilde{I}_{ks}^{max}$. Peak current of the s-th IG at the k-th probe, $\tilde{I}_{ks}^{max}$, is plotted in figure 5.8, for all 9 cases. With the exception of case C1, the contribution of each subsequent IG is lower than the previous one. Peak current $\tilde{I}_{ks}^{max}$ notably increases with V_0 and moderately with C (again, with the exception of C1) for all the IGs, but especially for IG2 and IG3.

Table 5.1: **Fitted model parameters (mean velocity $\bar{v}_s$, thermal spread c_s, location of the conical expansion vertex ζ_s, creation time t_s, initial surface charge density times effective probe collection area Q_sA), computed peak current $\tilde{I}_{ks}^{max}$ for the s-th IG at the k-th LP, and model errors $\sqrt{\varepsilon_k}$ and $\sqrt{\epsilon}$, for each parametric case.** B2 is the reference case.

Case	V_0 V	C μF	E_0 J	IG	$\bar{v}_s$ km/s	c_s km/s	ζ_s cm	t_s μs	Q_sA C	$\tilde{I}_{1s}^{max}$	$\tilde{I}_{2s}^{max}$ mA	$\tilde{I}_{3s}^{max}$	$\sqrt{\epsilon_1}$	$\sqrt{\epsilon_2}$ %	$\sqrt{\epsilon_3}$	$\sqrt{\varepsilon}$ -
A1	750	3	0.8	1	29	22	12.7	1.82	0.12	2.4	1.6	1.1	4.6	10.1	17.9	12.1
A2	1000	3	1.5	1	38	16	8.3	1.47	0.39	6.4	4.0	2.7	3.0	9.2	16.4	11.0
				2	5	15	10.1	4.04	0.16	0.8	0.5	0.4				
A3	1500	3	3.4	1	57	21	2.1	1.86	4.73	12.9	7.6	4.9	4.6	9.8	9.0	8.1
				2	33	15	3.5	2.38	2.69	9.7	5.8	3.8				
				3	14	8	2.0	3.77	4.89	2.6	1.5	1.0				
B1	750	6	1.7	1	56	11	2.7	1.57	0.59	4.0	2.4	1.6	8.9	8.8	18.0	12.6
				2	34	31	4.2	1.74	0.48	2.2	1.3	0.9				
				3	5	22	7.0	2.17	0.35	1.5	0.9	0.6				
B2	**1000**	**6**	**3**	**1**	**50**	**18**	**4.7**	**1.56**	**0.95**	**9.7**	**6.9**	**3.9**	**2.9**	**4.9**	**9.1**	**6.2**
				2	**32**	**9**	**8.3**	**1.85**	**0.28**	**4.9**	**3.1**	**2.1**				
				3	**18**	**10**	**15.0**	**4.65**	**0.14**	**2.3**	**1.5**	**1.1**				
B3	1500	6	6.8	1	43	16	12.0	1.11	0.54	18.0	11.6	8.1	3.3	5.8	4.5	4.7
				2	33	12	16.5	2.32	0.45	16.8	11.1	7.9				
				3	15	6	11.5	3.34	0.29	3.0	1.9	1.3				
C1	750	9	2.5	1	55	67	15.3	2.81	0.08	4.0	2.6	1.9	4.7	9.2	5.0	6.6
				2	34	21	9.4	2.87	0.46	7.3	4.6	3.1				
				3	24	7	13.3	4.01	0.05	1.2	0.8	0.5				
C2	1000	9	4.5	1	62	67	18.7	3.16	0.14	10.2	6.8	4.9	6.5	9.7	7.1	7.9
				2	43	26	15.7	3.24	0.21	8.1	5.3	3.8				
				3	22	15	26.5	3.27	0.23	7.5	5.2	3.8				
C3	1500	9	10.1	1	68	26	13.4	2.50	0.48	29.4	19.1	13.4	7.1	8.4	11.5	9.2
				2	46	25	24.1	3.41	0.35	23.8	16.4	12.0				
				3	20	30	45.5	6.28	0.27	15.3	11.2	8.6				

Second, the time-integrated current (i.e. the total charge, which is proportional to the total exhaust mass) recorded by each LP_k, $\int I_k(t)\ dt$, scales linearly with E_0, as depicted in Figure 5.9. On the other hand, the mean velocity of each IG, $\bar{v}_s$, does not vary much across cases, and they fall within the ranges ranges $\bar{v}_1$ = 50–70, $\bar{v}_2$ = 30–45 and $\bar{v}_3$ = 10–25 respectively, again consistent with [97, 98, 61, 96, 99, 95, 100, 94]. These trends suggest that the impulse bit, i.e. the momentum in the exhaust, is linear on E_0, in agreement with existing direct measurements [96, 142, 143].

Third, the thermal velocity c_s and parameter ζ_s do not follow a clear trend with C or V_0. Notwithstanding this, a larger thermal spread seems to exist for all IGs the larger the bank capacitance C, while ζ_s tends to be larger for the later IGs and to increase with the discharge energy E_0.

Finally, the largest integral error is $\sqrt{\varepsilon}$ = 12.6 for case B1. The error at each probe, $\sqrt{\varepsilon_k}$ remains below 10%, with exceptions in A1, A2 (the cases with less than 3 IGs), and B1, C3. Notice that the shape of the current curves becomes more complex with increasing C.

The discussion of the nature of the different IGs and their possible origin is now resumed. Two hypothesizes have been proposed above. First, that IGs 1 and 2 correspond to different charge/mass states, and second, that IG3 likely corresponds to a second breakdown taking place in the discharge when the voltage in the capacitors reverses.

The former is supported by previous observations in the literature, as reported in the Introduction, where different charge states of carbon and fluorine are identified [97, 61, 100]. As suggested in [97, 61], triply-charged ions and higher charge states would originate during the initial stages of the discharge, where high-energy electrons are available and the amount of ablated material is still small. Subsequent stages involve the continued desorption and dissociation of the ablated PTFE while electron energy begins to decrease, resulting in doubly-charged ions. Continued plasma formation would eventually yield singly-charged ions. The optical emission spectroscopy investigation in [61] additionally reveals a higher likelihood of generating multiply-ionized species for larger capacitances C. On the other hand, increasing the (initial) discharge

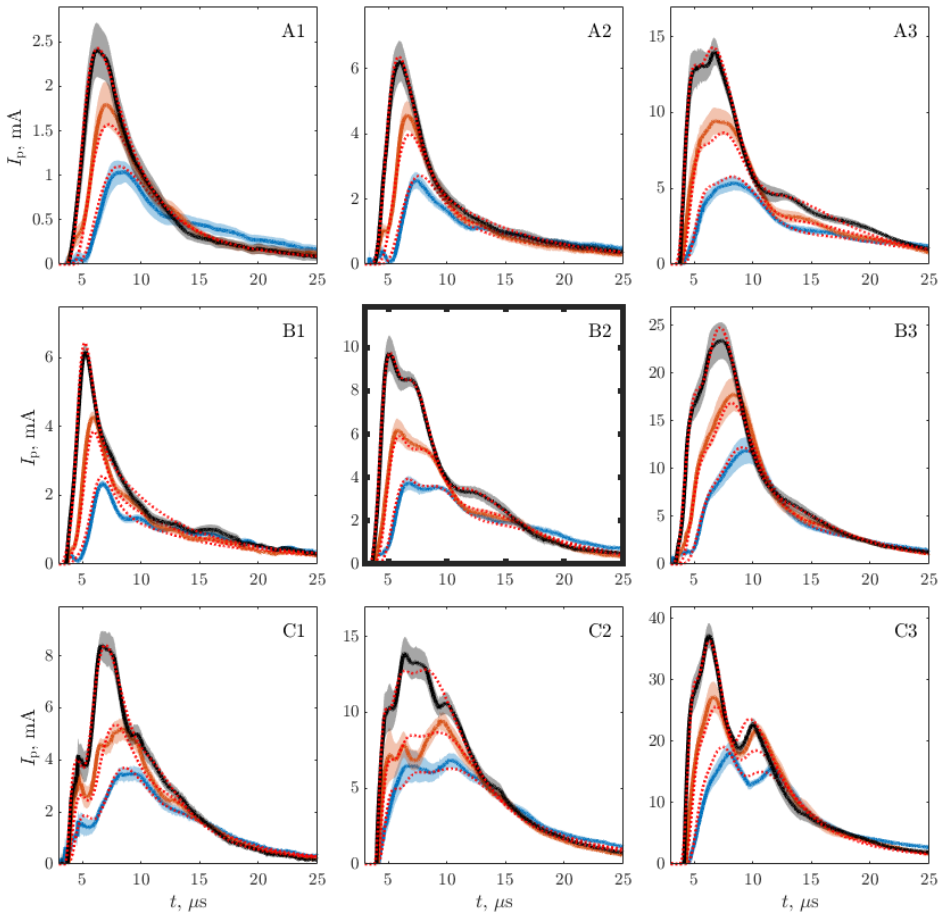

Figure 5.7: **Average ion saturation current $I_k(t)$ (solid lines) and standard deviation (shaded area) over multiple measurements for the three k Langmuir probes (LPs), and the reconstructed solution $\tilde{I}_k(t)$ (dashed lines)**. LP_1 in black, LP_2 in red, and LP_3 in blue. Case labels are described in Table 5.1. B2 is the central, reference case. Mind the different y-axis scale in each panel.

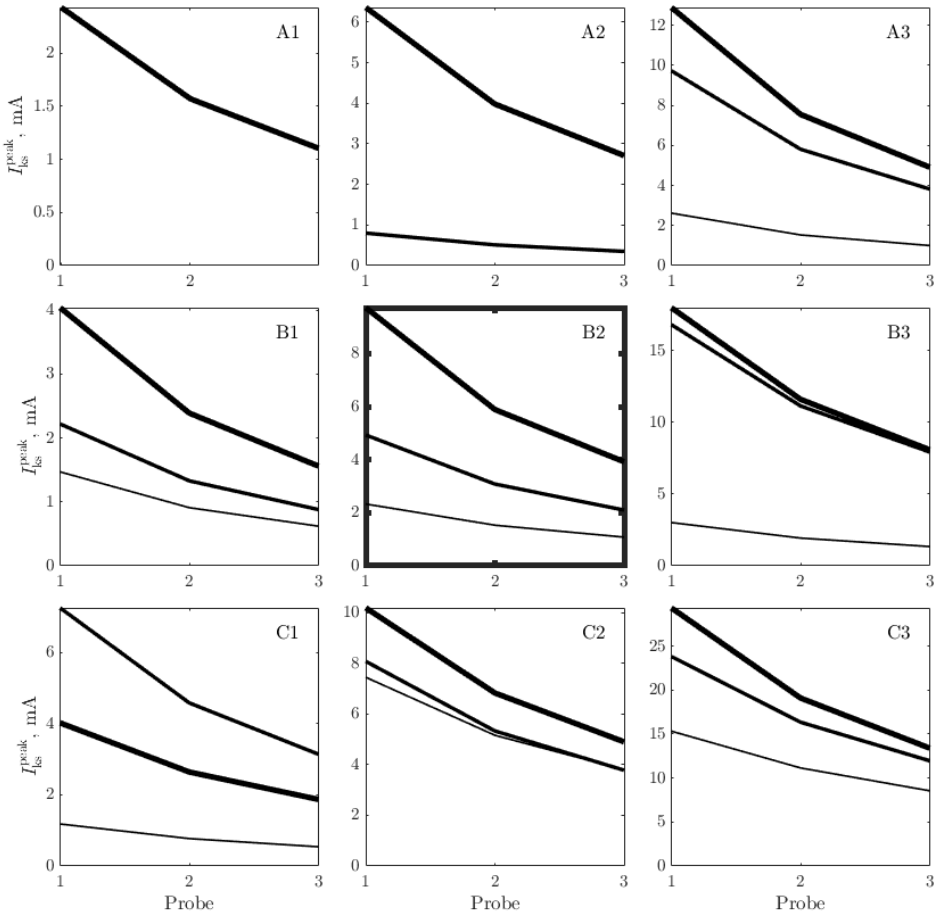

Figure 5.8: **Evolution of the peak current of the different ion groups** $s = 1, 2, 3$ **constituting the plume** $\tilde{I}_{ks}^{max}$ **along the axial probes** $k = 1, 2, 3$**.** Line width decreases from IG1 to IG2 to IG3. Case labels are described in Table 5.1. B2 is the central, reference case. Mind the different y-axis scale in each panel.

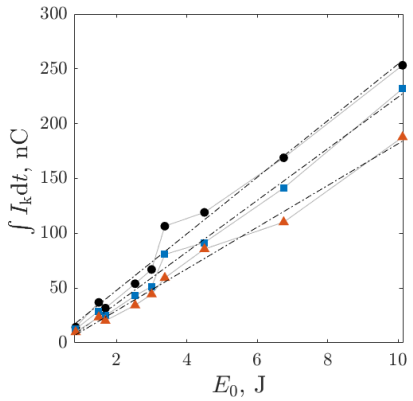

Figure 5.9: **Time-integrated ion saturation current** $\int I_k(t)\ dt$ **collected at each Langmuir probe (LP$_k$) in the time window** $t = [4, 30]$ μ**s, as a function of the discharge energy** E_0**.** LP$_1$ in black circle markers, I_1, LP$_2$ in blue square markers, I_2, and LP$_3$ in red triangle markers, I_3. Dashed lines are trend lines.

voltage V_0 also increased the overall emission intensity, but maintained a similar plasma composition. Incidentally, also in [91, 92] velocity is almost constant with C, and shows no clear trends with V_0. This aligns well with our findings.

Nevertheless, specifying which ion species corresponds to each ion population is not a straightforward task. This is exemplified in [95, 61], where different species were observed to have similar velocities, and, likewise, also different populations of the same type of ions with varying velocities were found [95]. Additional diagnostics, such as gridded energy analyzer [113], optical emission spectroscopy [61] or Retarded Potential Analyzers [162], among others, could help disambiguate the charge/mass ratio of each ion group, complementing the present technique.

Regarding support for our second hypothesis, secondary breakdowns are known to exist essentially in all PPTs [23, 100, 139, 135]. Moreover, as evidenced in [48, 163], Hydrogen (H) gas-fed PPT devices (which, by contrast to the complex mixture in PTFE plasmas can only create H^+ as ion species, if electrode materials are ignored) show the existence of two separate ionization waves. These can be attributed to different breakdown processes: the first is faster and has a larger current level than the second. This behavior is analogous to that of the IG1,2 and IG3 observed in this work, respectively.

5.4.3. Validity discussion of the plume expansion model

While Figure 5.6(b) shows that the model used in this work can accurately describe the ion exhaust of the PPT as the superposition of separate IGs, it is worth identifying and discussing the possible sources of error and its limitations.

First, there is the uncertainty in the effective collecting area of each LP_k (A_k), which depends on the sheath structure around the tip of each one of the three LPs. The sheath is a function of the unknown plasma density (n), which varies with distance to the thruster and time. Additionally, $I_k(t)$ may also be affected by the wake of any probes upstream. This makes the determination of A_k a complex problem, which affects the determination of the ion current density (j) from the probe signal ($I_k(t)$). By selecting a constant and identical A for all the LPs, here one is incurring in an error which likely underestimates the sheath size of LP_3 and overestimates LP_1, as it scales with $\sqrt{1/n}$ for a quasi-neutral plasma. The net effect of this error would be to underestimate plume divergence, inflating the value of ζ_s. Relatedly, the wake effect may explain why the error ε_k for the latter LPs is often larger than for the first one.

Second, it is noted that the model fit generally incurs in a larger relative error in the late-time part of the current curves ($t \gtrsim 12.5\ \mu$s), in some cases with partial evidence of the presence of a weak fourth IG. Although using a larger number of IGs (and therefore larger number of degrees of freedom) would yield a lower error, especially in cases B1, C1, and C2, it is found that the extra complexity does not provide much additional physical insight, and moreover, could result in an over-fitted model.

Third, a potential source of error comes from ignoring Lorentz forces, ambipolar acceleration, and collisions on the evolution of the different IGs outside of the channel. Also, the initial sheet thickness Δz_s around z_s and creation interval Δt_s around $t_s$of each IG_s have been ignored. Nevertheless, this is a good approximation provided that $z_k - z_s \gg \Delta z_s$ and $(z_k - z_s)/\bar{v}_s \gg \Delta t_s$. While the first of these orderings is easily satisfied in the current setup, the fulfillment of the latter requires that $\Delta t_s < 5\ \mu$s, the characteristic time of the first peak in $I_1(t)$ at LP_1. Inspection of Figure 5.5 suggests that $\Delta t_s < 1.5\ \mu$s, corresponding with half an oscillation cycle in $V(t)$, which would satisfy the constraint.

Last, it is worth noting that the determination of the model parameters ($\bar{v}_s$, c_s, ζ_s, t_s and $Q_s A$) is not necessarily well-conditioned in all cases, and may incur in a larger relative uncertainty on some of them. In particular, the determination of ζ_s and $Q_s A$ when $\zeta_s \ll z_k - z_s$ is ill posed. Placing additional probes, on-axis and off-axis, may improve the fit conditioning, as they would provide additional data on the plume divergence parameter ζ_s.

5.5. Conclusions

The exhaust of a small ablative pulsed plasma thruster prototype has been experimentally characterized, for three bank capacitances and three discharge initial voltages (under 11 J of discharge energy), by means of voltage probes and Langmuir probes operating in the ion saturation regime. The plume exhaust has been reconstructed by means of an original reinterpretation of the time-of-flight technique, based on modeling the discharge as the superposition of multiple independent ion groups, enabling a greater exploitation of the ion current curves. The proposed model provides an estimate of the axial velocity distribution of each one of the ion groups involved (characteristic velocity and thermal spread of each one of these ion groups, as well as their time of creation, magnitude and divergence rate).

The relevance of identifying and characterizing the existence of different ion groups is twofold. Firstly, it can be considered as a first step toward a clearer understanding of the discharge physics in PPTs, to be complemented by other diagnostics and models. And secondly, because of the negative impact that having multiple species and velocity spread has on propulsive performances: indeed an optimal device would expel all propellant particles as singly-charged ions with same velocity. Any other arrangement results in extraordinary ionization losses and a sub-optimal use of kinetic energy to generate thrust.

The fitted results reveal that three ion groups suffice to explain each one of the explored operation cases. The mean ion group velocities are in the range 50–70, 30–45 and 10–25 km/s, respectively for each one of the three ion groups. Each ion group probably describes a different ion species, with different charge/mass ratio, or ions generated at different instants of the discharge process. The total ion charge in the exhaust is mainly carried by the first two ion groups, and it scales with the discharge energy. The relative weight of the later two ion groups increases with respect to the first with the discharge initial voltage and, especially, with the capacitance. Less clear trends were obtained for the thermal spread and the divergence. The thermal velocity is below 31 km/s with two exceptions and is often lower for the later ion groups. The obtained divergence rate showed is larger for the first ion groups and at lower discharge energies.

The main source of uncertainty in the results is expected to come from the relative effective collection areas assigned to the probes. Attributing the same area to all probes is expected to overestimate ion current density downstream and therefore to underestimate exhaust divergence rate. Advanced sheath models that take into account the variable plasma density and the effect of the wakes of upstream probes are necessary to improve upon the present results. Despite this limitation, the proposed approach to time-of-flight analysis enables the identification and isolation of the different ion constituents in the exhaust of pulsed plasma thrusters.

5.6. Acknowledgments

This work was been supported by the MARTINLARA project, funded by the Comunidad de Madrid, under Grant reference P2018/NMT-4333 MARTINLARA-CM. Additional support came from the ESPEOS project, funded by the Agencia Estatal de Investigación (Spanish National Research Agency), under Grant number PID2019-108034RB-I00/AEI/10.13039/501100011033.

5.7. Data availability statement

Any data that support the findings of this study are included within the article. These data are also openly available at the following URL/DOI: https://doi.org/10.5281/zenodo.10908405.

6. RECONSTRUCTION OF THE PPT TRANSIENT PLUME CROSS-SECTION BY MEANS OF THE WAVES DIAGNOSTIC TECHNIQUE [21]

This chapter presents the reconstruction of the time-varying PPT exhaust reconstruction by a new diagnostic system consisting of a grid of electrostatic wire probes working in the ion saturation regime. The proposed technique is named WAVES (Wire Array for Variable Exhaust Scanning).

This chapter includes content taken verbatim from a published article [106]. Repetitions with other chapters are retained to maintain consistency with the original work. The author apologizes for any distraction this may cause to the reader.

Preliminary versions of this work were presented in [7, 9], while the consolidated version [106] is presented below.

This chapter presents the reconstruction of the time-varying PPT exhaust using a new diagnostic system composed of a grid of electrostatic wire probes operating in the ion saturation regime. The proposed technique, named WAVES (Wire Array for Variable Exhaust Scanning), enables detailed time-resolved mapping of the exhaust cross-section while significant time savings with respect to the state of the art. The content of this chapter is taken verbatim from a published article [106]. Some repetition with other chapters, particularly in the introduction and setup description, is retained to maintain consistency with the original work. The author apologizes for any distraction this may cause the reader. Preliminary versions of this research were presented in [7, 9].

6.1. Introduction

Ablative pulsed plasma thrusters (PPTs) [29, 96, 30, 45] are electromagnetic space propulsion systems that consist of a pair of electrodes (cathode-anode) forming a discharge channel, connected to an energy storage unit, typically a capacitor bank. At one end of the channel, a solid propellant, commonly polytetrafluoroethylene (PTFE), is placed between the electrodes. Once the capacitor bank is charged up to a sufficiently high voltage, a spark plug triggers a breakdown over the propellant surface. A fraction of the propellant is then ablated and ionized [69, 70, 71, 72]. The resulting discharge current generates a self-induced magnetic field that causes a Lorentz force, which accelerates the plasma downstream and away from the device, producing thrust. Since PPTs operate in pulsed mode, the discharge energy per pulse can be set independently and irrespectively of the available input power, by modifying the pulse rate. This, combined with their simplicity and their potential to be compact, makes ablative PPTs ideal for microsatellites [31, 30]. This contrasts with steady plasma thrusters, such as Hall thrusters, which are notoriously difficult to scale down to such low powers [85].

Multiple research teams have experimentally investigated PPTs [102, 61, 107], highlighting the complexity of its discharge physics [23, 108]. The simultaneity and spatial coincidence of different mechanisms hinder their separated analysis. Furthermore, for the usual propellants, the resulting time-varying plasma may be composed of multiple chemical species (also including electrode material), with different molecular mass and charge states, each with a different divergence angle [97, 95, 61, 100, 2]. The resulting exhaust divergence angle is always a concern for thruster integration in the spacecraft platform because of the impingement of energetic particles onto delicate surfaces, as instruments or solar panels.

Previous studies on PPT plume divergence are relatively scarce [95, 94, 101, 93, 98, 102], while a renewed interest in them has been shown in recent years by different research groups [103, 7, 2, 65, 104, 105].

[21] This chapter reproduces the journal paper: S. Barquero, J. Navarro-Cavallé and M. Merino, "**Reconstruction of the transient plume cross-section of a Pulsed Plasma Thruster**", Plasma Sources Science and Technology, vol. 34, no. 5, p. 055003, May 2025 [106]. Data DOI: 10.5281/ZENODO.13820945. CODE DOI: 10.5281/ZENODO.14653074.

All the identified studies on this matter refer to rectangular channel configurations running on PTFE, and typically fed by their channel breech [95, 94, 101, 93, 65, 98, 102, 103, 105], except for a non-volatile liquid-propellant PPT [104]. Plume divergence data from these works principally rely on current measurements, mostly carried out by electrostatic probes, Faraday probe (FP) [93, 65, 104] and Langmuir probes (LPs) [95, 94, 101, 98, 102, 103], with the exception of one case using a Rogowski coil instead [105]. Overall, these investigated plumes exhibit single-peaked cross-sections, with some degree of deviation from the thruster axis, and significantly wider divergence along the plane parallel to the electrodes compared to the plane perpendicular to them.

Crucially, many of those works ignore or have a limited treatment of the time-dependent aspects of the exhaust divergence. Time-resolved data [95, 65, 104, 2] are necessary to address the behavior of the distinct ion populations generated during the discharge, which may differ from time-averaged results. It is worthy to highlight the time-dependent off-axis characterizations carried out by Jakubczak et al. [65] and Antropov et al. [95]. By means of a FP Jakubczak et al. studied a 1 J/1 kV ablative PPT [65]. Their results principally revealed that the ion current density distribution dropped up to 10% of its maximum at about ±30° from the thruster axis for the cathode-anode direction, and ±45° for the direction parallel to the electrodes. The ion current distribution's divergence, defined at the point where the ion current falls below 10% of its maximum, shows two temporal peaks, with ion collection detectable at all times up to ±85°. Particularly remarkable is the work of Antropov et al. [95], who used cylindrical LPs to investigate the exhaust of a (side-fed) PPT operating between 80–100 J 2.5–2.8 kV. The study aimed to reconstruct the current-voltage curve at various times, which is challenging in pulsed plasmas due to the impossibility of performing a voltage sweep during a single firing. Although the procedure was briefly described and the curves themselves were not provided, the reported density results were proven to be valid using other diagnostic methods. Results, which exclusively referred to the plane parallel to the electrodes at one of the channel sides, exhibited a single peak in space that moved in time towards the thruster axis, on average located around 44° from the thruster axis. The magnitude dropped up to the 10% of its maximum at about 80°.

In addition, all the previous studies also rely on local probe measurements and on a single probe, which requires multiple firings to scan the full cross-section. This, combined with the need to achieve statistical significance at a single location through repetitive firing, makes the entire plume cross-section scanning process time-consuming. Increasing the number of firings will lead to higher propellant consumption and potentially greater electrode erosion, both affecting the response of the thruster throughout the entire characterization.

The present work aims to advance on the understanding of the geometry of the PPT exhaust by characterizing the transient expansion of the plume of a small rectangular PPT running on PTFE and nominally operated at 1000 V, 6 μF, 3 J. It focuses on the reconstruction of the time-resolved ion current density cross-sectional distribution. The method proposed here employs an array of fast-sampled tungsten-wire probes operating in the ion saturation regime. A straightforward algorithm, based on the variable separation method, is introduced to solve the inverse reconstruction problem. Finally, the time-evolution of the half-width at half-maximum plume divergence angle is assessed for the two cross directions. This study goes beyond the results reported in our previous work [2]. In that investigation the exhaust along the thruster axis was reconstructed by means of a plume expansion model based on Maxwellian distributions to represent the contribution of multiple (charge/mass) ion groups. These modeled ion distributions were fitted to the time-varying ion current collected on three LPs operating in the ion saturation regime.

The rest of the document is structured as follows. Section 6.2 presents the experimental setup, the PPT prototype and the novel diagnostic (plume cross section scanner). Section 6.3 describes the ion current density reconstruction algorithm. Section 6.4 collects and discusses the results. Finally, conclusions and next steps are summarized in Section 6.5.

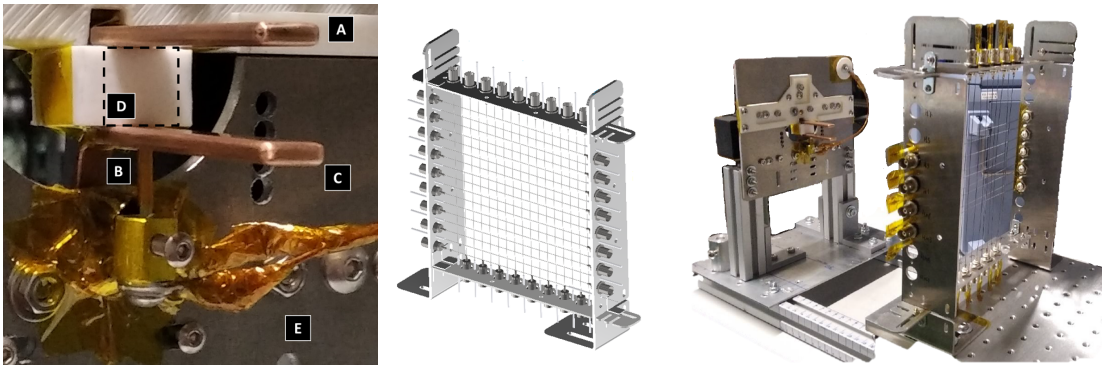

(a) (b) (c)

Figure 6.1: **(a): View of the thruster discharge channel of the PμLSA PPT prototype.** C: cathode electrode, A: anode electrode, B: spark plug, D: effective (PTFE) propellant surface, E: mounting structure. **(b): CAD view of the plume cross-section scanner positioned downstream. (c): Real view of the thruster prototype and the diagnostic system positioned downstream.** [Please note that subfigures (b,c) serves for illustrative purposes only, while the specifications relevant to the present work are described in Section 6.2.]

6.2. Experimental setup

6.2.1. PμLSA prototype

A low-power class ablative PPT breadboard model named PμLSA (PULSed Ablative PPT for micro/μ-propulsion) is used in this study. The thruster features a rectangular electrode configuration, exhibiting a 4.5 cm length, 1 cm height and 1 cm width discharge channel and uses PTFE as propellant, fed from the channel breech. PμLSA discharge channel is illustrated in Figure 6.1(a). The cathode is grounded. The overall architecture and its first ignition and some plume characteristics were reported in previous works [7, 2]. In this work, the same setup with a different capacitor model is used (Vishay MKP386M510200YT4)[22]. The thruster nominal operational point is set at 1000 V of discharge voltage and 6 μF of capacitance, resulting in a stored energy of 3 J.

The thruster is operated inside a $50\times50\times50$ cm cubic vacuum chamber, available at the EP2 laboratory at Universidad Carlos III de Madrid (UC3M). High voltage feedthroughs are used for the charging lines of the main and spark plug capacitor banks. The chamber is equipped with a mechanical vacuum pump, Edwards nXDS Scroll pump, 10 m^3/h; and a turbomolecular pump Edwards Next400, 400 L/s N_2. The ultimate pressure reached is in the 10^{-6} mbar range. At each firing, the pressure rises to values below $2\cdot10^{-5}$ mbar, and is restored to the dry ultimate pressure within a few seconds, before the next firing. [The firing frequency is set to under 0.1 Hz to accommodate the oscilloscope data-saving time requirement.]

Passive voltage probes are used to acquire any diagnostic signal with the oscilloscope. In particular, a PPE4KV 100:1/400 MHz Teledyne LeCroy high voltage passive probe is used for voltage monitoring of the main discharge capacitor bank (anode-cathode voltage). This signal is used as a trigger for the simultaneous data acquisition of all the probes using the eight-analog-channel Yokogawa DLM5058 oscilloscope. [The oscilloscope measurement vertical resolution was set at 8 bits.] The sampling frequency of interest is 100 MHz.

6.2.2. Plume cross section scanner

The new diagnostic system consists of a 22 × 22 cm aluminium frame that holds a series of independent vertical or horizontal electrostatic wire probes within the plume cross-sectional plane (xy). Figure 6.1(b) shows the frame in front of the thruster prototype. In the present work, 8 wire probes have been mounted simultaneously on the frame, distributed every 2 cm. Depending on the testing configuration, they have been aligned either vertically (direction x, perpendicular to the electrodes) or horizontally (direction y, parallel to the electrodes). The probes are naked tungsten filaments with a diameter of 0.5 mm, spanning a measurement length of 19.2 cm each. At one end, each wire-probe is soldered onto a screw-tightened BNC connector, which is secured to the aluminum frame. The BNC threaded part, and the soldered joint, are covered with ceramic paste to prevent them from collecting plasma. The other end of the wire is secured to the frame using a fitted PTFE tube, which guarantees its electrical insulation. The frame itself is electrically grounded (nevertheless, keeping it floating was seen to have no effect on the measurements). To minimize electromagnetic noise on the signals, coaxial cables and BNC feedthroughs are used.

Figure 6.2(a) defines the cross sectional plane under study, which is set at an axial distance z_{grid} = 10.8 cm from the discharge channel exit plane surface for both vertical and horizontal wires. This choice is guided by the constraints imposed by both the vacuum chamber geometry, which limits the farthest distance to the thruster, and the risk of interfering with the discharge, which limits the nearest distance, giving rise to spurious discharges as discussed below. [Note that the distance of the wires to the plasma source increases away from the center, and therefore the emitted ions are expected to arrive at different times to the different wires.]

To explore a cross-sectional domain as large as possible, the frame has been positioned at 4 regions. These 4 frame positions are distributed as in Figure 6.2(a), and named: right-bottom (RB), left-bottom (LB), right-top (RT), left-top (LT). Each of these frame positions share an overlapping stripe of 5 cm width with each of the two neighbouring frame positions. Acquiring data at this central 'cross-hair' of the study domain using probes from different frame positions allows one to check the repeatability of the measurements. In total, considering the four different positions of the frame, measurements are collected for 32 horizontal and 32 vertical probe locations. These correspond to 28 (horizontal) plus 28 (vertical) singly-sampled probe locations, and 2 (horizontal) plus 2 (vertical) doubly-sampled probe locations at the central "cross-hair".

The probes are sufficiently negatively biased with respect to ground to operate them in the ion saturation regime. Voltage is provided by a BK Precision PVS60085MR (8.5 A/600 V) power supply. A sensitivity analysis has been conducted to determine the appropriate bias voltage to apply, evaluating the effect of the applied bias on the collected current. It has been concluded that below -120 V, the collected current is essentially unaffected by the bias voltage, meaning that electrons are effectively shielded, thus not perturbing the current measurement[23]. The ion current collected by the probes is measured through 10 Ω-resistance shunt resistors[24] connected to each wire-probe and passive voltage oscilloscope probes (Yokogawa 701937 10:1/500 MHz).

[22] Battery 2B (2) in Table 2.2 of Chapter 2.

[23] As representative of the conclusions of the sensitivity analysis carried out, the current peak value at different voltage biases is presented at the end of the chapter in Figure 6.9 for the "cross hair" central probes. Two additional bias voltages, -100 and -140 V, are normalized with the -120 V case. The variations remain acceptably small (+-10%) within the +-20 V range, with deviations becoming smaller at more distant voltage values. Absolute bias voltages under 100 V are insufficient in high-density regions to reach the ion saturation regime, leading to incomplete electron shielding and excessive ΔV for the given shunt resistance, which cannot be further reduced without significantly increasing measurement error.

[24] Metallic-housed coiled resistors (RS Code:175-2428) are used for plume current measurements, while metallized carbon-film resistors (RSMOA0623DAMJ3303), purely resistive, are employed in Chapters 4 and 5. Although both resistor types yield equivalent measurements, the coiled resistors offer higher power ratings, which is advantageous during occasional probe discharges. However, their inductive component must be evaluated to ensure it does not dominate at the discharge's natural frequency. A Vector Network Analyzer (Keysight ES063A) was used for this assessment, and a correction factor of 1.15 was applied to the nominal resistance value for all data presented in this chapter.

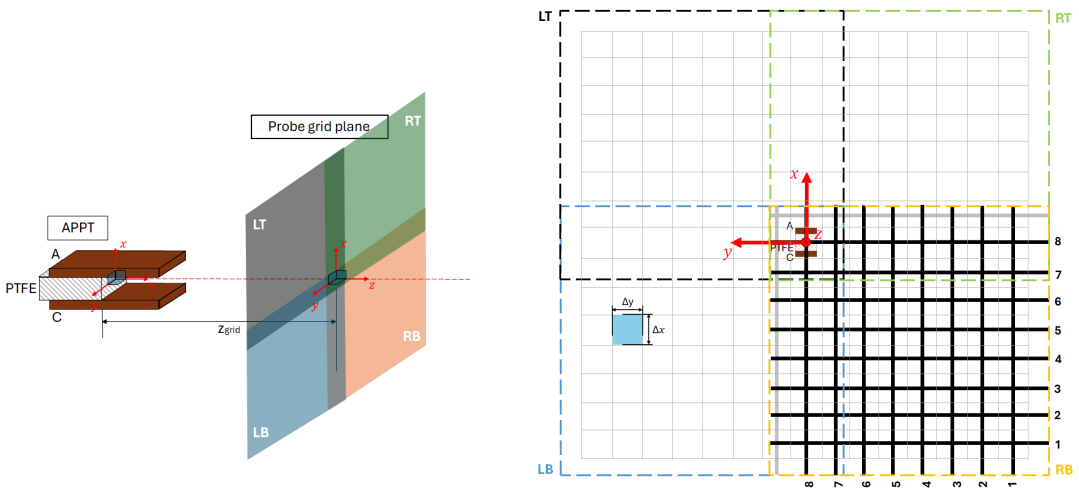

Figure 6.2: **(a): Sketch of the experimental setup.** "A" refers to the anode, and "C", to the cathode. The plume measuring plane is at z_{grid} cm from the channel exit plane. Right-bottom (RB), left-bottom (LB), right-top (RT) and left-top (LT) refer to the different frame positions. **(b): Cartesian grid used for the reconstruction of the domain of study of the plume cross section considering uniform cell size given by** Δx**,** Δy. The boundaries of the subgrids covering each of the four frame positions are defined by color dashed lines. Probe locations are shown for the RB frame position with thick black lines, while gray ones are borrowed from neighbouring frame positions to complete the data required to reconstruct its associated subgrid. Note that the z axis points towards the reader.

Two channels of the oscilloscope are reserved to monitor the power supply bias and the thruster voltage, while the others are used for sampling the current collected by up to six probes at once, during each thruster shot. Ideally, if the eight probes held by the frame could be monitored simultaneously, to measure the ion current density across the full cross-section only 4 frame repositionings for the horizontal arrangement and another 4 for the vertical arrangement would be required. Instead, 60 repositions are required if a single probe were used. Thus, the number of firings is reduced by a factor of $60/(4+4) = 7.5$.

We note that some of the firings had to be discarded due to spurious discharges or arcing to the probes, evidenced by an abnormal rise in the collected current at the probes. Spurious discharges were seen to become more frequent the closer the probes to the thruster, the higher the discharge voltage, and the lower the probe bias voltage. It is also considered that as plasma density rises, the frequency of spurious discharges can increase. The probe array distance and bias were selected to keep the occurrence of spurious discharges sufficiently low. Cases with such spurious discharges have been discarded.

At least 50 valid firings are considered to assess the repeatability, uncertainty/dispersion of the measurements. Over the experiment, no drift or secular changes have been noted in the measurements, concluding that the thruster/diagnostic do not experience any degradation. Nevertheless, minor surface changes on the wires and channel electrodes have been noted, likely due to contamination.

6.3. Cross-section reconstruction algorithm

The probe array diagnostic system allows for the reconstruction of the ion current density distribution in a planar cross section of the PPT exhaust as a function of time, $j(x, y, t)$. First, we discretize the cross section into a uniform Cartesian grid, as shown in Figure 6.2(b), with grid spacing $\Delta\ell = 2$ cm. Mind that the x axis points along the vertical direction, as indicated above. The model of $j(x, y, t)$ to be obtained is piece-wise constant over each cell of this grid, at each instant of time.

The wires for each frame position span a subgrid of the Cartesian grid; an example is presented in Figure 6.2(b), where the frame covers the RB position. Each of the N_h horizontal probes (parallel to the y axis) is located at a fixed x_i location ($i = 1, \ldots, N_h$); similarly, each of the N_v vertical probes (parallel to the x axis) is located at a fixed y_j ($j = 1, \ldots, N_v$). Each horizontal (respectively, vertical) probe falls along the centerline of a definite row (column) of N_v (N_h) grid cells, and spans a length Δy_j (Δx_i) on each of them. The total measuring length of each wire is $L_y = N_v \sum \Delta y_i$ ($L_x = N_h \sum \Delta x_j$).

In the used setup, we include two wires from neighboring frame positions, for a total of $N_h = 9$ horizontal wires and $N_v = 9$ vertical wires. The wires did not fully span the last cell near the central 'cross-hair' of the grid, covering only a length $0.75\Delta\ell$. Additionally, the wires protrude 1.7 cm beyond the outer edge of the grid. These facts are taken into account in the reconstruction algorithm by setting the corresponding Δy_j (Δx_i) accordingly. The rest of the cells are uniformly[25] distributed, so $\Delta y_j, \Delta x_i = \Delta\ell$ for them, as they are fully spanned by the probes.

To proceed, we need to estimate the ion-current collecting width of the wires. This necessarily requires introducing simplifying assumptions. In highly-supersonic plasma flows, negatively biased Langmuir probes facing the incident flow have been shown to predominantly collect the ion "ram" current, i.e. the flux of ions swept by the probe cross-sectional area perpendicular to the flow [141]. In our setup, this area is the product of the wire length L_y (L_x) and the effective collection width, w, equal to the wire diameter, 0.5 mm. This assumes the unknown sheath thickness ℓ_{sh}, which is a few times the Debye length λ_D, to be much smaller than the wire diameter. Indeed, reported densities and electron temperature in comparable PPT exhausts at similar z locations range between 1–2 eV and 1–5 $\cdot 10^{19}$ m^{-3} [98] (10^{18}–2.5 $\cdot 10^{20}$ m^{-3} [103]), which yield a Debye length of several micrometers. Therefore, the hypothesis $w \simeq 0.5$ mm $\gg \ell_{sh}$ is reasonably satisfied. For the purpose of simplicity, and in the absence of a precise density and sheath model, we shall assume that the ion-collecting width is equal to w. Note, however, that this may underestimate the collecting area, and therefere overestimate the current density.

Next, we formally write the probe collected ion currents H_i and V_j as

$$\begin{aligned} H_i(t) &= \int_{L_y} \int_{x=x_i-w/2}^{x=x_i+w/2} j(x,y,t)\ \mathrm{d}x\ \mathrm{d}y, && i = 1, \ldots, N_h; \\ V_j(t) &= \int_{L_x} \int_{y=y_j-w/2}^{y=y_j+w/2} j(x,y,t)\ \mathrm{d}y\ \mathrm{d}x, && j = 1, \ldots, N_v. \end{aligned} \tag{6.1}$$

We model the ion current density map $j(x, y, t)$ as the product of a magnitude $J(t)$ (i.e., the spatially-averaged ion current density over the subgrid of concern) and two spatially piece-wise uniform (dimensionless) functions $f(x, t)$ and $g(y, t)$, (i.e., uniform step functions),

$$j(x, y, t) = J(t) f(x, t) g(y, t). \tag{6.2}$$

The functions $J(t), f(x, t)$ and $g(y, t)$ are to be determined. Function f (g) has spatially constant values over each row, $f_i(t)$, (column, $g_j(t)$) of the subgrid spanned by the probes. Furthermore, the f (g) function satisfies the following normalization constraint at each instant of time:

$$\sum_i f_i = 1, \qquad i = 1, \ldots, N_h; \qquad\qquad \sum_j g_j = 1, \qquad j = 1, \ldots, N_v. \tag{6.3}$$

[25] While the generalized version of the algorithm is useful for experimental setups where fitting the measurement domain into a uniform cell distribution along a probe is not feasible, for alternative cases, an exact version assuming uniform cell size is presented in [9], whose CODE is also available in [14]. The exact version further straightforwards the solving process. For the developed PPT, the difference in results between both approaches has been assessed as negligible.

It is important to note that in [9], a conference proceeding, an erratum applies to some distributed versions regarding the expression for J obtained through the least squares solution. The correct formulation should yield the average of the two expressions involved.

Applying this functional decomposition to the integrals (6.1) yields the approximations

$$\tilde{H}_i(t) = J(t) f_i(t) \sum_j g_j(t) \Delta y_j w, \qquad i = 1, \ldots, N_h;$$
$$\tilde{V}_j(t) = J(t) g_j(t) \sum_i f_i(t) \Delta x_i w, \qquad j = 1, \ldots, N_v. \tag{6.4}$$

Equating

$$H_i(t) = \tilde{H}_i(t), \qquad V_j(t) = \tilde{V}_j(t), \tag{6.5}$$

and considering the normalization constraints (6.3), yields a set of $N_v + N_h + 2$ equations for the $N_v + N_h + 1$ unknowns $f_i(t)$, $g_j(t)$, and $J(t)$ at each frame position and for each instant of time. This set of equations is generally incompatible, as can be easily seen by considering the following sums, which would both determine $J(t)$:

$$\sum_i H_i = \sum_i \tilde{H}_i \equiv J(t) \Delta\bar{y} w, \qquad \sum_j V_j = \sum_j \tilde{V}_j \equiv J(t) \Delta\bar{x} w, \tag{6.6}$$

where $\Delta\bar{y} = \sum_j g_j(t) \Delta y_j$ and $\Delta\bar{x} = \sum_i f_i(t) \Delta x_i$ are very close to $\Delta\ell$ and are determined as part of the solution (incidentally, if all $\Delta x_i, \Delta y_j$ were equal to $\Delta\ell$, these $\Delta\bar{x}, \Delta\bar{y}$ would be exactly $\Delta\ell$). To resolve this incompatibility, at each instant of time, equations (6.6) are solved in a least-squares sense to find the unknowns J, f_i, g_j.

Finally, for the cells in the overlapping region of the Cartesian grid, referred to as the central "cross-hair", the mean of the multiple solutions is calculated. Each of these solutions is computed from a different frame position, and the differences among them are used to assess the uncertainty introduced by the different frame positions on the measurements.

6.4. Results

6.4.1. Electrical response of the discharge and propellant consumption

The anode discharge voltage response at the nominal point (1000 V of discharge voltage and 6 μF of capacitance) is shown in Figure 6.3 averaged over 50 firings; the shaded area represents the standard deviation estimate $\pm\sigma/2$. The signal exhibits damped oscillations with natural frequency on the order of magnitude of 100 kHz, releasing most capacitor energy within the first 5 μs, causing the amplitude to decay by a factor of 10 in that period. Good repeatability among pulses is observed, especially along the first cycle of the discharge. The current setup with the new capacitors exhibits a similar discharge time as the one used in our previous work [2], albeit with a slightly lower frequency. The estimated resistance and inductance values from fitting an RLC circuit with constant parameters to the first cycles of the discharge are around 40 mΩ and 40 nH respectively; the fit is included in Figure 6.3.

High-frequency noise of 10–20 MHz on the anode voltage signal exists around the breakdown instant, and often at the signal minima/maxima. The former corresponds to the spark plug noise and the breakdown process itself, while the latter could be related to late reignitions that may occur upon voltage inversion [23, 100, 139, 135, 48].

The mean ablated PTFE mass per firing falls within $m_{bit} = 3.9 \pm 0.2$ μg. This value was obtained after 4028 firings at the nominal operating point. No contamination was observed to accumulate on the PTFE surface after more than 10,000 firings.

6.4.2. Time-varying plume cross section characterization

Figure 6.4 displays the time response of the measured ion saturation current along the central probes, those at the overlap region or “cross-hair”. Two probe locations are horizontal H_R, H_L (at the right and left side

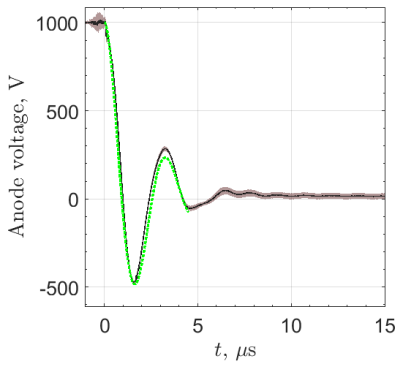

Figure 6.3: **Time signal of the anode voltage averaged over repetitive firing (solid black line).** Shaded area represents half a standard deviation with respect to the mean, $\pm\sigma/2$. The constant-parameter RLC equivalent circuit fit is plotted in red,thin line.

respectively, both at $x = 0$), and two vertical V_T, V_B (at the top and bottom respectively, both at $y = 0$). Each probe location is measured from the two neighbouring frame positions. Measurements are represented by its mean and the standard deviation σ, and a total of 50 firings are considered for each one.

Overall, plasma probes begin collecting current at around 2 μs after the initiation of the main discharge breakdown ($t = 0$) (see Figure 6.3), and the signal essentially vanishes 15–20 μs afterwards. The time interval between 0–2 μs primarily shows noise associated with the first instants after ignition. For this reason, hereafter, the study focuses solely on the 2–20 μs time-window. In addition, it can be seen that the shot-to-shot repeatability of the measured ion current signals is less than that of the anode voltage signal shown in Figure 6.3.

The agreement between line pairs in the former figure confirms that measurements remain consistent regardless of frame position, demonstrating the repeatability of results after frame repositioning. In general, along the four probe locations shown in Figure 6.4, the average time-response over the shots reveals that mainly three bumps[26]are visible between 2–20 μs. For reference, in Figure 6.4(a), plotting H_R, these peaks in time take place at $t_1 = 3.38$ μs, $t_2 = 5.34$ μs and $t_3 = 7.64$ μs respectively. These three peaks are hypothesized to correspond to distinct ion groups, likely of different charge/mass ratios, as was earlier discussed in our previous work [2], where each one of these ion constituents was characterized separately. [In that work, the mean speed of each of the main three ion groups was determined to be about 50, 32 and 18, km/s (with thermal spreads of about 18, 9 and 10 km/s respectively).] The second peak typically carries the largest current. However, in V_B in Figure 6.4(c) two exceptions to the former two statements are observed. On the one hand, while in the RB line three bumps are identifiable, in the LB line four bumps exist; the discrepancy involves the signal tail. On the other hand, the first bump reaches a higher value than the second in the two lines.

It is evident that H_R drives more current than the measurements at the other three central probe locations, followed by V_B. This already suggests that some asymmetry is present in the exhaust, whose maximum current seems to be deviated towards the RB sector. This is further confirmed below. In turn, the last exception applying to V_B described above may indicate subtle differences in the deviations experienced by the distinct ion groups.

In Figure 6.5(a),(b), the time-series measurements for some selected horizontal and vertical probes in frame position RB, H_{RBi} and V_{RBj}, are respectively presented. This frame position collects a higher current than any of the other three positions (RT, LB, LT), not shown in this paper.

[26]Another bump around 2 s appears consistently across cases. However, due to the complexities introduced by the noise region, a rigorous interpretation of this feature is challenging. For now, it is considered more conservative to attribute only the other three bumps to ion populations, as they coincide with speeds consistently reported in the literature. Nonetheless, these features warrant further investigation, particularly since exceptions at higher speeds have been reported [113, 114].

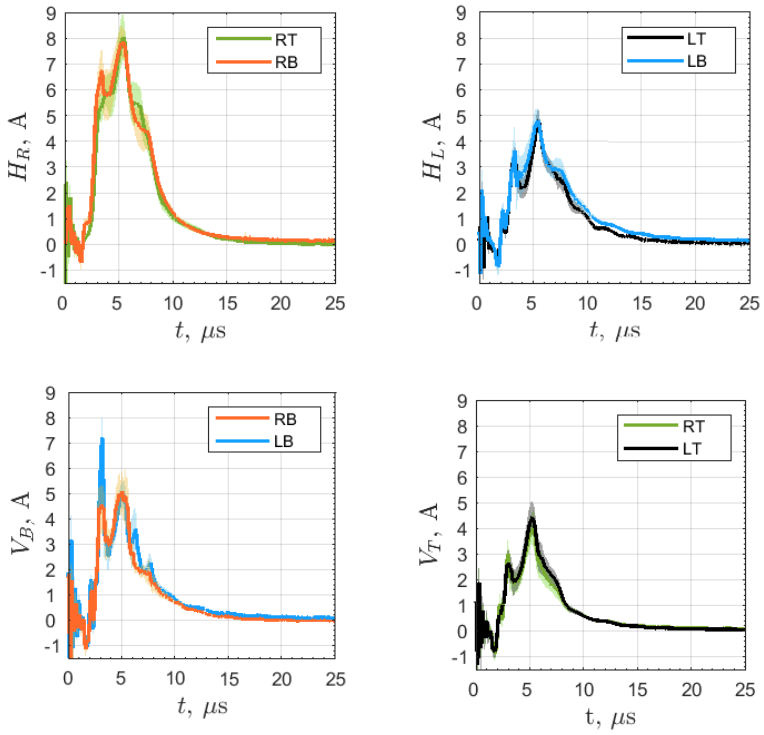

Figure 6.4: **Time-series of the mean ion saturation current measured along the central probes.** Two probe locations are horizontal H_R (a), H_L (b) (at the right and the left side of the domain respectively, both at $x = 0$), and two are vertical V_B (c), V_T (d) (at the bottom and top respectively, both at $y = 0$). Each probe location is measured twice, using probes from two neighbouring frame positions (Figure 6.2). Standard deviation σ represented with shaded area, covering $\pm\sigma/2$ with respect to the mean. A 5 MHz low-pass filter was applied to individual measurements.

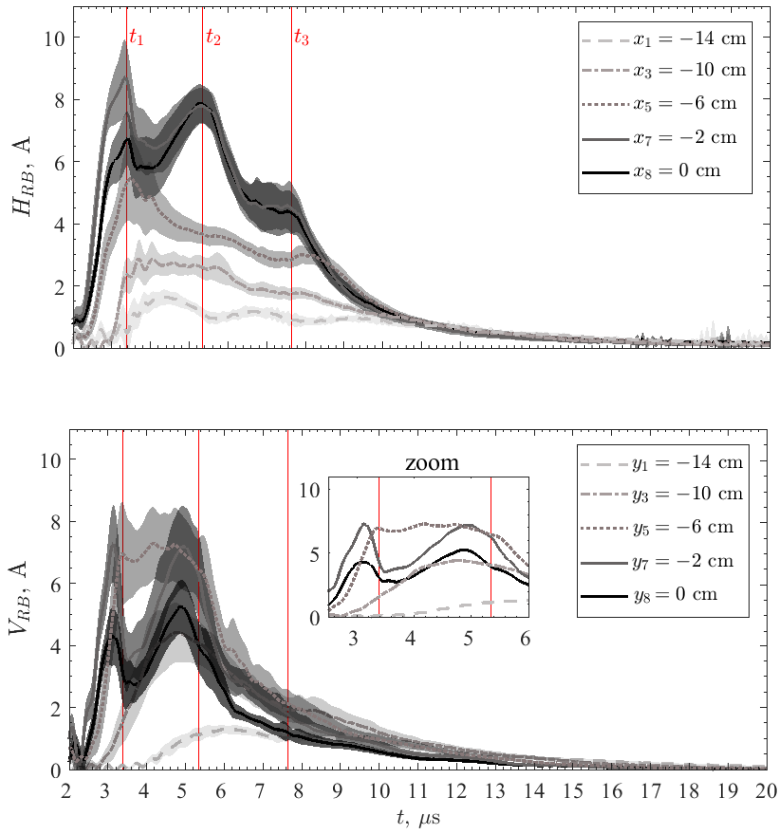

Figure 6.5: **Time-series ion saturation current collected at horizontal H_{RBi} (a) and vertical V_{RBj} probes (b) in the right-bottom RB frame position of the plume section** ($x, y < 0$ according to the setup described in Figure 6.2(b)). Mean ion current averaged over 50 firing (solid lines) and their standard deviation σ (shaded area is $\pm\sigma/2$ with respect to the mean). t_1, t_2, t_3 indicate the peak-current times along $H_{RB,x=0}$, serving as reference times for Figure 6.6.

Overall, the magnitude for horizontal measurements, H_{RBi}, is larger at $x = -2$ and 0 cm. They feature a near-identical response, except for the first maxima, which is around 8 A for $x = -2$ cm and 6 A for $x = 0$ cm. These two probes exhibit three distinct bumps, as in Figure 6.4. In contrast, probes at $x = -6, -10$ and -14 cm gather a smaller current with a flatter time response. This could indicate that on the exhaust periphery the contributions of the different ion groups become comparable and overlap in time. A small delay exists in the initial rise time of these three curves compared to those at $x = 0, -2$ cm, especially evident at $x = -10, -14$ cm due to the larger distance to the plasma source.

The measurements taken on vertical probes, V_{RBj}, show the largest currents at $y = -2$–-6 cm. Once again, two distinct behaviors are found, for the probes closer and farther away to the thruster axis. On the one hand, at probe locations $y = 0, -2$ cm, two ion groups are easily identifiable. The contribution of the third one, while less evident than in the central horizontal measurements, presumably contributes to the slow decay of the signals after $t = 6\,\mu$s. On the other hand, the probes at $y = -6, -10, -14$ cm, show a broad flat-peaked current curve, suggesting again that the contributions of the different ion groups are comparable and overlap at these locations. Similarly to the horizontal measurements, but more pronounced, current arrives at $y = -10, -14$ cm at a notable later time than at $y = 0, -2, -6$ cm. The arrival time is comparable to the time between ion groups at those distant locations. Overall, for all the four frame positions and probe orientations (H, V), the profile of the collected ion current at large $|x|, |y|$, presents the same features discussed here.

Figures 6.6(a),(b),(c) present the reconstructed 2D current density distribution $j(x, y, t)$ in the Cartesian

grid of the plume cross section, respectively at the three different times of interest $t_1 = 3.38$ μs, $t_2 = 5.34$ μs and $t_3 = 7.64$ defined above. These times are defined by the different bumps in time of the current measurement at the horizontal probe $H_{RB,x=0}$, plotted in Figure 6.5(a). Together with the $j(x, y, t)$ map, its row-wise and column-wise integral profiles are depicted. In addition, the value of the instantaneous total current collected in the full domain $I_{tot}(t)$ is given. Note that the displayed grid domain is trimmed in the plots to [−15, 15] cm in both directions, while the outer rows and columns actually extend to [−16.7, 16.7] cm, as described in Section 6.2.

At t_1, in panel (a), $j(x, y, t)$ decreases with $|x|$, with a stronger decaying rate for $+x$ than for $-x$. In contrast, the behavior of $j(x, y, t)$ with y exhibits a higher dispersion and reveals two bumps in space at $+y$ and $-y$ respectively, with the one at $-y$ driving more current. As the plasma expands over time, these bumps separate and gradually flatten, leading to a more uniform distribution across the cross-section, as shown at t_3 in panel (c). Because the double-peak is especially noticeable during the first instants of the discharge, this feature is mostly related to the first and second ion groups.

Taking the analogy of the "center-of-mass" in a non-uniform mass density body, the time evolution of the "center-of-mass" of the $j(x, y, t)$ distribution, $(c_{j_x}, c_{j_y}) = \sum_{i,j}(x_i, y_j) j_{i,j} \,/\, \sum_{i,j} j_{i,j}$, reveals certain displacement of the plume towards the RB sector. At t_1 (panel (a)), the center of the distribution is located at $(-1.9, -1.1)$ cm, slightly moving over time towards the center of the reference system (panel (b)), with this shift being particularly noticeable at t_3 (panel (c)), with $(-0.7, -0.9)$.

Integrating $j(x, y, t)$ over the full domain at each time instant provides the total current traversing the Cartesian grid, $I_{tot}(t)$, plotted in 6.7. [Mind that $I_{tot}(t)$ does not include the ion current not captured by the Cartesian grid.] $I_{tot}(t)$ peaks at about 3.3 kA at $t = 5$–6 μs. Note that in the individual probes, Figures 6.4 and 6.5, three bumps are identifiable; however, for $I_{tot}(t)$, the contributions of the three ion populations cannot be distinguished, although it peaks at a similar time to that associated with the second ion population. According to our previous work [2], this is likely related to a population of ions with an average velocity of 32 km/s, thermal spread around 10 km/s, and generated at the primary ignition. There, that value was characterized by isolating the different ion populations contributing to the current collected by axial probes. Here, we note that $I_{tot}(t)$ represents a quantity integrated over the planar cross section, where the contributions of distinct ion groups appear broadened and mixed. This is in part due to the differing distances between the points in the cross section and the thruster, which results in different travel times for ions of a given group. The former makes it difficult to separate the various ion populations in $I_{tot}(t)$, which is better accomplished by inspecting $j(x, y, t)$.

The surface charge density distribution, $\rho(x, y) = \int j(x, y, t)\ \mathrm{d}t$, computed in the time-window 2–20 μs, is presented in Figure 6.6(d), together with its row- and column-wise integral profiles, and its integral along the full grid domain to compute the total charge collected over the setup, Q_{tot}. The $\rho(x, y)$ distribution is driven mainly by the first instants of the discharge, when the current density is larger, and confirms the previous conclusions about asymmetries. That is, ions distribute differently along x (i.e. the direction of the applied electric field across the electrodes), and along y (i.e., the direction of the self-induced magnetic field). Along x, they show a single peak, while two peaks are exhibited along y, one at each side of the centerline, with the $-y$ one weighing more. The "center-of-mass" of the charge distribution is on the RB sector, at $(c_{\rho_x}, c_{\rho_y}) = (-1.3, -0.7)$ cm; the maximum of the distribution, around $660{\cdot}10^{-3}$ Cm^{-2}, locates at $(-2, -6)$ cm.

The reconstructed total collected charge in the time-window (2–20 μs), Q_{tot}, is about $20.3 \pm 2.8 \cdot 10^{-3}$ C. The error is estimated as the time-integrated $\sigma/2$ within the same time-window, in which σ is the standard deviation. [Mind that the estimates of total current and charge are based on the listed assumptions in Section 6.3, such as negligible sheath effects, ion-ram current collection, and omission of potential additional ion populations within the plume. These may lead to overestimation of the results.]

The study domain covers a half-angle defined from the discharge channel exit plane of about 57° in the x and y directions. Therefore, our cross-section unavoidably misses some of the current emitted by

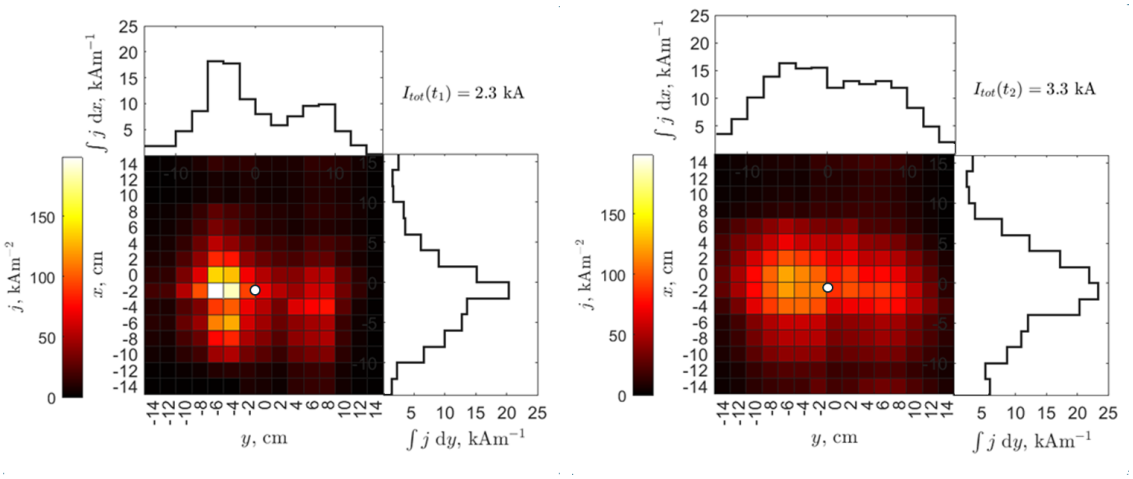

(a) j map at $t_1 = 3.38\ \mu$s. $(c_{j_x}, c_{j_y}) = (-1.9, -1.1)$ cm.

(b) j map at $t_2 = 5.34\ \mu$s. $(c_{j_x}, c_{j_y}) = (-1.7, -0.8)$ cm.

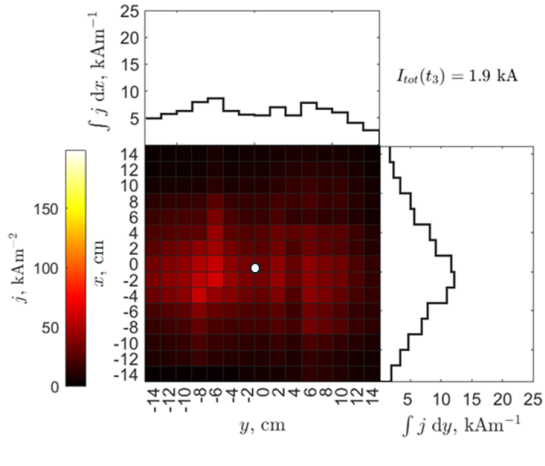

(c) j map at $t_3 = 7.69\ \mu$s. $(c_{j_x}, c_{j_y}) = (-0.7, -0.9)$ cm.

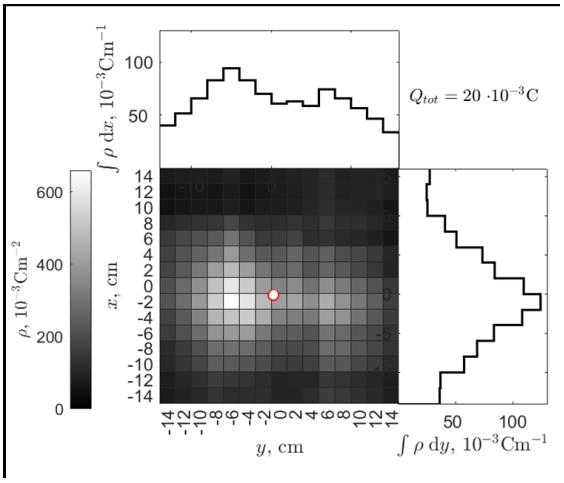

(d) ρ map with $(c_{\rho_x}, c_{\rho_y}) = (-1.3, -0.7)$ cm.

Figure 6.6: **Reconstructed current density $j(x, y, t)$ (a,b,c) and surface charge density $\rho(x, y)$ (d) distribution maps and their row- and column-wise integral profiles**. The $j(x, y, t)$ map is plotted at the three times of interest t_1, t_2, t_3; these times correspond to those identified in Figure 6.5. The white dots locate at the respective "center-of-mass" of each distribution. The integral of the distributions $j(x, y, t)$ and $\rho(x, y)$ over the study domain, $I_{tot}(t)$ and Q_{tot}, are also reported alongside the plots. The integration time-window considered ranges between [2 20] μs.

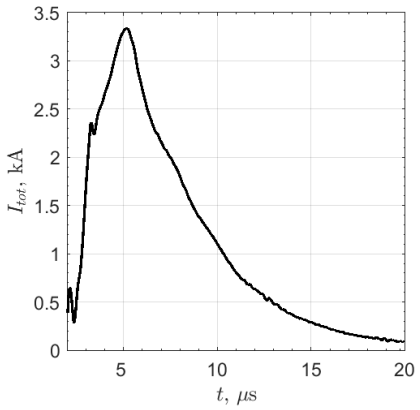

Figure 6.7: **Reconstructed total current collected by the Cartesian grid, $I_{tot}(t)$, along the effective ion collection time-window**.

the PPT. Nevertheless, effective instantaneous and average divergence angles can be estimated using the half-width at half-maximum (HWHM) approach along x and y directions. Figure 6.8(a) plots the HWHM angles, the instantaneous $\theta_{j,x}$ and $\theta_{j,y}$, respectively defined as the angle at which the local value of the projected profile of $j(x, y, t)$ onto the x-axis or y-axis reaches half of its maximum at a given time, and $\theta_{\rho,x}$ and $\theta_{\rho,y}$, analogously computed from $\rho(x, y)$. Both $\theta_{j,x}$ and $\theta_{j,y}$ overall increase over time until they reach the setup-limitation of 57°. The increase rate of $\theta_{j,y}$ is faster, thus, reaching the limit angle before $\theta_{j,x}$. Concerning $\theta_{\rho,x}$ and $\theta_{\rho,y}$, the former exhibits a value around 45 °, while $\theta_{\rho,y}$ lies at the limit angle. Figure 6.8(b) helps visualize how charge accumulates with x (y), presenting the curves that result from integrating $\rho(x, y)$ between a $[-x\ +x]$ stripe ($[-y\ +y]$), Q_{stripe_x} (Q_{stripe_y}). These results corroborate once more that the charge is more concentrated along the x direction.

We now compare our findings on the asymmetries observed in the distribution maps with those reported in the literature. First, plasma spreads more along the plane parallel to the electrodes than to the perpendicular one. This has also been reported for other rectangular PPTs [94, 65], potentially suggesting this as a characteristic of such configurations. This x-y asymmetry can be attributed to the plasma being unobstructed along the parallel direction to the electrodes (y) whereas in the x direction, the presence of the electrodes constrains and limits the plasma expansion. Furthermore, we agree with the suggestion by Zhang et al. [105], for which the self-induced magnetic field (y) would not restrict the plasma expansion along its parallel direction, whereas it can hinder somewhat the expansion in the perpendicular one (x).

Second,the present results also show that the peak of $j(x, y, t)$, and that of $\rho(x, y)$, deviate towards the $-y$ channel side and $-x$ (cathode). Concerning the plume skewing within the plane parallel to the electrodes (y), this has been consistently observed in other rectangular PPTs as well [93, 104, 105]. Nevertheless, we agree that this could be driven by minor manufacturing/alignment defects of the experimental setup. In addition, reported literature results often indicate plasma canting towards the cathode ($-x$) [93, 65, 54, 103, 105].

Lastly, we return to the single-peaked profile found along the cathode-to-anode direction (x) and the asymmetric double-peaked profile that characterizes the distribution along y. The literature primarily reports single-peaked profiles in both the x and y directions [65, 104, 95, 93], nonetheless, in some of the reviewed studies broadened and doubly-peaked profiles are also found along y [94] and x [103]. Thus we believe that this is a setup-dependent result that cannot be generalized, even for similar configurations.

6.5. Conclusion

The present work has assessed the transient expansion of the exhaust of a small rectangular ablative PPT, operated at 1000 V and 6 μF (3 J) and running on PTFE, through the reconstruction of its time-resolved

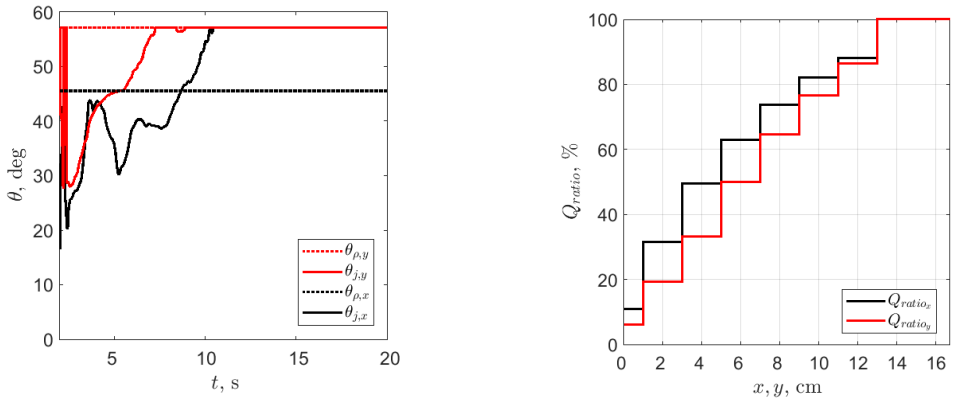

Figure 6.8: **(a) Time evolution of the half-width at half-maximum divergence angles computed from the current density (æ(x, y, t)) and surface charge density ($\rho(x, y)$) distributions, θ_j (continuous line) and θ_ρ (dot line), for the x and y directions. (b) $Q_{ratio} = Q_{stripe}/Q_{tot}$ ratio: time-integrated charge collected within a grid stripe between $[-x\ +x]$ ($[-y\ +y]$) over the total charge collected by the study domain.** The integration time-window considered for the charge distribution ranges between [2 20] μs.

ion current density on a cross-sectional plane. A novel[27] diagnostic method was used, employing an array of electrostatic wire probes working in the ion saturation regime. These probes measure the line integrals of the ion current density distribution on the PPT plume cross section. A variable-separation algorithm has been proposed to solve the inverse reconstruction problem across the study domain.

The reconstruction of the 2D maps have allowed us to discuss the time evolution of the lateral expansion of the plume. Our findings agree with different discharge features reported for comparable PPTs, such as the existence of multiple ion populations in the exhaust and the existence of spatial asymmetries within the plume cross-section. The current results offer a more complete understanding of the PPT exhaust geometry, and can aid in modeling validation. Additionally, they also complement the findings reported in our previous experimental work characterizing the axial plume expansion by separating the different ion constituents [2].

On the one hand, time-wise, three bumps can be generally observed in the ion current probe signal, consistent with the prior identification of different ion groups [2]. The second group arriving at the probes drives the major part of the plume current, peaking at about 5–6 μs after the breakdown. On individual wire probes, these ion groups are only easily identifiable close to the thruster axis. For probes near the periphery, typically farther than 8 cm from the centerline, the contributions of the three ion groups become comparable and overlap in time. This is partially explained by the variation of the time of arrival of each ion group along the length of the probe, which in general can be comparable to the time between ion groups at those far probe locations.

On the other hand, the reconstruction of the distribution maps have allowed the identification of asymmetries in the ion beam. These results principally reveal that the PPT plume spreads less along the cathode-to-anode direction (i.e., aligned with the applied electric field); this feature seems to be characteristic of

[27]Extended discussion about the novelty: Outside the field of PPT research, a computed tomography applied to an electrospray plume cross-section has been reported [164] in parallel to the present work. In that case, a radial sweep with an individual wire probe has been performed to collect data, followed by the application of the well-known Filtered Back Projection (FBP) algorithm to resolve the inverse of the Radon Transform (operation that maps a 2D function to its projections along various angles) [165].A comprehensive radial scan is required to achieve accurate results, but it demands probe translation systems and increases testing time, as discussed among the drawbacks of using individual probes in Section 1.1.1 of Chapter 1. Concerning the algorithm, the *WAVES* proposal is novel and stands out by simplifying the resolution of the inverse problem through a systematic division of the study domain into a Cartesian grid. This approach enables the implementation of a straightforward variable separation algorithm. Additionally, the present method is less affected by non-uniform data sampling, as each point has the chance of being covered by two distinct probes, one horizontal and one vertical, unlike the radial sweep approach. In addition, a miniaturized beam profiler has also been and reported in commercial [166], with the base technology exploited under a Centre national de la recherche scientifique (CNRS) licence. Differently to *WAVES*, it bases on secondary electron emission and does not provides the reconstruction of the 2D map.

rectangular PPT configurations [94, 65, 104]. This is consistent with the potential influence of the asymmetric distribution of the self-induced magnetic field in shaping the plume. Second, as also reported in the literature of comparable PPTs [93, 65, 104, 103, 167, 54, 105], the current density and charge peak deviate towards a channel side and towards the cathode. Lastly, a single-peaked profile along the cathode-to-anode axis at all times is seen, whilst a double-peaked profile characterizes the distribution along the parallel direction to the electrodes. The current density distribution becomes more uniform at later times as the distribution flattens. The ion current density outside of our measurement grid is unknown. Nevertheless, by defining the divergence angles based in the usual half-width at half-maximum approach, we conclude that the plume divergence is smaller in the cathode-anode direction.

The proposed diagnostic tool offers a simple, cost-effective approach to perform a 2D, time-resolved scan of a transient plume cross-section to reconstruct the corresponding current density distribution. Compared to state-of-the-art methods [65, 95], relying on movable probes, this approach significantly reduces the number of tests and firings required, streamlining the experimental study of lateral expansion in transient exhausts. Nevertheless, the applied method can be refined in several ways. First, a larger cross sectional area of the plume can be covered, e.g., by either increasing the number of frame positions or developing a larger frame (currently constrained by the dimensions of the vacuum chamber access point). Second, an alternative arrangement of frame positions that includes one centered with the thruster axis could be advantageous. Third, other models (e.g. piece-wise linear) are viable extensions for the reconstruction method, and may be explored in the future. Finally, this work could be combined with the proposed plume expansion model in our previous work [2] to perform a 3D plume reconstruction and characterize the different ion constituents.

Acknowledgments

This work was initiated with the support of the ESPEOS project, funded by the Agencia Estatal de Investigación (Spanish National Research Agency) under Grant number PID2019-108034RB-I00/AEI/10.13039/501100011033. Additional support was provided by the ADAPT project, which fully supports this work at the time of publication, co-funded by the Agencia Estatal de Investigación (Spanish National Research Agency) and the European Union under Grant number PID2023-150052OB-I00.

We would also like to thank the referees of this paper, whose suggestions during the peer-review process helped to substantially improve its quality.

Data availability statement

Any data that support the findings of this study are included within the article. These data are also openly available at the following URL/DOI: 10.5281/zenodo.13820945. This DOI additionally includes a video showing the plume cross-section current density distribution changing over time. Furthermore, the implementation of the proposed algorithm is available as open-source code that can be accessed at https://github.com/scherezade/WAVES/tree/v1.0 and is registered under DOI 10.5281/zenodo.14653074.

Complementary material corresponding to footnote 21:

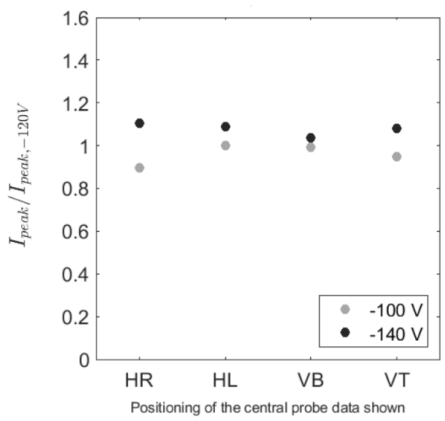

Figure 6.9: **Current peak values for the "cross-hair" central probe measurements at** -100 **V and** -140 **V, normalized to the** -120 **V case.** HR(HL): horizontal probe-right(left) side; VB(VT): Vertical probe-bottom(top) side. [The current peak coincides with that of the ion group 2.]

7. CONCLUSIONS

This final Chapter collects the main conclusions that can be extracted from the research done on Pulsed Plasma Thrusters (PPT) within this PhD thesis. In addition, future research line perspectives are discussed at the end of the chapter in Section 7.1.

The investigation done contributes to the field of experimental plasma diagnostic methodologies for flowing transient plasmas, as exemplified on a PPT plume. Accordingly, the work has been structured around two main objectives. While the second objective represents the core contribution of this thesis, namely, the description and implementation of two novel experimental plasma diagnostic techniques for transient plume reconstruction, the first focuses on the development of the thruster prototype, which is essential for the application of those techniques.

To this end, first, the design, development, and base discharge characterization of a low-power-class PPT module with potential as a technology demonstrator for onboard micropropulsion is presented. The breadboard model has been named PμLSA (PULsed Ablative plasma thruster for micropropulsion) and constitutes the first PPT developed and tested in Spain as well as the first Spanish plasma-based micropropulsion proposal.

Thereafter, the proposal of the two experimental diagnostic tools have been created for time-varying exhaust reconstruction is addressed. Both techniques are low-complexity and cost-effective, and are respectively named TIME-SERIES ToF (Time-of-Flight) [2] and WAVES (Wire Array for Variable Exhaust Scanning) [106]. They are based on single-electrode electrostatic probes working in the ion saturation regime. The former, TIME-SERIES ToF, focuses on reconstructing plume expansion based on local axial measurements. It enables the isolation of different ion contributions by considering the full time-series probe data and proposing a model for the plume expansion. This offers deeper insights than traditional ToF methodologies, solely based on feature probe correlation. This technique is applicable applicable to the exhaust of any unsteady electric propulsion (EP) system. The latter, WAVES, accurately reconstructs the plume cross-sectional current density distribution by providing off-axis data at each instant, with a faster approach than existing alternatives (at least by a factor of 7.5). This tool is applicable to both transient plumes and steady-state electric propulsion systems. Its particularity lies in performing the reconstruction from integral line measurements, using an inverse problem-solving algorithm, which significantly reduces testing time with respect to comparable studies. The two experimental methods are valuable as standalone diagnostic tools, and their utility is further enhanced when their results are combined, offering a more comprehensive understanding of the transient plume dynamics in unsteady electric propulsion systems across both time and space.

After a plume campaign using traditional ToF analysis, which relies solely on feature correlation between probes, the two new techniques were implemented to study the exhaust of the developed PPT breadboard model to further characterize it.

The developed PμLSA PPT breadboard model has been designed as a versatile platform to ease experimental research. It nominally features a rectangular configuration, with a 4.5 cm length x 1 cm height x 1 cm width discharge channel and is fed by each breech. It nominally operates at 1000 V of discharge voltage and 6 μF of capacitance (and, thus, 3 J of discharge energy), and uses Polytetrafluoroethylene (PTFE or TEFLON™, $(C_2F_4)_n$) as the propellant. A custom metal-insulator-metal spark plug triggers the discharge at around 1.5 kV. The research PPT platform supports operational point adjustments and channel geometric modifications, alongside adaptable power and triggering electronics.

The prototype has been validated for reliable ignition and examined across a defined operational envelope. While the characterization has encompassed both operational and geometric parameter spaces, particular emphasis has been placed on the former. Accordingly, electrical and plume characterization has

been conducted as a function of the initial discharge voltage and bank capacitance, with values up to 2500 V and 9 μF, respectively. Provided results involve statistical significance by performing repetitive firing compared among them. Reliable ignition has been validated at discharge initial voltages equal to or greater than 750 V for a 1 cm-height channel. The main-firing discharge signal shows damped oscillations of hundreds of kHz with signal amplitude decaying by a factor of 10 after about 5 μs, and high repeatability. At nominal conditions the current waveform peaks at 10 kA and each firing consumes about 4 μg, exhibiting negligible charring on the propellant surface. Increased discharge voltage boosts waveform amplitude, while higher capacitance essentially lowers the natural frequency. Enhancing the electric field, by increasing the discharge voltage or reducing channel height, increases propellant consumption uniformity and reduces the accumulation of discharge byproducs and charring along its surface. In-channel plasma imaging reveals non-uniform profiles, with hot spots distributed along them. Electrode surface observations show contamination near electrode edges with increasing height, with electrode erosion only visually perceptible around the spark plug. Enhancing the energy area ratio improves propellant consumption uniformity, decreasing charring. Finally, ablation is seen to increase with the discharge voltage.

Concerning the plume study carried out, note that the relevance of identifying and characterizing the existence of different ion groups is twofold. On the one hand, it can be considered as a first step toward a clearer understanding of the discharge physics in PPTs, to be complemented by other diagnostics and models. And on the other hand, because of the negative impact that having multiple species and velocity spread has on propulsive performances. In the literature, current measurements using single Langmuir probes are reported to provide, at best, only average ion velocity [94, 98], with more comprehensive plasma characterization requiring more complex setups [97, 95, 102, 111, 65]. In addition, characterizing the plume lateral expansion is of special relevance for thruster integration in the spacecraft platform, because the impingement of energetic particles onto delicate surfaces, as instruments or solar panels, is always a concern. However, historically, PPT data focused on characterizing the PPT plume divergence are relatively scarce [95, 94, 93, 102, 65, 103, 105] and dependent on local measurements taken by individual probes, which requires translation and multiple firings to scan the cross-section. In this way, scanning the entire plume cross-section can be a time-consuming process, requiring a large number of firings. When using individual probes, implementing a controlled translation stage can ensure systematic coverage, though it adds complexity to the setup.

The motivation behind the followed workflow is outlined before compiling the corresponding findings about the PPT exhaust. First, a typical Time-of-Flight (ToF) analysis applied to ion current measurements recorded by axially distributed single-electrode electrostatic probes was carried out [7]. This approach is based on peak-current correlation between probes, and is traditionally employed to estimate average ion speed [94, 98, 35] but is here extended to provide a first approximation of the plume expansion rate [7]. Nonetheless, while useful for initial estimates, this methodology has limitations, as peak features may result from combining contributions from multiple ion populations with distinct properties. These ions groups potentially originate at different times, with distinct charge/mass ratios, velocities, densities, thermal spreads and divergence rates. Additionally, accurate plume expansion rate characterization must account for downstream reductions in ion current density due not only to plume divergence but also to thermal spread.

To address the former drawback, it has been proposed a novel method for time-varying reconstructing the ion populations contributing to the exhaust by establishing a model of their expansion based on the superposition of multiple Maxwellian-like distributions, and thus considering the complete time series probe data. The presented technique, named TIME-SERIES ToF, relies on the data of three single Langmuir probes downstream axially distributed and working in the ion saturation regime. Thus, this method enables a greater exploitation of the ion current curves than by applying traditional ToF, providing an estimate of the axial velocity distribution of each one of the ion groups involved (which bases on different parameters, such as a characteristic velocity and thermal spread of each one of these ion groups, as well as their time of creation, magnitude and divergence rate).

Then, the PμLSA transient plume has been reconstructed through the implementation of the proposed

TIME-SERIES ToF method. The fitted results reveal that the reinterpreted ToF approach enables the identification and isolation of the different ion constituents in the PPT exhaust across the entire operational parametric space of study, consistent to reported data of comparable PPTs [97, 95, 102, 111, 65]. However, less clear trends were obtained for the thermal spread and the divergence, likely due to the model parameters being not well-conditioned in certain scenarios, leading to greater uncertainty in parameters such as divergence. In addition, while a sheath model is not yet available, which would take into account the variable plasma density and the effect of the wakes of upstream probes, the main source of uncertainty in the results is expected to come from the relative effective collection areas assigned to the probes. Attributing the same area to all probes is expected to overestimate ion current density downstream and therefore to underestimate exhaust divergence rate. In the absence of a sheath model accounting for variable plasma density and the effects of the wakes of upstream probes, placing supplementary on-axis and off-axis probes to provide additional probe data could improve upon the present results, by improving fit conditioning, particularly for the plume divergence parameter.

Hence, a second novel diagnostic system named WAVES is proposed to, on the one hand, address the limitations of the TIME-SERIES ToF method in accurately describing plume divergence in specific scenarios solely relying on axial measurements. On the other hand, the proposed method streamlines the acquisition of off-axis data compared to the current State of the Art, primarily by saving testing time. The new technique resolves the cross-sectional expansion of steady or transient plumes. It consists of a grid of electrostatic wire probes working in the ion saturation regime. These probes measure the time-evolution of the line integrals of the cross-section distribution of the ion current density of a plasma exhaust, and a variable-separation algorithm is used to solve the inverse problem at each time-step. Two versions of this algorithm are proposed: an exact approach [9], and a generalized version that accommodates non-uniform domain cell sizes [106].

The WAVES technique has been applied to experimentally characterize the exhaust of the PPT breadboard model. The reconstructed current density distribution faithfully reproduces the measured ion saturation current time-series data, capturing key PPT features such as the presence of multiple ion populations in the exhaust and spatial asymmetries within the plume cross-section. [94, 65, 104]. These findings have contributed to a better understanding of the discharge behavior.

"Beyond their diagnostic utility, the data obtained from applying the new techniques to the exhaust of the developed PPT also offer valuable insights. They enable deeper analysis of ion population characteristics and allow for time-resolved assessment of plume divergence, making it possible to identify spatial asymmetries. The principal findings regarding the PPT exhaust, derived from the implementation of the three plume diagnostic techniques described above, are as follows:

1. Three ion groups are overall suffice to explain each one of the explored operational cases. Each ion group probably describes a different ion species, with different charge/mass ratio, or ions generated at different instants of the discharge process. The mean ion group velocities respectively are in the range 50–70, 30–45 and 10–25 km/s for each one of the three ion groups, consistent to other reported works [97, 98, 61, 96, 99, 95, 100, 94].

2. Local axial measurements reveal that the ion charge in the exhaust is mainly carried by the first two ion groups. The cross-sectional analysis allows to identify that is the second ion group arriving at the probes which drives the major part of the collected plume current.

3. Concerning the nature of the different ion groups and their possible origin, two statements have been revealed based on the obtained figures for the TIME-SERIES ToF model parameters. First, that the first two ion groups correspond to different charge/mass states, and second, that the third of them likely corresponds to a second breakdown taking place in the discharge when the voltage in the capacitors reverses.

   Although potential species for the ion populations characterized in Chapter 5 have been inferred, accurately identifying which ion species correspond to each population remains challenging without

supplementary diagnostic methods. This complexity arises from the fact that the mass ratio between carbon and fluorine is closer to the charge-to-mass ratio between the first two ion groups. Additionally, the literature reveals cases where different species exhibit similar velocities or, conversely, the same species display distinct velocities [95, 61].

4. Ion velocities remain largely unaffected across the explored operational parametric space, agreeing well with [91, 92]. Whilst, results indicate that the relative contributions of the second and third ion groups increase compared to the first as the initial discharge voltage rises, with this effect being even more pronounced with higher capacitance. Notably, the literature [61] reports that while increasing the initial voltage enhances the overall emission intensity, it does so without altering the plasma composition significantly.

5. Time-integrated probe current from axial measurements is found to exhibit a linear trend with discharge energy. Combined with the observation that ion velocities for each population remain relatively constant across study operational cases, these findings support the linearity of the impulse bit with discharge energy, in agreement with existing direct measurements [96, 142, 143].

6. The cross-sectional current data have allowed to assess the instantaneous lateral expansion of the ion jet and its evolution in time, identifying the existence of asymmetries and distinct distributions along the two cross directions:

   (a) The PPT plume spreads less along the cathode-to-anode direction (i.e., aligned with the applied electric field), which seems to be characteristic of rectangular PPT configurations [94, 65, 104], which is consistent with the potential influence of the asymmetric distribution of the self-induced magnetic field in shaping the plume.

   The ion current density outside of our measurement WAVES grid is unknown. Nevertheless, by defining the divergence angles based in the usual half-width at half-maximum approach, we conclude that the plume divergence is smaller in the cathode-anode direction.

   (b) The current density map is slightly concentrated towards a channel side along the plane parallel to the magnetic field, which might be due to minor manufacturing defects, and towards the cathode. Consistent deviation of the ion beam with respect to the thruster axis is also reported in the literature of comparable PPTs [93, 104, 93, 65, 103, 167, 105, 54].

   (c) Third, a single-peaked profile along the cathode-to-anode axis at all times is seen, whilst a two-peak profile characterizes the distribution along the parallel direction to the self-induced magnetic field. While this observation has not been explicitly reported thus far, as far as we know, it may be consistent with data published in several works [103, 94, 105], warranting further investigation.

Finally, establishing a foundation for future research, a plasma-physics based fluid model for in-channel plasma ionization and acceleration in planar pulsed plasma thrusters (PPTs) has been developed alongside the experimental work of this thesis. The unsteady PPT flow dynamics are simplified by decomposing it into the two predominant flow directions, along the thruster channel and the discharge current axes, resulting in a paraxial model, where the definition of the cross discharge current remains independent. In this document, the building blocks for the numerical implementation of the model have been presented by outlining the assumptions and deriving the governing equations for the different species, listing the boundary and initial conditions, proposing the Method of the characteristics to solve the system and finally providing a potential algorithm.

7.1. Future areas of research

Although many aspects could be studied, such as the formation of the discharge plasma, the proposed next steps are related to immediate actions derived from the work addressed throughout the thesis. Hence, the

proposed future research can be compiled into four work lines. Out of the four, the first three are directly connected to the work detailed in this document: the first two respectively align with the two primary objectives of this thesis, while the third extends the proposed plasma-physics-based numerical research.

Experimental plume data from the implementation of the WAVES probe array, including ion saturation current and floating measurements, have been collected under various operational discharge conditions and at different axial locations. These data are available for further analysis to support the development of some of the next steps discussed below.

1. In one respect, the PPT prototype subsystems allow for further engineering efforts to: (a) be scaled down to CubeSat size, and (b) flight qualify it. Finally, (c) defining a plan for in-orbit verification for the technology demonstrator would be required.

2. From another standpoint, concerning the science approach of this thesis, the presented diagnostic techniques for time, 3D-reconstruction of transient plasma exhausts can be further improved in several ways.

   (a) Some parameters of the expansion model proposed as part of the TIME-SERIES ToF experimental method, such as the divergence, suffer from the limitation on its conditioning in some scenarios; this has been thorough discussed in Section 5.4.3. To improve it, e.g., a more comprehensive definition of the model can be addressed. For example, extending it to the cross axes, for which the incorporation of additional on- and off-axis measurements would be necessary to prevent overfitting. In addition, exploring different types of ion velocity distributions could be of interest for certain devices [106, 65, 104].

   In addition, the application of other diagnostics means, such as a gridded energy analyzer [113], a retarded potential analyzer [162] or optical emission spectroscopy [61], could help disambiguate the charge/mass ratio of each ion group provided by the model, complementing the present technique.

   (b) In the case of the WAVES experimental technique, on the one hand, other models are viable extensions for the reconstruction and may be explored in the future. E.g., through piece-wise linear extrapolation of the node values to the cells.

   Additionally, repeating the measurements using an alternative probe type, such as a Faraday Cup, could be beneficial to reduce uncertainty in the absolute magnitude of the collected current.

   On the other hand, regarding to the specific case of its application on PμLSA, it has been noticed that covering a larger plume cross-sectional area with the scanner grid would benefit the determination of the divergence angle, especially for the plasma distribution parallel to the magnetic field where spreading is more pronounced. Furthermore, the double-peaked plasma distribution along this axis, which has been only minimally reported in the literature [105, 94, 103], warrants further investigation for clear elucidation.

   (c) Last, improvement in the accuracy of both reconstruction methods at times and probe locations with low plasma density could be achieved through advanced sheath modeling, allowing for a more precise definition of a probe's effective collection width. These models would account for variable plasma density and, for applicability to axial ToF setups, also incorporate the influence of upstream probe wakes. Such advancements would require time- and space-resolved electron density data in the PPT exhaust, which is currently unavailable.

3. The foundation proposed for numerically exploring the in-channel ionization and acceleration stages of the PPT through a paraxial model can now be implemented.

   Additionally, extending the present model to a more realistic framework is also considered a potential direction for future work. For example, this could involve extending the model to two dimensions or exploring more sophisticated approaches in terms of species involved beyond the current three-fluid simplification.

A fully 2D framework could be pursued by incorporating a plasma-based cathode-to-anode current density model, i.e., modeling electron emission and the electrode sheaths to resolve the plasma potential drop across them.

4. Finally, a fourth future line can involve the development of the thrust balance design proposed in [21]. This work has been supervised under the frame of the present PhD research as described in the Published and submitted content chapter, in page viii.

A. OVERVIEW OF ABLATIVE PPT PROTOTYPES

A.1. Context

A planar ablative PPT [29, 31, 44, 45, 52, 62, 168] was the first EP system in orbit. Since then, various PPT prototypes, predominantly ablative, planar and using PTFE, considered the standard for its simplicity, have been flight-qualified [29, 169, 30, 170, 32, 170, 64]. Some promising miniaturized APPT prototypes have been commercially available in recent years by companies as Mars Space, Busek, Stadoko and CU Aerospace [75, 32, 170, 171]. Numerous research and technology demonstration missions have validated its feasibility for diverse applications in orbit [75], with approximately 25 prototypes flown typically exhibiting a 100–1000 s specific impulse and a 10–100 μNs impulse bit. All these efforts have focused on secondary propulsion, involving different tasks such as thruster attitude control, constellation and station keeping, attitude control and precision propulsion [75, 96, 130]. While more ambitious maneuvers such as orbit transfer have historically been beyond PPT applications, though some high energy proposals exist [172], nearly all PPTs deployed in the past two decades have been on satellites under 50 kg, primarily micro and nanosatellites, highlighting their growing potential for primary propulsion in these [173]. Indeed, typically ablative PPTs and electrosprays have constituted more than 30% of all the reported launches in that satellite mass category [75]. The pulsed-nature and structural benefit present ablative PPTs as preferable to other electric thrusters to be miniaturized [85]. Consistently, the low mass, low voltage and low cost increasing demands for the next generation of propulsion systems has increased the interest in the ablative PPT, which has been the only PPT in-orbit so far, and together with the vacuum arc thruster [34, 35, 36] the only pulsed electromagnetic plasma thrusters flown [75, 174, 64, 73, 48, 52, 55].

Low-power PPTs, typically operating below 10 J of discharge energy, are promising candidates for primary propulsion in power- and size-limited satellites[28], particularly ablative ones [75, 169, 30, 31, 32, 170, 64] due to their structural simplicity. Table A.1 summarizes the characteristics of some selected low-power ablative planar PPTs. In addition to the easiness of handling non-toxic or corrosive solid propellants, in contrast to liquid-fed [50, 51, 52, 55, 104] and gas-fed [46, 47, 48] PPTs, there is no involvement of injection valves, piping nor pressurized propellant tanks, which adds costs and complexities for down scalability, as well as reduces system reliability increasing in-orbit failure risk. In turn, the lack of propellant hazardousness or pressurized gasses also open ablative PPTs to a wider range of launch opportunities [31, 75, 66, 175, 64]. Within this category, planar configurations are structurally simpler, easing design and manufacturing and facilitating a more uniform discharge along the propellant surface, making them the standard. Additionally, they allow visual access to the in-channel plasma, useful for research.

Nonetheless, engineering challenges remain in ablative PPTs. For example, electrode degradation due to discharge byproduct accumulation and erosion, as well as charred material buildup on the dielectric gap from nonuniform ablation [112, 126, 30, 71, 176, 177, 121, 178]. Indeed, the potential advantages of PTFE are not without challenges that also warrant attention for efficiency improvements, such as the deposition of charred byproducts in the channel, late-time ablation, and concerns regarding the reactive fluorine compounds generated [179]. Additionally, a triggering system is required regardless of the injection mode. While alternative methods, such as laser-assisted ignition [180, 181], have been explored, spark plugs are commonly used for their simplicity and lack of moving parts. Nevertheless, these are prone to experience reliability issues, related to the same factors described above. Another critical issue to address for satellite integration is electromagnetic compatibility with the spacecraft, which is directly related to ignition [161, 168], along with the evaluation of plume-spacecraft interaction [2, 65, 3].

The advantages of the structural simplicity also contrast with the complexity of the physical mechanisms involved in the plasma formation and evolution, critical to deal with the thruster efficiency, typically below

[28] Micro- and nanosatellites generally operate below 30 W and 10 W respectively [87].

Thruster	Discharge energy E_0, J	Energy to Area ratio E_0/A, J/cm^2	Discharge voltage V, kV	Capacitance C, μF	Specific impulse I_{sp}, s	Impulse bit I_{bit}, μNs
LES-6 (B) [96, 93, 182, 142, 29]	<7 (1.85)	<2.6	500-2000	0.66 -6	590 (300)	<90 (26)
SMS (B) [29]	8.4	1.15	-	-	450	133
EO-1 (B) [29, 130]	<10 (8.5)	0.88	-	-	650	<100 (90)
Dawgstar (B) [130, 59]	5.23	2.27	500-2000	-	483	56
PPT-B20/TMIT-X (B) [131, 183]	2.3-3.6 (3.38)	(6.76)	1500	1-3	(960)	(22)
STSAT-2 (B) [184]	1.8	-	>1500	1.6	800	25
PPTCUP (S) [89, 185, 122, 186, 133]	(1.7)	(2-2.3)	<1500	2.4-3.2/ SP: 333pF	590	(29)
BIT* (B) s[187, 177, 134]	-	-	<1500	(2)/ SP: 0.18µF	-	-

Table A.1: **Selected sample of low-power class ablative, planar, breech-fed, PTFE-propelled pulsed plasma thrusers.** Values between brackets correspond to published nominal operation points, while ranges and non-bracketed figures belong to parametric studies. The channel size varies from a device to another one, but is generally based on the magnitude order of the cm; often, the height is larger than the width and cathode and anode share the same length. Usually, the channels are covered, typically involving a dielectric nozzle. (*) Segmented electrodes. Legend: (B)-Breech-fed, (S)-Side-fed/ SP-Spark plug. Commonly, spark plugs (SP) operate at around 1 kV, however, specific endurance analysis, as the one performed with PPTCUP, reveal reliable ignition at voltages between 3-5kV (333pF).

20% [188, 189, 91, 92]. Figure A.1 illustrates PPT performance scaling down with discharge energy, exhibiting different behaviors with capacitance and discharge voltage. This effect does not necessarily align with reported ion speed trends [91, 92], highlighting the need for further research to comprehensively study the plasma beyond performance metrics. It has also been consistently documented that performance declines as the system is miniaturized, indeed especially compromised under 10 J, which constitutes the typical range for low-power class PPTs. Table A.1 collects a representative sample of ablative PPTs.

Research over six decades of EP development highlights sustained interest in PPTs, with numerous groups contributing through experimental and numerical activities. Concerning ablative PPTs [97, 94, 99, 95, 136, 110, 98, 139, 113, 161, 102, 126, 30, 143, 100, 61, 92, 107, 116, 109, 145, 72], an overview of the research groups focusing on ablative PPTs is outlined in Section A.2. Research on gas-fed PPTs, or plasma (deflagration) guns [190, 191, 192, 48, 193, 194], has developed alongside ablative PPT studies for decades, while liquid-fed PPTs which were initially focused on water-fed designs [195] aligning more with the former category, are less common and often use non-volatile liquids [49, 50, 51, 52, 53, 54, 55, 56, 57, 58],thus exhibiting behavior closer to ablative ones. Gas-fed discharge studies have advanced the understanding of transversal phenomena such as canting during in-channel acceleration, e.g., works at Princeton University in the 1990s and 2000s [151, 196, 197, 191], and the existence of multiple ionization waves, as the works carrying out at Stanford University [46, 192, 47, 48], including the identification of high-energy ion populations in their hydrogen plasma.

Beyond serving to characterize the performances of specific prototypes, laboratory measurements of the plasma exhaust are essential to supplement the models and to help in the understanding of APPTs. Until then, designs and optimization efforts were mostly based on scaling laws and semi-empirical formulation, constrained to particular geometries and operating conditions [147, 198, 189, 142]. As well, the existing modeling efforts approaching the discharge dynamics along the channel were limited to electromechanical

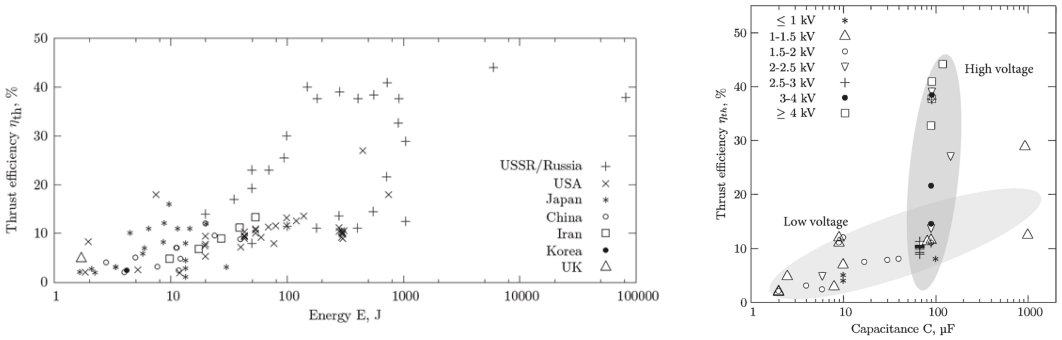

(a) (b)

Figure A.1: **Efficiency against (a) bank energy [91] and (b) bank capacitance and initial discharge voltage [92] for different pulsed plasma thrusters.**

approximations, where the plasma is assumed as a mobile sheet with associated resistance and inductance [23, 29, 151, 152, 153, 92, 147, 150, 154]. These are useful to investigate trends and performance scaling parameter but lacking in physical insight [155], however they are the ones broadly addressed in the literature even now. Hence, more accurate modeling towards the elucidation of the discharge physics started at that moment, as specific modules to study the ablation and flashover phenomena in certain cases [148, 108, 149, 150, 145] or approaches to the ionization-acceleration stages as the MACH2 code research line by the Ohio State University, or, years later, other hybrid MHD-PIC ones [156, 157, 158, 159, 160]. However, to date available models suffer from different limitations to constitute a complete theoretical formulation that adequately predicts the discharge characteristics, taking into account all the major phenomena self-consistently at all its stages [147].

These studies aim to elucidate the complex ablative PPT discharge process, where in-channel physics involve multiple stages, including breakdown, plasma generation, and ejection. The simultaneity and spatial overlap of these mechanisms hinder their independent analysis [108]. Efficiency is impacted by various losses, including poor energy coupling into the ablated propellant and inefficient plasma acceleration, influenced by factors such as late-time ablation [144, 95, 96, 97, 72, 145], secondary breakdowns [23, 100, 139, 135, 48, 2], and particulate emission [136, 137]. As a consequence, addressing inefficient energy transfer to the ablated propellant, which results in low ionization, requires studying late-time ablation and the role of neutrals in reignition processes. Additionally, for commonly used propellants, the time-varying plasma may consist of multiple chemical species, including eroded or sputtered electrode material, with varying molecular masses and charge states, and exhibit a wide divergence angle [97, 95, 61, 100, 2], which also translates into a loss of performance.

A.2. Ablative PPT prototype examples

The first qualified PPT models involved parallel-rail breech-fed configurations. [From now on, all the devices described are ablative, planar, PTFE-propelled unless the opposite is indicated.] After the 50 J PPT mounted on the soviet Zond-2 probe, next missions were carried out under the U.S. Air Force's Lincoln Experimental Satellites Program, with the MIT Lincoln Research Laboratory and some NASA centers as main actors together with private partners, as Fairchild Republic Company [96, 93, 188, 182, 142]. This program initially led to the successful LES 6 mission launched in 1968, based on 1.85 J PPT technology for station keeping and accumulating about 8900 hours of thruster operation along 5 years [23, 175]. Its subsequent evolution was the improved LES 8/9 version, with 19.9 J PPTs, designed for providing three axis attitude control and orbit control, but that finally was replaced by chemical propulsion because of electronics issues [199]. The former US research consolidated the use of PPTs for spacecraft auxiliary

propulsion along the 70s with the GEO SMS mission, based on a 4.2 J PPT type for station keeping and fine pointing [200, 29], and the LEO TIP and NOVA mission series [201, 29], launched along the 70s and 80s respectively, based on 20 J PPTs for drag makeup. In parallel, some low-energy class PPTs were launched by Japan in 1982 with the ETS-IV mission, with 2.25 J [202, 203, 204], and China also in 1981 with the MDT-2A mission, with 4 J [205].

The advancement in small satellites necessitated highly efficient low-thrust EP systems that offer a balance of low mass, power consumption, long lifespan, and high total thrust impulse and they all were the prelude of improved versions in the coming years that relied, on one side, on powerful devices for proposals aimed at exploring orbit raising and initiating and maintaining clusters of small satellites, while on another hand, highly promising, the focus was placed on low-energy PPTs, typically under 10 J. The growing exploitation of increasing small spacecrafts [75, 175, 169, 30, 37, 32, 85, 170, 86, 64] created chances for them to play, in addition to precise attitude control and positioning, and formation flying, primary propulsive roles taking advantage of their simplicity in design, cost-effectiveness, and independence from power consumption. Finally, NASA's New Millennium program opened with the LEO EO-1 mission launched at the beginning of the 2000s, carrying an 8–50 J PPT directly evolved from the prototypes above, for pitch axis attitude control. Private partners associated to this new generation were Primex Aerospace, Nyma or Olin Aerospace [206, 29, 207]. In recent years, research on PPTs has expanded, with growing focus on the low-energy range, investigating the influence of channel geometry and operational parameters. Multiple launches have taken place, further advancing the field, while the potential for commercialization has become increasingly evident [175]. Some examples are listed below:

- The University of Illinois shifted to a breech-fed coaxial configuration, transforming part of their research towards electrothermal, including their 9 J PPT device [190]. Furthermore, in collaboration with the related company CU Aerospace, and under an U.S. Air Force contract, another proposal evolved to an advanced design based on a capillary discharge chamber [88] with an initial high-pressure electromagnetic pinch region [208], originally planned to launch in the small sat Mightysat II.2 mission, for orbit raising. This research is still on-going with the 8–32 J patented fiber-fed PPT (FPPT) [208, 171].

- Scaled down from the EO-1 thruster, a qualified PPT [130, 59, 30] for the Dawgstar satellite was developed by the University of Washington. It provided formation keeping/orbit maintenance/attitude control for satellites in the 10–100 kg range.

- Also along the early 2000s, under the NASA's In-Space Propulsion (ISP) Solar Sail Program, the Arizona University developed the planar breech-fed 13 J PPT150 PPT prototype for providing its solar 100 kg sail proposal for attitude control by using several devices [209].

- By that time, the Tokyo Metropolitan Institute of Technology together with other Japanese partners, developed the planar breech-fed PPT TMIT-PPT for the μ-Lab Sat II as a tech demo [139, 183, 210]. based on the previous Japanese experience with the ETS-IV mission [202, 203, 204].

- In 2005, a new launch since the EO-1 mission took place putting a PPT in orbit by Korea with the STSAT-2, with 1.8 J for attitude control [184, 211].

- In 2007, a new launch since the EO-1 mission took place putting a PPT in orbit with the military FalconSat-3. It was used by Busek to do the tech demo of its 1.96 J MPCAS PPT prototype [170].

- In 2012, the 15 kg PROITERES I nanosatellite was inserted in LEOwith with a coaxial electrothermal PPT named JOSHO as a tech demo. Research leaded by Osaka Institute of Technology placed, the peculiarity of this design, tested between 4.5–15 J, resides on having a PTFE channel between the anode, at the thruster back, and the coaxial cathode nozzle. The prototype is aimed to be commercialized. Further work involving higher power versions has been developed along the 2010s under the PROITERES II mission [212, 213, 214, 38, 215, 39]. In 2020, another nano-satellite/probe

R&D project started at the Osaka Sangyo University (OSU) based on the lessons learned from the PROITERES missions, around a prototype consisting in a multi-discharge room named MDR-PPT [216, 217].

- In 2012, the 3.5 kg STRaND-1 3U CubeSat was launched, being the first European PPT in orbit, as well as the first nanosatellite with three axis control, and, in addition, the first with EP on board. It had on board an 8-PPT propulsion module, which was also used for the UKUBE-1 nanosat. Both projects were collaborations of the Surrey Space Centre with Surrey Satellite Technology Limited and UK Space Agency respectively [71, 132].

- In 2013, two of the three PPT were launched to orbit, were developed by the Cornell University for attitude control and orbit maintenance on 25 kg satellites [75].

- The third launch of 2013 was a commercial tech demo by StaDoko named WREN with 250g [75].

- In 2014, the Russian APPT-45-2 was mounted on board the small spacecraft MKA-FKI PN2. This was the result of the renewed interest in the USSR arisen in the late 1990s mainly at the RIAME in collaboration with other private partners as TECHCOM, with the development of second-generation PPT models, after previous decades of slowered research because of the socio-economico-political situation. Their thrusters typically range between 20-155J. In the last years, efforts have been focused on the development of the improved APPT-250, intended for the orbit maintanance of the constellation of small communication satellite, with a power consumption from 60 to 120 W [218, 174].

- The second launch chance for Europe took place with the QB50 project is an international project with the goal of sending an extended number of nanosatellites, a.k.a. CubeSats, into the Thermosphere. In 2017, the Austrian CubeSat PEGASUS was inserted into the Thermosphere under the frame of the QB50 project, carrying among other payloads a miniaturized PPT for tech demo, even though it was designed for 2 axes ADCS purposes [219]. It was developed by the University of Applied Sciences Wiener Neustadt, in collaboration with the University of Vienna, FOTEC GmbH, TU of Viena and the University of Oslo.

- The AOBA-VELOX-3 CubeSat was launched in 2016 to go into the low Earth's orbit in 2017 by the Nanyang University (NTU) with an PPT for orbit maintenance [75]. The subsequent four-head propulsion module for the 2kg AOBA VELOX-IV mission, again by NTU, in collaboration with the Kyushu Institute of Technology (Kyutech), addressed the attitude and orbit control challenges (orbit maintenance, attitude control, and momentum dumping) in Moon's orbit [220].

- Again in Europe, the parallel rail PPTCUP low-power class PPT prototype and an even more miniaturized version NanoPPT have been qualified along the 2010s, COTS commercially available now, by the Southaptom University, Marspace Ltd and Clyde Space Ltd under an ESA funded project [89, 185, 122, 186, 133, 32]. PPTCUP, which was original designed and developed under the frame of La sapienza University, can provide translational and orbital control to Cubesat platforms. PPTCUP is characterized by an averaged specific impulse of about 650 s and a deliverable total impulse around 50 Ns.

- Continuing with research lines leaded by European countries, in 2022, PETRUS, a 1 J version of the 1–68 J scalable coaxial PPT designed at the Institute for Space Systems of the University of Stuttgart, was launched as a secondary payload on board of the 3U GreenCube sat. This mission served as a technology demonstration to test the thruster's basic functionality, its interaction with other satellite systems, and its lifetime relative to ground data. PETRUS marks the first in-orbit demonstration of the coaxial PPT family [221, 64], with reported efficiencies up to around 10 %. PETRUS is the result of over 20 years of research by the IRS, building on previous work such as the SIMPLEX and its improved version, ADD-SIMPLEX [222, 60, 223, 91, 61, 92, 135, 111, 224, 225, 105], which achieved 30% efficiency, one of the highest for its class. These investigations, carried out in

collaboration with the University of Tokyo, have been crucial for recent promising low-power class PPT proposals globally. The research faced challenges with efficiency across different prototypes, evolving through electrothermal designs before arriving at PETRUS.

- Additional examples of recent work in both prototype design and fundamental research include low-power class PPTs developed at Institute of Plasma Physics and Laser Microfusion in Poland [65], and in China, research at Hebei University of Engineering [107], Hefei Institute of Physical Science [103], Beijing Institute of Technology [167] and Beihang University [226]. Some collaborative work between the latter two institutions exist [114, 227], such as the investigation on segmented electrodes [187, 177, 134, 227]. In addition, in Japan, University of Yamanashi is also involved in low-power class PPT prototyping [228].

B. GOOD PRACTICES FOR OPERATING ELECTROSTATIC PROBES IN THE ION SATURATION REGIME TO EXPLORE PPT EXHAUSTS

B.1. Introduction

The testing time required by the plume experimental campaigns to obtain an adequate dataset in the ion saturation regime, especially when involving the implementation of the WAVES technique, has led to the identification of a series of good practices. This has been due to the significant challenge of identifying the appropriate operational range for the various parameters involved in the implementation of the different diagnostic systems used, ensuring clear measurements while maintaining an acceptable number of firings without spurious discharges.

Concerning the spurious discharges, these occur on the probe electrode and can happen at any time during plasma interception by the probe. In the case of wire electrostatic probes, these spurious discharges can occur at any position along it. In addition, the duration of a spurious discharge has been observed to vary significantly among firings, ranging from a time-localized event that does not further perturb the intended ion current measurement to one that extends up to several orders of magnitude beyond the firing discharge time. As spurious discharge essentially short-circuits the measuring circuit.

A spurious discharge experienced by a probe affects the signal measured by the remaining probes simultaneously monitored, at least locally at the time at which the undesirable event begins. However, it does not necessarily trigger a short-circuit in the other operating probes. The spurious discharge invalidates the capability of the affected probe to capture the ion saturation current during the time that it lasts while introduces uncertainty in the other probe measurements.

Tests were conducted at different grid axial placements, thruster discharge voltages and probe bias voltages in order to gain insight to set the experiment conditions. A greater odds for spurious discharges was observed for central probe locations (which are closer to the thruster axis) when placing the array closer to the thruster, when operating with a higher discharge voltage and the more negative the probe bias was. While detailed characterization of these events is outside the scope of this work, we understand that their frequency increases with larger discharge voltages (and, consequently, discharge energy).

The remainder of the appendix includes Section B.2, which details the criteria for setting the probe system parameters.

B.2. Criteria for setting probe system parameters

Given the discharge voltage V_0, the parameters of a standard Langmuir probe measuring circuit to determine are the probe base bias voltage V_b, the shunt resistor R_{shunt} and the probe axial location z_p within the plume. A trade-off is required between these to obtain ion saturation current measurements while dealing with spurious discharges.

In general, the setup parameters are selected based on the needs of the most demanding probe location within the plume explored domain, where the highest plasma density is. Firings are repeated until a sufficiently large dataset of non-spurious firings has been gathered, to offer rigorous statistical significance to the mean measurement is reached.

Requirements and advice for setting z_p, V_b and R_{shunt} are described below:

- First, the selection of the grid's axial placement z_p is guided by several considerations. These include the constraints imposed by the vacuum chamber geometry, which determine the farthest allowable

location, and the risk of affecting the discharge when measuring too close to the thruster (e.g. spurious discharges become more likely closer to the thruster). Preferable z_p locations should enable the visual, even approximate, identification of the different ion populations present in the plume, a task that becomes more challenging as the plume expands.

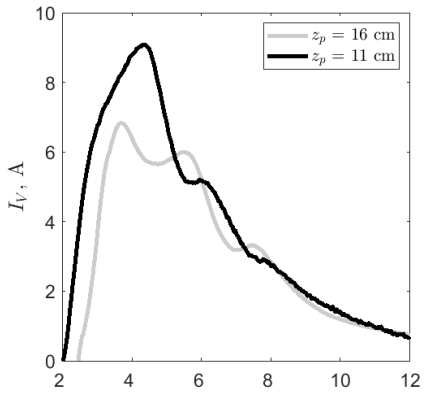

Figure B.1: **Ion saturation current measurements at different probe axial locations z_p for a central vertical wire electrostatic probe I_V at nominal thruster capacitance (6μF) and 1500 V of discharge voltage.**

- Second, regarding R_{shunt}, its value must be carefully chosen to alow for a low perturbation of probe voltage $V_p(t)$ with respect to the effective probe bias $V_{b,eff}(t)$, which constitutes the effective reference bias seen by the plasma probe during the measurement. This ensures that the probe remains in the ion saturation regime throughout the discharge time. The upper limit, $R_{shunt,max}$, depends on plasma density, while the lower limit, $R_{shunt,min}$, is set by the equivalent resistance of the circuit, which must be significantly lower than R_{shunt}. Within this suitability range, $[R_{shunt,min}, R_{shunt,max}]$, measurement resolution can be optimized by adjusting R_{shunt} (see Figure B.2). Additionally, the resistor should exhibit temperature stability, and periodic checks to its specifications are necessary to guarantee that R_{shunt} has not degraded, particularly due to power peaks from spurious discharges.

- Lastly, the bias voltage supplied by the power source V_b must be sufficiently negative to ensure the probe operates in the ion saturation regime. Overall, the higher V_0 or the closer z_p is, the higher $|V_b|$. However, increasing $|V_b|$ also raises the likelihood of spurious discharges.

  Some practical considerations follow in the selection of this parameter:

  (a) The ion saturation regime is ensured when: (1) the initial electron bulk[29] reaching the probe is sufficiently shielded, allowing the probe to collect only ions. A non-shielded electron bulk appears as a valley below V_b before the first positive bump in the probe current signal;

  (b) and (2) The rest of V_p remains well below the plasma potential and shows minimal variation with increasing $|V_b|$, a condition inherently met if (1) holds.

  In experimental studies with varying operating conditions, maintaining a single V_b across all cases is preferable. Consequently, mind that the selected V_b, suitable at least for nominal conditions, may not be optimal for all cases across the operational parameter space.

  (c) Among the different ion populations, for the case problem, it is the first one arriving at the probe the one constituting the most critical scenario, as it is the one perturbing more $V_{b,eff}(t)$ with respect to V_b.

[29] While in principle nothing would prevent the formation of negative ions, especially given the high electronegativity of fluorine atoms, we assume that the initial negative population arriving at the probes is more likely to consist of electrons, as we are not aware of any reported observations of negative ion populations.

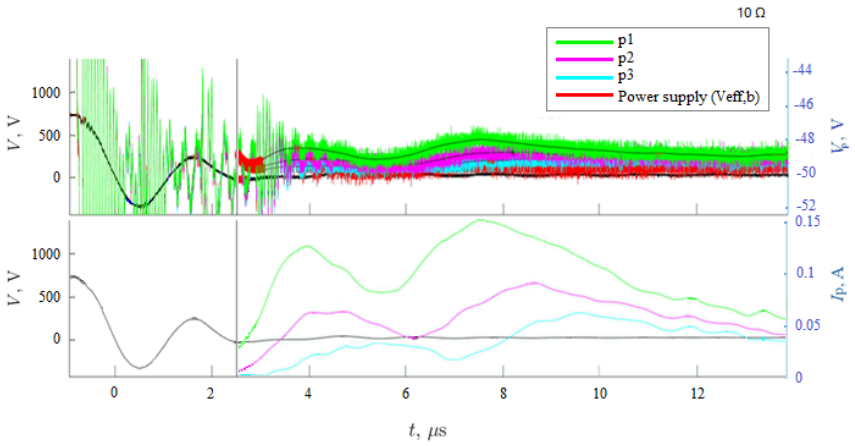

(a)

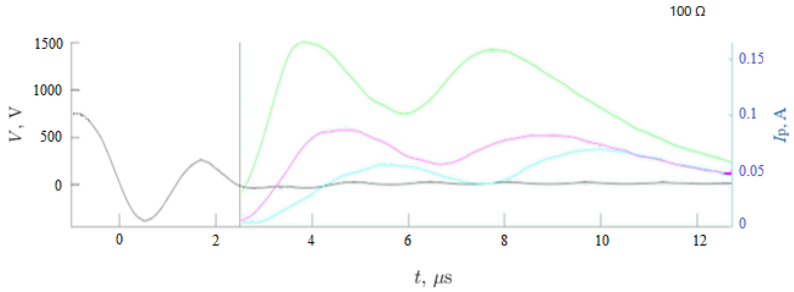

(b)

Figure B.2: **Ion saturation current measurements of two different firings at identical discharge conditions obtained through same-class shunt resistors of different resistance.** (a): 10 Ω; (b): 100 Ω. Left vertical axis represents the anode discharge voltage $V(t)$, filtered, while right vertical axes include the plasma probes voltage and current waveforms $V_p(t)$ and $I_p(t)$ (raw in the top panel, and low-pass filtered in the bottom one). The bias signal $V_{b,eff}(t)$ is also represented on the top panels. [Example from Chapter 4-Section 4.3.5.2 data, from a Time-of-Flight setup consisting of three wire electrostatic probes, axially distributed and perpendicularly aligned to the plasma flow.]

The power supply's current rating at the frequency of interest and its slew rate should be sufficient to avoid saturation during plasma arrival at the probes under test. the power supply slew rate must also be high enough to minimize the perturbation of $V_{b,eff}(t)$ with respect to V_b.

In spite of these precautions, it is not uncommon that some spurious discharges occur. However, their likelihood decreases with repeated firings and progressively increased bias during preliminary shots, warranting further investigation. This enables measurements at higher-density conditions, as shown in Figure Figure B.1, although it results in a longer testing process.

C. UNSTEADY PARAXIAL FLUID MODEL FOR PLANAR PPTS [30]

Developed in parallel with the experimental work of this thesis, and with the aim of supporting future research, a plasma-physics-based numerical model was initiated, focused on in-channel plasma ionization and acceleration in planar pulsed plasma thrusters (PPTs). The model addresses unsteady PPT plasma dynamics along the thruster channel, whose description is simplified by applying variable separation. Then, the plasma dynamics is decomposed into the two predominant flow directions, along the thruster channel and the discharge current axes. The resulting formulation then relies on a paraxial approach, with the definition of the cross-discharge current remaining independent.

The coordinate system is defined as follows: z runs along the thruster firing direction, x spans from the anode to the cathode, and y extends out of the plane, forming a right-handed trihedron. [Note that the x and y axes are oriented oppositely to those used in the experimental work of this dissertation.] Hence, the axial direction (z) governs the plasma flow along the channel and the transverse direction (x) accounts for the discharge current distribution.

The present content focuses on the axial modeling (z). The modeling of the dynamics perpendicular to the electrodes (x), which aims to determine the current density in that direction and the fluxes to the electrodes (i.e., the losses), is beyond the scope of this work. In addition to excluding the description of plasma–electrode interactions, this work does not address the ablation stage or the presence and role of multiple species of the particle types considered.

For the present modeling purpose, a three-fluid MHD model is adopted as the basis for describing the in-channel plasma dynamics. This initial effort is intended to define the modeling strategy rather than to present results. The focus is thus placed on outlining the proposed approach and establishing a foundation for future, more comprehensive investigations.

The rest of the structure of this appendix is organized as follows. The core of the chapter is constituted by the present paraxial modeling efforts. In Section C.1 the assumptions are outlined; in Section C.2 the equations for the different species are detailed; in Section C.4 the initial and boundary conditions required to solve the system are defined. Once presented the governing flow equations, in Section C.5 the Method of the Characteristics is introduced, the characteristic lines of the governing equations derived, and the explored algorithm is described. Finally, Section C.6 closes the appendix with a summary of it.

C.1. Model assumptions

Hence, consider a purely two-dimensional planar PPT (generally known as rectangular PPTs). It consists of two perfect conductor electrodes, a cathode (−, above) and an anode (+, below), separated by a distance h and extending infinitely in the out-of-plane direction. In addition, the thruster channel is long, of length L_z, and paraxial, i.e., slow changes within h. A propellant supply is located at the rear. The specifics of the propellant supply and the breakdown initiation are beyond the scope of this model; replaced by the injection from the channel back with a prescribed time law of a gas of mass m with a non-zero ionization fraction.

Continuous flow is assumed. A magnetohydrodynamics (MHD) framework is adopted, justified by the high plasma densities reported in similar PPTs—ranging from 10^{19} to $2 \cdot 10^{20}$ m^{-3} at distances of 20 and 6 cm from the PTFE surface, respectively [98].

As a start point, single populations of neutrals, singly-charged positive ions and electrons are considered in the model. All species are considered Maxwellian and isotropic. Electrons are assumed to be polytropic and massless. Additionally, the variation in electron pressure along the channel is assumed to be primarily

[30] Research branch under the supervision of Professors Eduardo Ahedo and Mario Merino.

due to changes in density.Ions are assumed cold, $T_i \ll T_e$, although this assumption may be weak in dense plasmas. For simplicity, neutrals are regarded as isothermal, and, consistently to above, assumed cold too. The neutral speed u_{zn} is taken as a constant in order to simplify the problem. This assumption allows for the avoidance of resolving its dynamics, based on the premise that its rate of change in momentum is negligible enough to affect the plasma dynamics through the source terms. Ions and neutrals share the same mass m; electron inertia is neglected $m_e \ll m$. In addition, the bulk of the plasma, i.e. everything but the thin sheaths near the walls, is considered quasineutral equaling ion and electron density ($n_e \simeq n_i$). Regular plasma sheaths constitute any plasma bulk - wall interfaces, which involves ions entering a sheath at sonic or supersonic speed. Sheaths remain out of the scope of this work.

Regarding the collisions expected to affect the plasma dynamics, electron-neutral ionization, ion-neutral charge-exchange (CEX) collisions and Coulomb collisions are considered. Furthermore, to avoid that charge can build up on the propellant surface, it is assumed that any ion reaching it is recombined into a neutral. Any ion reaching the electrode walls also does. The velocity of those recombined neutrals responds to a certain accommodation factor. However, taking constant u_{zn} for the neutral bulk, the global effect of collisions and recombination is assumed to not impact the neutrals' dynamics.

On the other hand, the electrodes are driven by an external circuit that establishes their electric potential ϕ; it may also vary over time. To further simplify the analysis, the cathode is grounded by setting its potential to 0. The flow of electric current throughout the circuit composed by the generated plasma, the electrodes and the circuit defines the discharge current j along the channel and discharge time. To prevent the build-up of electric charge, it is imposed that the total current going to the cathode must equal the current coming out of the anode at all times. The discharge current, predominantly j_x, induces a magnetic field assumed to be purely y-component B_y. Note that time variations in the magnetic field generate a solenoidal component of the electric field (Faraday's law). However it is assumed irrotational, with the curl contribution considered negligible compared to the potential one ($\Delta\phi$).

Disregarding the x- with respect to z- derivatives of particle velocities and densities present in the macroscopic equations under the paraxial-channel assumption, the model essentially decomposes into two components: a 1D model along the thruster axis, coupled to the (cross) discharge current j_x, that allows for solving of the axial dynamics of the plasma. While j_x is here prescribed, it should be the output of a radial model, which is beyond the scope of this work.

Future extensions of the plasma model to a fully 2D framework will require modeling electron emission and the electrode sheaths to resolve the plasma potential drop across them. Electrode emission modeling should enable the evaluation of contributions from secondary electron emission due to impacts from electrons or ions on the walls, as well as from thermionic emission, the Schottky effect, and field emission. Alternatively, electromechanical models [23], such as the Snowplow model discussed in Section 2.4 in Chapter 2, provide a simpler approach to estimate j_x.

C.2. Governing equations

C.2.1. Neutral bulk equations

According to the assumptions, only the continuity equation needs to be solved:

$$\frac{\partial n_n}{\partial t} + u_{zn}\frac{\partial n_n}{\partial z} = -S, \tag{C.1}$$

where u_{zn} is constant. In this work the neutrals lost or generated through the source term $S = S_{ion} - (S_{zi} + S_{xi})$ are defined as the summation of the ionization component S_{ion} and the recombination losses at the propellant wall S_{zi} and at the electrode walls S_{xi}. S_{zi} is defined through a boundary condition, while S_{xi} and S_{ion} have to be provided by the radial and a collisional models respectively.

C.2.2. Ion bulk equations

The ion continuity equation to solve is presented:

$$\frac{\partial n_i}{\partial t} + u_{zi}\frac{\partial n_i}{\partial z} + n_i\frac{\partial u_{zi}}{\partial z} = S. \tag{C.2}$$

The momentum equations are included below. Although the z-component is the one of our interest, the x-component is also given for descriptive purposes:

$$mn_i u_{zi}\frac{\partial u_{xi}}{\partial z} = -en_i u_{zi}B_y + A_{xi} - mu_{xi}S, \tag{C.3}$$

$$mn_i\left[\frac{\partial u_{zi}}{\partial t} + u_{zi}\frac{\partial u_{zi}}{\partial z}\right] = E_z + en_i u_{xi}B_y + A_{zi} - mu_{zi}S, \tag{C.4}$$

where the collision term A_i is modeled with the contribution of the gain of momentum due to ionization and Coulomb collisions, and losses because of CEX collisions and recombination at the walls. Note that the Coulomb $z-$contribution vanishes under the assumption of free axial current as the relative axial speed between ions and electrons also does.

C.2.3. Electron bulk equations

On the one hand, the z-component of the ion momentum equation (Eq. C.4) can be combined with the analogous one for electrons, below, to provide a convenient plasma momentum equation.

$$E_z = -k_B T_e\frac{\partial n_i}{\partial z} - en_i u_{xe}B_y + A_{ze} \tag{C.5}$$

where the ideal gas relation is used and $\partial T_e/\partial z \ll \partial n_i/\partial z$ assumed as listed in Section C.1. It is worth it to mention that while the source term $m_e u_{ze}S$ is disregarded under the electron massless assumption, the collisional term A_{ze}, being also a product of m_e, cannot be neglected, as it is expected to be significant in a collisional plasma.

The proposed equation manipulation yielding a plasma momentum expression, by removing the explicit reference to E_z in Eq. C.4, serves the purpose of having an explicit reference to the current density $j_x = en_i(u_{xi} - u_{xe})$, where e is the elementary charge.

E_z is the key mechanism for ion acceleration: electrons experience the Lorentz force, but the electrostatic field, effectively transmitted by the ions, decelerates them while accelerating the ions instead.

On the other hand, note that in a axially current-free quasineutral flow, $u_{zi} = u_{ze}$. This equals the left-hand side (LHS) of the continuity equation for ions and electrons.

C.2.4. Induction equation

The magnetic field, assumed to be B_y, satisfies the Ampere's equation in the bulk:

$$\frac{\partial B_y}{\partial z} = -\mu_0 j_x. \tag{C.6}$$

with $j_x = en_i(u_{xi} - u_{xe})$ and having disregarded the time derivative of the electric field with respect to j_x. [Note that retaining the z-component of the B_y equation would require considering $\partial B_y/\partial x$, which is currently disregarded, further supporting the assumption of an axially current-free flow.]

C.3. Global equation system

By applying the assumptions outlined in Section C.1, the derivation proof of the equations involved in the study the in-channel ion PPT physics trough a paraxial MHD model results in a closed set of four equations. These are the hyperbolic conservation laws: (1) the continuity for neutrals, (2) the continuity for ions and (3) the plasma dynamics equation (from combining Eq. C.4 for ions and C.5 for electrons), together with (4) the Ampère law:

$$\frac{\partial n_n}{\partial t} + u_{zn}\frac{\partial n_n}{\partial z} = -S \tag{C.7}$$

$$\frac{\partial n_i}{\partial t} + u_{zi}\frac{\partial n_i}{\partial z} + n_i\frac{\partial u_{zi}}{\partial z} = S \tag{C.8}$$

$$mn_i\frac{\partial u_{zi}}{\partial t} + mn_i u_{zi}\frac{\partial u_{zi}}{\partial z} + \gamma T_e\frac{\partial n_i}{\partial z} = j_x B_y + A'_{zi} \tag{C.9}$$

$$\frac{\partial B_y}{\partial z} = -\mu_0 j_x \tag{C.10}$$

where T_e[31], u_{zn} and m are constant, j_x profile is not time dependent and $A'_{zi} = A_{zi} - mu_{zi}S$. γ is the heat capacity ratio. The problem involves four problem time-dependent variables n_i, n_n, u_{zi} and B_y, in addition of the two constants T_e and u_{zn}, in case of not being assumed known. Sufficient initial and boundary conditions need to be provided to solve this system, which are defined in Section C.4.

Finally, the equation system to solve is normalized according to the following dimensionless relations for the problem variables:

$$z = z^* L_z \tag{C.11}$$

$$u_{zi} = u^*_{zi} u_0, \qquad \text{with } u_0 = \sqrt{\gamma T_e/m} \tag{C.12}$$

$$t = t^* t_0, \qquad \text{with } t_0 = L_z/u_0 \tag{C.13}$$

$$n_i = n^*_i n_0 \tag{C.14}$$

$$n_n = n^*_n n_0 \tag{C.15}$$

where n_0 is the reference in-channel plasma density, taking from reported figures in comparable PPTs [98]. Hence, the normalized equation system is presented below:

$$\frac{\partial {n_n}^*}{\partial t^*} + \frac{u_{zn}}{u_0}\frac{\partial n^*_n}{\partial z^*} = -S^* \tag{C.16}$$

$$\frac{\partial n^*_i}{\partial t^*} + u^*_{zi}\frac{\partial n^*_i}{\partial z^*} + n^*_i\frac{\partial u^*_{zi}}{\partial z^*} = S^* \tag{C.17}$$

$$\frac{\partial u^*_{zi}}{\partial t^*} + u^*_{zi}\frac{\partial u^*_{zi}}{\partial z^*} + \frac{\partial \ln n^*_i}{\partial z^*} = \frac{1}{n^*_i}\left[j^*_x B^*_y + A'^*_{zi}\right]. \tag{C.18}$$

$$\frac{\partial {B_y}^*}{\partial z^*} = -\mu^*_0 j^*_x \tag{C.19}$$

where the right-hand side (RHS) dimensionless parameters and terms,

$$S = S^* S_0, \qquad \text{with } S_0 = n_0/t_0 \tag{C.20}$$

$$B_y = B^*_y B_0, \qquad \text{with } B_0 = m/et_0 \tag{C.21}$$

$$j_x = j^*_x j_0, \qquad \text{with } j_0 = en_0u_0 \tag{C.22}$$

$$A'_{zi} = A'^*_{zi} * A_{zi0}, \qquad \text{with } A_{zi0} = mn_0u_0/t_0 \tag{C.23}$$

$${\mu_0}^* = \mu_0 L_z B_{y_0} j_{x0}. \tag{C.24}$$

[31] Alternative for not solving the governing equation system for T_e: Given T_e as a initial condition, the polytropic equation can be added to the system to update T_e at each time step as a function of the n_i profile and the polytropic index γ as a function of z, but keeping the assumption of $\partial T_e/\partial z \ll \partial n_i/\partial z$.

C.4. Boundary and initial conditions

The boundary and initial conditions necessary to integrate the normalized paraxial equation system presented in Section C.3 are the following ones:

- Boundary conditions:
  - At $z = 0$:
    1. Bohm condition: Sonic or supersonic entry to the sheaths applies to the ions, so that $u^*_{zi} \leq -1$.
    2. Additionally, the existence of axial plasma wall losses implies that any ion-electron pair reaching $z = 0$ are recombined into a neutral. [These neutrals are assumed not to affect the momentum of the neutral population, allowing for disregarding the velocity at which they are generated.]
  - At $z = L_z$:
    1. Neumann condition: B^*_y is assumed zero far downstream.
    2. Open duct. [Note that this implies that, in the absence of external information, only sonic or supersonic solutions are valid, $u^*_{zi} \geq 1$. This condition limits the fluid particles at the channel exit to be solely influenced by fluid within the channel.]

- Initial profiles:
  1. At $t = 0$, n^*_n, n^*_i and u^*_{zi} are provided representing neutral injection with first free charge-carriers. [Neutral injection can be time-dependent as a way to approach late-time ablation.]
  2. A law is needed to define the j^*_x channel profile at any t. [Note that if j_x is time-dependent, the time derivative term on the LHS of the induction equation (Eq. C.6) needs to be retained.]

C.5. Proposed procedure for numerical solving

This section proposes the use of a Riemann finite-volume scheme [229]. The method discretizes the spatial domain into control volumes of continuous flow, where the governing system of equations presented in Section C.3 is applied, and employs Riemann solvers at the interfaces to update their solution.

Within each control volume, the "Method of the Characteristics" can be applied. It is a numerical technique used to solve hyperbolic partial differential equations by transforming them into a set of ordinary differential equations along characteristic lines, which represent the path along which information propagates in the flow field.

Following a standard approach inherent to the proposed method, Section C.5.1 describes the characteristic lines. The basis of a marching algorithm tailored to the specific wave patterns of the problem, applied to Cartesian mesh grids, are outlined in Section C.5.2.

C.5.1. Characteristic lines

Each governing equation for a hyperbolic system typically has two characteristic lines associated with the wave propagation in the system. In case of compressible flows, these two lines represent the directions of the Mach waves. The pathline is an additional concept that tracks the motion of a fluid particle over time, which can be considered as the third characteristic lines.

The characteristic lines along which the fluid properties propagate within the (z,t) plane associated to each one of the model system equations presented in Section C.3 are:

1. In the ampere equation, the integration line has $\mathrm{d}z/\mathrm{d}t = 0$ slope.

2. The combination of the plasma momentum and ion continuity equations, respectively Eq. C.17 and C.18, reveals the two Mach lines. The derivation process for these two Mach lines is detailed in Section C.5.1.1. On the other hand, there is also the pathline, necessarily located inside the influence cone as it goes with u_{zi}.

3. For neutrals, n_n would be constantly transported by the bulk motion according to $\mathrm{d}z/\mathrm{d}t = u_{zn}$ in case of null RHS. It represents the pathline. [Additionally, two Mach lines apply; the derivation is analogous to that introduced above for the plasma case.]

Different type of wave-patters exist depending on the characteristic lines. In the case of a positive constant-velocity slope in a homogeneous flow, a uniform flow region takes place. However, if this condition is not met with a non-null RHS, as in the case of collisional plasma, simple and non-simple wave regions can form:

- In simple wave regions, the property advection is driven by a wave belonging to only one family of characteristic lines. Compression waves occur when the flow accelerates opposite to the wave direction, converging the pathlines. Conversely, expansion waves result in divergence, preventing interaction.

- In non-simple wave regions, two families of waves interact. Such interactions can occur due to wave reflections at flow boundaries, such as closed ends (where the reflected wave mirrors the incident one), or open ends (where reflection occurs only in subsonic flows, and an opposite wave is reflected if the exit pressure is constant). When continuous waves interact, the resultant wave pattern depends on the type of waves involved and the direction of propagation of the incident waves, the resulting wave pattern depends on the wave types and the direction of propagation, with the same type of waves being transmitted after the interaction.

- Compression wave regions, may eventually coalesce into a discontinuity, known as shock wave or centered compression wave. On the other hand, centered expansion waves exist when a discontinuity propagates into the high pressure region. The governing equations do not apply through them, which have to be treated as mathematical discontinuities between continuous flow regions.

C.5.1.1 Derivation of the plasma Mach lines

To identify the plasma characteristic line(s) s, it has to be found the linear combination of the plasma momentum and ion continuity equations, respectively Eq. C.17 and C.18, which allows for the LHS to be written as follows: [The dimensionless superindex * is ignored within the present subsection for the sake of brevity.]

$$\Omega_1 \frac{\mathrm{d}n_i}{\mathrm{d}s} + \Omega_2 \frac{\mathrm{d}u_{zi}}{\mathrm{d}s}. \tag{C.25}$$

Initially, the Jacobians of the two equations are presented introducing the σ coefficients:

$$\left[\begin{array}{cc|cc} \sigma_1 & \sigma_1 u_{zi} & 0 & \sigma_1 n_i \\ 0 & \sigma_2 & \sigma_2 n_i & \sigma_2 n_i u_{zi} \end{array}\right] \cdot \left[\begin{array}{c} \partial n_i/\partial t \\ \partial n_i/\partial z \\ \hline \partial u_{zi}/\partial t \\ \partial u_{zi}/\partial z \end{array}\right] \tag{C.26}$$

where Eq. C.18 is multiplied by n_i. From the expression above, the LHS of the plasma compatibility equation can be provided. It can be expressed as follows:

$$\sigma_1 \frac{\mathrm{d}n_i}{\mathrm{d}t} + \sigma_2 n_i \frac{\mathrm{d}u_{zi}}{\mathrm{d}t} \tag{C.27}$$

where the coefficients of the time partial derivatives are factored out for convenience in writing, allowing for an explicit reference to $\mathrm{d}/\mathrm{d}t = \partial/\partial t + \lambda\partial/\partial z$, with $\mathrm{d}t = \mathrm{d}s$ and $\lambda = \mathrm{d}z/\mathrm{d}t$. λ is the system eigenvalue, defined by the compatibility equation Eq. C.27 as:

$$\lambda = \frac{\sigma_1 u_{zi} + \sigma_2}{\sigma_1} = \frac{\sigma_1 n_i + \sigma_2 n_i u_{zi}}{\sigma_2 n_i} \tag{C.28}$$

or, equivalently:

$$\begin{aligned} \sigma_1(u_{zi} - \lambda) + \sigma_2 = 0 \\ \sigma_1 n_i + \sigma_2(n_i u_{zi} - \lambda n_i) = 0 \end{aligned} \tag{C.29}$$

Equations C.29 constitute the characteristics of the flow limiting the domain of influence of a fluid particle. To solve them for σ_1,σ_2 beyond the trivial solution, the determinant of the coefficient matrix has to be null. This is fulfilled by the double λ solution:

$$\lambda = u_{zi} \pm 1 \tag{C.30}$$

respectively associated to two families of Mach lines, left-running (−) and right-running (+) ones. Any of these families may represent either a compression wave or an expansion wave.

Finally, for each λ-characteristic and taking $\sigma_1 = 1, \sigma_2 = \pm 1$, the dimensionless compatibility equation presented in Eq. C.27 is expressed in its complete form as:

$$\frac{\mathrm{d}(\ln n_i \pm u_{zi})}{\mathrm{d}t} = RHS \tag{C.31}$$

with RHS = $1/n_i\ [S \pm (j_x B_y + A_{zi})]$.

C.5.2. Algorithm

Above of all, by setting the Neumann condition to B_y, the induction equation (Eq. C.19) can be solved along any t-line, by means of applying finite differences with a backwards scheme.

The characteristics of the remaining two fluid equations, Eq. C.16 for neutrals' continuity and Eq. C.31 for plasma momentum in its compatibility equation form, have non-null slope, thus, t and z axes are coupled. This enables the implementation of a numerical scheme that propagates properties along the characteristics, offering a more physically insightful alternative to the conventional finite difference method (which could be applied using a forward scheme).

Hence, given a continuous-flow channel z segment:

- For the plasma, the advection process within z,t is more complex. A fluid particle in a continuous plasma flow region is influenced by the domain enclosed by the rearward Mach cone whose vertex sets at its location, while the domain this fluid particle affects is bounded by the two Mach lines emerging from it. In addition, when solving for electron pressure (i.e., T_e) as the third plasma problem variable apart from n_i, u_{zi}, the pathline can be used as the third characteristic line.

  In this case, a numerical scheme based on an inverse time-marching method to identify the backward influence Mach cone may result appropriate as a predictor. The proposed algorithm is top-level outlined in the flowchart shown in Figure C.1. The basis of the unit process to propagate a continuous-flow point, is outlined in the flowchart of Figure C.2, described below:

  1. First, the identification of the footpoint X_t associated to each one of the three backward characteristics of a solution node $X_{t+\Delta t}$, by correspondingly considering the propagation slopes $u^*_{zi} + 1$, u^*_{zi} and $u^*_{zi} - 1$. This is standard process is illustrated in Figure C.3(a).

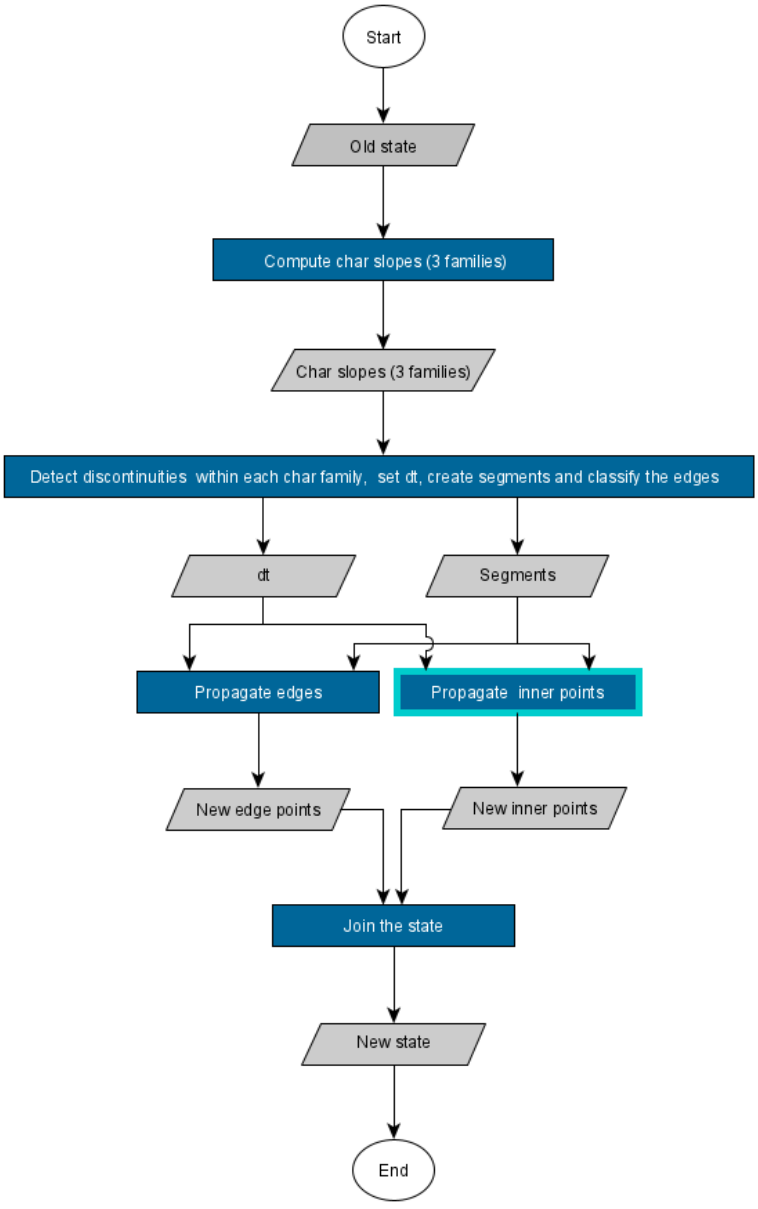

Figure C.1: **High-level scheme of the proposed algorithm to propagate the channel profile from the *old state* at t to the *new state* at $t + \mathbf{d}t$.** Dark blue rectangular blocks correspond to function blocks, and gray rhomboid ones to function input/outputs. Highlighted function block is described in Figure C.2.

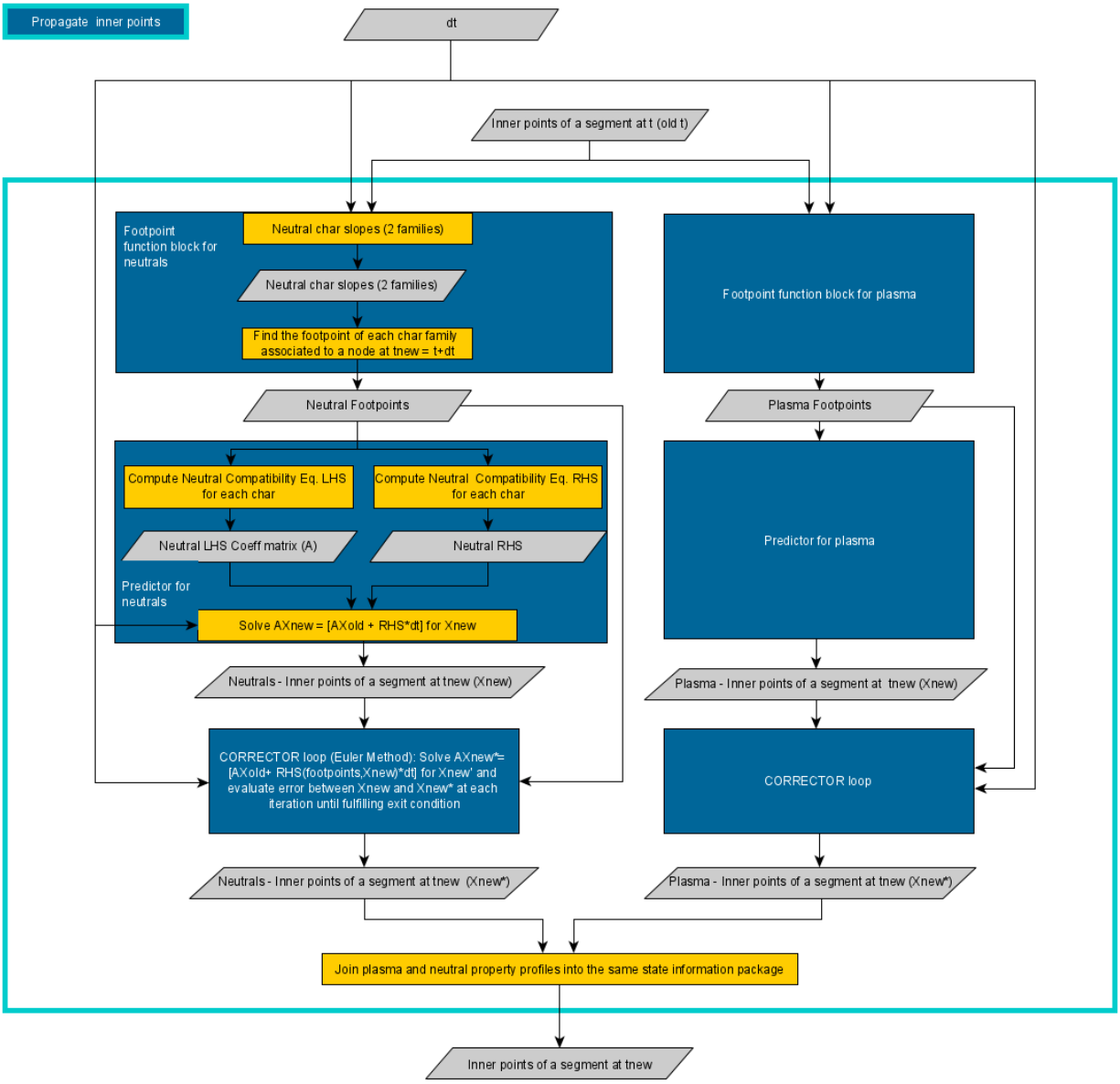

Figure C.2: **Low-level scheme of the function to propagate a point belonging to a continuous-flow region from old t to new t at $t + \mathrm{d}t$.** Dark blue and yellow rectangular blocks respectively correspond to function blocks and subfunctions, and gray rhomboid boxes to function input/outputs.

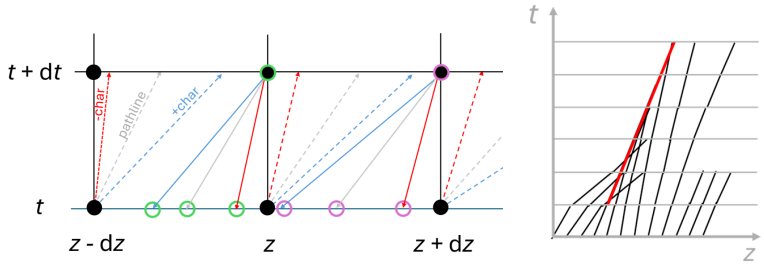

Figure C.3: **Some standard schemes about the numerical implementation of the Method of the characteristics: (a) Forward characteristics from t-line points (dot lines) and backward characteristics from points at $t + \Delta t$ (continuous lines).** Footpoints associated to a node at $t + \mathrm{d}t$ are highlighted with the same color. **(b) Coalescence of a compression wave (represented by a single family of characteristics) into a shock wave (in red).**

2. After that, solving of the equation system composed by the three compatibility equations (Eq. C.31) at the solution node $X_{t+\Delta t}$, by means of a forward scheme of finite differences which propagates the properties at the footpoints X_t plus the RHS contribution.

Typically, these steps are implemented within a predictor-corrector iterative scheme, which recalculates $X_{t+\Delta t}$ to enhance accuracy.

- In the case of the neutral population, the same procedure described for the plasma case can be used, nonetheless only two equations are required to solve u_{zn} and n_n. As u_{zn} is constant, the flow properties at a t-line are straightforwardly transported throughout a continuous right-running family of waves. Note that the advection slope of each fluid particle $\mathrm{d}z/\mathrm{d}t$ is modified by the non-null RHS, being u_{zn} only in the inhomogenous case.

Note that the subdivision of a t-state into different z-segments for separate propagation depends on the presence between them of a discontinuity in a family of characteristics. For the problem case, it is a shock wave [229], provoked by the coalescence of a compression wave that did not dissipate, as illustrated in Figure C.3(b). Proper time step selection enables the distinction between a severe compression and the limiting scenario, in which a discontinuity exists and it cannot be avoided. In the figure, it can be seen as a shock wave create a region of emptiness in the involved characteristic line family behind their direction of propagation, as these characteristics converge into it; the shock will overtake the characteristic lines of that family in front of it advances. However, a real shock wave transmits a weak continuous wave of the same family time-ahead of it towards the "empty" region. They have to be detected as they arise and to determine the properties on either side it, shock waves have to be treated as mathematical discontinuities. Serving to this purpose, the Rankine–Hugoniot jump relations can be applied in combination to the adaptation of the unit process described above (by distinguishing between the two sides of the discontinuity, only one family of characteristics exists behind the shock wave, while three families are present in front of it).

C.6. Summary

This work presents the assumptions and governing equations for an axial, three-fluid, unsteady MHD model. This provides a foundational step for future research towards a more comprehensive physical description of the in-channel physics of a PPT discharge. While the presented model is focused on the axial dynamics, to capture the full behavior of the system, it must be complemented by a radial treatment and a discharge model.

In addition, a finite-volume scheme is identified as suitable for the numerical integration of the proposed system.

Potential next steps are outlined in Section 7.1 in Chapter 7.

D. PERFORMANCE CHARACTERIZATION OF THE μ10 ELECTRON-CYCLOTRON-RESONANCE ION THRUSTER USING ALTERNATIVE PROPELLANTS: KRYPTON VS. XENON[32]

(**Abstract:**) A first krypton vs. xenon experimental comparison of the Hayabusa2 and DESTINY$^+$ μ10 Electron Cyclotron Resonance (ECR) gridded ion sources, and their ECR neutralizer, is presented. When operating on krypton, the ion sources deliver similar current in the same ropellant consumption range and provide equivalent thrust levels. Nevertheless, the system experiences about 30% of thruster efficiency loss as the neutralizer propellant demand for comparable current levels more than doubles.

D.1. Introduction

The μ10 Gridded Ion Thruster technology has more than two decades of flight operation heritage as the main propulsion system, on board the Japanese Hayabusa missions [230, 231, 232, 233, 234, 235, 236, 237]. It has pioneered the use of Electron Cyclotron Resonance (ECR) technology to produce the plasma. New improvements, focused on enhancing performances and lifetime, are being carried out for the DESTINY$^+$ mission, scheduled for launch in 2024 [238, 239].

Thanks to its low ionization energy (12.13 eV), large atomic mass (131.293 amu), and inertness, xenon (Xe) is the standard propellant used in electric propulsion, despite its limited availability and cost. In recent times, the interest in alternative propellants, to be used alone or in Xe mixtures, is rising noticeably. Iodine —similar mass, solid and less ionization energy, but corrosive—, krypton (Kr) and argon (Ar) —both inert, but less massive and higher ionization energy, especially the latest— are being actively studied. Krypton (14 eV, 83.798 amu), about 10% of xenon price, stands out as a promising prospect [240, 241, 242, 243, 244] for easier handling than Iodine.

The work reported throughout this appendix constitutes the first experimental comparison of the use of Kr vs. Xe on three different devices: Hayabusa2 and DESTINY$^+$ and μ10 ion sources, and the ECR neutralizer they use [245, 246]. Thruster performance is derived from electrical measurements.

The rest of the document is structured as follows. Section D.2 describes the experimental setup. Section D.3 shows the measurements and the overall performance metrics for the two ion sources and the cathode. Finally, Section D.4 summarizes the conclusions.

D.2. Experimental setup

The μ10 ion sources of Hayabusa2 and DESTINY$^+$ are composed of an ECR ionization chamber and the ion optics, i.e., a set of screen, acceleration, and deceleration grids as shown in Figure D.1. Permanent magnets generate a resonant magnetic field with the microwave power injected through the waveguide, heating up electrons beyond ionization energies [230]. Ions are extracted and accelerated by the three-grid system. The discharge chamber is electrically connected to the screen grid, at positive high voltage. In the present experiments, the sources are operated without external neutralizer, by grounding the deceleration grid. The operating conditions are detailed in Table D.1. The DESTINY$^+$ ion source is a redesign of the Hayabusa2 one to increase its performance [236, 238]. Both are essentially identical except for the arrangement of the downstream magnets, the grid sizing, and the location of the gas injectors, to increase the performance of the redesigned ion source. As detailed in [238], the new magnet arrangement enlarges the plasma generation

[32]This chapter reproduces the journal paper: S. Barquero, K. Tabata, R. Tsukizaki, M. Merino, J. Navarro-Cavallé, and K. Nishiyama, "**erformance characterization of the μ10 electron-cyclotron-resonance ion thruster using alternative propellants: krypton vs. xenon**", Acta Astronautica, vol. 211, p. 750-754, October 2023 [4]. DOI: 10.1016/J.ACTAASTRO.2023.06.036.

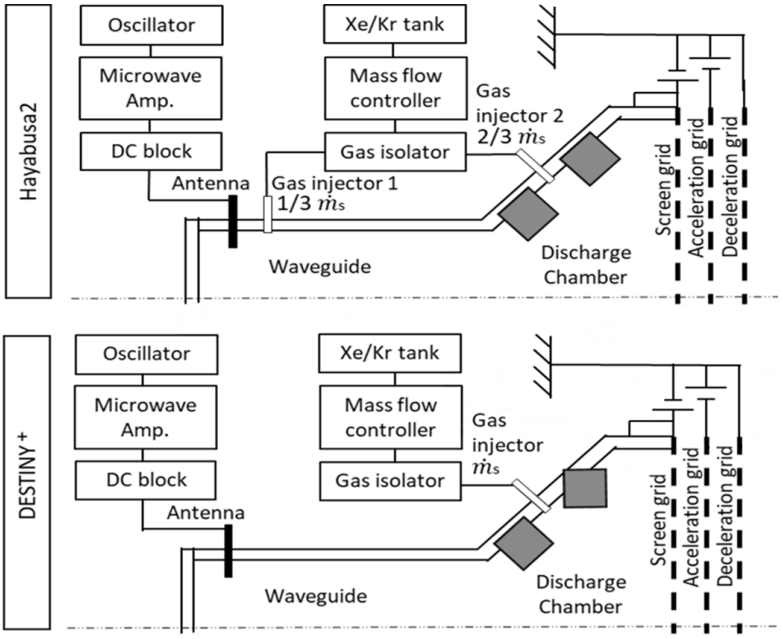

Figure D.1: **Schematic of the ion beam extraction experiment of the μ10 sources using krypton and xenon.** Materials: waveguide in aluminum, ionization chamber in iron, Samarium–cobalt (SmCo) magnets, connection to the screen grid in titanium, insulation between grids with ceramic and ceramic insulating the molybdenum antenna.

volume by almost 50% (using Xe). Also, having only the propellant injector near the ECR region (Figure D.1) improves plasma production [236, 238].

From charge conservation, the electric current to the screen grid and chamber walls (I_{sc}) equals in absolute value the electric current of ions coming through the screen grid. The ion current lost to the acceleration grid is denoted as I_{ac}. These currents have been measured with a resolution of 1 and 0.1 mA, respectively. The current to the deceleration grid (I_{de}), arising from slow charge-exchange and neutralizer ions in the near plume, was found to be about 2% of I_{sc} for Xe. Neglecting I_{de} and secondary emission from the grids, the ion beam current (I_b) is defined as $I_{sc} - I_{ac}$ [230, 231, 232, 233, 234, 235, 236, 237, 238, 239, 247, 248]. Thrust is proportional to I_b [249], and in-orbit determination computations of the Hayabusa2 mission [230] agree well with the simplified definition of I_b above.

The neutralizer consists of an ECR ionization chamber, with a single gas injector at the back, and an orifice downstream, as shown in Figure D.2. It operates [245] on the same principle as the sources, except that the waveguide is replaced by an antenna, around which the ionization happens. Electron current is extracted through the exit hole [245]. The cathode has been tested separately from the ion sources, using an auxiliary anode. For each discharge current (I_n) set, the anode voltage (V_n) is measured with a resolution of 0.01 V. Apart from the current extracted from the device, ionization outside of it is known to contribute to I_n [245, 246]. V_n was kept under 50 V. Table D.2 summarizes the main characteristics and operating conditions of the ECR neutralizer setup.

Forward (P_{MW}) and reflected ($Pref$) microwave powers have been measured for the ion sources and the neutralizer by means of the power amplifiers of the ground test facility. From now on, P_{MW} will be used in any calculation as, apart from being the one which is controllable in space operation, the power coupling keeps almost constant along the period of interest —$Pref < 0.1 P_{MW}$ for the two the three devices with both propellants. P_{MW} can be found in Tables D.1 and D.2.

Table D.1: **Ion beam extraction experiment characteristics of the μ10 sources using Kr and Xe.**

	Unit	Hayabusa2	DESTINY$^+$
Magnet configuration		Inner: 45°/Outer: 45°	Inner: 45°/Outer: 90°
Propellant injection points		Waveguide & Discharge chamber	Discharge chamber
SC grid thickness	mm	0.8	0.5
AC grid thickness	mm	1.0	1.0
Ion source length	cm	30	
AC grid orifice diameter	mm	1.5	1.2–1.4
SC-AC grid distance	mm	0.5	0.6
Open area diameter	mm	105.0	
Wave frequency	GHz	4.25	
Forward microwave power delivered to the ion source	W	34	
Screen Voltage	kV	1.52	1.525
Acceleration Voltage	V	−370	
Propellant flow rate*	sccm	Xe: 1.0 – 3.4 Kr: 1.0–5.0	Xe: 1.0–3.1 Kr: 1.0–4.1
Background pressure	Pa	Base: 10^{-5}. During operation: $< 5.0 \cdot 10^{-3}$.	
*) 1.0 sccm Xe = 0.098 mg/s = 4.4950 $\cdot 10^{17}$ particles/s. 1.0 sccm Kr = 0.062 mg/s = 4.4556 $\cdot 10^{17}$ particles/s.			

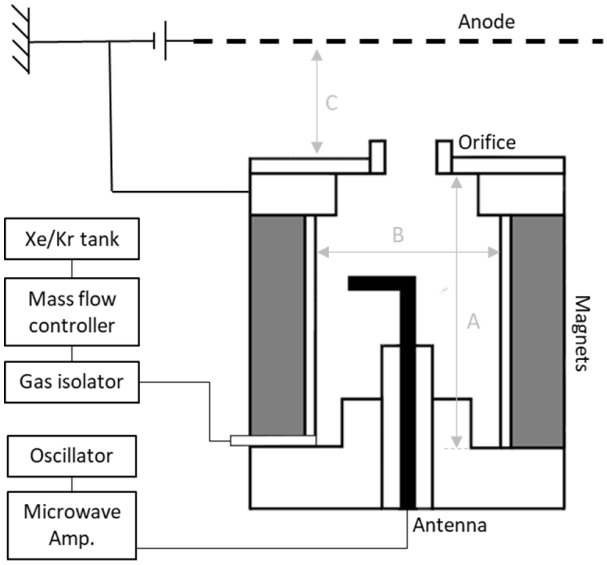

Figure D.2: **Schematic of the diode-mode test of the electron-cyclotron-resonance (ECR) neutralizer-cathode, which is used for neutralizing the plumes of the Hayabusa2 and DESTINY$^+$ ion sources.** A–C dimensions have been defined in Table D.2. Materials: ionization chamber in iron, SmCo magnets, thoriated tungsten covering the magnets at their exposed face to the plasma cavity, the exit plate and the orifice, and ceramic insulating the molybdenum antenna.

Table D.2: **Characteristics of the diode-mode test of the ECR neutralizer-cathode using krypton and xenon.** A–C dimensions have been defined in Figure D.2.

	Unit	Neutralizer-cathode
Orifice depth	mm	4
Inner height (A)	mm	12
Inner diameter (B)	mm	18
External diameter	mm	30
Auxiliary anode – neutralizer distance (C)	mm	11
Wave frequency	GHz	4.25
Forward microwave power delivered to the cathode	W	8
Anode voltage	V	<50
Propellant flow rate*	sccm	Xe: 0.3–0.8 Kr: 0.3–3.0
Background pressure	Pa	Base: 10^2. During operation: $< 4.0 \cdot 10^3$
*) 1.0 sccm Xe = 0.098 mg/s = 4.4950·10^{17}particles/s. 1.0 sccm Kr = 0.062 mg/s = 4.4556 · 10^{17} particles/s.		

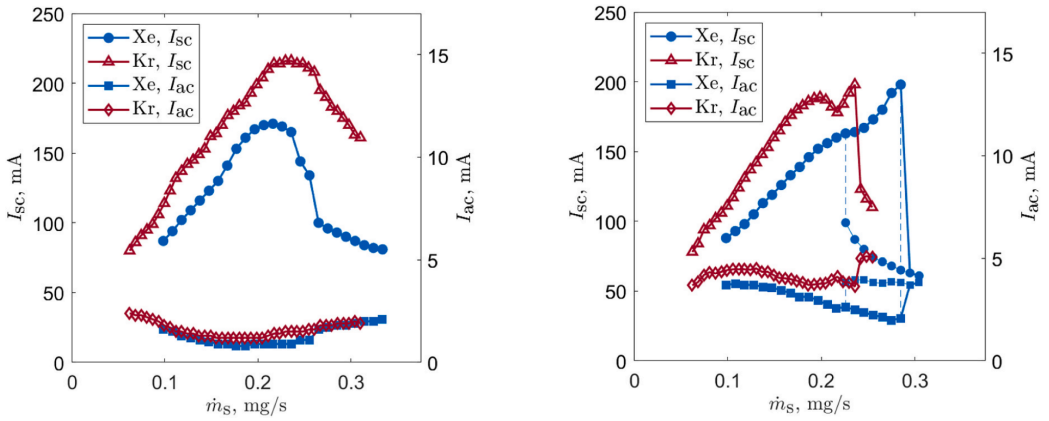

(a) (b)

Figure D.3: **Krypton vs. xenon comparison of the screen current I_{sc} and acceleration current I_{ac} of the Hayabusa2 (a) and DESTINY$^+$ (b) μ10 ion source configurations, as a function of the mass flow rate $\dot{m}_s$.**

D.3. Results

Figure D.3 collects the measured currents I_{sc} and I_{ac} for the two tested ions sources as a function of the mass flow rate ($\dot{m}_s$) for Kr and Xe. In the Hayabusa2 source, the I_{sc} shows a single maximum for both propellants. This maximum current is larger for Kr (216 mA) than for Xe (171 mA), but it is reached at slightly higher $\dot{m}_s$, 0.24 (3.8) vs. 0.22 mg/s (2.2 sccm) respectively. This I_{sc} peak experiences the maximum absorbed power, and beyond it, I_{sc} transitions from the "high current mode" (HCM) into the inefficient "low current mode" (LCM), with a higher P_{ref}. For both propellants, P_{ref} keeps around 3 W along the HCM prior to drop with the I_{sc} peak, to gradually increase to 8.5 W after it. In the LCM, the plasma within the waveguide-discharge chamber boundary region acquires an enhanced role [247, 248]. The transition to the LCM seems to be more abrupt for Xe than Kr. On the other hand, I_{ac} presents a minimum at 0.18 (1.8) – 0.19. mg/s (1.9 sccm) and 0.16 (2.5) – 0.20 mg/s (3.3 sccm) for Xe and Kr correspondingly.

In the updated ion source DESTINY$^+$, for Xe, I_{sc} is 15% higher than in the Hayabusa2 source and grows monotonically with $\dot{m}_s$, reaching 200 mA at 0.28 mg/s (2.9 sccm). Instead, the curve for Kr has a local maximum at 0.20 mg/s (3.2 sccm) and a minimum around 0.22 mg/s (3.5 sccm), prior to reaching the highest current in the measurement range, 200 mA at 0.24 mg/s (3.8 sccm). The transition between the HCM and LCM with $\dot{m}_s$ is more sudden for DESTINY$^+$ than for Hayabusa2. For DESTINY$^+$ and only

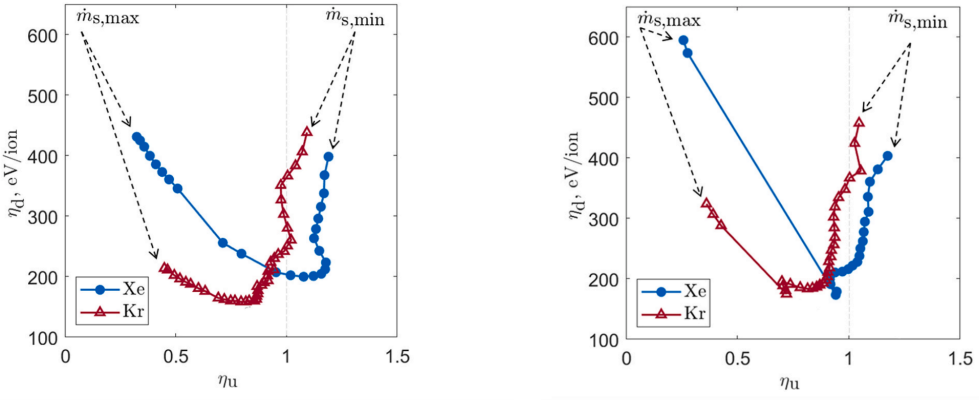

Figure D.4: **Krypton vs. xenon comparison of the estimates of the ion source discharge loss η_d, as the forward microwave power divided by the beam current P_{MW}/I_b, vs. the mass utilization efficiency η_u, formulated for singly charged ions as the ratio between the ionized and the propellant mass flow rate $\dot{m}_{s,ionized}/\dot{m}_s$, for the Hayabusa2 (a) and DESTINY$^+$ (b) μ10 ion source configurations [249].**

in the case of Xe, any of the two modes [247, 248] may occur at each $\dot{m}_s$ between 0.23 mg/s (2.3 sccm) and 0.28 mg/s (2.9 sccm), as represented in Figure D.3 (right). Beyond $\dot{m}_s$ 0.24 mg/s (3.8 sccm), only the LCM can be found. By contrast, for Kr, the transition seems to happen at a single $\dot{m}_s$, 0.24 mg/s (3.8 sccm). In DESTINY$^+$, for both propellants, P_{ref} sets under 2 W for the HCM, also lowers with the peak I_{sc}, and rises beyond 10 W in the LCM. The ion extraction efficiency is lower in DESTINY$^+$ than Hayabusa2 [238]; I_{ac} is generally larger than in the Hayabusa2 source and decreases monotonically with $\dot{m}_s$. For the two ion sources, at identical particle injection rates during the HCM, Xe provides higher I_{sc} than Kr —which involves larger $\dot{m}_s$ for Kr. This is expected due to the ionization energy gap. However, the transition to the LCM happens —or, in the case of DESTINY$^+$, may happen—at a lower I_{sc} for Xe than for Kr. This allows Kr to reach the highest I_{sc}. Figure D.4 depicts the discharge loss $\eta_d = P_{MW}/I_b$ vs. the mass utilization efficiency $\eta_u = \dot{m}_{s,ionized}/\dot{m}_s$, formulated in [249] —in case of "coexistence" of modes with $\dot{m}_s$, just the HCM is plotted. η_u has been computed assuming singly charged ions. The graph represents the source production performance at certain ion current, given the $\dot{m}_s$ and the P_{MW}. η_d is minimal at an intermediate $\dot{m}_s$ where I_b is maximum, for both prototypes and propellants. As described above, for the two devices, the $\dot{m}_s$ of this minimum η_d is larger for Kr than for Xe. The minimum η_d is lower for Kr than for Xe, unless the transition to the LCM considered for DESTINY$^+$ is the one that can happen at the highest $\dot{m}_s$. In that case, the minimum η_d is essentially shared by the two propellants. The lowest η_d occurs for the Hayabusa2 source and Kr, with only 150 eV/ion at 0.24 mg/s (3.8 sccm). η_u is almost saturated at $\dot{m}_s$ below the I_b peak and decreases after it with increasing $\dot{m}_s$ —consistently, with η_d growing up after its minimum. The authors note those values $\eta_u > 1$ obtained for the lower $\dot{m}_s$, especially for Xe, are an artifact, mainly due to the ignored presence of multiply charged ions. Doubly and triply charged ions for Xe operation were reported in [238], these could represent up to 16 and 4% of the total ion current, respectively, at the highest I_b, for the two configurations.

The characterizing I_n- V_n curves of the neutralizer-cathode are shown in Figure D.5. For the two propellants, at different mass flow rates ($\dot{m}_n$) —unstable operation at, approximately, $V_n < 25$ V for Xe and $I_n < 60$ mA for Kr. For a given $\dot{m}_n$, the V_n increases smoothly with the I_n drawn. In the range explored, increasing $\dot{m}_n$ results in a lower V_n for a set I_n. Overall, a higher amount of Kr is required to operate the cathode at the same I_n- V_n point, e.g., at 200 mA-45 V, 0.17 mg/s (2.8 sccm) for Kr vs. 0.07 mg/s (0.7 sccm) for Xe; which means the neutralizer is less efficient with Kr. Additionally, small but measurable hysteresis was observed at some values of $\dot{m}_n$ while increasing/decreasing I_n, shown as a shaded area. This behavior is more pronounced when operating with Kr, especially noticeable at any $\dot{m}_n$ between 0.11 (1.8) – 0.15

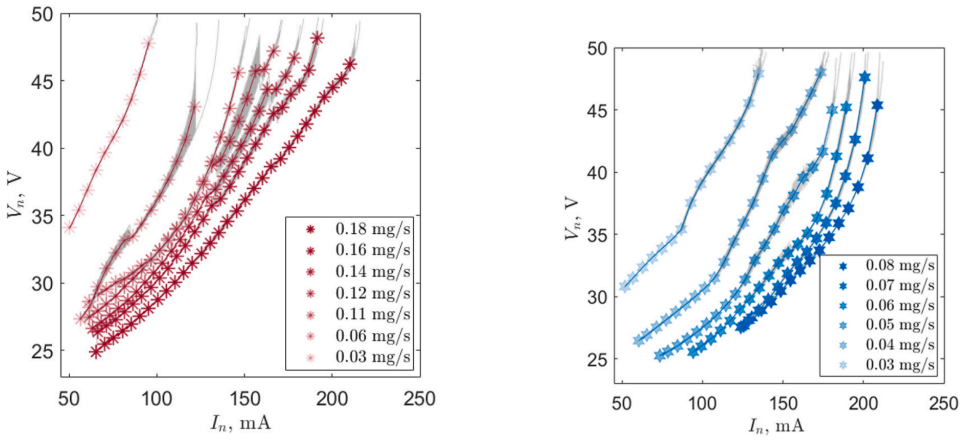

(a) (b)

Figure D.5: **Krypton (a) vs. xenon (b) measured current-voltage I_n-V_n curves of the neutralizer cathode operating in diode mode as a function of the mass flow rate $\dot{m}_n$. The shaded area represents the hysteresis detected during the experiment when increasing/decreasing the neutralizer current I_n.**

Table D.3: **Krypton vs. xenon comparison of the Hayabusa2 and DESTINY$^+$ performances at the operating point where the beam current I_b becomes maximum in each case, in the mass flow rate explored range. Performance figures are defined as in [249].**

	Unit	Hayabusa2		DESTINY$^+$	
		Krypton	Xenon	Krypton	Xenon
Ion source flow rate	mg/s	0.24	0.22	0.24	0.28
	(sccm)	(3.8)	(2.2)	(3.8)	(2.9)
Cathode flow rate	mg/s	0.18	0.06	0.17	0.08
	(sccm)	(2.9)	(0.6)	(2.6)	(0.8)
Beam current	mA	215	170	194	196
Thrust	mN	10.2	10.1	9.2	11.7
Specific impulse	s	2502	3774	2402	3290
Total power	W	489	408	458	455
Thruster (or total) efficiency	%	26	46	24	41

mg/s (2.4 sccm). Among others, this could be attributable to mode transitions in the ECR discharge of the neutralizer and deserves further work.

Finally, the results from the separated experiments of the ion sources and the neutralizer have been considered together to estimate the overall thruster performance. Table D.3 summarizes the main propulsive figures of merit as defined in [249], for the operating point that maximizes I_b in each case. The total thrust correction factor [249] used, which includes the corrections for the divergence and multiply charged species, is 0.92, from the Hayabusa2 flight model for Xe [230]. This value is valid for the two sources as the multi-charged ion efficiency and the beam divergence are alike [238]. The efficiency and specific impulse of both systems (Hayabusa2 and DESTINY$^+$) are degraded for Kr, mainly because the required $\dot{m}_n$ becomes comparable to $\dot{m}_s$. This situation is not compensated by the smaller η_d shown by Kr (Hayabusa2) discussed above. The calculated thrusts for Hayabusa2 are similar for Kr and Xe, around 10 mN. For DESTINY$^+$, a slightly lower thrust is expected for Kr (9.2 mN against 11.7 mN for Xe), a result driven mainly by the atomic mass decrease.

D.4. Conclusions

By adjusting the operating point, krypton can reach equivalent thrust levels to xenon for the Hayabusa2 and DESTINY$^+$ μ10 thrusters for comparable ion mass flow rates. Nevertheless, a deterioration of the overall performance of about 30% occurs, mainly due to the increased neutralizer mass flow rate. As a consequence, its redesign could be beneficial for krypton operation.

Further work is required to evaluate the effect of the propellant gas on the durability of the devices. Measuring multiply charged ions as a function of the mass flow rate for the two propellants is also advisable to improve the characterization of the mass utilization efficiency of the ion sources. Lastly, the physical mechanisms responsible for the delayed drop in power absorption with increased mass flow rate for krypton with respect to xenon should be investigated.

Acknowledgments

This work has been supported by the Japan Aerospace Exploration Agency (JAXA). The contribution of the UC3M researchers has been financed by the project ESPEOS under grant PID2019-108034RB-I00, MCIN/AEI/10.13039/501100011033. Furthermore, the authors would like to thank the JAXA Advanced Machining Technology Group for technical assistance.

BIBLIOGRAPHY

[1] UC3M, UPM, UCM, INTA, IAC, CAY, AIRBUS-DS, ATN, and SENER, "MARTINLARA Project Website," Accessed on February 16th, 2024.

[2] Barquero, S., Navarro-Cavallé, J., and Merino, M., "Pulsed plasma thruster exhaust reconstruction," *Plasma Sources Science and Technology*, Vol. 33, No. 4, 4 2024, pp. 045007.

[3] Barquero, S., Navarro-Cavallé, J., and Merino, M., "Reconstruction of the transient plume cross-section of a pulsed plasma thruster," *Plasma Sources Science and Technology*, Vol. 34, No. 5, may 2025, pp. 055003.

[4] Barquero, S., Tabata, K., Tsukizaki, R., Merino, M., Navarro-Cavallé, J., and Nishiyama, K., "Performance characterization of the μ10 electron-cyclotron-resonance ion thruster using alternative propellants: krypton vs. xenon," *Acta Astronautica*, Vol. 211, 2023, pp. 750–754.

[5] "Equipo de Propulsion Espacial y Plasmas," http://ep2.uc3m.es.

[6] Barquero, S., Merino, M., and Navarro-Cavallé, J., "Design of an experimental ablative pulsed plasma thruster for micropropulsion," *Space Propulsion Conference 2021*, No. 00254, Association Aéronautique et Astronautique de France, March 17-19, 2021.

[7] Barquero, S., Merino, M., and Navarro-Cavallé, J., "Experimental plume characterization of a low-power Ablative Pulsed Plasma Thruster (APPT)," 37th *International Electric Propulsion Conference*, No. IEPC-2022-556, Electric Rocket Propulsion Society, Boston, MA, June 19-23, 2022.

[8] Barquero, S., Merino, M., and Navarro-Cavallé, J., "Time-Resolved Reconstruction of the Plume of a Pulsed Plasma Thruster (PPT)," *10th EUCASS Conference*, Lausanne, Switzerland, July 9–13, 2023.

[9] Barquero, S., Navarro-Cavallé, J., and Merino, M., "Cross-sectional characterization of the exhaust of a Pulsed Plasma Thruster," 38th *International Electric Propulsion Conference*, No. IEPC-2024-387, Electric Rocket Propulsion Society, Toulouse, France, June 23-28, 2024.

[10] Barquero, S., Tabata, K., Tsukizaki, R., Merino, M., Navarro-Cavallé, J., and Nishiyama, K., "Alternative propellant study (krypton vs. xenon) of the μ10 ECR Gridded Ion Thruster at its Hayabusa2 and DESTINY$^+$ Missions," *34th ISTS Conference*, 2023.

[11] Barquero, S., Navarro-Cavallé, J., and Merino, M., "Data from: Pulsed plasma thruster exhaust reconstruction (10.5281/zenodo.10908405)," 2024.

[12] Barquero, S., Navarro-Cavallé, J., and Merino, M., "Data from: Reconstruction of the transient plume cross-section of a Pulsed Plasma Thruster (10.5281/zenodo.13820945)," 2024.

[13] Barquero, S., Navarro-Cavallé, J., and Merino, M., "Time-series ToF code for: Pulsed plasma thruster exhaust reconstruction," 2024.

[14] Barquero, S., Navarro-Cavallé, J., and Merino, M., "WAVES code for: Reconstruction of the transient plume cross-section of a Pulsed Plasma Thruster (10.5281/zenodo.14653074)," 2024.

[15] Barquero, S., Merino, M., and Navarro-Cavallé, J., "Preliminary test campaign of an ablative pulsed plasma thruster for micropropulsion," 5th *International Workshop on Micropropulsion and CubeSats*, Toulouse (online), 2021.

[16] Navarro-Cavallé, J., Inchingolo, M., Perrotin, T., Barquero, S., Fajardo, P., Merino, M., and Ahedo, E., "Experimental activities at the Plasma and Space Propulsion Team (EP2-UC3M)," *EPIC Workshop, Naples, May 9-12*, 2023.

[17] S., B., "Pulsed Plasma Thruster Design," Tech. rep., NANOSTAR Student Challenges - Report, NANOSTAR consortium - Interreg Sudoe Programme through the European Regional Development Fund (ERDF), 2021.

[18] S., B., "Informe de modelado, simulación, requisitos y diseño preliminar de sistema de micropropulsión PPT (M18)," Tech. rep., Millimeter wave Array at Room Temperature for INstruments in LEO Altitude Radio Astronomy (MARTINLARA) Project Report - Objective 4.1, Co-funded by the Consejería de Ciencia, Universidades e Innovación of the Comunidad de Madrid and the European Union, 2023.

[19] S., B., "Informe de ensayo y experimentación con prototipos PTT (M42)," Tech. rep., Millimeter wave Array at Room Temperature for INstruments in LEO Altitude Radio Astronomy (MARTINLARA) Project Report - Objective 4.3, Co-funded by the Consejería de Ciencia, Universidades e Innovación of the Comunidad de Madrid and the European Union, 2023.

[20] S., B., "Informe de desarrollo de modelo de ingeniería de sistema de micropropulsión PPT (M48)," Tech. rep., Millimeter wave Array at Room Temperature for INstruments in LEO Altitude Radio Astronomy (MARTINLARA) Project Report - Objective 4.4, Co-funded by the Consejería de Ciencia, Universidades e Innovación of the Comunidad de Madrid and the European Union, 2023.

[21] Cabello López, A., "Design and Development of a micro-PPT Thrust Balance," 2020.

[22] A. Cabello López, S. B., "Informe de preparación de micro balanza de empuje y puesta a punto de laboratorio (M24)," Tech. rep., Millimeter wave Array at Room Temperature for INstruments in LEO Altitude Radio Astronomy (MARTINLARA) Project Report - Objective 4.2, Co-funded by the Consejería de Ciencia, Universidades e Innovación of the Comunidad de Madrid and the European Union, 2023.

[23] Jahn, R., *Physics of Electric Propulsion*, Dover, 2006.

[24] Martínez-Sánchez, M. and Pollard, J., "Spacecraft Electric Propulsion — An Overview," *Journal of Propulsion and Power*, Vol. 14, No. 5, Sept. 1998, pp. 688–699.

[25] Garrigues, L. and Coche, P., "Electric propulsion: comparisons between different concepts," *Plasma Physics and Controlled Fusion*, Vol. 53, 2011, pp. 124011.

[26] Ahedo, E., "Plasmas for space propulsion," *Plasma Physics and Controlled Fusion*, Vol. 53, No. 12, 2011, pp. 124037.

[27] Saleh, J. H., Geng, F., Ku, M., and Walker, M. L., "Electric propulsion reliability: Statistical analysis of on-orbit anomalies and comparative analysis of electric versus chemical propulsion failure rates," *Acta Astronautica*, Vol. 139, 2017, pp. 141–156.

[28] ESA, "OneWeb (Eutelsat Group)." Accessed on April 6th, 2025.

[29] Burton, R. and Turchi, P., "Pulsed plasma thruster," *Journal Propulsion and Power*, Vol. 14, 1998, pp. 716–735.

[30] Rayburn, C. D., Campbell, M. E., and Mattick, A. T., "Pulsed Plasma Thruster System for Microsatellites," *Journal of Spacecraft and rockets*, Vol. 1, No. 42, 2005.

[31] Molina-Cabrera, P., Herdrich, G., Fausolas, S., Schönherr, T., and Komurasaki, K., "Pulsed Plasma Thrusters: a worldwide review and long yearned classification," *32nd Int. Electric Propulsion Conf. (IEPC), Wiesbaden, Germany, September 11–15th*, 2011.

[32] Ciaralli, S., Coletti, M., and Gabriel, S., "Results of the qualification test campaign of a Pulsed Plasma Thruster for Cubesat Propulsion (PPTCUP)," *Acta Astronautica*, Vol. 121, 2016, pp. 314–322.

[33] O'Reilly, D., Herdrich, G., Schäfer, F., Montag, C., Worden, S. P., Meaney, P., and Kavanagh, D. F., "A Coaxial Pulsed Plasma Thruster Model with Efficient Flyback Converter Approaches for Small Satellites," *Aerospace*, Vol. 10, No. 6, 2023.

[34] Michaux, E., Mazouffre, S., and Blanchet, A., "Time evolution of plasma parameters in the jet of a low-power vacuum arc thruster," *Journal of Electric Propulsion*, Vol. 1, 06 2022.

[35] Michaux, E. and Mazouffre, S., "Time-of-Flight Measurements in the Jet of a High-Current Vacuum Arc Thruster," *Aerospace*, Vol. 10, No. 12, 2023.

[36] Keidar, M., Schein, J., Wilson, K., Gerhan, A., Au, M., Tang, B., Idzkowski, L., Krishnan, M., and Beilis, I. I., "Magnetically enhanced vacuum arc thruster," *Plasma Sources Science and Technology*, Vol. 14, No. 4, sep 2005, pp. 661.

[37] Keidar, M., Zhuang, T., Shashurin, A., Teel, G., Chiu, D., Lukas, J., Haque, S., and Brieda, L., "Electric propulsion for small satellites," *Plasma Physics and Controlled Fusion*, Vol. 57, No. 1, nov 2014, pp. 014005.

[38] Kamimura, T. and Tahara, H., *R&D, Launch and Initial Operation of the Osaka Institute of Technology 1st PROITERES Nano-Satellite with Electrothermal Pulsed Plasma Thrusters and Development of the 2nd and 3rd Satellites*.

[39] Ono, K., Morikawa, N., Ryuho, K., Enomoto, K., Kanaoka, K., Fujita, R., Tahara, H., Takada, K., and Wakizono, T., "Development of Commercially-Available Electrothermal Pulsed Plasma Thruster System for Micro/Nano-Satellites at Osaka Institute of Technology," *35th International Electric Propulsion Conference IEPC-2017*, Vol. 92, 2017, pp. 8–12.

[40] Cao, B., Ma, Z., Cao, Z., Wang, J., Geng, Y., and Wang, Z., "Ignition Stability of Electrothermal Pulsed Plasma Thruster," *2023 30th International Symposium on Discharges and Electrical Insulation in Vacuum (ISDEIV)*, 2023, pp. 549–552.

[41] Bathgate, S., Bilek, M., and Mckenzie, D., "Electrodeless plasma thrusters for spacecraft: a review," *Plasma Science and Technology*, Vol. 19, No. 8, 2017, pp. 083001.

[42] Inchingolo, M., *Design, development, and characterization of a microwave electrodeless plasma thruster*, Ph.D. thesis, Universidad Carlos III de Madrid, Leganés, Spain, 2024.

[43] Merino, M., *Analysis of magnetic nozzles for space plasma thrusters*, Ph.D. thesis, Universidad Politécnica de Madrid, 2013.

[44] Ling, W., Zhang, Z., and Tang, H., "Progress in Fundamental Pulsed Plasma Thruster Research," *35th International Electric Propulsion Conference, Electric Rocket Propulsion Soc., IEPC Paper*, Vol. 140, 2017.

[45] Zhang, Z., Ling, W. Y. L., bin Tang, H., Cao, J., Liu, X., and fei Wang, N., "A review of the characterization and optimization of ablative pulsed plasma thrusters," *Reviews of Modern Plasma Physics*, Vol. 3, No. 5, 2019.

[46] Cheng, D. Y., "Plasma deflagration and the properties of a coaxial plasma deflagration gun," *Nuclear Fusion*, Vol. 10, No. 3, sep 1970, pp. 305.

[47] Rieker, G. B., Poehlmann, F., and Cappelli, M. A., "A Thomson-type mass and energy spectrometer for characterizing ion energy distributions in a coaxial plasma gun operating in a gas-puff mode." *Physics of plasmas*, Vol. 20 7, 2013, pp. 73115.

[48] Loebner, K. T. K., Underwood, T. C., and Cappelli, M. A., "Evidence of Branching Phenomena in Current-Driven Ionization Waves," *Phys. Rev. Lett.*, Vol. 115, Oct 2015, pp. 175001.

[49] Schönherr, T., Abe, Y., Okamura, K., Koizumi, H., and Arakawa, Y., "Influence of Propellant in the Discharge Process of PPT," 07 2012.

[50] Rachubinski, H., Barral, S., Kurzyna, J., Szelecka, A., Remirez, E., Martin, R., Ortiz, P., Alonso, J., Bottinelli, S., Mabillard, Y., Zaldivar, A., Rangsten, p., and Koppel, C., "First Experimental Characterization of a Pulsed Plasma Thruster with Non-Volatile Liquid Propellant," 05 2014.

[51] Ling, W. Y. L., Schönherr, T., and Koizumi, H., "Characteristics of a non-volatile liquid propellant in liquid-fed ablative pulsed plasma thrusters," *Journal of Applied Physics*, Vol. 121, No. 7, 02 2017, pp. 073301.

[52] Rezaeiha, A. and Schönherr, T., "Review of worldwide activities in liquid-fed pulsed plasma thruster," *Journal of Propulsion and Power*, Vol. 30, No. 2, 2014, pp. 253–264.

[53] Ling, W. Y. L., Schönherr, T., and Koizumi, H., "Characteristics of a non-volatile liquid propellant in liquid-fed ablative pulsed plasma thrusters," *Journal of Applied Physics*, Vol. 121, No. 7, 2017, pp. 073301.

[54] Huang, M., Ling, W. Y. L., Zhang, S., Liu, X., and Wang, N., "Spectroscopic plasma plume study of a non-volatile liquid-fed pulsed plasma thruster," *Acta Astronautica*, Vol. 198, 2022, pp. 76–86.

[55] Zhang, S., Wu, Z., Huang, T., Fu, H., and Ling, W. Y. L., "Study on the ablation of a pulsed plasma thruster with a non-volatile liquid propellant," *Vacuum*, Vol. 216, 2023, pp. 112380.

[56] Jakubczak, M., Riazantsev, A., Cichorek, O., Jardin, A., Kurzyna, J., Drożdż, P., Palacz, T., Chuchla, M., Łabuz, R., and Bywalec, G., "Design and performance of a 1 J ablative pulsed plasma thruster fed with non-volatile liquid propellant," *Acta Astronautica*, Vol. 228, 2025, pp. 813–827.

[57] Jakubczak, M., Jardin, A., and Kurzyna, J., "Plume measurements of a 1 J ablative pulsed plasma thruster fed with non-volatile liquid propellant," *Plasma Sources Science and Technology*, Vol. 34, No. 1, jan 2025, pp. 015010.

[58] Riazantsev, A., Jakubczak, M., Cichorek, O., and Kurzyna, J., "Side and front fast imaging of solid and liquid fed ablative pulsed plasma thruster's discharge," *Acta Astronautica*, Vol. 225, 2024, pp. 583–594.

[59] Rayburn, C., Campbell, M., Hoskins, W., and Cassady, R., "Development of a micro pulsed plasma thruster for the Dawgstar nanosatellite," *36th AIAA/ASME/SAE/ASEE Joint Propulsion Conference and Exhibit*, 2000, p. 3256.

[60] Nawaz, A., R, A., and Auweter-Kurtz, M., "Thrust efficiency optimization of the pulsed plasma thruster SIMP-LEX," *Acta Astronautica*, Vol. 67, 2010, pp. 440–448.

[61] Schönherr, T., Nees, F., Arakawa, Y., Komurasaki, K., and Herdrich, G., "Characteristics of plasma properties in an ablative pulsed plasma thruster," *Physics of Plasma*, Vol. 20, No. 3, 2013, pp. 033503.

[62] Shaw, P., *Pulsed Plasma Thrusters for Small Satellites*, Ph.D. thesis, University of Surrey, 2012.

[63] Guarducci, F., *Design and Testing of a Micro PPT for CubeSat Applications*, Ph.D. thesis, University of Southampton, 2012.

[64] Schäfer, F., Montag, C., Herdrich, G., Laufer, R., Santoni, F., Piergentili, F., Marzioli, P., Amadio, D., Frezza, L., Dannenmayer, K., and Armo, J., "Flight results of the PETRUS pulsed plasma thruster on the 3u CubeSat GreenCube," 09 2022.

[65] Jakubczak, M., Jardin, A., and Kurzyna, J., "Analysis of composition and dynamics of the plasma plume emitted by a 1 J pulsed plasma thruster fed with polytetrafluoroethylene and determination of thruster efficiency components," *Physics of Plasmas*, Vol. 31, No. 5, 05 2024, pp. 053501.

[66] LING, W. Y. L., ZHANG, S., FU, H., HUANG, M., QUANSAH, J., LIU, X., and WANG, N., "A brief review of alternative propellants and requirements for pulsed plasma thrusters in micropropulsion applications," *Chinese Journal of Aeronautics*, Vol. 33, No. 12, 2020, pp. 2999–3010.

[67] Glascock, M. S., Rovey, J., Williams, S., and Thrasher, J., *Plasma Plume Characterization of Electric Solid Propellant Micro Pulsed Plasma Thrusters*, 2015.

[68] Sze, S. M. and Ng, K. K., *Physics of Semiconductor Devices*, Wiley-Interscience, Hoboken, NJ, 3rd ed., 2006.

[69] Miller, H. C., "Surface flashover of insulators," *IEEE Transactions on Electrical Insulation*, Vol. 24, No. 5, 1989, pp. 765–786.

[70] Brady, M. E. and Aston, G., "Pulsed plasma thruster ignitor plug ignition characteristics," *Journal of Spacecraft and Rockets*, Vol. 20, No. 5, 1983, pp. 450–451.

[71] Shaw, P. and Lappas, V., "Modeling of a pulsed plasma thruster; simple design, complex matter," *2nd Space Propulsion Conference*, 2010.

[72] Bogatyi, A. V., D'yakonov, G. A., and Semenikhin, S., "Mechanisms for the Formation of Parasitic Propellant Consumption in an Ablative Pulsed Plasma Thruster," *Cosmic Research*, Vol. 57, 2019, pp. 310 – 316.

[73] Polzin, K., Martin, A., Little, J., Promislow, C., Jorns, B., and Woods, J., "State-of-the-Art and Advancement Paths for Inductive Pulsed Plasma Thrusters," *Aerospace*, Vol. 7, No. 8, 2020.

[74] Mazouffre, S., "Electric Propulsion for Satellites and Spacecraft: established Technologies and Novel Approaches," *Plasma Sources Science and Technology*, Vol. 25, No. 3, 2016, pp. 033002.

[75] Lev, D., Myers, R. M., Lemmer, K. M., Kolbeck, J., Koizumi, H., and Polzin, K., "The technological and commercial expansion of electric propulsion," *Acta Astronautica*, Vol. 159, 2019, pp. 213–227.

[76] Choueiri, E., "A critical history of electric propulsion: The first 50 years (1906-1956)," *Journal of Propulsion and Power*, Vol. 20, No. 2, 2004, pp. 193–203.

[77] "European Space Agency Website," Accessed on February 17th, 2024.

[78] del Amo, J. A., "Electric Propulsion at the European Space Agency (ESA)," 2021.

[79] Page, G. S., "Gunter's Space Page," Accessed on April 6th, 2025.

[80] Group, T., "Thales Group website," Accessed on April 6th, 2025.

[81] Rosati Azevedo, E., Berhe, M., Jones-Tett, K., Sadler, J., Potrivitu, G.-C., Laterza, M., Mark, L. J. W., Muñoz Tejeda, J., Moloney, R., and Knoll, A., "Joint Development of a Water Electrolysis Propelled Hall Effect Thruster and LaB6 Hollow Cathode," 06 2024.

[82] "Starlink (SpaceX)." Accessed on February 17th, 2024.

[83] "OneWeb (Eutelsat Group)." Accessed on February 17th, 2024.

[84] Dale, E., Jorns, B., and Gallimore, A., "Future Directions for Electric Propulsion Research," *Aerospace*, Vol. 7, No. 9, 2020.

[85] Levchenko, I., Bazaka, K., Ding, Y., Raitses, Y., Mazouffre, S., Henning, T., Klar, P. J., Shinohara, S., Schein, J., Garrigues, L., Kim, M., Lev, D., Taccogna, F., Boswell, R. W., Charles, C., Koizumi, H., Shen, Y., Scharlemann, C., Keidar, M., and Xu, S., "Space micropropulsion systems for Cubesats and small satellites: From proximate targets to furthermost frontiers," *Applied Physics Reviews*, Vol. 5, No. 1, 02 2018, pp. 011104.

[86] O'Reilly, D., Herdrich, G., and Kavanagh, D. F., "Electric Propulsion Methods for Small Satellites: A Review," *Aerospace*, Vol. 8, No. 1, 2021.

[87] Lemmer, K., "Propulsion for CubeSats," *Acta Astronautica*, Vol. 134, 2017, pp. 231–243.

[88] Bromaghim, D., Spanjers, G., Spores, R., Burton, R., Carroll, D., and Schilling, J., "A proposed on-orbit demonstration of an advanced pulsed-plasma thruster for small satellite applications," *2000 IEEE Aerospace Conference. Proceedings (Cat. No.00TH8484)*, Vol. 4, 2000, pp. 75–84 vol.4.

[89] Guarducci, F., Coletti, M., and Gabriel, S., "Design and testing of a micro pulsed plasma thruster for Cubesat application," *International Electric Propulsion Conference*, 2011, pp. 2011–239.

[90] Space, I., "IENAI Space website," Accessed on April 6th, 2025.

[91] Schönherr, T., Nees, F., Koizumi, H., Arakawa, Y., Manna, S., Lau, M., Herdrich, G., and Fasoulas, S., "Mass and Plasma Characteristics in the Current Sheet of a Pulsed Plasma Thruster," *32nd International Electric Propulsion Conference*, 09 2011.

[92] Schönherr, T., Komurasaki, K., and Herdrich, G., "Propellant Utilization Efficiency in a Pulsed Plasma Thruster," *Journal of Propulsion and Power*, Vol. 29, No. 6, 2013, pp. 1478–1487.

[93] Vondra, R., Thomassen, K., and Solbes, A., "A pulsed electric thruster for satellite control," *Proceedings of the IEEE*, Vol. 59, No. 2, 1971, pp. 271–277.

[94] Myers, R. M., Arrington, L. A., Pencil, E., Carter, J., Heminger, J., and Gatsonis, N., "Pulsed plasma thruster contamination," *32nd joint propulsion conference and exhibit*, 1996, p. 2729.

[95] Antropov, N., Gomilka, L., Diakonov, G., Krivonosov, I., G.Popov, and M.Orlov, "Parameters of plasmoids injected by PPT," *33rd Joint Propulsion Conference and Exhibit*, 1997.

[96] Solbes, A., Thomassen, K., and Vondra, R., "Analysis of solid teflon pulsed plasma thruster," *Journal of Spacecraft and Rockets*, Vol. 7, No. 12, 1970, pp. 1402–1406.

[97] Thomassen, K. I. and Vondra, R. J., "Exhaust velocity studies of a solid Teflon pulsed plasma thruster," *Journal of Spacecraft and Rockets*, Vol. 9, No. 1, 1972, pp. 61–64.

[98] Gatsonis, N. A., Eckman, R., Yin, X., Pencil, E. J., and Myers, R. M., "Experimental investigations and numerical modeling of pulsed plasma thruster plumes," *Journal of Spacecraft and Rockets*, Vol. 38, No. 3, 2001, pp. 454–464.

[99] Markusic, T. and Spores, R., "Spectroscopic emission measurements of a pulsed plasma thruster plume," *33rd Joint Propulsion Conference and Exhibit*.

[100] Koizumi, H., Noji, R., Komurasaki, K., and Arakawa, Y., "Plasma acceleration processes in an ablative pulsed plasma thruster," *Physics of Plasmas*, Vol. 14, No. 3, 2007.

[101] Rudolph, L. and Jones, R., "Pulsed plasma thruster contamination studies," *14th International Electric Propulsion Conference*, 1979.

[102] Gatsonis, N. A., Byrne, L. T., Zwahlen, J. C., Pencil, E. J., and Kamhawi, H., "Current-mode triple and quadruple Langmuir probe methods with applications to flowing pulsed plasmas," *IEEE transactions on plasma science*, Vol. 32, No. 5, 2004, pp. 2118–2129.

[103] LING, W. Y. L., LIU, S., LIU, X., WU, Z., and WANG, N., "Volumetric Langmuir probe mapping of a transient pulsed plasma thruster plume," *Plasma Science and Technology*, Vol. 22, No. 9, jul 2020, pp. 094010.

[104] Jakubczak, M., Jardin, A., and Kurzyna, J., "Plasma plume composition of a pulsed plasma thruster fed with perfluoropolyether," *38th International Electric Propulsion (IEPC-2024-336)*, 2024.

[105] Zhang, Z., Schäfer, F., Ali, M. R., Ling, W. Y. L., and Liu, X., "Vector-time-resolved in-plume plasma current density flux measurement in a pulsed plasma thruster," *Acta Astronautica*, Vol. 226, 2025, pp. 1–10.

[106] Barquero, S., Navarro-Cavallé, J., and Merino, M., "Reconstruction of the transient plume cross-section of a pulsed plasma thruster," *Plasma Sources Science and Technology*, Vol. 34, No. 5, may 2025, pp. 055003.

[107] Wang, W., Liu, F., Wang, X., and Liang, R., "Study on electron temperature in an ablative pulsed plasma thruster by optical emission spectroscopy," *Europhysics Letters*, Vol. 101, No. 5, mar 2013, pp. 55001.

[108] Keidar, M., Boyd, I. D., and Beilis, I. I., "Ionization and ablation phenomena in an ablative plasma accelerator," *Journal of Applied Physics*, Vol. 96, 2004, pp. 5420–5428.

[109] Pellegrini, G., Mancini, E., Paganucci, F., and Andrenucci, M., "Development and Characterization of a Pulsed Plasma Thruster," *Space Propulsion 2018*, 2018.

[110] Eckman, R., "Pulsed plasma thruster plume diagnostics," *36th AIAA Aerospace Sciences Meeting and Exhibit*.

[111] Schönherr, T., Stein, M., Komurasaki, K., and Herdrich, G., "Observation of discharge arc properties in pulsed plasma thruster," *2014 International Symposium on Discharges and Electrical Insulation in Vacuum (ISDEIV)*, IEEE, pp. 705–708.

[112] Keidar, M., Boyd, I. D., Gulczinski III, F. S., Antonsen, E. L., and Spanjers, G. G., "Analyses of Teflon surface charring and near field plume of a micro-pulsed plasma thruster," *International Electric Propulsion Conference*, 2001.

[113] Parker, K., "Pulsed Plasma Thruster plume analysis," *Acta Astronautica*, Vol. 53, No. 4, 2003, pp. 789–795.

[114] Ling, W. Y. L., Zhang, Z., Tang, H., Liu, X., and Wang, N., "In-plume acceleration of leading-edge ions from a pulsed plasma thruster," *Plasma Sources Science and Technology*, Vol. 27, No. 10, oct 2018, pp. 104002.

[115] Tani, Y., Tsukizaki, R., Koda, D., Nishiyama, K., and Kuninaka, H., "Performance improvement of the 10 microwave discharge ion thruster by expansion of the plasma production volume," *Acta Astronautica*, Vol. 157, 2019, pp. 425–434.

[116] Coletti, M., Ciaralli, S., and Gabriel, S. B., "PPT Development for Nanosatellite Applications: Experimental Results," *IEEE Transactions on Plasma Science*, Vol. 43, No. 1, 2015, pp. 218–225.

[117] Hu, T., Wu, Z., Huang, T., Zhang, Z., Yang, L., and Zhang, S., "Study on the influence of ignitor position on a coaxial pulsed plasma thruster," *Vacuum*, Vol. 218, 2023, pp. 112644.

[118] Raizer, Y., *Gas Discharge Physics*, Springer, Berlin, 1991.

[119] Dyke, W. P. and Trolan, J. K., "Field Emission: Large Current Densities, Space Charge, and the Vacuum Arc," *Phys. Rev.*, Vol. 89, Feb 1953, pp. 799–808.

[120] Peschot, A., Bonifaci, N., Lesaint, O., Valadares, C., and Poulain, C., "Deviations from the Paschen's law at short gap distances from 100 nm to 10 μm in air and nitrogen," *Applied Physics Letters*, Vol. 105, No. 12, 09 2014, pp. 123109.

[121] Sun, G. and Wu, Z., "Ignition mechanism in ablative pulsed plasma thrusters with coaxial semiconductor spark plugs," *Acta Astronautica*, Vol. 151, 2018, pp. 120–124.

[122] Ciaralli, S., Coletti, M., Guarducci, F., and Gabriel, S., "PPTCUP lifetime test results," *33rd International Electric Propulsion Conference, Washington DC, USA*, Citeseer, 2013.

[123] Ju.E., F., P.D., L., V.A., L., and A.V., L., "Ionization spark plug patent RU 2 192 082 C1," Accessed on April 6th, 2025.

[124] Anderson, R. A. and Brainard, J. P., "Mechanism of pulsed surface flashover involving electron-stimulated desorption," *Journal of Applied Physics*, Vol. 51, No. 3, 03 1980, pp. 1414–1421.

[125] III, F. G., Dulligan, M., Lake, J., and Spanjers, G., *Micropropulsion research at AFRL.*

[126] Keidar, M., Boyd, I. D., Antonsen, E. L., Gulczinski, F. S., and Spanjers, G. G., "Propellant Charring in Pulsed Plasma Thrusters," *Journal of Propulsion and Power*, Vol. 20, No. 6, 2004, pp. 978–984.

[127] Keidar, M., Boyd, I. D., Antonsen, E. L., Burton, R., and Spanjers, G. G., "Optimization Issues for a Micropulsed Plasma Thruster," *Journal of Propulsion and Power*, Vol. 22, No. 1, 2006, pp. 48–55.

[128] Wu, Z., Sun, G., Yuan, S., Huang, T., Liu, X., Xie, K., and Wang, N., "Discharge reliability in ablative pulsed plasma thrusters," *Acta Astronautica*, Vol. 137, 2017, pp. 8–14.

[129] Since, H. J. H., Sijher Taninder, S., and Kai, B. J., "The impact of capacitors selection and placement to the ESL and ESR," *2005 International Symposium on Electronics Materials and Packaging*, 2005, pp. 258–261.

[130] Cassady, R. J., Hoskins, W. A., Campbell, M., and Rayburn, C., "A micro pulsed plasma thruster (PPT) for the" Dawgstar" spacecraft," *2000 IEEE Aerospace Conference. Proceedings (Cat. No. 00TH8484)*, Vol. 4, IEEE, 2000, pp. 7–14.

[131] Uezu, J., Iio, J., Kamishima, Y., Takegahara, H., Wakizono, T., and Sugiki, M., "Study on pulsed plasma thruster configuration to expand impulse bit range," *International Electric Propulsion Conference*, Vol. 234, 2005.

[132] Shaw, P., Lappas, V., and Underwood, C., "Design, development and evaluation of an 8 μPPT propulsion module for a 3U CubeSat application," *32nd International Electric Propulsion Conference*.

[133] Coletti, M., Ciaralli, S., and Gabriel, S. B., "PPT development for nanosatellite applications: Experimental results," *IEEE Transactions on Plasma Science*, Vol. 43, No. 1, 2014, pp. 218–225.

[134] Shangmin, W., Licheng, T., Weiwei, F., Tianping, Z., Xinwei, C., Changwen, C., Xingda, L., Jun, G., and Weidong, L., "μ-PPT electro-propulsion system Development and First fight Application," *system*, Vol. 1, 2017, pp. 9.

[135] Lau, M., Manna, S., Herdrich, G., Schönherr, T., and Komurasaki, K., "Investigation of the plasma current density of a pulsed plasma thruster," *Journal of Propulsion and Power*, Vol. 30, No. 6, 2014, pp. 1459–1470.

[136] Spanjers, G. G., Lotspeich, J. S., McFall, K. A., and Spores, R. A., "Propellant Losses Because of Particulate Emission in a Pulsed Plasma Thruster," *Journal of Propulsion and Power*, Vol. 14,No 4, 1998, pp. 554–559.

[137] Keidar, M., Boyd, I. D., and Beilis, I. I., "Model of Particulate Interaction with Plasma in a Teflon Pulsed Plasma Thruster," *Journal of Propulsion and Power*, Vol. 17, No. 1, 2001, pp. 125–131.

[138] Li, Z., Liu, J., Ohki, Y., Chen, G., Gao, H., and Li, S., "Surface flashover in 50 years: Theoretical models and competing mechanisms," *High Voltage*, Vol. 8, No. 5, 2023, pp. 853–877.

[139] Kumagai, N., Igarashi, M., Sato, K., Tamura, K., Kawahara, K., and Takegahara, H., "Plume Diagnostics in Pulsed Plasma Thruster," *38th Joint Propulsion Conference and Exhibit*, 2002.

[140] Keidar, M., Boyd, I. D., Antonsen, E. L., Burton, R., and Spanjers, G. G., "Optimization Issues for a Micropulsed Plasma Thruster," *Journal of Propulsion and Power*, Vol. 22, No. 1, 2006, pp. 48–55.

[141] Lobbia, R. B. and Beal, B. E., "Recommended Practice for Use of Langmuir Probes in Electric Propulsion Testing," *Journal of Propulsion and Power*, Vol. 33, No. 3, 2017, pp. 566–581.

[142] Guman, W. J., "Solid Propellant Pulsed Plasma Propulsion System Design," *J. Spacecraft*, Vol. 13, No. 1, 1976, pp. 51–53.

[143] Edamitsu, T. and Tahara, H., "Experimental and numerical study of an electrothermal pulsed plasma thruster for small satellites," *Vacuum*, Vol. 80, No. 11-12, 2006, pp. 1223–1228.

[144] Mikellides, P. and Turchi, P., "Modeling of late-time ablation in Teflon pulsed plasma thrusters," *32nd Joint Propulsion Conference and Exhibit*.

[145] Peradzyński, Z., Makowski, K., and Kurzyna, J., "Early stage of the discharge in ablative pulsed plasma thrusters," *Plasma Sources Science and Technology*, Vol. 28, No. 2, feb 2019, pp. 024001.

[146] Keidar, M., Boyd, I. D., Antonsen, E. L., Burton, R., and Spanjers, G. G., "Optimization Issues for a Micropulsed Plasma Thruster," *Journal of Propulsion and Power*, Vol. 22, No. 1, 2006, pp. 48–55.

[147] Mikellides, P. G., Henrikson, E. M., and Rajagopalan, S. S., "Theoretical Formulation for the Performance of Rectangular, Breech-Fed Pulsed Plasma Thrusters," *Journal of Propulsion and Power*, Vol. 35, No. 4, 2019, pp. 811–818.

[148] Keidar, M., Boyd, I. D., and Beilis, I. I., "On the model of Teflon ablation in an ablation-controlled discharge," *Journal of Physics D*, Vol. 34, 2001, pp. 1675–1677.

[149] Henrikson, E. and Mikellides, P., *Modeling of Ablation-Fed Pulsed Plasma Thruster Operation Using a New Approach to the Ablation Process*.

[150] Cho, M. and Sung, H.-G., "Numerical Modeling of Pulsed Plasma Thruster Performance with Teflon Ablation and Ionization," *International Journal of Aeronautical and Space Sciences*, Vol. 20, 2019, pp. 415–422.

[151] Ziemer, J. and Choueiri, E., "Dimensionless performance model for gas-fed pulsed plasma thrusters," *34th AIAA/ASME/SAE/ASEE Joint Propulsion Conference and Exhibit*, 1998, p. 3661.

[152] Brito, C. M., Elaskar, S. A., Brito, H. H., and Paoletti, N. R., "Zero-Dimensional Model for Preliminary Design of Ablative Pulsed Plasma Teflon Thrusters," *Journal of Propulsion and Power*, Vol. 20, No. 6, 2004, pp. 970–977.

[153] Pottinger, S. J., Krejci, D., and Scharlemann, C. A., "Pulsed plasma thruster performance for miniaturised electrode configurations and low energy operation," *Acta Astronautica*, Vol. 68, No. 11, 2011, pp. 1996–2004.

[154] Misra, K., "Detonation–deflagration one-dimensional mode transition analysis for parallel-plate plasma accelerators," *CEAS Space Journal*, Vol. 12, 2019, pp. 203 – 212.

[155] Polzin, K. A., Sankaran, K., Ritchie, A. G., and Reneau, J. P., "Inductive pulsed plasma thruster model with time-evolution of energy and state properties," *Journal of Physics D: Applied Physics*, Vol. 46, No. 47, oct 2013, pp. 475201.

[156] Turchi, P., Mikellides, I., Mikellides, P., and Schmahl, C., *Theoretical investigation of pulsed plasma thrusters*.

[157] Gatsonis, N. A. and Yin, X., "Hybrid (Particle-Fluid) Modeling of Pulsed Plasma Thruster Plumes," *Journal of Propulsion and Power*, Vol. 17, No. 5, 2001, pp. 945–958.

[158] Thio, Y. C., Cassibry, J., and Wu, S., "2-D Magnetohydrodynamic Modeling of A Pulsed Plasma Thruster," *NASA STI/Recon Technical Report N*, Vol. 3, 12 2001, pp. 02827.

[159] Henrikson, E. M., Mikellides, P. G., and Kamhawi, H., "Experimental and numerical characterization of ablation-fed pulsed plasma thruster prototype," *Proc. of 31st International Electric Propulsion Conference, University of Michigan, Ann Arbor, MI. IEPC-2009-246*, 2009.

[160] Popov, G., Khrustalev, M., Khrabrov, V., Antropov, N., and Lyubinskaya, N., "Physicomathematical Model of Plasma Acceleration in an Ablative Pulsed Plasma Thruster," *Plasma Physics Reports*, Vol. 40, 05 2014, pp. 336–342.

[161] Hoskins, W. A., Rayburn, C., and Sarmiento, C. J., "Pulsed Plasma Thruster Electromagnetic Compatibility: History, Theory, and the Flight Validation on E0-1," *39th AIAA/ASME/SAE/ASEE Joint Propulsion Conference and Exhibit*, 2003.

[162] Kronhaus, I., Laterza, M., and Linossier, A. R., "Experimental Characterization of the Inline-Screw-Feeding Vacuum-Arc-Thruster Operation," *IEEE Transactions on Plasma Science*, Vol. 46, No. 2, 2018, pp. 283–288.

[163] Poehlmann, F. R., Cappelli, M. A., and Rieker, G. B., "Current distribution measurements inside an electromagnetic plasma gun operated in a gas-puff mode," *Physics of Plasmas*, Vol. 17, No. 12, 12 2010, pp. 123508.

[164] Villegas-Prados, D., Kazadi, J., Fajardo, P., and Wijnen, M., "Emission characterization of externally wetted electrospray thrusters using computed tomography," *38th International Electric Propulsion Conference*, 2024.

[165] Ramlau, R. and Scherzer, O., "The first 100 years of the Radon transform," *Inverse Problems*, Vol. 34, No. 9, jul 2018, pp. 090201.

[166] Pantechnik, "OneWeb (Eutelsat Group)." Accessed on November 28th, 2024.

[167] Zhang, Z., Zhang, Z., Ling, W. Y. L., Han, X., Zhou, J., Tang, H., and Cao, J., "Time-resolved investigation of the asymmetric plasma plume in a pulsed plasma thruster," *Journal of Physics D: Applied Physics*, Vol. 53, No. 47, aug 2020, pp. 475201.

[168] Hoskins, A., Sarmiento, C., Rayburn, C., and Campbell, M., *Pulsed Plasma Thruster Electromagnetic Compatibility Studies*.

[169] Meckel, N., Hoskins, W., Cassady, R., Myers, R., Oleson, S., and McGuire, M., *Improved pulsed plasma thruster systems for satellite propulsion*.

[170] Hruby, P., Demmons, N., Courtney, D., Tsay, M., Szabo, J., and Hruby, V., "Overview of Busek electric propulsion," *36th International Electric Propulsion Conference (University of Vienna, Vienna, Austria*, 2019, pp. 15–20.

[171] Woodruff, C. A., Parta, M., King, D. M., Burton, R. L., and Carroll, D. L., "Fiber-fed Pulsed Plasma Thruster (FPPT) with Multi-axis Thrust Vectoring," *37th International Electric Propulsion Conference*, 2022.

[172] Markusic, T., Thio, Y., and Cassibry, J., "Design of a High-energy, Two-stage Pulsed Plasma Thruster," *Joint Propulsion Conference and Exhibit*, AIAA 2002-4125, Indianapolis, IN, 2002.

[173] Páscoa, J. C., Teixeira, O., and Filipe, G., "A Review of Propulsion Systems for CubeSats," *Volume 1: Advances in Aerospace Technology*, 2018.

[174] Antropov, N., Bogatyy, A., Boykachev, V., Dyakonov, G., Lyubinskaya, N., Popov, G., Semenikhin, S., Tyutin, V., and Yakovlev, V., "Development of Russian Next-generation Ablative Pulsed Plasma Thrusters," *Procedia engineering*, Vol. 185, 2017, pp. 53–60.

[175] Myers, R., Oleson, S., McGuire, M., Meckel, N., and Cassady, R., "Pulsed plasma thruster technology for small satellite missions," 12 1995.

[176] Lau, M. and Herdrich, G. H., "Pulsed Plasma Thruster Endurance Operation Stress Testing at IRS IEPC-2013-255," 2013.

[177] Wu, Z., Sun, G., Liu, Z., Liu, X., Xie, K., and Wang, N., "Characteristics of plasma properties in double discharge ablative pulsed plasma thrusters," *Physics of Plasmas*, Vol. 24, No. 11, 2017, pp. 113521.

[178] Shimhanda, S., Hiraka, K., Murakami, H., Toyoda, K., and Cho, M., "A Performance Comparison of Solid Propellants in Surface Arc Thruster: Sulfur and Teflon," 09 2019.

[179] Xi, W., Guo, L., Liu, D., Zhou, R., Wang, Z., Wang, W., Liu, Z., Wang, X., Ostrikov, K. K., and Rong, M., "Upcycle hazard against other hazard: Toxic fluorides from plasma fluoropolymer etching turn novel microbial disinfectants," *Journal of Hazardous Materials*, Vol. 424, 2022, pp. 127658.

[180] Li, Y., Ou, Y., Wu, J., and Zhang, Y., "Experimental Investigation on Plume Characteristics of PTFE-Filled Carbon, Graphite, Graphene for Laser-Assisted Pulsed Plasma Thruster," *Applied Sciences*, Vol. 13, 08 2023, pp. 9283.

[181] Zhu, C., Jin, X., Zhang, Z., and Li, N., "Design and test of a laser assisted pulsed plasma thruster prototype," *IOP Conference Series: Earth and Environmental Science*, Vol. 300, No. 4, jul 2019, pp. 042074.

[182] Guman, W. J. and Nathanson, D. M., "Pulsed Plasma Microthruster Propulsion System for Synchronous Orbit Satellite," *J. Spacecraft*, Vol. 7, No. 4, 1970, pp. 409–415.

[183] KUMAGAI, N., SATO, K., TAMURA, K., KAWAHARA, K., KOIDE, T., TAKEGAHARA, H., SUGIKI, M., WAKIZONO, T., and HASHIMOTO, H., "RESEARCH AND DEVELOPMENT STATUS OF LOW POWER PULSED," .

[184] Shinohara, S. and Tanikawa, T., "Characteristics of a large volume, helicon plasma source," *Physics of Plasmas*, Vol. 12, 2005, pp. 044502.

[185] Coletti, M., Guarducci, F., and Gabriel, S., "A micro PPT for Cubesat application: Design and preliminary experimental results," *Acta Astronautica*, Vol. 69, No. 3, 2011, pp. 200–208.

[186] Mingo Perez, A., Coletti, M., and Gabriel, S., "A micro PPT for Nano-satellite applications: Design and experimental results," *48th AIAA/ASME/SAE/ASEE Joint Propulsion Conference & Exhibit*, 2012, p. 4279.

[187] Huang, T., Wu, Z., Liu, X., Xie, K., Wang, N., and Cheng, Y., "Study of breakdown in an ablative pulsed plasma thruster," *Physics of Plasmas*, Vol. 22, No. 10, 2015, pp. 103511.

[188] Guman, W. J., "Pulsed Plasma Technology in Microthrusters," 1968.

[189] Gessini, P. and Paccani, G., "Ablative Pulsed Plasma Thruster System Optimization for Microsatellites," 2001.

[190] Burton, R. and Bushman, S., *Probe measurements in a coaxial gasdynamic PPT*.

[191] Markusic, T. E., Berkery, J. W., and Choueiri, E. Y., "Visualization of current sheet evolution in a pulsed plasma accelerator," *IEEE Transactions on Plasma Science*, Vol. 33, No. 2, 2005, pp. 528–529.

[192] Poehlmann, F. and Gascon, N., "The Deflagration - Detonation Transition in Gas-Fed Pulsed Plasma Accelerators," 2007.

[193] Polzin, K., Greve, C., and Sankaran, K., "Pulsed Plasma Acceleration Modeling in Detonation and Deflagration Modes," *IEPC*, Vol. 893, 2019, pp. 2019.

[194] Ziemer, J., Cubbin, E., Choueiri, E., Birx, D., Ziemer, J., Cubbin, E., Choueiri, E., and Birx, D., "Performance characterization of a high efficiency gas-fed pulsed plasma thruster," *33rd Joint Propulsion Conference and Exhibit*, paper 1997-2925, American Institute of Aeronautics and Astronautics, Reston, VA, Seattle, Washington, July 6-9, 1997.

[195] Scharlemann, C. A., *Investigation of thrust mechanisms in a water-fed pulsed plasma thruster*, Ph.D. thesis, The Ohio State University, 2003.

[196] Ziemer, J., Choueiri, E., and Birx, D., "Comparing the performance of co-axial and parallel-plate gas-fed PPTs," *26th International Electric Propulsion Conference, Kitakyushu, JAPAN*, 1999, pp. 99–209.

[197] Berkery, J. and Choueiri, E. Y., "Canted current sheet mass leakage and its impact on pulsed plasma thruster performance," *40th AIAA Joint Propulsion Conf., Fort Lauderdale, FL*, 2004.

[198] Ziemer, J. and Choueiri, E., "Scaling laws for electromagnetic pulsed plasma thrusters," *Plasma Sources Science and Technology*, Vol. 10, No. 3, 2001, pp. 395.

[199] VONDRA, R., "A final report on the LES-8/9 pulsed plasma thruster," .

[200] Guman, W. J. and Williams, T. E., "Pulsed plasma microthruster for synchronous meteorological satellite," *Journal of Spacecraft and Rockets*, Vol. 11, No. 10, 1974, pp. 729–731.

[201] EBERT, W., KOWAL, S., and SLOAN, R., "Operational Nova spacecraft teflon pulsed plasma thruster system," *25th Joint Propulsion Conference*, 1989, p. 2497.

[202] HIRATA, M. and MURAKAMI, H., *Electromagnetic noise measurement study of pulsed plasma engine*.

[203] Hirata, M. and Murakami, H., "Exhaust Gas Analysis of a Pulsed Plasma Engine," *AIAA Paper*, 1984.

[204] Hirata, M. and Murakami, H., "Development of a Pulsed Plasma Engine," *17th IEPC*, 1984.

[205] An, S.-M., Wu, H.-J., Feng, X.-Z., and Liu, W.-X., "Space Flight Test of Electric Thruster System MDT-2A," *Journal of Spacecraft and Rockets*, Vol. 21, No. 6, 1984, pp. 593–593.

[206] Arrington, L. A., Haag, T. W., Pencil, E. J., and Meckel, N. J., *A performance comparison of pulsed plasma thruster electrode configurations*, National Aeronautics and Space Administration, Lewis Research Center, 1997.

[207] Zalawski, C., Benson, S., Smernan, P., and Hoskins, A., "On-Orbit Testing of the EO-1 Pulsed Plasma Thruster," .

[208] Burton, R., Woodruff, C., King, D., and Carroll, D., "Analysis of Fiber-Fed Pulsed Plasma Thruster Performance," *Journal of Propulsion and Power*, Vol. 37, 10 2020, pp. 1–3.

[209] Murphy, D. and Wie, B., "Robust Thrust Control Authority for a Scalable Sailcraft," 2004.

[210] Kawahara, K., Kumagai, N., Sato, K., Tamura, K., Koide, T., Harima, K., Fukushima, T., and Takegahara, H., "Study on plume characteristics of pulsed plasma thruster," *International Electric Propulsion Conference Paper*, 2003, pp. 03–160.

[211] Sin, G.-H., Nam, M.-Y., Gang, G.-I., Im, J.-T., and Cha, W.-H., "On Stability of the Pulsed Plasma Thruster for STSAT-2 based on the Lyapunov Function," *Journal of the Korean Society for Aeronautical & Space Sciences*, Vol. 34, No. 1, 2006, pp. 95–102.

[212] Tahara, H., Ishii, Y., Tanaka, M., Naka, M., and Watanabe, Y., "Flowfield calculation of electrothermal pulsed plasma thrusters for the proiteres satellite," *32nd International Electric Propulsion Conference*, 2011.

[213] Kisaki, S., Ikeda, T., Inoue, Y., Egami, N., and Tahara, H., "Development of highly-functional nano/small satellites with pulsed plasma engines," *2012 International Conference on Renewable Energy Research and Applications (ICRERA)*, 2012, pp. 1–7.

[214] Fujita, R. and Tahara, H., *Development of Electrothermal Pulsed Plasma Thruster Systems onboard Osaka Institute of Technology PROITERES Nano-Satellites*.

[215] Ryuho, K., Fujita, R., Kanaoka, K., Ono, K., Morikawa, N., Enomoto, K., Hasse, T., and Wakizono, T., "Numerical Calculation of Electrothermal Pulsed Plasma Thrusters by One-Dimensional Flowfield Model," *35th International Electric Propulsion Conference*, 2017.

[216] Unegawa, T., Uedahira, M., Aoyagi, K., Shimada, T., Tahara, H., Ikeda, T., Takao, Y., and Wakizono, T., "Research and Development of High Total Impulse Electrothermal Pulsed Plasma Thruster Systems from Charging Electric Energy/Power: 1J/1W for 1U(1kg) Cubesats to 50J/50W for 50cm Cube (50kg) Nano Satellites," *37th International Electric Propulsion Conference*, 2022.

[217] Aoyagi, K., Shimada, T., Uedahira, M., Unegawa, T., Itsuki, T., Tahara, H., Ikeda, T., Takao, Y., and Wakizono, T., "Development of Osaka Sangyo University 1U Cubesat OSU 1 with 1J/1W Pulsed Plasma Thruster Systems for Powered Flight, and Development Features of Nano Satellites and Probes OSU 2, 3 and 4," *37th International Electric Propulsion Conference*, 22022.

[218] Antropov, N., Bogatyy, A., Dyakonov, G., Lyubinskaya, N., Popov, G., Semenikhin, S., Tyutin, V., Khrustalev, M., and Yakovlev, V., "A new stage in the development of ablative pulsed plasma thrusters at the RIAME," *Solar System Research*, Vol. 46, No. 7, 2012, pp. 531–541.

[219] Scharlemann, C., Seifert, B., Schnitzer, R., Kralofsky, R., Obertscheider, C., Taraba, M., Dorn, T., Turetschek, T., Fauland, H., Plötzeneder, R., Stockinger, R., Schmid, M., Riel, T., Sinn, A., Janisch, G., Deisl, F., Kohl, D., Lybekk, B., Hoang, H., and Trondsen, E., "PEGASUS-a review of in-orbit operation and obtained results," 01 2018.

[220] Kim, S., Orger, N. C., Cordova-Alarcon, J. R., Hernandez-Herrera, M., Masui, H., Yamauchi, T., Toyoda, K., Cho, M., Duy Vu, B. T., Vinh, T. Q., Seng, L. W., and Hiang, C. T., "AOBA VELOX-IV: 2U CubeSat for the technological demonstration of lunar horizon glow mission," *Acta Astronautica*, Vol. 161, 2019, pp. 328–337.

[221] Zhang, Z., Schäfer, F., Zhang, G., Tang, H., Ling, W. Y. L., Herdrich, G., and York, T. M., "Investigation on operational stability of a pulsed plasma thruster with a pressure probe," *Acta Astronautica*, Vol. 197, 2022, pp. 60–68.

[222] Nawaz, A., Lau, M., Herdrich, G., and Auweter-Kurtz, M., "Investigation of the Magnetic Field in a Pulsed Plasma Thruster," *AIAA Journal*, Vol. 46, No. 11, 2008, pp. 2881–2889.

[223] Schönherr, T., Komurasaki, K., Kawashima, R., Arakawa, Y., and Herdrich, G., "Evaluation of discharge behavior of the pulsed plasma thruster SIMP-LEX," *46th AIAA/ASME/SAE/ASEE Joint Propulsion Conference & Exhibit*, 2010, p. 6530.

[224] Tony Schönherr, Kimiya Komurasaki, S. H. Y. A. and Herdrich, G., "Application of Mechanical Probes for Evaluation of Plasma Acceleration in Ablative PPT," *IEEE Transactions on Plasma Science*, Vol. 43, No. 1, 2015.

[225] Schönherr, T., Stein, M., Komurasaki, K., and Herdrich, G., "Investigation of discharge arc phenomena in ablative PPT," *IEPC-2015-79*, 2015.

[226] Zhang, Z., Zhang, Z., Tang, H., Ling, W. Y. L., Qi, J., and Cao, J., "Diagnostics of ion and electron diffusion in pulsed plasma thrusters using neutral gas injection," *Plasma Sources Science and Technology*, Vol. 29, No. 4, mar 2020, pp. 045006.

[227] Zhang, Z., Ren, J., Tang, H., Ling, W. Y. L., and York, T. M., "An ablative pulsed plasma thruster with a segmented anode," *Plasma Sources Science and Technology*, Vol. 27, No. 1, dec 2017, pp. 015004.

[228] Aoyagi, J., Oguri, Y., Batchuluun, B., and Mori, A., "Effect of Electrodes Dimensions of 2 J Electromagnetic Pulsed Plasma Thruster for Small Satellites," *37th International Electric Propulsion Conference*, No. IEPC-2022-567, Electric Rocket Propulsion Society, Fairview Park, OH, 2022.

[229] LeVeque, R. J., *Finite Volume Methods for Hyperbolic Problems*, Cambridge Texts in Applied Mathematics, Cambridge University Press, 2002.

[230] Kuninaka, H., Nishiyama, K., Funaki, I., Yamada, T., Shimizu, Y., and Kawaguchi, J., "Powered flight of electron cyclotron resonance ion engines on Hayabusa explorer," *Journal of Propulsion and Power*, Vol. 23, No. 3, 2007, pp. 544–551.

[231] Kuninaka, H., Nishiyama, K., Funaki, I., Shimizu, Y., Yamada, T., and Kawaguchi, J., "Assessment of Plasma Interactions and Flight Status of the HAYABUSA Asteroid Explorer Propelled by Microwave Discharge Ion Engines," *IEEE Transactions on Plasma Science*, Vol. 34, No. 5, 2006, pp. 2125–2132.

[232] TSUKIZAKI, R., KOIZUMI, H., HOSODA, S., NISHIYAMA, K., and KUNINAKA, H., "Improvement of the Thrust Force of the ECR Ion Thruster mu;10," *TRANSACTIONS OF THE JAPAN SOCIETY FOR AERONAUTICAL AND SPACE SCIENCES, AEROSPACE TECHNOLOGY JAPAN*, Vol. 8, No. ists27, 2010, pp. $Pb_6 7 - -Pb_7 2$.

[233] Nishiyama, K., Hosoda, S., Tsukizaki, R., and Kuninaka, H., "In-flight operation of the Hayabusa2 ion engine system on its way to rendezvous with asteroid 162173 Ryugu," *Acta Astronautica*, Vol. 166, 2020, pp. 69–77.

[234] Kuninaka, H. and Satori, S., "Development and demonstration of a cathodeless electron cyclotron resonance ion thruster," *Journal of Propulsion and Power*, Vol. 14, No. 6, 1998, pp. 1022–1026.

[235] Kuninaka, H., Nishiyama, K., Shimizu, Y., and Toki, K., *Flight Status of Cathode-Less Microwave Discharge Ion Engines Onboard HAYABUSA Asteroid Explorer*.

[236] Tsukizaki, R., Ise, T., Koizumi, H., Togo, H., Nishiyama, K., and Kuninaka, H., "Thrust enhancement of a microwave ion thruster," *Journal of Propulsion and Power*, Vol. 30, No. 5, 2014, pp. 1383–1389.

[237] Tsukizaki, R., Yamashita, Y., Kinefuchi, K., and Nishiyama, K., "Neutral atom density measurements of xenon plasma inside a 10 microwave ion thruster using two-photon laser-induced fluorescence spectroscopy," *Vacuum*, Vol. 190, 2021, pp. 110269.

[238] Tani, Y., Tsukizaki, R., Koda, D., Nishiyama, K., and Kuninaka, H., "Performance improvement of the 10 microwave discharge ion thruster by expansion of the plasma production volume," *Acta Astronautica*, Vol. 157, 2019, pp. 425–434.

[239] Ozaki, N., Yamamoto, T., Gonzalez-Franquesa, F., Gutierrez-Ramon, R., Pushparaj, N., Chikazawa, T., Tos, D. A. D., Çelik, O., Marmo, N., Kawakatsu, Y., Arai, T., Nishiyama, K., and Takashima, T., "Mission design of DESTINY+: Toward active asteroid (3200) Phaethon and multiple small bodies," *Acta Astronautica*, Vol. 196, 2022, pp. 42–56.

[240] Fazio, N., Gabriel, S., and Golosnoy, I., "Alternative propellants for gridded ion engines," 05 2018.

[241] Fazio, N., Gabriel, S., Golosnoy, I., and Wollenhaupt, B., "Mission Cost for Gridded Ion Engines using Alternative Propellants," 09 2019.

[242] Kim, Y., Lee, D., Doh, G., Park, J., and Choe, W., "Performance comparison of xenon and krypton discharges in a 300 W-class Hall thruster," 06 2022.

[243] Su, L. L. and Jorns, B. A., "Investigation into the Acceleration Region Dynamics of a Magnetically Shielded Hall Thruster Operating on Krypton," *2022 IEEE International Conference on Plasma Science (ICOPS)*, 2022, pp. 1–2.

[244] Esteves, B., Drag, C., Bourdon, A., Alvarez Laguna, A., and Chabert, P., "Experimental and numerical investigation of a gridded ion thruster running with different propellants (I2, Xe, Kr, Ar)," 06 2022.

[245] Morishita, T., Tsukizaki, R., Nishiyama, K., and Kuninaka, H., "Plasma parameters measured inside and outside a microwave-discharge-based plasma cathode using laser-induced fluorescence spectroscopy," *Journal of Applied Physics*, Vol. 131, No. 1, 2022.

[246] Yamashita, Y., Tsukizaki, R., Kinefuchi, K., Koda, D., Tani, Y., and Nishiyama, K., "Neutral ground state particle density measurement of xenon plasma in microwave cathode by two-photon laser-induced fluorescence spectroscopy," *Vacuum*, Vol. 168, 2019, pp. 108846.

[247] Yamashita, Y., Tsukizaki, R., and Nishiyama, K., "Investigation of plasma mode transition and hysteresis in electron cyclotron resonance ion thrusters," *Plasma Sources Science and Technology*, Vol. 30, No. 9, sep 2021, pp. 095023.

[248] Yamashita, Y., Tsukizaki, R., Daiki, K., Tani, Y., Shirakawa, R., Hattori, K., and Nishiyama, K., "Plasma hysteresis caused by high-voltage breakdown in gridded microwave discharge ion thruster 10," *Acta Astronautica*, Vol. 185, 2021, pp. 179–187.

[249] Goebel, D., Katz, I., and Mikellides, I., *Fundamentals of electric propulsion*, John Wiley & Sons, 2023.